Dynamic chirality and failure in structured materials with applications

Marta Garau

Submitted in partial fulfilment of the requirements of the degree of

Doctor of Philosophy

School of Computing and Mathematics, Keele University.

March 2020

Declaration

I certify that this thesis submitted for the degree of Doctor of Philosophy is the result of my own research, except where otherwise acknowledged, and that this thesis (or any part of the same) has not been submitted for a higher degree to any other university or institution.

Signed: Marta Garau

Date: .....

Abstract

We consider the vibration of two classes of discrete periodic systems and the resulting dynamic effects. We analyse elastic lattices connected to arrays of gyroscopic spinners, that confer chirality to the elastic system. It is shown in the time-harmonic regime that these systems support special dynamic phenomena at various frequencies, including interfacial waves in elastic materials attached to inhomogeneous arrays of spinners. We derive a new asymptotic model that characterises the interaction between a gyroscope and an elastic truss system in the transient regime. This asymptotic model is verified with an independent finite element simulation and the model is used to confirm the identified waveforms can be realised through a transient analysis, where initial conditions and loading of the system play a greatrole. Two advanced technological applications of gyro-elastic systems are also proposed, including a topological insulator and an elastic cloaking device for a discrete lattice.

The influence of vibration on failure processes in discrete flexural systems is also studied. We consider the model of a flexural system undergoing failure at an uniform rate as a result of the action of a remote mechanical sinusoidal load. This simplified model may represent the collapse of a civil engineering structure, such as a bridge, rooftop or pipeline system, exposed to hazardous vibrations resulting from, say, an earthquake. The problem is reduced to a functional equation of the Wiener-Hopf type, through the Fourier transform, that allows for the characterisation of possible failure regimes and the dynamics of the structure undergoing failure through its solution. The model is used to predict the outcomes of a numerical scheme developed in *Matlab* to analyse the failure in a sufficiently long finite medium subjected to a sinusoidal load.

Acknowledgements

First of all, I would like to express my gratitude to my supervisor Dr. Michael Nieves for giving me the opportunity to get in touch with the world of the research. I am grateful for the help he provided and his willingness demonstrated to me in these three years that enabled me to understand the work considered and allowed me to write this thesis. I was also grateful to have worked with him on the EU H2020 grant MSCA-IF-2016-747334-CAT-FFLAP on which a majority of this work was completed.

Thank you to Prof. Julius Kaplunov, my second supervisor, for his support and in helping disseminate the results of this work.

A rightful thanks goes to the Liverpool Waves Group, Prof. Natasha Movchan, Prof. Alexander Movchan and Prof. Ian Jones, who provided me with the possibility to collaborate with them, and to Prof. Michele Brun from the University of Cagliari, which provided me with fundamental help.

A special thanks to Dr Giorgio Carta for his important support in not only with the work undertaken but also for his moral support, together with Maria's. I was able to count on them in moments of happiness and discouragement in the doctoral course.

Furthermore, I would like to thank Oz, Luca, Sara, Domenico, Stewart, Bibinur and Anar, in which I found good friends that in different ways have enriched my life in the last years.

A big thank you to my parents, my brother and his wonderful family. Their unfailing support brought me to achieving this goal. Finally, thanks to Pierluigi, my force, I could never take this important path without him.

Disseminations

Journal Papers

M. Garau, G. Carta, M.J. Nieves, I.S. Jones, N.V. Movchan and A.B. Movchan (2018): *Interfacial waveforms in chiral lattices with gyroscopic spinners*, Proc. Roy. Soc. A. 474, 20180132.

M. Garau, M.J. Nieves, G. Carta and M. Brun (2019): *Transient analysis of a gyro-elastic structured medium: unidirectional waveforms and cloaking*, Int. J. Eng. Sci. (accepted)

M. Garau, M.J. Nieves and I.S. Jones (2019): *Alternating strain regimes for failure in flexural systems*, Q. J. Mech. Appl. Math, 0, doi.org/10.1093/qjmam/hbz008.

Conference Papers

M.J. Nieves, M. Garau, G. Carta, I.S. Jones, N.V. Movchan and A.B. Movchan (2018): *Design of a chiral elastic structure supporting interfacial waveforms.* 12^{th} International Congress on Artificial Materials for Novel Wave Phenomena - Metamaterials 2018, Espoo, Finland.

M. Garau, M.J. Nieves, G. Carta and M. Brun (2019): *A gyro-elastic device for cloaking of elastic waves in micro-structured materials.* 13^{th} International Congress on Artificial Materials for Novel Wave Phenomena - Metamaterials 2019, Rome, Italy. (accepted)

Presentations

The 60th British Applied Mathematics Colloquium (BAMC 2018), Saint Andrews, Scotland, 26-29 March 2018 (28th March 2018).

The 10th European Solid Mechanics Conference (ESMC 2018), Bologna, Italy, 2-6 July 2018 (3rd July 2018).

Nomenclature

Chapters 2-3

Quantity	Symbol of Dimensional Quantity	Unit	Normalised Quantity	Page
Density	ρ	kg/m^3		
Displacement	w, u, W, U	m		
Young's modulus	E	N/m^2		
Cross section	A	m^2		
Applied load	P	N		
Link stiffness	c	N/m	$\tilde{c} = 1$	57
Link length	l	m		
Mass	m	kg		
Radian frequency	ω	rad/s	$\tilde{\omega} = \omega\sqrt{m/c}$	57
Wave number	k	1/m	$\tilde{k} = kl$	57
Time period	τ	s		
Phase speed	v_f	m/s		
Stress	σ	N/m^2		
Group velocity	v_g	m/s		
Euler's angles	ϕ, θ, ψ	rad		
External moments	M_{x_1}, M_{x_2}, M_{x_3}	N m		
Moments of inertia	I_0, I_1	kg m^2		

Chapters 2-3 (Continued)

Quantity	Symbol of Dimensional Quantity	Unit	Normalised Quantity	Page
Spin rate	Ω	rad/s		
Spinner constant	β	kg	$\tilde{\beta} = \beta/m$	57
Spinner matrix	$\mathbf{A}$	kg	$\tilde{\mathbf{A}} = \mathbf{A}/m$	57
Stiffness matrix	$\mathbf{C}$	N/m	$\tilde{\mathbf{C}} = \mathbf{C}/c$	57

Chapters 4-5

Quantity	Symbol of Dimensional Quantity	Unit	Normalised Quantity	Page
Link length	L	m		
Gyroscope length	l	m	$\tilde{l} = 1$	100
Gyroscope parameter			α	90
Gyricity	Ω	rad/s		
Time	t	s	$\tilde{t} = t\sqrt{\frac{c}{m\,(1+I_0/(m\,l^2))}}$	100
External force	F	N	$\tilde{F} = F/(c\,L)$	100
External moment	M_e	N m	$\tilde{M}_e = M_e/(c\,L\,l)$	100
Moments of inertia	I_0, I_1	kg m^2	$\tilde{I}_j = \frac{I_j}{m\,l\,L}$, $j = 0, 1$	100

Chapter 6

Quantity	Symbol of Dimensional Quantity	Unit	Normalised Quantity	Page
Mass	M	kg		
Young's modulus	$E_j, j = 1, 2$	N/m^2		
Second moment of area	$I_j, j = 1, 2$	m^4		
Link length	a	m		
Displacement	$w_m(t)$	m	$w_m(t)/a$	161
Time	t	s	$\tilde{t} = t\sqrt{\frac{E_1 I_1}{M a^3}}$	161
Speed	V	m/s	$\tilde{v} = V\sqrt{\frac{M a}{E_1 I_1}}$	161
Applied load	$Q_m(t)$	N	$\tilde{Q}_m(\tilde{t}) = \frac{a^2 Q_m(t)}{E_1 I_1}$	161

Contents

List of Figures

List of Tables

Chapter 1

Introduction and Literature Review

1.1 Motivation

Metamaterials, or media with microstructure, are currently paving new pathways in the design of the novel materials. There exists a significant amount of research into the modelling and experimental design of metamaterials as they possess special properties and can achieve counter intuitive effects that cannot be realised in conventional materials. Some effects include rendering objects invisible by appropriately guiding electromagnetic waves in light, materials that expand in the directions perpendicular to the direction in which they are stretched and materials that contract when heated. Due to modern manufacturing techniques, some of these materials have been realised. Moreover, the applications of metamaterials are wide, ranging from small scale applications such as the design of new materials to large scale applications to control civil engineering structures.

From a modelling perspective, mechanical metamaterials can be easily designed by using fundamental mechanical elements such as beams, rods and masses to form their microstructure, and the properties of these elements can be tuned to achieve remarkable effects. More recently, a new breed of metamaterials has emerged that utilise the notion of a gyroscope interacting with an elastic structure. These "gyro-

elastic" materials have led to design of innovative materials with properties that are capable of being used in applications such as earthquake protection, cloaking (to hide defects from external disturbances) and shielding (to create a protective or deflection barrier).

A main aim of the present work is to expand on the existing knowledge of gyro-elastic metamaterials to create new concepts for designing these systems with a view to obtaining special dynamic effects that can be used in technologically advanced applications.

Additionally, most of the research into metamaterials is being carried out with the objective of finding new methods for controlling and supporting surprising wave phenomena. However, these studies are mostly conducted without considering the structural integrity of the metamaterials and questions about their ability to withstand these wave processes still remain. This is paramount, especially if the metamaterials are designed for civil engineering applications, where ignoring this factor could lead to a detrimental impact on human life. Research into how such systems undergo failure is limited. Therefore, with this in mind, in this thesis we will also further develop the analysis of failure processes in a particular class of metamaterials that may represent a simplified model of how a bridge, rooftop or pipeline system collapses.

1.2 Literature review

Gyro-elastic interactions and systems

Gyro-elastic structured media possess unique dynamic properties, achievable at both low and high frequencies, that cannot be realised with other mechanical systems. A gyro-elastic structured medium is comprised of arrays masses, connected to each other by elastic links (such as rods or beams) and attached to gyroscopic spinners (a device which is essentially a body or mass which spins on its axis). The latter supply a dynamic “chiral" nature to the lattice system, which bestows the medium

with special dynamic properties.

"Chirality" is the property of an object whereby it cannot be superimposed onto its mirror image [Thomson (1894)]. Chirality is commonly used in the design of elastic lattices that can effectively behave as auxetic materials [Prall and Lakes (1997), Spadoni and Ruzzene (2012)] and to alter the dynamic properties of a system [Spadoni et al. (2009), Bacigalupo and Gambarotta (2016)]. It has also been used to generate negative refraction [Zhu et al. (2014), Tallarico et al. (2016)] in structured materials.

The first gyro-elastic system was proposed in [Brun, Jones and Movchan (2012)], where both a monatomic and a biatomic triangular lattice attached to uniform arrays of gyroscopic spinners were analysed. The dispersion properties of a monatomic gyro-elastic lattice were discussed in more detail in [Carta et al. (2014)], with the attention focused on wave polarisation and standing waves. In [Carta et al. (2017a)], a uniform elastic structured medium attached to a doubly periodic array of gyroscopic spinners was shown to support vibrations in the form of a Gaussian beam at a specific frequencies. There, when the medium is loaded at particular frequencies the energy produced by the load is confined to a single line of the lattice. In particular, by interchanging the arrangement of gyroscopes in regions of this lattice, it was demonstrated that the path of the Gaussian beam can be controlled, without producing any scattering into the bulk of the lattice. This has led to designs of structured materials that can force waves resulting from a harmonic load to follow a closed path without significant reduction of the load amplitude. This phenomenon has been named DASER (Dynamic Amplification by Spinners in Elastic Reticulated systems). These effects are further described in Chapter 3.

The design of gyro-elastic lattices uses concepts taken from structural mechanics to describe the overall movement of the structured medium, together with those from classical mechanics governing the motion point masses and the gyroscopes. Recently, a renewed interest in structural mechanics has been prompted by the wide technological applications that structured systems can offer, including applications in locomotion [Bigoni et al. (2014), Dal Corso et al. (2017), Rafsanjani et al. (2018)], structural

folding [Bosi et al. (2015)], soft robotics [Armanini et al. (2017), Cazzolli and Dal Corso (2019)], and metamaterials [Kochmann and Bertoldi (2017), Misseroni et al. (2016), Bordiga et al. (2018), Cabras, Movchan and Piccolroaz (2017), Piccolroaz, Movchan and Cabras (2017a), Piccolroaz, Movchan and Cabras (2017b)], and the use of quasi-periodic microstructural geometries to control wave phenomena in rods [Morini and Gei (2018)], with a view to the extension in analysing the dynamics of layered composites with a quasi-crystalline type stratification [Morini, Eyzat and Gei (2019)]. In particular, gyroscopic effects in mechanical systems and their stability in the presence of non-conservative forces has been studied in [Kirillov (2009), Kirillov (2013)].

The transient motion of a gyroscopic spinner is geometrically non-linear, which results from the solution of a collection of non-linear differential equations known as Euler-equations. However, if one of the three angles which characterise the gyroscope, the nutation angle, is small, its motion and influence on an elastic structure can be described by a linearised model, as carried out in [Brun, Jones and Movchan (2012)] for the time-harmonic regime. Here, we present for the first time a novel asymptotic model characterising the transient motion of such systems and show that this brings new physical effects and parameters to the modelling of a gyro-elastic system (see Chapter 4). Even within this linearised setting, masses in a gyro-elastic medium can undergo a range of atypical trajectories depending on the properties of the system.

Applications of gyro-elastic systems to wave-guiding

Gyroscopic spinners can be utilised to break time-reversal symmetry and create *topologically protected modes*. Recently, systems supporting *topologically protected edge modes* have attracted increasing attention. In such systems, known as "topological insulators", waves propagate along the edges of the medium. These waves are not scattered backwards and do not propagate inside the medium, even when interacting with imperfections or discontinuities (such as sharp vertices and defects). Topological insulators generally possess a non-trivial topology within the band structure, associated with the presence of dispersion degeneracies or Dirac points at the corners

of the Brillouin zone.

The existence of edge modes propagating in one preferential direction is a phenomenon first identified for photonic crystals [Raghu and Haldane (2008), Wang et al. (2008), Wang et al. (2009), He et al. (2010), Khanikaev et al. (2013), Lu et al. (2014), Gao et al. (2015), Skirlo et al. (2015)], and can be linked to electronic edge states in systems exhibiting the quantum Hall effect [Klitzing et al. (1980)]. Unidirectional topologically protected interfacial states have been identified in [Siroki, Huidobro and Giannini (2017)] for photonic crystals composed of two regions, each containing hexagonally arranged dielectric rods with different radii distributed on a triangular lattice. Photonic materials possessing singular points on their boundaries have been developed in [Luo et al. (2012)] for the purpose of developing broadband energy harvesting techniques. Topological insulators have also appeared in the study of optical lattices [Goldman et al. (2014)]. In plasmonics, surface modes were "mimicked" by utilising microstructured surfaces [Pendry, Martin-Moreno and Garcia-Vidal (2004)]. Periodic honeycomb plasmonics that support uni-directional edge states have been studied in [Jin et al. (2017), Nalitov, Solnyshkov and Malpuech (2015)].

In the context of classical mechanics, only a few examples exist where edge states in structured media have been observed. Topologically protected sound modes in acoustic metamaterials have been realised by introducing circulating fluids into a lattice [Ni et al. (2015), Yang et al. (2015), Chen and Wu (2016), Souslov et al. (2017)] or by creating interfaces between two phononic materials with contrasting geometrical properties [He et al. (2016)]. Arrays of acoustic resonators distributed within a hexagonal lattice have been used to study the influence of defects on the robustness of topological edge wave propagation [Khanikaev et al. (2015)].

Dynamic trapped modes can also be observed along coastlines in the presence of structured barriers [Evans and Linton (1993)], or when the fluids are stratified [Adamou, Craster and Smith (2007)]. Interfacial waves have been realised in elastic metamaterials, comprised of two slabs with arrays of multi-scale defects [Mousavi, Khanikaev and Wang (2015)]. Topological protection can also be achieved in flexural

plates by attaching a hexagonal array of resonators possessing different masses to break the time-reversal symmetry [Pal and Ruzzene (2017)].

Preferential directionality of wave modes has been obtained in lattice structures by modifying the tension of the springs connecting the lattice nodes [Kariyado and Hatsugai (2015)] or by locally changing the arrangement of masses at the junctions within the structure [Vila et al. (2017)]. Localised interfacial modes for circular periodic clusters of inclusions in membranes were obtained in [Maling and Craster (2017)]. An approach based on group theory and topological concepts was used in [Makwana and Craster (2018a), Makwana and Craster (2018b)] to create platonic crystals, i.e. plates with periodically distributed inclusions, possessing topological valley super-networks and multi-directional energy splitters that admit interfacial waves. One-way interfacial rotational waves were generated in a granular crystal, where the interaction between the beads is based on non-central contact forces [Zheng et al. (2018)].

The analogue of the quantum Hall effect for mechanical systems has been realised by attaching arrays of coupled pendular to lattice systems, in [Süsstrunk and Huber (2015)], to achieve topologically protected edge modes both analytically and experimentally. This concept has been further addressed in the review [Huber (2016)], of recent attempts to bridge the gap between quantum and classical mechanics for the purposes of realising topological states in mechanical media.

Based on the concepts introduced in [Brun, Jones and Movchan (2012)], gyroelastic hexagonal lattices with internal restraints were used to create topological insulators in [Wang, Lu and Bertoldi (2015)]. Analysed in the transient regime, these materials were shown to produce one-way edge states. Further, experimental investigations in [Nash et al. (2015)] have also shown that uni-directional edge waves gyroscopic metamaterials can be achieved.

Here, in Chapter 4, the attention is focussed on different lattice systems that can support and control interfacial waves using gyroscopic spinners. For this medium, we show it is possible to derive an analytical expression for the dispersion relation and we show the spinners alter the topology or behaviour of the band structure

close to dispersion degeneracies or Dirac points. This is used as a predictive tool for establishing interfacial waves with preferential directionality. The existence of these regimes are also verified in the steady-state and transient regimes.

Gyroscopic spinners can also be used to design elastic cloaking devices [Milton, Briane and Willis (2006), Norris (2008), Brun, Guenneau and Movchan (2009), Farhat et al. (2009), Norris and Shuvalov (2011), Parnell (2012), Brun et al. (2014a), Colquitt et al. (2014)]. In [Brun, Jones and Movchan (2012)], the time-harmonic equations of the triangular gyro-elastic lattice were homogenised to provide the design for an inertial micro-polar elastic continuum. This elastic metamaterial was shown to strongly reduce the scattering caused by a stiff defect situated in an isotropic elastic continuum as demonstrated in the time-harmonic regime. In this thesis, (see Chapter 5) we use the concept of a gyro-elastic lattice to construct a cloaking device for discrete materials and the effectiveness of this cloak is analysed in the transient regime.

Continuous gyro-elastic systems

Chirality is also a property that can be bestowed to continuous structural elements, including beams and plates, by using the notion of "distributed gyricity". The theory of flexural gyro-elastic continuous flexural elements was proposed in [D'Eleuterio and Hughes (1984)] and later extended in [Huges and D'Eleuterio (1986)], [D'Eleuterio (1988)], [Yamanaka, Heppler and Huseyin (1996)], [Hassanpour and Hepper (2016a)], [Hassanpour and Hepper (2016b)], where the study of the eigenfrequencies and eigenmodes of these structural elements was carried out. Gyro-elastic continua can also be used in aerospace engineering applications, where they can aid in controlling the attitude and shape of aviation craft [Hughes (1986), D'Eleuterio and Hughes (1987), Yamanaka, Heppler and Huseyin (1996), Hassanpour and Hepper (2016a), Hassanpour and Hepper (2016b)]. Gyroscopic problems in elasticity were studied in [Padovan (1978), Padovan (1979), Padovan and Adams (1980)]. Gyroscopic coupling is also exploited to design smart structures that optimise the dissipation of vibration energy [Del Vescovo and Giorgio (2014)].

The concept of a gyro-elastic system introduces a potentially vast array of new pathways in the design methods for controlling the response of microstructured materials and large-scale structures commonly encountered in our environment, such as buildings, bridges and pipeline systems. Civil engineering structures, attached to tunable resonator systems that utilise gyroscopic effects, can become more resilient to the initiation of failure processes. In [Carta et al. (2017b)] it was shown that gyro-elastic flexural elements or *gyrobeams* can be implemented in long span flexural system, such as a bridge, to filter vibrations in the low-frequency regime for the purposes of earthquake protection. Dynamic failure processes in flexural systems, representing simplified models of civil engineering structures, have been considered in [Brun, Movchan and Slepyan (2013), Brun et al. (2014b), Nieves, Mishuris and Slepyan (2016), Nieves, Mishuris and Slepyan (2017)]. The use of gyrobeams has one drawback, in that the gyricity is a theoretical quantity not written in terms of fundamental mechanical quantities. In practice, gyro-elastic beams can be realised by attaching gyroscopic spinners to elastic beams [Carta et al. (2018), Nieves et al. (2018)]. This idea has led to the novel models of microstructured flexural systems that describe the motion of the gyrobeam in the low frequency regime. Microstructured flexural systems are of wide utility and their applications range from small scale advanced technological applications, such as using functionally graded microstructured beams in the design of micro-electro-mechanical systems [Ghayesh, Farokhi and Gholipour (2017), Farokhi et al. (2017), Ghayesh (2018), Ghayesh (2019)] to controlling the response of large scale civil engineering systems, whose ability to withstand deformation is crucial in building safer structures in society.

The time-harmonic models for the gyro-elastic lattices studied in [Brun, Jones and Movchan (2012), Carta et al. (2014), Carta et al. (2017a), Garau et al. (2018)] demonstrate how the gyroscopic spinners situated at the lattice junctions affect the dynamics of the system, providing a variety of special dynamic phenomena. In particular, the spinners create a coupling in the angular momentum balance of the gyroscopic spinners and the linear momentum balance of the lattice particles. In Chapter 4, this coupling is investigated in the transient regime and exploited to fully

describe the evolution of various dynamic phenomena, such as unidirectional waves and highly localised waveforms. This transient analysis enables us to also completely determine the performance of the new generation of structured elastic metamaterials, with a view to new technological applications, such as those proposed in Chapter 5.

1.2.1 Dynamic failure of structured materials

Phase transition and failure in mass-spring systems

As mentioned above, the modelling of structured materials also have applications in understanding the response of large scale structures, such as those found in society including buildings, bridges, rooftops, pipeline systems and many more. The structural integrity of such systems is of paramount importance, especially when in operation as they can encounter hazardous vibrations and extreme environmental conditions. Understanding how these systems fail as a result of such conditions also provides insight in how to avoid these catastrophic scenarios.

There exists a great deal of literature concerning the modelling of failure in structured mass-spring systems. These models help in understanding processes on both the macro- and micro-level that can occur in the failure of materials [Marder and Gross (1995)].

Motivated by this, Mode III fracture of an infinite square-cell mass-spring system was considered in [Slepyan (2001a)], in addition to Mode I and II fracture in an infinite triangular elastic lattice in [Slepyan (2001c)]. In these models, the failure is assumed to occur at a uniform rate and is physically represented by a removal of lattice links between two neighboring rows of the lattice when the failure occurs. This failure process is assumed to be sustained by energy delivered by a remote load and these models reveal micro-level waves that can be radiated into the lattice when a lattice link ruptures.

The fracture process considered may be considered also as a type of phase transition, where the physical properties of the links can change when some threshold condition governing the phase transition is met. For the analysis of phase transition,

corresponding to the weakening of the links at a uniform rate in structured mass-spring systems see also [Slepyan (2001b)].

The method for handling dynamic lattice fracture is developed in [Slepyan (2002b)], were an overview of fracture mechanics in the last century is given. These micro-structural dynamic effects encountered in the fracture process can be captured through using the Fourier transform to reduce the governing equations of the lattice system to a functional equation of the Wiener-Hopf type posed along the line of the fault in the lattice. The equation contains a kernel function that possesses information about the lattice dynamics and potential steady failure regimes. Using the Wiener-Hopf technique [Noble (1958)], the solution to the problem can be obtained and information about potential non-steady lattice failure regimes can be extracted from this, [Marder and Gross (1995)].

An analogous approach to that encountered in [Slepyan (2002b)] utilising the $Z-$ transform has also been implemented in [Sharma (2015), (2016a), (2016b), (2016c), (2017)] to analyse the anti-plane scattering and diffraction of waves created by semi-infinite line defects and inhomogeneities in lattices.

Numerical models can also be implemented to get a better understanding of failure processes that can occur in structured materials. The numerical modelling of Mode I and II crack growth inside triangular lattice strips has been executed in [Slepyan and Ayzenberg-Stepanenko (2002a)], and revealed some surprising periodic patterns of fault propagation not identified by the analytical models of [Slepyan (2001c)].

Since the advent of metamaterials, or materials possessing a tunable microstructure, there has been a flurry of activity aimed at developed the approach of [Slepyan (2002b)] to understand the failure of a new breed of mass-spring systems whose microstructure can be tuned for different vibration guiding purposes. In particular, micro-structural lattice heterogeneities can influence the regimes where steady crack propagation is possible. The role of lattice inhomogeneities on Mode III crack propagation in two-dimensional lattices has been analysed in [Mishuris, Movchan and Slepyan (2007)]. The dynamic failure of mass-spring chains with dissimilar material

properties have been analysed in the [Berinskii and Slepyan (2017), Gorbushin et al. (2017)]. Failure of an anisotropic elastic lattice has been considered in [Nieves et al. (2013)]. The study of Mode III failure in inertial lattices in [Slepyan (2005)] has also revealed how inertia affects wave radiation processes involved in the crack growth.

Structured interfaces contained in a lattice have been shown to induce and sustain failure mechanisms caused by phenomena known as "knife waves" contained in the interface [Mishuris, Movchan and Slepyan (2009)]. Numerical simulations of crack growth in a high-contrast interface were later performed in [Slepyan, Movchan and Mishuris (2010)] and revealed non-steady failure regimes such as clustering, where a crack may propagate in periodic bursts.

One can also introduce and analyse different failure processes in the microstructured medium, such as the extraction of a mass-spring chain from the lattice in [Mishuris, Movchan and Slepyan (2008a)] and the propagation of bridge cracks in [Mishuris, Movchan and Slepyan (2008b)]. The influence of the fracture criteria on possible steady fracture regimes can also be analysed as in [Gorbushin et al. (2018)], where time-dependent fracture criteria were considered. Reversible failure processes have been considered in decohesion models of elastic layers, associated with the denaturation of DNA, in [Maddalena et al. (2009)].

When solving the Wiener-Hopf problems arising in the above mentioned models of failure in structured media, attention should be given to the admissibility of the solution. This important question has been discussed in [Marder and Gross (1995), Slepyan (2002b), Marder (1993)] and later readdressed in [Gorbushin and Mishuris (2017)] in the low-crack velocity regime. Admissibility of the solution can also be influenced by the lattice loading conditions such as in [Gorbushin and Mishuris (2018)] where this was considered for Mode III fracture regimes supported by moving loads. A transient analysis of potential failure regimes induced by thermal shocks in triangular lattices is presented in [Carta et al. (2013), Trevisan et al. (2016)] and in [Tallarico et al. (2017)], where cracks with chiral coatings were considered.

In the above models, nodes within the lattice are assumed to interact with their nearest neighbors. Failure regimes in discrete structures with non-local interactions

and their effects on the fracture wave radiation processes were studied in [Gorbushin and Mishuris (2016)]. For structured media with additional non-linearities in the connections see [Truskinovsky and Vainchtein (2005)].

Mass-beam systems and their dynamic failure

In contrast to the study of dynamic fracture in mass-spring systems, very few articles exist in the literature with the focus on failure of flexural systems. Symmetric and skew-symmetric bending static failure modes of 2D discrete flexural structures, composed of beams connecting masses, can be found in [Ryvkin and Slepyan (2010)]. The analysis of static Mode III cracks in a three-dimensional beam lattices, representing open cell foams, is presented in [Ryvkin (2012)]. The fracture toughness of structured materials or foams with cracks and broken elements, is considered in [Kucherov and Ryvkin (2014)]. The influence of suddenly appearing small flaws in periodic materials on wave processes is investigated in [Aboudi and Ryvkin (2014)]. Quasi-static damage propagation in two-dimensional beam structures has been considered in [Cherckaev and Ryvkin (2018)], leading to designs of fault-tolerant beam lattices in [Cherckaev and Ryvkin (2019)].

In connection with modelling the failure of civil engineering systems such as bridges, the phase transition of mass-beam chains supported by an elastic foundation was studied in [Brun, Movchan and Slepyan (2013)] and later developed in [Brun et al. (2014b)] to predict the collapse rate of the San Saba rail road bridge, Texas, in 2013. Phase transitions in continuous flexural systems have been shown to support non-steady failure behaviour [Slepyan, Ayzenberg-Stepanenko and Mishuris (2015)], known as forerunning failure modes. Flexural structures incorporating pre-stress, damage and their associated effects have also been analysed in great detail in [Carta and Brun (2015)], [Gei, Movchan and Bigoni (2009), Carta, Brun and Movchan (2014)].

Experimentally, counter-intuitive fracture behaviour in materials has been observed in rubber sheets [Marder, Deegan and Sharon (2007)], where analytical and numerical studies of this process have been performed in [Marder (2006)]. The

influence of lattice dynamics and wave radiation processes on the stability of crack trajectories in silicon crystals is treated experimentally and numerically, using molecular dynamics simulations, in [Sherman and Be'ery (2004), Sherman (2011), Atrash and Sherman (2012)].

In [Nieves, Mishuris and Slepyan (2016)], the dynamic failure of a discrete flexural structure subjected to a remote sinusoidal load was studied. Further, in [Nieves, Mishuris and Slepyan (2017)] the transient failure process was numerically modelled and the results of [Nieves, Mishuris and Slepyan (2016)] were verified.

1.3 Structure of the thesis

In Chapter 2, we review some introductory elements of the theory of waves in solids and structures. This also includes the introduction of the Bloch-Floquet conditions and their application, which forms an essential tool in the analysis of waveforms in the time-harmonic regime for the lattice systems considered in subsequent chapters. In Chapter 3, we consider waves propagating in gyro-elastic lattices in the time-harmonic regime and establish a method for realising interfacial waveforms in inhomogeneous gyro-elastic systems. This method will be identified in connection to novel hexagonal gyro-elastic lattices and in this Chapter we also show the results that may be extended to allow one to generate interfacial waveforms in triangular elastic systems with soft internal links.

We re-emphasise that the work carried out in [Garau et al. (2018)] and in Chapter 3 assumes the waves propagate inside the system when it has settled to the time-harmonic regime. An important question to ask is "Can these waveforms be realised in the transient regime"? This question is addressed in Chapter 4, where we consider elastic systems embedding gyroscopes at the junctions in the transient regime. We derive the effective forcing input given by the gyroscopic spinners to the junctions of the lattice systems and in doing so we obtain a new analytical model characterising this gyro-elastic interaction. This analysis brings new features in terms of physical parameters not previously identified in the time-harmonic regime and

provides a new tool with which to construct novel structured media. This model is also exploited in this Chapter to show that the waveforms identified in Chapter 3 and [Garau et al. (2018)] can be realised under different initial conditions of the lattice, various loading conditions and under different physical conditions associated with gyroscopes. The transient models considered there also reveal new dynamic phenomena not encountered in [Garau et al. (2018)].

In Chapter 5, we use the novel transient model of Chapter 4 that characterises the interaction between elastic trusses and gyroscopic spinners, to develop two important and novel applications of gyro-elastic systems. The first example illustrates that these systems can be used to construct a gyro-elastic topological insulator containing a hole that supports waves on the exterior of the lattice and prevents them from propagating into the bulk system, so that the lattice acts as a protective barrier for object situated inside the hole. The second example shows that we can use gyro-elastic structured media to design a new effective cloaking device for a discrete lattice, that reduces the scattering produced by stiff defect situated inside the lattice. All examples in this Chapter are studied in the transient regime in order to establish the effectiveness of the devices constructed.

A majority of the research into metamaterials focuses on their ability to support and control the propagation of waves. This is particularly the case in Chapters 3-5, where the materials possess dynamic properties that have potential applications in the design of seismic protection systems. However, in the analysis of the metamaterials it is seldom that the structural integrity of these systems is considered when they vibrate. This is particularly important especially when their applications are aimed at protecting structures in civil engineering. As an alternative, if one can understand how these structures undergo failure processes then this information can be used to mitigate or inhibit these catastrophic effects.

In Chapter 6, we consider a simplified model of a structured flexural system that can represent the model of a bridge or rooftop. We are interested in the analysis of steadily propagating failure modes in such a system. In this Chapter, we utilising the Wiener-Hopf technique to identify information about this phenomena and analyse

wave radiation occurring in the structure as a result of such processes. The analytical work is accompanied by numerical simulations that verify the model developed and that can be used to identify information about non-steadily propagating failure regimes.

Finally in Chapter 7, we give some conclusions of the work considered in this thesis.

Chapter 2

Techniques for modelling of waves in periodic media

In this Chapter, we give some details necessary for the theoretical and numerical developments presented in the remaining part of the thesis concerning the modelling of waves in structured periodic systems. Here, we will tackle problems for continuous and discrete solids in the regime where the deformation is assumed to be small. In particular, we consider homogeneous problems, where the knowledge of loading configurations is not required and the associated equations are determined through the analysis of forces produced by internal elastic resistance of the material to motion and the inertial properties of the system. For these problems we are interested with the non-trivial solutions associated with the eigenfrequency spectrum of the medium.

We begin with an introductory problem concerning longitudinal waves in an elastic rod in Section 2.1. Following this, we investigate the micro-structural model for an uniform infinite rod in Section 2.2, where we introduce the theoretical approaches adopted in the thesis, including the use of the Floquet-Bloch quasi-periodicity conditions. We provide further examples of how to use the techniques developed in Section 2.2 to study vibration in inhomogeneous 1D micro-structured systems in Section 2.3 and a uniform triangular lattice in Section 2.4. Finally, in Section 2.5 we give some concluding remarks based on the examples presented.

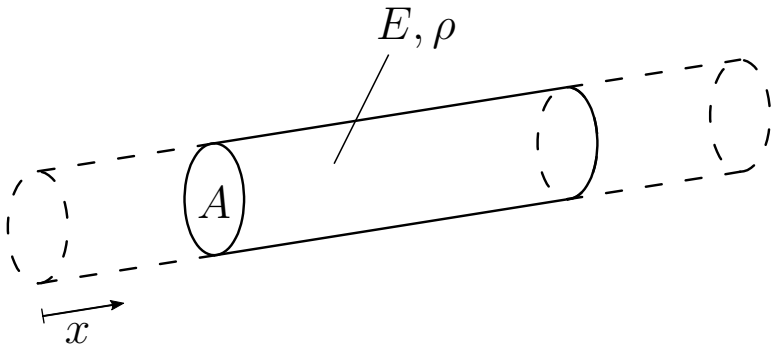

Figure 2.1: An infinite rod with Young's modulus E, circular cross-section A and mass density ρ.

2.1 Introductory example: Longitudinal waves in an infinite rod

First, we consider the problem of longitudinal vibrations in an infinite rod (see Figure 2.2), corresponding to stress pulse propagating along the axis of the rod. For simplicity, we consider a rod with constant cross-section A, Young's modulus E and density ρ, (see Figure 2.1, where an infinite rod with circular cross-section is shown).

According to [Graff (1975)], the governing equation for the displacement $w(x,t)$ of the cross-section at position x in the rod and at time t is

$$\rho\frac{\partial^2 w(x,t)}{\partial t^2} = E\frac{\partial^2 w(x,t)}{\partial x^2}\ , \qquad x \in \mathbb{R}, t > 0\ , \tag{2.1}$$

which is the one-dimensional wave equation, whose multi-dimensional analogue also describes a variety of other physical phenomena including waves in water, acoustic waves and those in light. We are concerned about real waves propagating along the rod, which may take the form:

$$w(x,t) = P\cos(kx - \omega t)\ , \tag{2.2}$$

or

$$w(x,t) = P\sin(kx - \omega t)\ , \tag{2.3}$$

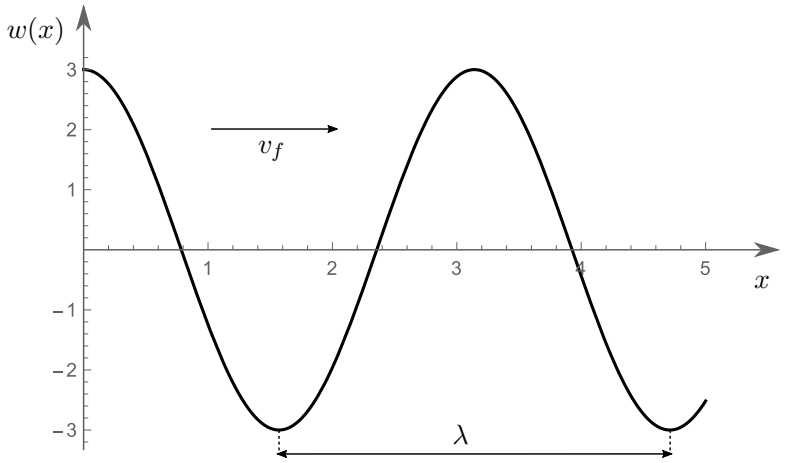

Figure 2.2: Diagram of harmonic cosine wave with wave number $k = 2$, frequency $\omega = kv_f = 3.5$ and amplitude $P = 3$ at the time $t = 0$. The wave length $\lambda = 2\pi/k$ and v_f is the phase velocity.

but the most convenient form, taking into account information related to (2.2) and (2.3), is to use a complex form of the wave given by the expression

$$w(x,t) = Pe^{\mathrm{i}(kx-\omega t)} \,, \tag{2.4}$$

where (2.2) and (2.3) appear as the real and imaginary parts, respectively, of the previous expression. The above representations are known as *standing waves* in the literature (see for instance [Graff (1975)]). Here, ω is the radian frequency of the wave, which we assume to be positive, $P > 0$ is the amplitude and k is the wavenumber. A graphical presentation of the harmonic wave in (2.2) is given in Figure 2.2. There, λ represents the wavelength of the wave and is determined from the wavenumber via

$$\lambda = \frac{2\pi}{k} \,. \tag{2.5}$$

The time period of the wave τ, which determines the time taken for the wave to undergo one cycle in time, is defined by

$$\tau = \frac{2\pi}{\omega} \,.$$

We note (2.4) is not valid for any k and ω as these quantities depend on each other

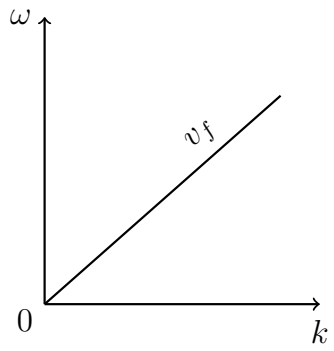

Figure 2.3: Graphical representation of the relation (2.7) governing waves in a non-dispersive infinite rod.

in order for equation (2.1) to be satisfied by (2.4), as we now show. To determine the feasible ω and k for which the representation (2.4) is valid, we substitute this into (2.1) and obtain

$$(\rho\omega^2 - Ek^2)Pe^{\mathrm{i}(kx-\omega t)} = 0 \ .$$

Since the complex exponent is non-zero and we assume P is non-zero (to avoid the trivial solution to the problem), the above implies

$$\rho\omega^2 - Ek^2 = 0 \ , \tag{2.6}$$

should be satisfied for this wave solution. This is valid if and only if

$$\omega = v_f k \ , \tag{2.7}$$

where

$$v_f = \sqrt{\frac{E}{\rho}} \ , \tag{2.8}$$

which is known as the *phase speed* of the wave. Relation (2.7) governs those waves which can propagate through the medium with a speed v_f, determined from the slope of the diagram in Figure 2.3. This speed can be controlled with the material properties of the rod as shown in (2.8), and, for example, this speed can be increased by considering a rod with large Young's modulus (corresponding to a stiff rod) or a rod with low mass density (corresponding to a light).

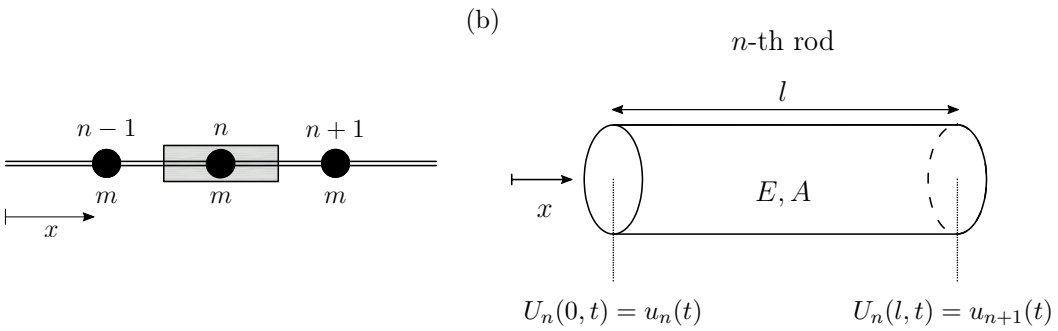

Figure 2.4: (a) The infinite chain formed from periodically placed masses (black circles), associated with an index n and connected by massless rods of length l. The shaded region represents the n-th elementary unit cell of the medium of length l. (b) The configuration for the n-th massless rod connecting nodes n and $n+1$.

The model considered here concerns longitudinal waves propagating through a rod on the macro-scale, where the relation governing the propagation of the waves is given by (2.8). In fact, due to the linear nature of the relation in (2.7), the rod is known as a *nondispersive medium*. However, typically when waves propagate through a medium there are also micro-scale processes that can arise. For this purpose, when considering the rod, one can use a lattice model to determine information about vibrations on the micro-scale of the medium, which is discussed in the next Section. In particular, there we find such media are dispersive as their ability to support vibrations is governed by nonlinear dependencies of the frequency ω on the wavenumber k.

2.2 Waves in a mass-spring chain

As discussed above, here we consider a micro-scale model of an infinite rod, which we show can be represented by the classical model of a mass-spring chain formed from periodically placed masses connected by massless springs. This structure is shown in Figure 2.4(a) and, before analysing waves in this system, we first describe how to construct the governing equations for the structure, which will serve as a building block for the subsequent study of a variety of discrete media considered in this thesis.

2.2.1 Derivation of the governing equations for the micro-scale model of an infinite rod

Each mass within the structure is assigned an index $n \in \mathbb{Z}$. The longitudinal displacement of the n-th mass is represented by $u_n(t)$, that depends on time t. Each mass is connected by a massless rod of length l, Young's modulus E and cross-sectional area A (see Figure 2.4(b)). In this scenario, following from (2.1), the governing equation for the displacement U_n in the n-th rod is

$$\frac{\partial^2 U_n(\tilde{x},t)}{\partial \tilde{x}^2} = 0 \ , \tag{2.9}$$

where $\tilde{x} = x - ln$, $n \in \mathbb{Z}$ is the local coordinate along the n-th rod and $0 \leq \tilde{x} \leq l$. Note that in (2.9), the dynamic term associated with the link density does not appear as a result of the assumption the beam is massless.

Moreover, the n-th rod connects the n-th mass to the $(n+1)$-th mass. Hence, the displacement function U_n should satisfy the boundary conditions

$$U_n(0,t) = u_n(t) \qquad \text{and} \qquad U_{n+1}(l,t) = u_{n+1}(t) \ . \tag{2.10}$$

The equation (2.9) is readily solved and provides a linear function in the local variable $\tilde{x}$, with time dependent coefficients that are determined by the boundary conditions (2.10) for the n-th rod. Therefore, it follows from (2.9) and (2.10) that

$$U_n(\tilde{x},t) = (u_{n+1}(t) - u_n(t))\frac{\tilde{x}}{l} + u_n(t) \ . \tag{2.11}$$

Next, as each mass is assumed to undergo translational motion in the x-direction only, we need only perform the linear momentum balance for the n-th mass to obtain the governing equations for the nodes of the structure. The linear momentum balance for the n-th mass takes the form

$$m\ddot{u}_n(t) = (\sigma_n(0,t) - \sigma_{n-1}(l,t))A \ , \tag{2.12}$$

where $\sigma_n(\tilde{x}, t)$ represents the stress, i.e. force per unit area, in the n-th rod, given as

$$\sigma_n(\tilde{x}, t) = E\frac{\partial U_n(\tilde{x}, t)}{\partial \tilde{x}} \ . \tag{2.13}$$

Recall that we are studying eigenmodes of the structure and information about the cause of such waves is not needed. In such a scenario, we should look for non-trivial solutions to a homogeneous problem that are associated with the eigenfrequencies of the system.

Thus, using (2.11)–(2.13) leads us to governing equation for the n-th mass

$$m\ddot{u}_n(t) = c(u_{n+1}(t) + u_{n-1}(t) - 2u_n(t)) \ , \tag{2.14}$$

where $c = EA/l$ is the *effective stiffness* of the rods and this shows the considered model is equivalent to the classical mass-spring model.

2.2.2 Floquet-Bloch modes and dispersion relation

Next we consider special vibration modes in the mass-spring chain, known as Floquet-Bloch modes, in the time-harmonic regime. The Floquet-Bloch modes are periodic vibration modes that can be identified inside the structure when the system has settled to the steady-state vibration process. For the time-harmonic representation of the waves, we assume the longitudinal displacements $u_n(t)$ have the explicit time dependence

$$u_n(t) = A_n e^{-\mathrm{i}\omega t} \ , \tag{2.15}$$

where ω is the radian frequency of vibration and the amplitude A_n depends on the spatial variable n. For the subsequent study, in order to determine periodic waves in the structure, we have divided the structure into cells corresponding to the index n and of equal length l, with each cell containing a single mass. The n-th cell is shown as the shaded region in Figure 2.4(a).

This analysis does not consider what causes the wave and we note the waves deduced in this way are important in describing transient phenomena associated

with problems supplied with initial conditions and loading terms (using eigenfunction expansions of the time dependent solution).

We are searching for a vibration mode that is periodic across the cells and as such we assume this mode satisfies some quasi-periodicity conditions or the so-called Floquet-Bloch periodicity conditions. These conditions relate the behaviour of wave in one elementary cell of the structure to the next via an exponential factor embedding the wavenumber and the distance between each cell.

The considered structure is periodic and it is therefore natural to assume the structure supports periodic waveforms, [Brillouin (1946)]. As the waves considered are periodic, we should define their periodicity, which is taken to be a single unit cell in the studies presented here. Namely, for the considered medium, imposing the Floquet-Bloch periodicity conditions on the amplitude A_n results in using the following periodicity condition on the amplitudes:

$$A_{n+a} = A_n e^{\mathrm{i}kla} \ , \ \text{for } a \in \mathbb{Z} \ , \tag{2.16}$$

with k being the wavenumber and A_n the amplitude of the wave. In this case, substitution of (2.15) into (2.14) yields

$$-m\omega^2 A_n e^{-\mathrm{i}\omega t} = c(A_{n+1} + A_{n-1} - 2A_n)e^{-\mathrm{i}\omega t} \ , \tag{2.17}$$

where the time-harmonic factor in both sides can then be cancelled and the conditions (2.16) are then be used to obtain

$$[c(2 - e^{\mathrm{i}kl} - e^{-\mathrm{i}kl}) - m\omega^2]A_n = 0 \ ,$$

which can be simplified to

$$[2c(1 - \cos(kl)) - m\omega^2]A_n = 0 \ ,$$

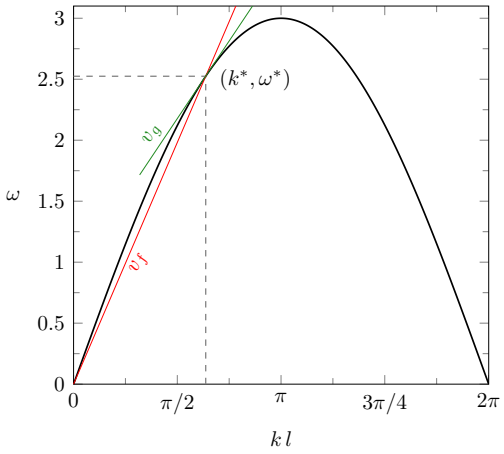

Figure 2.5: The dispersion relation (2.20) for the mass-spring chain, plotted as a function of the wavenumber kl. The material parameters are $m = 1$, $l = 1$ and $c = 2$. A coordinate $(k^*, \omega^*) = (2, 2.52)$, highlighted by the dashed lines on the curve, corresponds to the wave with the given wavenumber and frequency that can propagate in the structure. The phase velocity of the wave (the slope of the red line) is computed with (2.23) and is 1.26, whereas the group velocity (the slope of the green line) is computed with (2.24) and is 0.81.

or

$$[4c\sin^2(kl/2) - m\omega^2]A_n = 0\ . \tag{2.18}$$

Here, owing to the fact we are looking for non-trivial amplitudes, implies

$$4c\sin^2(kl/2) - m\omega^2 = 0\ , \tag{2.19}$$

and from this we obtain the *dispersion relation* for the medium (which predicts the resonance modes),

$$\omega(k) = 2\sqrt{\frac{c}{m}}|\sin(kl/2)|\ , \tag{2.20}$$

that describes the dependency of the radian frequency of vibration ω on the wavenumber k for waves, satisfying (2.15) and (2.16), to propagate in the medium. Relation (2.20) is a 2π-periodic function in kl. A typical representation of this curve is given in Figure 2.5. In contrast to the uniform infinite rod studied in Section 2.1, the frequency of the waves that can propagate through the mass-spring chain has a non-linear dependency on the wavenumber k, which makes this medium *dispersive*. Moreover, in comparison to the case of the infinite rod, the expression (2.20) only covers a finite frequency range.

Pass and stop-bands

The finite frequency range covered by (2.20) is defined by

$$0 < \omega \leq 2\sqrt{\frac{c}{m}} \tag{2.21}$$

and any wave with a frequency contained in this interval will propagate through the structure, with the minimum and maximum occurring at $k = 0$ and $k = \pi/l$, respectively, (see also Figure 2.5 for an illustrative example). Such an interval is known as the *pass-band* for the structure. If the medium is excited at a frequency in this interval of frequencies, waves possessing this frequency can propagate through the medium. Clearly, the range of the pass-band can be altered through the choice of the material parameters of the microstructure. For instance, a decrease in the effective stiffness of links or an increase in the mass of the nodes located at the junctions, decreases the ability of the structure to support waves as the size of the pass-band is reduced.

For a wave whose frequency lies in the pass-band, one can draw a horizontal line corresponding to its frequency and use the intersection of the line with the dispersion curve to identify the corresponding wavenumber of the wave. An example is shown for the point (k^*, ω^*) in Figure 2.5 that defines a wave that can propagate through the medium.

On the other hand, for the interval corresponding to

$$\omega > 2\sqrt{\frac{c}{m}}\,, \tag{2.22}$$

waves cannot propagate inside the structure and this is known as the *stop-band* for the medium. Instead, for frequencies in the stop-band, the solution defined by (2.15) and (2.16) possesses wave numbers with an imaginary component. Physically, when the structure is excited at those frequencies *evanescent modes* are produced that decay exponentially in the medium and produce local deformations to the excitation.

Phase and group velocity

As we have described, the frequency and the wavenumber associated with a point along the dispersion curve can be used to determine the *phase velocity* v_f of the wave in the medium by

$$v_f = \frac{\omega}{k} \, , \tag{2.23}$$

as demonstrated in Figure 2.5 for the point (k^*, ω^*).

Simultaneously, the *group velocity*, which indicates the speed and direction that the wave carries energy inside the medium, can also be calculated using such a point by computing the derivative of the dispersion relation in (2.20) with respect to k, i.e.,

$$v_g = \frac{\mathrm{d}\omega(k)}{\mathrm{d}k} \, , \tag{2.24}$$

and this has also been computed in Figure 2.5 for the point (k^*, ω^*). In addition, this quantity and the phase velocity coincide and are equal zero when $kl = 2\pi$, (see Figure 2.5), which corresponds to a *standing wave* of the medium where neighbouring masses in the structure move out of phase (see (2.16)).

We note that for the non-dispersive medium of Section 2.1, the group and phase velocities coincide for any k, whereas for a dispersive media these two quantities can differ.

Connection between the mass-spring system and the infinite rod

The model of the infinite mass-spring system can be linked to the model for an infinite rod in the regime where the wavelength of the waves propagating through the discrete system is large in comparison to the separation of the masses constituting this medium.

In this scenario, the quantity kl is small (see (2.5)). This can be used to expand the left-hand side in (2.19) to receive

$$c(kl)^2 - m\omega^2 + O((kl)^3) = 0 \, . \tag{2.25}$$

Thus to leading order we have

$$c(kl)^2 - m\omega^2 = 0 \ .$$

By dividing this through by l^3 and comparing the resulting expression with the (2.6) for the infinite rod, we see that the discrete medium in the long wavelength regime behaves like the infinite rod, with the effective densities and Young's modulus equal to $\rho = m/l^3$ and $E = c/l$, respectively.

In the example provided above for the discrete mass-spring system, we used the so-called Floquet-Bloch conditions (see (2.16)). The structure considered was uniform in its material and geometrical properties. However, clearly we are free to design the microstructure of such media in a variety of ways that may introduce non-uniformity in the structure or increase the structure's dimension. In particular, in those cases we will also consider structures with some inherent periodicity. Hence, we need to extend the notion of the Floquet-Bloch conditions in order to understand vibration in these new materials. This is tackled in the next Section.

2.2.3 General form of the Floquet-Bloch quasi-periodicity conditions

As shown in the previous example, when analysing waves in a periodic discrete medium, it is convenient to study waves in the time-harmonic regime. The use of the quasi-periodicity conditions allowed the governing equations for the medium to be reduced to a homogeneous problem, leading to a dispersion relation. These are standard techniques used in the analysis of waves in periodic media.

When dealing with more complex discrete systems it is useful to have a general approach for implementing the Floquet-Bloch conditions (see also [Joannopoulos et al. (2008)]) that allows us to use standard tools in determining the dispersive features of the medium. These conditions depend on the nature and geometry of the elementary cell used to define the periodicity of the medium. For a periodic

discrete structure in $\mathbb{R}^s$, $s = 1$ or 2, the elementary cell can be defined by a set of s-dimensional vectors, $\mathbf{t}^{(j)}$, $j = 1, \ldots, s$, and they represent the smallest cell in the medium that may be repeated to obtain the entire structure of infinite lattice. It is also useful to define the $s \times s$ matrix

$$\mathbf{T} = [\mathbf{t}^{(1)}, \ldots \mathbf{t}^{(s)}] \ , \quad s = 1 \text{ or } 2 \ .$$

Let $\mathbf{W}(\mathbf{x_n})$ be a vector representing the generalised coordinates describing the motions of the lattice nodes whose position is defined by $\mathbf{x_n} = \mathbf{x} + n_1\mathbf{t}^{(1)} + \cdots + n_s\mathbf{t}^{(s)}$, $n_j \in \mathbb{Z}$, $j = 1, .., s$, where $\mathbf{x}$ is the position vector of a reference particle in the medium. Then the Floquet-Bloch conditions for the medium take the form

$$\mathbf{W}(\mathbf{x_n}) = \mathbf{W}(\mathbf{x})e^{\mathbf{i}\mathbf{k}\cdot\mathbf{T}\mathbf{n}} \ , \tag{2.26}$$

where $\mathbf{n} = (n_1, \ldots, n_s)^T$ and here $\mathbf{k} = (k_1, \ldots, k_s)^T$ is the called Bloch vector. This identity relates the motion in the cell defined by $\mathbf{x_n}$ to that in the cell of interest defined by $\mathbf{x}$. As we will see in the examples below, in s-dimensions, $s = 1$ or 2, this allows one to reduce the study of waves in an s-dimensional lattice to an s-dimensional homogeneous system from which the dispersive properties of the structure can be determined, along with the associated modes. This was already demonstrated in the previous Section, concerning waves in a one-dimensional mass-spring chain, where $s = 1$, $\mathbf{n} = n$, $\mathbf{k}^{(1)} = k$ and $\mathbf{t}^{(1)} = l$ (i.e. the vector quantities mentioned here are scalars for the one-dimensional system).

In (2.26), we note the relation possesses periodicity in $\mathbf{k}$ due to the presence of the imaginary exponent, and this allows one to consider the dispersive features of the micro-structured medium within a limited region of $\mathbf{k}$-space, called the *irreducible Brillouin zone*. This region can be defined by a set of basis vectors $\mathbf{b}^{(j)}$, $j = 1, \ldots, s$, and in what follows we describe how to find these vectors. In this case, the behaviour of dispersion relations in the entire $\mathbf{k}$-space can then be recreated through shifting of the irreducible Brillouin zone using appropriate multiples of the basis vectors $\mathbf{b}^{(j)}$,

$j = 1, \ldots, s$.

In view of the periodicity of relation (2.26), we note the exponential shift is equal to unity if

$$\mathbf{k} \cdot \mathbf{Tn} = 2\pi N \ ,$$

with N being an integer. This identity provides us with a way to find a basis in $\mathbf{k}$-space that defines the irreducible Brillouin zone. Here, the basis $\mathbf{b}^{(j)}$, $j = 1, \ldots, s$, in $\mathbf{k}$-space, is chosen so that

$$\mathbf{b}^{(i)} \cdot \mathbf{t}^{(j)} = 2\pi\delta_{ij} \ , \quad \text{for } i, j = 1, \ldots, s \ , \tag{2.27}$$

with δ_{ij} being the Kronecker delta:

$$\delta_{ij} = \begin{cases} 1 \ , & \text{if } i = j \ , \\ 0 \ , & \text{otherwise.} \end{cases} \tag{2.28}$$

A natural choice for the basis defining the irreducible Brillouin zone, and which is adopted throughout this thesis, for $s = 1$ is

$$\mathbf{b}^{(1)} = 2\pi/|\mathbf{t}^{(1)}| \tag{2.29}$$

whereas for $s = 2$, we choose

$$\mathbf{b}^{(j)} = [V_1^{(j)}, V_2^{(j)}]^T, \quad j = 1, 2, \tag{2.30}$$

with $V_i^{(j)}$, $i, j = 1, 2$, being the first two components of the three dimensional column vectors $\mathbf{V}^{(j)} = [V_i^{(j)}]_{i=1}^3$ defined by:

$$\mathbf{V}^{(1)} = 2\pi \frac{\boldsymbol{\tau}^{(2)} \times \boldsymbol{\sigma}}{\boldsymbol{\tau}^{(1)} \cdot (\boldsymbol{\tau}^{(2)} \times \boldsymbol{\sigma})}, \quad \mathbf{V}^{(2)} = 2\pi \frac{\boldsymbol{\sigma} \times \boldsymbol{\tau}^{(1)}}{\boldsymbol{\tau}^{(1)} \cdot (\boldsymbol{\tau}^{(2)} \times \boldsymbol{\sigma})}, \tag{2.31}$$

where $\boldsymbol{\tau}^{(j)} = ((\mathbf{t}^{(j)})^T, 0)^T$, $j = 1, 2$, and $\boldsymbol{\sigma}$ is the unit vector perpendicular to the plane of the lattice. It is possible to check by direct substitution of (2.29) or (2.30)

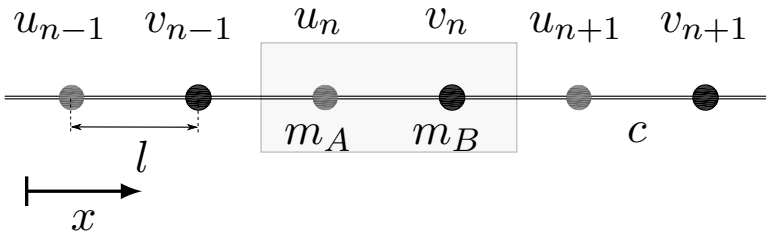

Figure 2.6: Diatomic chain composed of periodically placed masses, connected by rods of length l. There are two types of nodes in the medium with mass m_A and m_B and displacements u_n and v_n, respectively. The elementary cell describing the periodicity of the structure is indicated by the shaded region and has length $2l$.

into the left-hand side of (2.27) that this identity is satisfied. In the next Sections, we explore some more examples demonstrating how we adopt the above convention.

2.3 Waves in a diatomic chain

In this Section, we consider a more complex model of the mass-chain system considered in Section 2.2, involving an infinite chain composed of rods connecting two types of masses nodes (see Figure 2.6). In this structure the elementary cell is a macro-cell of length $2l$ (see shaded region in Figure 2.6). There are two nodes contained in this cell, one having mass m_A and the other has mass m_B. The type of mass alternates in the structure.

In the n-th unit cell, the nodes with mass m_A or m_B have displacements $u^{(n)}$ or $v^{(n)}$, respectively, in the direction aligned with the chain. Following a similar approach outlined in Section 2.2.1, we can determine the equations of motion for the structure in Figure 2.6. These governing equations can be written as

$$m_A \ddot{u}_n = c(v_n + v_{n-1} - 2u_n), \tag{2.32}$$

$$m_B \ddot{v}_n = c(u_{n+1} + u_n - 2v_n). \tag{2.33}$$

Next we introduce the complex time-harmonic displacements

$$u_n = A_n e^{-\mathrm{i}\omega t}\,, \quad v_n = B_n e^{-\mathrm{i}\omega t}\,, \tag{2.34}$$

and the Floquet-Bloch conditions for their amplitudes as

$$A_{n+a} = A_n e^{2\mathrm{i}kal} \quad \text{and } B_{n+a} = B_n e^{2\mathrm{i}kal}\,, \quad \text{for } a \in \mathbb{Z}\,, \tag{2.35}$$

that is accordance with Section 2.2.3 (where $\mathbf{t}^{(1)} = 2l$ is a scalar equal to the length of the unit cell in this example). Inserting (2.34) and (2.35) into (2.32) and (2.33) gives

$$-m_A\omega^2 A_n = c(B_n - 2A_n + B_n e^{-2\mathrm{i}kl}), \tag{2.36}$$

$$-m_B\omega^2 B_n = c(A_n e^{2\mathrm{i}kl} - 2B_n + A_n), \tag{2.37}$$

Using the vector $\mathbf{W} = (A_n, B_n)^T$ we may write this system in the matrix-vector form

$$[\mathbf{C} - \omega^2\mathbf{M}]\mathbf{W} = \mathbf{0}. \tag{2.38}$$

Here, $\mathbf{C}$ is the stiffness matrix

$$\mathbf{C} = c\begin{bmatrix} 2 & -(1+\,e^{-2ikl}) \\ -(1+\,e^{2ikl}) & 2 \end{bmatrix},$$

and $\mathbf{M}$ denotes the mass matrix given as

$$\mathbf{M} = \begin{bmatrix} m_A & 0 \\ 0 & m_B \end{bmatrix}.$$

We seek non-trivial solutions of the homogeneous system (2.38), i.e. we would like $\mathbf{W} \neq \mathbf{0}$. Moreover we need to identify the dispersive properties of this structure. Hence we should identify when determinant of the coefficient matrix is zero, i.e.

$$\det(\mathbf{C} - \,\omega^2\mathbf{M}) = 0\,, \tag{2.39}$$

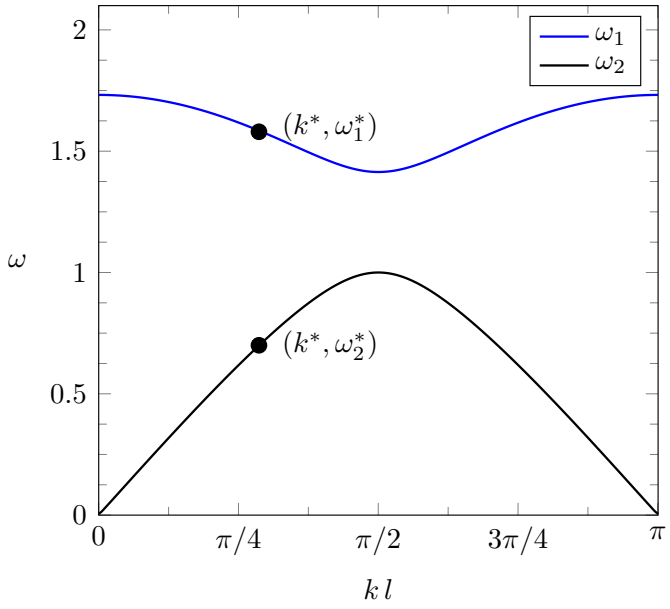

Figure 2.7: Dispersion curves for the diatomic structure in Figure 2.6 as a function of the dimensionless quantity kl. The computations are based on (2.40) and (2.41) and the choice of parameters $2m_A = m_B = 2$ and $c = 1$. For the coordinates indicated by dots along the curves, the corresponding eigenmodes are presented in Figure 2.8.

In order to find the dependence of ω on the wavenumber k. This yields the equation

$$(2c - m_A\omega^2)(2c - m_B\omega^2) - 2c^2(1 + \cos(2kl)) = 0\ ,$$

which is a bi-quadratic equation for the radian frequency ω. Solving this equation for ω provides two positive roots:

$$\omega_1 = \sqrt{c\left(\frac{m_A + m_B + \sqrt{m_A^2 + m_B^2 + 2m_Am_B\cos(2kl)}}{m_Am_B}\right)} \tag{2.40}$$

and

$$\omega_2 = \sqrt{c\left(\frac{m_A + m_B - \sqrt{m_A^2 + m_B^2 + 2m_Am_B\cos(2kl)}}{m_Am_B}\right)}. \tag{2.41}$$

These solutions are shown in Figure 2.7, for $m_A = 1$ and $m_B = 2$ and $c = 1$, where they are plotted as a function of the wavenumber k over the irreducible Brillouin zone $[0, \pi]$ (see (2.29) and Section 2.2.3). The dispersion curves involve one which goes to the origin as $k \to 0$ (see (2.41)), called an *acoustic curve*, and a curve that is

non-zero in the same limit (see (2.40)), called an *optical curve*. In particular, the pass-band structure is formed from 2 disjoint intervals determined by the inequalities

$$0 < \omega < \sqrt{c\left(\frac{1}{m_A} + \frac{1}{m_B} - \left|\frac{1}{m_A} - \frac{1}{m_B}\right|\right)}$$

and

$$\sqrt{c\left(\frac{1}{m_A} + \frac{1}{m_B} + \left|\frac{1}{m_A} - \frac{1}{m_B}\right|\right)} < \omega < \sqrt{2c\left(\frac{1}{m_A} + \frac{1}{m_B}\right)}$$

and outside these frequency intervals is one a finite and one semi-infinite stop-band, which are associated with frequencies where waves cannot propagate in the medium. From these expressions, it can be seen that the limits of the stop-bands can be controlled by adjusting the mass of the nodes and the stiffness of the rods. In particular, one can completely close the finite stop-band by taking $m_A = m_B$ that reduces the problem to that of the uniform chain, except in this case there is an additional curve corresponding to the waves that are doubly periodic across the elementary cell.

The modes of the diatomic system can be identified from (2.38) for degenerate points (k, ω) of the coefficient matrix (located along the curves (2.40) and (2.41)). Indeed, for such a point (k^*, ω^*) the eigenvector $\mathbf{W}$ can then be obtained in the form

$$\mathbf{W} = \begin{bmatrix} 1 \\ \dfrac{2c - m_A(\omega^*)^2}{c(1 + e^{-2\mathrm{i}k^*l})} \end{bmatrix} \tag{2.42}$$

or alternatively

$$A_n = 1, \qquad B_n = \frac{2c - m_A(\omega^*)^2}{c(1 + e^{-2\mathrm{i}k^*l})} \tag{2.43}$$

that shows the amplitude of vibration for both nodes in the elementary cell can differ and depend on the material properties of the microstructure. Combining (2.43) with (2.34) and (2.35), and taking the real or imaginary part of the result allows one to determine the real displacements of the masses in the diatomic chain. An example of such modes are shown in Figure 2.8 corresponding to the coordinates of the dots in Figure 2.7.

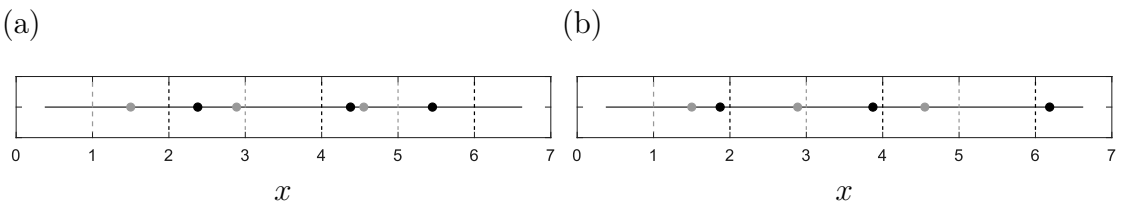

Figure 2.8: Some examples of modes for the system shown in Figure 2.6. The dots in grey (black) show the displacements for each mass from their initial positions in the medium indicated by the vertical grey (black) dashed lines, assuming $l = 1$. The modes have been computed for $k^* = 0.9$ and (a) $\omega_2^* = \omega_2(k^*) = 0.70$, (b) $\omega_1^* = \omega_1(k^*) = 1.58$, and the corresponding points on the dispersion curves are indicated by the dots in Figure 2.7.

2.4 Vibrations in a two-dimensional triangular lattice

Here, we focus the attention on using the theoretical approach discussed in Section 2.2 to determine information about waves that can propagate in a triangular lattice system, composed of rods connecting periodically placed masses. In the low-frequency range, such a model represents the response of an elastic material as described in [Slepyan (2002b)]. The material properties of this structure are assumed to be uniform i.e. the nodes at the junctions of the structure have mass m and are connected by massless rods of length l and stiffness c. The masses are assumed to displace in the plane of the lattice but do not rotate in this structure. Additionally, the displacements are assumed to be small so that the motion in the lattice can be described by linear equations. The elementary cell of the medium is shown by the grey parallelogram in Figure 2.9. This is defined by the vectors

$$\mathbf{t}^{(1)} = (l, 0)^{\mathrm{T}} , \quad \mathbf{t}^{(2)} = l(1/2, \sqrt{3}/2)^{\mathrm{T}} , \tag{2.44}$$

and in what follows we will use the matrix

$$\mathbf{T} = [\mathbf{t}^{(1)}, \mathbf{t}^{(2)}] . \tag{2.45}$$

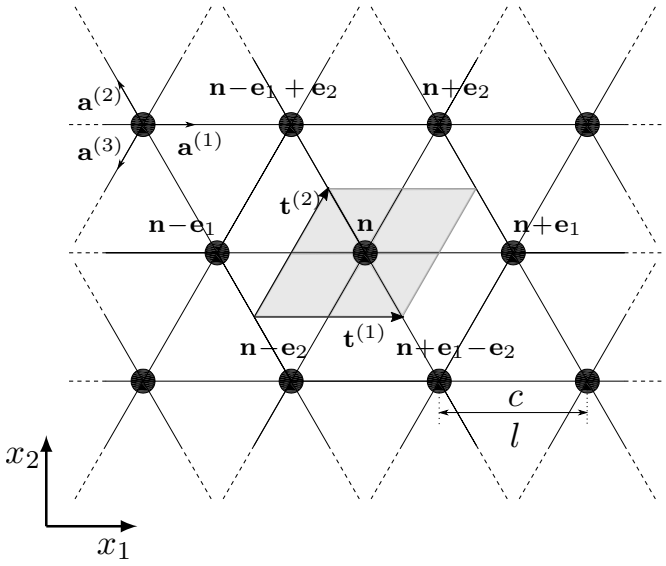

Figure 2.9: A two-dimensional triangular lattice system composed of periodically distributed masses m connected to each other by links of length l and stiffness c.

The approach developed here is applicable to other types of periodic elastic lattices composed of elementary cells that tessellate.

This elementary cell in Figure 2.9 is associated with the index $\mathbf{n} = (n_1, n_2)^{\mathrm{T}}$ and contains one node that has the displacement $\mathbf{u}(\mathbf{x}, t) = (u_1(\mathbf{x}, t), u_2(\mathbf{x}, t))^{\mathrm{T}}$, with $\mathbf{x} = n_1\mathbf{t}_1 + n_2\mathbf{t}_2$, having two components u_1 and u_2 associated with the movement of the mass in the horizontal and vertical directions, respectively. Here, we will also use the following notation

$$\mathbf{u}^{(\mathbf{n}+\mathbf{q})}(t) = \mathbf{u}(\mathbf{x} + q_1\mathbf{t}^{(1)} + q_2\mathbf{t}^{(2)}, t) \ . \tag{2.46}$$

where $\mathbf{q} = (q_1, q_2)^{\mathrm{T}}$ is multi-index, $q_j \in \mathbb{Z}$, $j = 1, 2$. We will also need the basis vectors that describe the principal lattice directions

$$\mathbf{a}^{(1)} = (1, 0)^{\mathrm{T}}, \quad \mathbf{a}^{(2)} = (-1/2, \sqrt{3}/2)^{\mathrm{T}} \quad \text{and} \quad \mathbf{a}^{(3)} = (-1/2, -\sqrt{3}/2)^{\mathrm{T}} \ ,$$

(see Figure 2.9). The node in cell $\mathbf{n}$ is connected by rods to six neighbouring nodes. In what follows, we calculate the elastic forces exerted on the node in the cell $\mathbf{n}$, in order to determine the equations of motion governing the junction points in the

lattice.

Elastic restoring forces of the rods and the lattice equations of motion

We already have shown in Section 2.2 that the massless rods deform linearly with respect to their axial local coordinates. The small deformations of the links imply their deformed configuration differs only by a small amount from their undeformed configuration and subsequently the change in the angle of the link during its motion is small. As a result, the elongation of a link can be determined by comparing the deformed and undeformed configurations as follows. We project the deformation of the rod onto the undeformed rod. In this case, in the cell defined by the index $\mathbf{n}$, the elongation of the rods aligned with $\pm\mathbf{a}^{(j)}$ are given as

$$E^{(\mathbf{n},\pm\mathbf{q}_j)} = \pm(\mathbf{u}^{(\mathbf{n}\pm\mathbf{q}_j)}(t) - \mathbf{u}^{(\mathbf{n})}(t)) \cdot \mathbf{a}^{(j)} \tag{2.47}$$

for $j = 1, 2$ and 3. Here

$$\mathbf{q}_1 = \mathbf{e}_1, \quad \mathbf{q}_2 = \mathbf{e}_2 - \mathbf{e}_1, \quad \text{and} \quad \mathbf{q}_3 = \mathbf{e}_2, \tag{2.48}$$

and

$$\mathbf{e}^{(1)} = (1,0)^T \quad \text{and} \quad \mathbf{e}^{(2)} = (0,1)^T\,, \tag{2.49}$$

that allow us to describe the position of the neighbouring nodes to the mass in cell $\mathbf{n}$, and to compute their displacements in accordance with (2.46) (see Figure 2.9). Thus the elastic restoring forces exerted by the rods are expressed using the elongations as

$$Q^{(\mathbf{n},\pm\mathbf{q}_j)} = cE^{(\mathbf{n},\pm\mathbf{q}_j)}\,, \tag{2.50}$$

where $c = EA/l$ is the effective stiffness of the rod. Then, the linear momentum balance for the node in the cell defined by $\mathbf{n}$ is

$$m\ddot{\mathbf{u}}^{(\mathbf{n})}(t) = \sum_{j=1}^{3} Q^{(\mathbf{n},\mathbf{q}_j)}\mathbf{a}^{(j)} - \sum_{j=1}^{3} Q^{(\mathbf{n},-\mathbf{q}_j)}\mathbf{a}^{(j)}\,, \tag{2.51}$$

where the product in the summands on the right-hand side gives the projection of the force $Q^{(\mathbf{n},\pm\mathbf{q_j})}$ directed along $\pm\mathbf{a}^{(j)}$ onto the x_1x_2-axes. In the expanded form, using (2.47) and (2.50), we obtain from (2.51):

$$\begin{aligned} m\ddot{\mathbf{u}}^{(\mathbf{n})} &= c\Big[(\mathbf{a}^{(1)}\cdot[\mathbf{u}^{(\mathbf{n}+\mathbf{q}_1)}+\mathbf{u}^{(\mathbf{n}-\mathbf{q}_1)}-2\mathbf{u}^{(\mathbf{n})}])(\mathbf{a}^{(1)}) \\ &\quad +(\mathbf{a}^{(2)}\cdot[\mathbf{u}^{(\mathbf{n}+\mathbf{q}_2)}+\mathbf{u}^{(\mathbf{n}-\mathbf{q}_2)}-2\mathbf{u}^{(\mathbf{n})}])(\mathbf{a}^{(2)}) \\ &\quad +(\mathbf{a}^{(3)}\cdot[\mathbf{u}^{(\mathbf{n}+\mathbf{q}_3)}+\mathbf{u}^{(\mathbf{n}-\mathbf{q}_3)}-2\mathbf{u}^{(\mathbf{n})}])(\mathbf{a}^{(3)})\Big]\,, \end{aligned} \tag{2.52}$$

(see also [Slepyan (2002b)]).

2.4.1 Dispersion relations for the triangular structured medium

Next, we introduce the time-harmonic form of the function $\mathbf{u}^{(\mathbf{n})}$ as

$$\mathbf{u}^{(\mathbf{n})}(t)=\mathbf{U}^{(\mathbf{n})}e^{-\mathrm{i}\omega t} \tag{2.53}$$

and the amplitude vector $\mathbf{U}^{(\mathbf{n})}$, describing the amplitude of the displacements, satisfies the Floquet-Bloch conditions (see Section 2.2.3):

$$\mathbf{U}^{(\mathbf{n}+\mathbf{q})}=\mathbf{U}^{(\mathbf{n})}e^{\mathrm{i}\mathbf{k}\cdot\mathbf{T}\mathbf{q}}\,. \tag{2.54}$$

Substitution of this into (2.52) then gives

$$\begin{aligned} -m\omega^2\mathbf{U}^{(\mathbf{n})}e^{-\mathrm{i}\omega t} &= 2c\Big[[\cos(\mathbf{k}\cdot\mathbf{T}\mathbf{q}_1)-1](\mathbf{a}^{(1)}\cdot\mathbf{U}^{(\mathbf{n})})(\mathbf{a}^{(1)}) \\ &\quad +[\cos(\mathbf{k}\cdot\mathbf{T}\mathbf{q}_2)-1](\mathbf{a}^{(2)}\cdot\mathbf{U}^{(\mathbf{n})})(\mathbf{a}^{(2)}) \\ &\quad +[\cos(\mathbf{k}\cdot\mathbf{T}\mathbf{q}_3)-1](\mathbf{a}^{(3)}\cdot\mathbf{U}^{(\mathbf{n})})(\mathbf{a}^{(3)})\Big]e^{-\mathrm{i}\omega t}\,, \end{aligned} \tag{2.55}$$

that in cancelling the time-harmonic factor, after further simplification, we arrive at the homogeneous equation:

$$\begin{aligned} \Big[&-m\omega^2\mathbf{I}-2c[\cos(\mathbf{k}\cdot\mathbf{T}\mathbf{q}_1)-1](\mathbf{a}^{(1)}\otimes\mathbf{a}^{(1)})-2c[\cos(\mathbf{k}\cdot\mathbf{T}\mathbf{q}_2)-1](\mathbf{a}^{(2)}\otimes\mathbf{a}^{(2)}) \\ &+2c[\cos(\mathbf{k}\cdot\mathbf{T}\mathbf{q}_3)-1](\mathbf{a}^{(3)}\otimes\mathbf{a}^{(3)})\Big]\mathbf{U}^{(\mathbf{n})}=0\,, \end{aligned} \tag{2.56}$$

where $\mathbf{I}$ is the 2×2 identity matrix. The terms involving the Bloch vector $\mathbf{k}$ can be condensed using (2.45), (2.48) and (2.49) to allow for a compact representation of the above equation:

$$[\mathbf{C} - \omega^2 \mathbf{M}]\mathbf{U}^{(\mathbf{n})} = \mathbf{0}. \tag{2.57}$$

In the preceding equation, the stiffness matrix $\mathbf{C}$ has the representation

$$\mathbf{C} = \begin{bmatrix} C_{11} & C_{12} \\ C_{12} & C_{22} \end{bmatrix} = c \begin{bmatrix} 3 - 2\cos(k_1 l) - \frac{\cos(\eta)+\cos(\gamma)}{2} & \frac{\sqrt{3}(\cos(\gamma)-\cos(\eta))}{2} \\ \frac{\sqrt{3}(\cos(\gamma)-\cos(\eta))}{2} & 3 - 3\frac{\cos(\eta)-\cos(\gamma)}{2} \end{bmatrix}, \tag{2.58}$$

with $\eta = k_1 l/2 + k_2\sqrt{3}l/2$ and $\gamma = k_1 l/2 - k_2\sqrt{3}l/2$. In addition, the mass matrix $\mathbf{M} = m\mathbf{I}$. Once more, non-trivial solutions to the homogeneous system (2.57) are obtained by imposing the determinant of the matrix on the left-hand side is equal to zero:

$$\det[\mathbf{C} - \omega^2 \mathbf{M}] = \mathbf{0}.$$

The above may also be written as

$$(-m\omega^2 + C_{11})(-m\omega^2 + C_{22}) - C_{12}^2 = 0 \, ,$$

which after simplification gives the following biquadratic equation in terms of ω:

$$m^2\omega^4 - m\mathrm{tr}(\mathbf{C})\omega^2 + \det(\mathbf{C}) = 0 \, .$$

Thus, from this, we have the positive solutions for the radian frequency ω are

$$\omega_1 = \left[\frac{1}{2m}\{\mathrm{tr}(\mathbf{C}) - [(\mathrm{tr}(\mathbf{C}))^2 - 4\det(\mathbf{C})]^{1/2}\}\right]^{1/2} \tag{2.59}$$

and

$$\omega_2 = \left[\frac{1}{2m}\{\mathrm{tr}(\mathbf{C}) + [(\mathrm{tr}(\mathbf{C}))^2 - 4\det(\mathbf{C})]^{1/2}\}\right]^{1/2} . \tag{2.60}$$

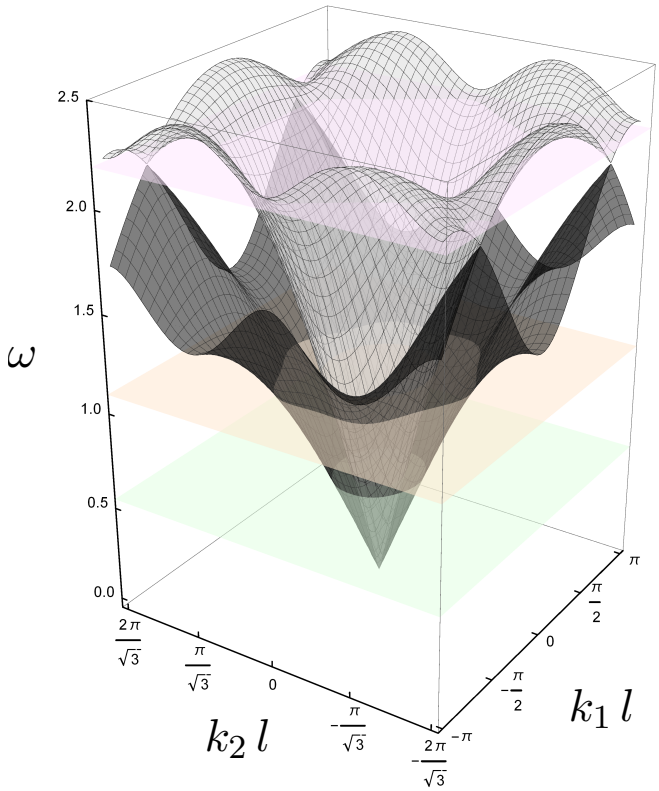

Figure 2.10: Dispersion surfaces for the triangular lattice based on (2.59) and (2.60) as functions of the dimensionless quantity kl. The materials parameters of the lattice are $m = c = 1$. The light grey surface is connected with pressure waves that can be excited in the medium, whereas the dark grey surface corresponds to shear waves. Horizontal planes in green, orange and pink corresponding to the frequencies $\omega = 0.55, 1.1$ and 2.2 in the pass-band for the medium are shown. The slowness contours defined by these planes are shown in Figure 2.11.

2.4.2 Illustrative examples: Dispersive nature of the triangular lattice

In this Section, we analyse the dispersion relations obtained for the triangular system and highlight some interesting vibration properties of this medium.

The dispersion relations (2.59) and (2.60) provide dispersion surfaces characterising the dynamic behaviour of the medium. These are shown in Figure 2.10, where both surfaces shown are of the acoustic type (i.e. intersect the origin when $k_1 = k_2 = 0$). Clearly, Figure 2.10 shows the medium possesses a finite pass-band covered by the dispersion surfaces. Additionally, the medium is dispersive due to the nonlinear nature of the surfaces. The lower surface governs the propagation of *shear*

waves in the medium, while the upper surface is associated with the propagation of *pressure waves*. A semi-infinite stop-band exists for frequencies outside the range covered by pressure wave dispersion curve.

For the triangular lattice system, vibration modes can be analysed by investigating *slowness contours* found by the intersection of the surfaces with horizontal planes corresponding to the frequency of vibration. The outward unit normal vector $\boldsymbol{\nu}$ to these contours indicate the direction of propagation of the waves when the medium is excited. This vector can be calculated using as

$$\boldsymbol{\nu} = \frac{\nabla\omega(\mathbf{k})}{|\nabla\omega(\mathbf{k})|} \,, \tag{2.61}$$

where $\omega = \omega_j$, $j = 1$ or 2, and $\mathbf{k}$ is located along the slowness contour. Here, the numerator in the right-hand side is the *group velocity* for the wave defined by $\mathbf{k}$ and ω.

In Figure 2.10, we show three planes that intersect the dispersion surfaces. The intersection of these planes with the surfaces provide slowness contours. The slowness contours corresponding to these planes are presented in Figure 2.11(a), (c) and (e), which show as the frequency of vibration is increased the shape and number of the contours can differ. In addition, in these plots we indicate the irreducible Brillouin zone for the medium, that according to Section 2.2.3, are defined by the vectors:

$$\mathbf{b}^{(1)}l = 2\pi(1, -1/\sqrt{3})^T \,, \qquad \mathbf{b}^{(2)}l = 2\pi(0, 2/\sqrt{3})^T \,.$$

For low frequencies, Figure 2.11(a) shows the two slowness contours in the irreducible Brillouin zone produced by the dispersion curves are almost circular. This indicates that at this frequency the lattice under external excitation will behave dynamically isotropic, i.e. waves will propagate in all directions. The interior contour is connected with pressure waves, whereas the shear waves are linked to the exterior contour. The corresponding eigenmode has been computed with *Comsol* in Figure 2.11(b) for a triangular lattice subjected to an oscillating point force in the vertical

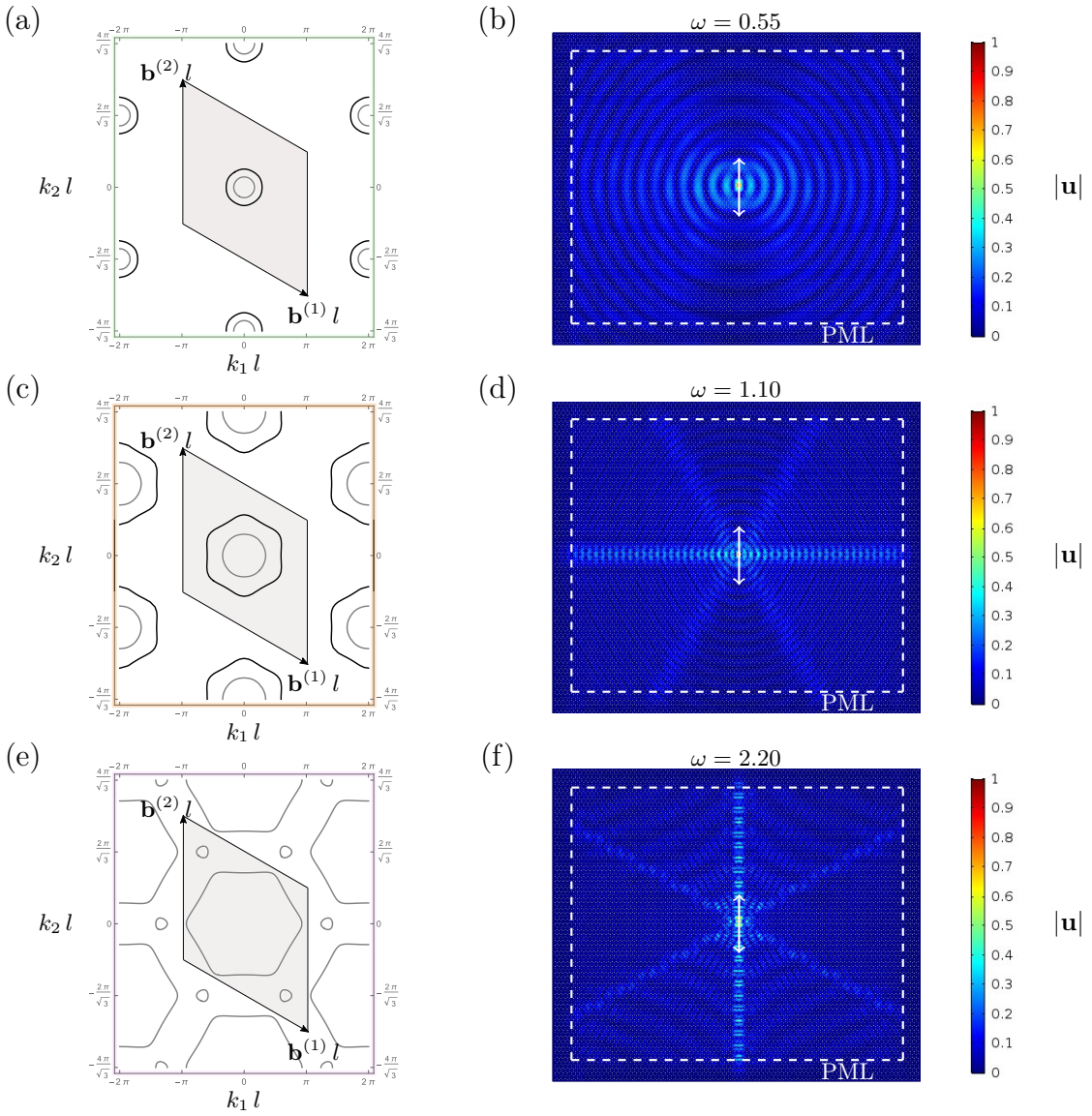

Figure 2.11: Slowness contours for the triangular lattice and the dynamic response of a sufficiently large finite triangular lattice. Slowness contours are shown as functions of $k_j l$, $j = 1, 2$, in (a) $\omega = 0.55$, (c) $\omega = 1.1$ and (e) $\omega = 2.2$ and are associated with the green, orange and pink planes, respectively in Figure 2.10. The irreducible Brillouin zone defined by $\mathbf{b}^{(j)}\, l$, $j = 1, 2$ is also indicated in each diagram by the shaded region. In (b), (d) and (f), we show *Comsol* computations illustrating the response of a triangular lattice subjected to a vertically acting in-plane oscillating point force, positioned at the centre of the lattice, with the frequencies associated with (a), (c) and (e), respectively. The total displacement $|\mathbf{u}|$ in the lattice is plotted. In the *Comsol* computations, a region of Perfectly Matched Layers (PML) has been used to reduce the reflections from the external boundaries and to simulate the infinite medium.

direction. As expected, vibrations propagate in all directions. We note the pressure waves possess a longer wavelength than the shear waves, which is consistent with Figure 2.11(a). The shear waves can be seen in Figure 2.11(b) propagating to the left and right of the source. The pressure waves propagate in the vertical directions from the applied force. We note the strength or intensity of the waves observed in each direction also depends on the direction of the lattice forcing.

Figure 2.11(c), shows the slowness contours for a higher frequency. Here, the pressure-type contour remains circular, whereas the shear-type slowness contour appears to almost hexagonal. The latter produces what is known as *dynamic anisotropy* in the lattice, where waves propagate in preferential directions when the structure is excited. This is evident in Figure 2.11(d), where the lattice response to vertical excitation shows six clear directions or rays corresponding to angles $j\pi/3$, $j = 0, 1$ and 2, measured in the anticlockwise direction, along which the shear waves propagate. In this mode we also have the interaction of shear and pressure waves. In particular, in the vertical direction, the pressure waves (having a larger wavelength) can be still seen to propagate away from the source.

Finally, in Figure 2.11(e), we show the slowness contours corresponding to the highest frequency in Figure 2.10. In this case, only one slowness contour exists in the irreducible Brillouin zone, which governs the excitation of pressure waves in the lattice. Moreover, the contour indicates that the response of the lattice will be dynamically anisotropic, as evidenced in Figure 2.11(f), were only pressure waves excited by the force can be clearly seen propagating in six preferential directions defined by $\pi(2j + 1)/6$, $j = 0, 1$ and 2 measured in the anti-clockwise direction.

2.5 Concluding remarks

In this Section, we have introduced several model examples of discrete media and described the general procedure for analysing their vibration properties, which includes the use of quasi-periodicity conditions, known as the Floquet-Bloch conditions, and techniques from linear algebra. The examples provided here lay the foundation

for the works presented in the Chapters that follow. In addition, we have shown that lattice materials can be used to describe the microstructure of a continuous material within the low frequency range. We have also shown that information about vibration modes in discrete materials, obtained from analytical models, can be used to determine important information allowing one to predict the response of structures exposed to dynamic loads in independent numerical models. A key result shown here concerns the dynamic anisotropic properties of two-dimensional discrete systems, which is a characteristic of materials possessing micro-structure and we note such effects are not found in models of vibration in continuous materials.

Chapter 3

Dynamic phenomena in gyro-elastic structured media

In this Chapter, we introduce the notion of gyro-elastic structured medium, involving a discrete elastic lattice whose junctions are attached to gyroscopic spinners. This model first appeared in [Brun, Jones and Movchan (2012)] for a triangular lattice system, where the interaction between a gyroscope and a truss system was also developed in the time-harmonic regime. In particular, we will exploit this model to create discrete gyro-elastic hexagonal systems and demonstrate a new method for achieving topologically protected states. We show for such a medium that one can manipulate the locations of stop-bands and dispersion degeneracies, or Dirac points, by tuning the parameters of the spinners. In the proximity of such points, uni-directional interfacial waveforms can be created in an inhomogeneous lattice and the direction of such waveforms can be controlled. We also study the effect of inserting additional soft internal links into a hexagonal system, transforming it into a heterogeneous triangular lattice, and we show the hexagonal lattice represents a limit case of the heterogeneous triangular lattice with soft links. We also demonstrate how inhomogeneous discrete gyro-elastic triangular media can support interfacial waves.

The structure of this Chapter is as follows. In Section 3.1, we give an overview of existing results concerning the analysis of gyro-elastic discrete materials and demonstrate some of their remarkable wave guiding properties. We extend the

model of [Brun, Jones and Movchan (2012)] in Section 3.2 to study the dynamics of discrete hexagonal gyro-elastic systems. Section 3.3 is dedicated to the analysis of such systems and their application in designing inhomogeneous discrete hexagonal gyro-elastic materials that support interfacial waves. In Section 3.4, we show that the hexagonal chiral system developed here can be linked to an inhomogeneous chiral triangular lattice containing soft internal links and we also demonstrate the capability of the latter in supporting interfacial waveforms. In Section 3.5, we give some conclusions and discussion related to the results in this Chapter.

3.1 Chiral triangular elastic lattices

We begin by introducing the analytical model developed in [Brun, Jones and Movchan (2012)], that describes the motion of a triangular lattice system, whose junctions are attached to an array of gyroscopic spinners (see Figure 3.1(a)). To determine the governing equations for such a system, it is necessary to find the forcing terms attributed to the action of the gyroscopes, which is discussed in Section 3.1.1. Once this has been identified, the model corresponding to the interaction between a gyroscope and a truss system can be exploited to develop lattice systems attached to arrays of spinners with special dynamic properties. We give a brief overview of the analysis and properties of such systems in Section 3.1.2.

3.1.1 The interaction between a gyroscope and a truss system in the time-harmonic regime

Here we follow the derivation outlined in [Brun, Jones and Movchan (2012)] for identifying how a spinner interacts with a mass embedded in a truss system (see Figure 3.1(b)). In particular, the force given by the spinner to the mass is identified.

The gyroscope is treated as a rigid body, which is pinned in the low end, and its motion is characterised by the generalised coordinates known as the Euler's angles ϕ, θ, ψ that govern the precession, nutation and spin of the gyroscopic spinner,

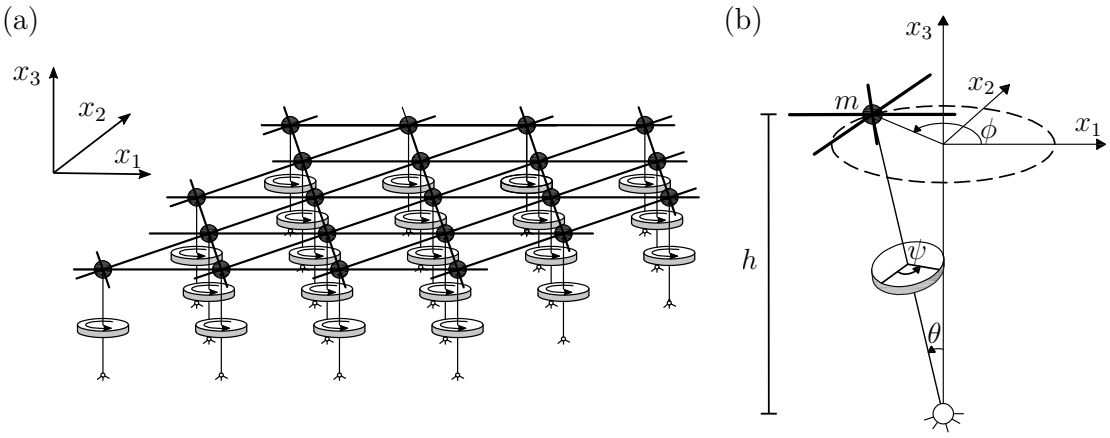

Figure 3.1: (a) Triangular lattice attached to a uniform distribution of gyroscopic spinners introduced in [Brun, Jones and Movchan (2012)]. (b) Schematic description of a node of mass m, embedded in a truss and attached to gyroscopic spinner, where ψ, ϕ and θ are the angles of spin, precession and nutation, respectively. The spinner is also hinged at the base.

respectively. The axis of the spinner is assumed to initially be perpendicular to the plane of the lattice.

Following [Goldstein, Poole and Safko (2001)], one can write the angular momentum balance for the spinner, which takes the form of three non-linear time-dependent differential equations:

$$\begin{aligned} M_{x_1} &= I_0\ddot{\theta} + (I_1 - I_0)\dot{\phi}^2 \sin(\theta)\cos(\theta) + I_1\dot{\phi}\dot{\psi}\sin(\theta) \,, \\ M_{x_2} &= I_0\ddot{\phi}\sin(\theta) + (2I_0 - I_1)\dot{\phi}\dot{\theta}\cos(\theta) - I_1\dot{\theta}\dot{\psi} \,, \\ M_{x_3} &= I_1(\ddot{\phi}\cos(\theta) - \dot{\phi}\,\dot{\theta}\sin(\theta) + \ddot{\psi}) \,, \end{aligned} \tag{3.1}$$

where the dot denotes the derivative with respect to time, I_0 and I_1 are the moments of inertia of the gyroscope about the x_1 (or x_2) and x_3-axes, respectively and M_{x_j}, are external moments about the x_j-axis $j = 1, 2$ and 3. We assume the displacement of the lattice particle is small throughout its motion, and hence the nutation angle of the gyroscopic spinner is also small, namely $|\theta| \ll 1$. Accordingly, one can linearise the above equations using Taylor's expansion with respect to θ and retrieve to leading

order the equations of motion:

$$
\begin{aligned}
M_{x_1} &= I_0\ddot{\theta} + (I_1 - I_0)\dot{\phi}^2\theta + I_1\dot{\phi}\dot{\psi}\theta \ , \\
M_{x_2} &= I_0\ddot{\phi}\theta + (2I_0 - I_1)\dot{\theta}\dot{\phi} - I_1\dot{\theta}\dot{\psi} \ , \\
M_{x_3} &= I_1(\ddot{\psi} - \dot{\phi}\,\dot{\theta}\theta + \ddot{\phi}) \ .
\end{aligned} \tag{3.2}
$$

Additionally, it is assumed that the spin rate of the gyroscope is constant, i.e. $\dot{\psi} = \Omega = \text{Const}$ and since the lattice particles are assumed to move in the plane of the lattice, the moments M_{x_1} and M_{x_2} are taken as zero. Hence, we arrive at

$$0 = I_0\ddot{\theta} + (I_1 - I_0)\dot{\phi}^2\theta + I_1\dot{\phi}\Omega\theta \ , \tag{3.3}$$

$$0 = I_0\ddot{\phi}\theta + (2I_0 - I_1)\dot{\theta}\dot{\phi} - I_1\,\Omega\,\dot{\theta} \ , \tag{3.4}$$

$$M_{x_3} = -I_1\dot{\phi}\,\dot{\theta}\theta + \ddot{\phi}I_1 \ . \tag{3.5}$$

As we are considering the time-harmonic regime, the nutation angle θ is taken in the form:

$$\theta = \Theta e^{i\omega t} \ , \ \text{with} \quad |\Theta| \ll 1 \ , \tag{3.6}$$

where ω is the radian frequency of the truss system. If we assume the precession rate is constant ($\ddot{\phi} = 0$), then (3.4) gives

$$\dot{\phi} = \frac{I_1}{2I_0 - I_1}\Omega \ . \tag{3.7}$$

Substituting (3.6) into (3.3) and using (3.7), we determine the following compatibility condition between the spin rate Ω and the radian frequency ω:

$$\Omega = \pm\frac{2I_0 - I_1}{I_1}\omega \ . \tag{3.8}$$

Comparing (3.7) and (3.8), it is possible to observe that $\dot{\phi} = \pm\omega$.

Finally, using (3.5) and (3.6), the expression for the moment M_{x_3} imposed about

the x_3-axis can be derived as:

$$M_{x_3} = \mp i\omega^2\theta^2 I_1. \tag{3.9}$$

In the small nutation/displacement regime, the nutation angle is given by $\theta = |\mathbf{u}|/h$, where $|\mathbf{u}|$ is the magnitude of the (in-plane) particle displacement and h is the distance of the lattice to the base of the spinner, see Figure 3.1(b). Hence, the force applied to the lattice particle by the gyroscopic spinner is

$$F = \frac{M_{x_3}}{|\mathbf{u}|} = \mp i\frac{I_1}{h^2}\omega^2|\mathbf{u}| \ . \tag{3.10}$$

Here, we set

$$\beta = \frac{I_1}{h^2} \ , \tag{3.11}$$

which is known as the spinner constant (see [Brun, Jones and Movchan (2012)]).

3.1.2 Discrete triangular lattice with gyroscopic spinners

Having evaluated the magnitude of the forcing terms provided by the gyroscopes to a single junction inside a truss system we now consider the governing equations for a discrete triangular lattice attached to gyroscopic spinners (see Figure 3.1(a)). As assumed in [Brun, Jones and Movchan (2012)], the gyroscopes provide a forcing perpendicular to the displacement of a node inside the lattice. Based on this and the results of Section 2.4 and those of the previous section (see (3.10) and (3.11)), in the time-harmonic regime, the governing equations for a node in the triangular lattice may be written as

$$\begin{aligned} -m\omega^2\mathbf{U}^{(\mathbf{n})} \ = \ & c\Big[(\mathbf{a}^{(1)}\cdot[\mathbf{U}^{(\mathbf{n}+\mathbf{q}_1)}+\mathbf{U}^{(\mathbf{n}-\mathbf{q}_1)}-2\mathbf{U}^{(\mathbf{n})}])(\mathbf{a}^{(1)}) \\ & +(\mathbf{a}^{(2)}\cdot[\mathbf{U}^{(\mathbf{n}+\mathbf{q}_2)}+\mathbf{U}^{(\mathbf{n}-\mathbf{q}_2)}-2\mathbf{U}^{(\mathbf{n})}])(\mathbf{a}^{(2)}) \\ & +(\mathbf{a}^{(3)}\cdot[\mathbf{U}^{(\mathbf{n}+\mathbf{q}_3)}+\mathbf{U}^{(\mathbf{n}-\mathbf{q}_3)}-2\mathbf{U}^{(\mathbf{n})}])(\mathbf{a}^{(3)})\Big] + \mathrm{i}\beta\omega^2\mathbf{R}\mathbf{U}^{(\mathbf{n})} \ , \end{aligned} \tag{3.12}$$

where $\mathbf{U}^{(\mathbf{n})}$ is the displacement amplitude vector of the node in the cell associated with the index $\mathbf{n}$, $\mathbf{a}^{(j)}$, $j = 1, 2, 3$ are the lattice basis vectors, m is the mass of the nodes at the junctions of the lattice and c is the stiffness of the rods connecting each mass in the system. The last term in the right-hand side represents the influence of the gyroscopic spinner on the mass, which confers chirality to the lattice, and

$$\mathbf{R} = \begin{pmatrix} 0 & 1 \\ -1 & 0 \end{pmatrix} , \tag{3.13}$$

which provides a coupling between the components of displacement for a lattice node. As shown in Chapter 2, one can use the Floquet-Bloch conditions imposed on the displacement amplitude vector $\mathbf{U}^{(\mathbf{n})}$ to allow one to reduce (3.12) to a homogeneous system. Following this the dispersion relations for this chiral medium can be obtained. In view of this and the results of Section 2.4.1, Chapter 2, this can be written as

$$(m^2 - \beta^2)\omega^4 - m\mathrm{tr}(\mathbf{C})\omega^2 + \det(\mathbf{C}) = 0 , \tag{3.14}$$

where $\mathbf{C}$ is given in (2.58). The solutions of the above for $\beta \neq m$ are

$$\omega_1 = \left[\frac{m}{2(m^2 - \beta^2)} \{ \mathrm{tr}(\mathbf{C}) - [(\mathrm{tr}(\mathbf{C}))^2 - 4 \left(1 - \frac{\beta^2}{m^2} \right) \det(\mathbf{C})]^{1/2} \} \right]^{1/2} \tag{3.15}$$

and

$$\omega_2 = \left[\frac{m}{2(m^2 - \beta^2)} \{ \mathrm{tr}(\mathbf{C}) + [(\mathrm{tr}(\mathbf{C}))^2 - 4 \left(1 - \frac{\beta^2}{m^2} \right) \det(\mathbf{C})]^{1/2} \} \right]^{1/2} , \tag{3.16}$$

where we note if the spinner constant is chosen equal to the mass, this leads to a degenerate case with only one dispersion surface (see (3.14)):

$$\omega = \sqrt{\frac{\det(\mathbf{C})}{m\mathrm{tr}(\mathbf{C})}} .$$

For $\beta > m$ only the surface defined by (3.15) exists. We do not present this analysis of the dispersive properties here, but comment on some interesting results concerning

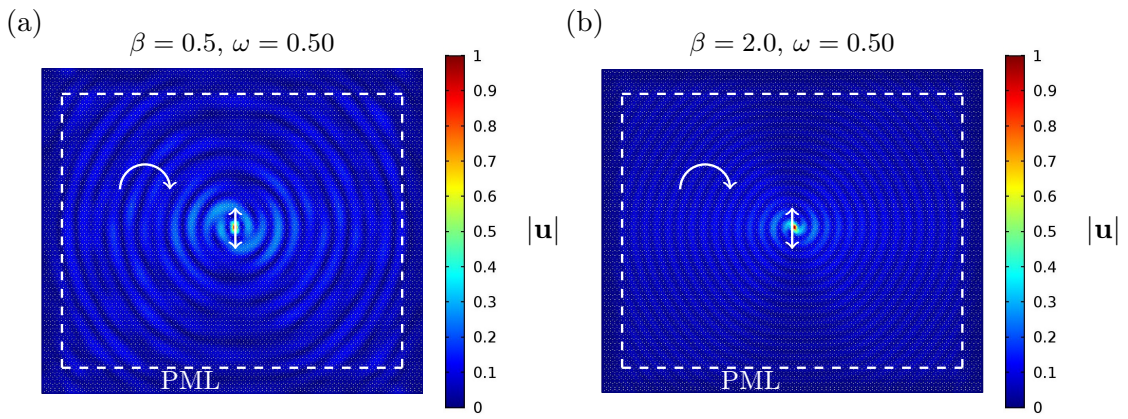

Figure 3.2: The low frequency response of a finite gyro-elastic lattice. The lattice is subjected to a vertically acting harmonic point force, whose position is indicated by the vertical arrow. The forcing frequency is $\omega = 0.5$. We show the response of a medium attached to a uniform array of gyroscopes described by the spinner constant (a) $\beta = 0.5$ and (b) $\beta = 2.0$. In both computations, the lattice boundaries have been supplied with a layer of PMLs to reduce the effects of internal reflections and to simulate an infinite medium.

the dispersive properties of gyro-elastic systems found in [Brun, Jones and Movchan (2012)] and [Carta et al. (2014)]. A detailed analysis of such systems will be given later, when new gyro-elastic systems will be considered. In [Brun, Jones and Movchan (2012)], it was shown that a uniform array of gyroscopic spinners attached to a homogeneous triangular lattice allows the elastic lattice to suppress pressure waves at low frequencies. Figure 3.2(a) shows the response of the medium, attached to a uniform array of spinners $\beta = 0.5$, when loaded by a harmonic force of amplitude equal to unity and frequency $\omega = 0.5$. The result shows a vortex type wave originating from the vertically acting load. In this instance, the lattice produces a dynamically isotropic response formed from a mixture of shear and pressure waves. In Figure 3.2(b), we demonstrate that by changing the type of spinner attached to the lattice, we can suppress the propagation of pressure waves in the medium, and only shear waves (possessing a shorter wavelength) are produced by the load. Once more, we note in this case, the lattice supports a vortex-type wave that appears to be dynamically isotropic.

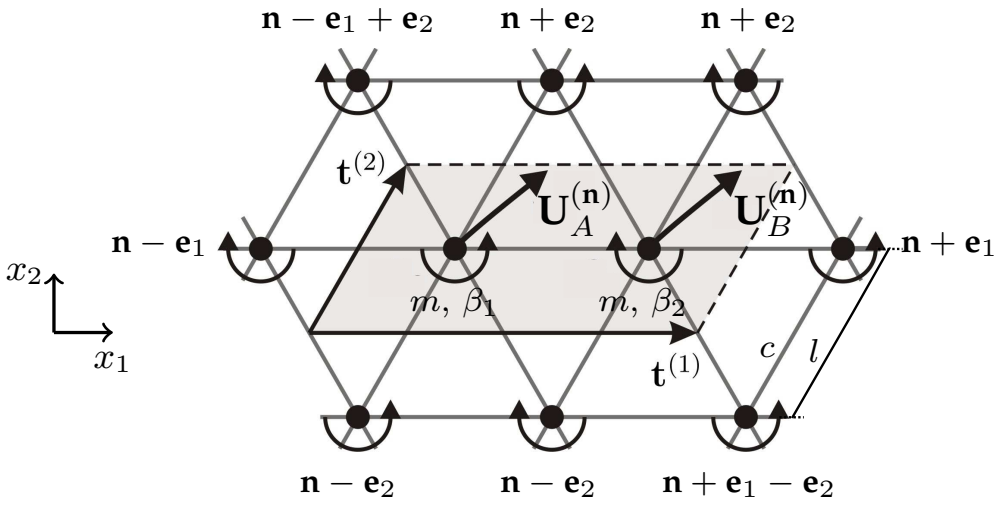

Figure 3.3: Gyro-elastic triangular lattice attached to a non-uniform distribution of gyroscopic spinners. Here $\mathbf{U}_A$ ($\mathbf{U}_B$) represent the displacement amplitude for the mass m attached to a gyroscope with spinner constant β_1 (β_2). The nodal points are connected by links of stiffness c and length l. The unit cell of the periodic system is indicated by the shaded region and are defined by the vectors $\mathbf{t}^{(1)} = l(2,0)^{\mathrm{T}}$ and $\mathbf{t}^{(2)} = l(1/2,\sqrt{3}/2)^{\mathrm{T}}$.

Inhomogeneous gyro-elastic triangular lattice and highly localised waveforms

In particular, one can use an inhomogeneous array of gyroscopic spinners to achieve special methods for controlling vibrations. In [Carta et al. (2017a)], a uniform triangular lattice attached to a doubly periodic array of gyroscopic spinners (see Figure 3.3) was shown to admit highly localised waves forms. In this case, the equations for the nodes in the elementary cell or macro-cell can be written as

$$\begin{aligned} -m\omega^2\mathbf{U}_A^{(\mathbf{n})} &= c\Big[(\mathbf{a}^{(1)}\cdot[\mathbf{U}_B^{(\mathbf{n}+\mathbf{q}_1)}+\mathbf{U}_B^{(\mathbf{n}-\mathbf{q}_1)}-2\mathbf{U}_A^{(\mathbf{n})}])(\mathbf{a}^{(1)}) \\ &\quad +(\mathbf{a}^{(2)}\cdot[\mathbf{U}_B^{(\mathbf{n}+\mathbf{q}_2)}+\mathbf{U}_B^{(\mathbf{n}-\mathbf{q}_3)}-2\mathbf{U}_A^{(\mathbf{n})}])(\mathbf{a}^{(2)}) \\ &\quad +(\mathbf{a}^{(3)}\cdot[\mathbf{U}_A^{(\mathbf{n}+\mathbf{q}_3)}+\mathbf{U}_A^{(\mathbf{n}-\mathbf{q}_3)}-2\mathbf{U}_A^{(\mathbf{n})}])(\mathbf{a}^{(3)})\Big]+\mathrm{i}\beta_1\omega^2\mathbf{R}\mathbf{U}_A^{(\mathbf{n})} \end{aligned} \tag{3.17}$$

and

$$\begin{aligned} -m\omega^2\mathbf{U}_B^{(\mathbf{n})} &= c\Big[(\mathbf{a}^{(1)}\cdot[\mathbf{U}_A^{(\mathbf{n}+\mathbf{q}_1)}+\mathbf{U}_A^{(\mathbf{n})}-2\mathbf{U}_B^{(\mathbf{n})}])(\mathbf{a}^{(1)}) \\ &\quad +(\mathbf{a}^{(2)}\cdot[\mathbf{U}_A^{(\mathbf{n}+\mathbf{q}_3)}+\mathbf{U}_A^{(\mathbf{n}-\mathbf{q}_2)}-2\mathbf{U}_B^{(\mathbf{n})}])(\mathbf{a}^{(2)}) \\ &\quad +(\mathbf{a}^{(3)}\cdot[\mathbf{U}_B^{(\mathbf{n}+\mathbf{q}_3)}+\mathbf{U}_B^{(\mathbf{n}-\mathbf{q}_3)}-2\mathbf{U}_B^{(\mathbf{n})}])(\mathbf{a}^{(3)})\Big]-\mathrm{i}\beta_2\omega^2\mathbf{R}\mathbf{U}_B^{(\mathbf{n})}. \end{aligned} \tag{3.18}$$

Here, the influence of two different spinners is characterised by the last terms in the right-hand sides of (3.17) and (3.18), where one gyro has the spinner constant β_1 and the other β_2.

From the analysis of the dispersive features of this medium presented in [Carta et al. (2017a)], it follows that if the spinner constants are chosen such that $|\beta_1| \neq |\beta_2|$, then one can find a frequency of vibration where the associated slowness contours are parallel straight lines that give rise to special dynamic phenomena in the system.

This is explored in the example shown in Figure 3.4(a), which shows the dispersion surfaces for the medium of Figure 3.4 for a given $\beta_1 \neq \beta_2$. A plane that intersects the highest surface, corresponding to a high-frequency of vibration for the medium, is also shown and the associated slowness contours are presented in Figure 3.4(b). It can be seen that the slowness contours are straight lines parallel to each other. The normal to these lines describe the direction of wave propagation in the lattice system (which is at 60° anti-clockwise from the horizontal).

To understand the response of the medium, we use *Comsol* to model the doubly periodic gyro-elastic finite lattice subjected to a vertically acting oscillating point source. The dimensions of the lattice are $90l \times 76.2l$, $(l = 1)$, and a layer of PML has been supplied on the exterior boundary of the computational domain to reduce reflections produced by the boundaries. The frequency of the point force is chosen equal to the frequency that produces the slowness contours in Figure 3.4 for the analogous infinite medium. The response of the lattice shows the medium supports a highly localised wave propagating at 60° inside the medium.

Further, in [Carta et al. (2017a)] it was also shown that the arrangement of spinners can be modified within sub-domains in the lattice to control the direction of propagation of this localised waveform, enabling one to send waves between any two points in the lattice.

We revisit some of the models presented in [Carta et al. (2017a)], in Chapter 4 where we perform a transient analysis of such systems. Next, we focus on adapting the model of [Brun, Jones and Movchan (2012)], to model hexagonal elastic lattices attached to arrays of gyroscopic spinners and we identify their special vibration

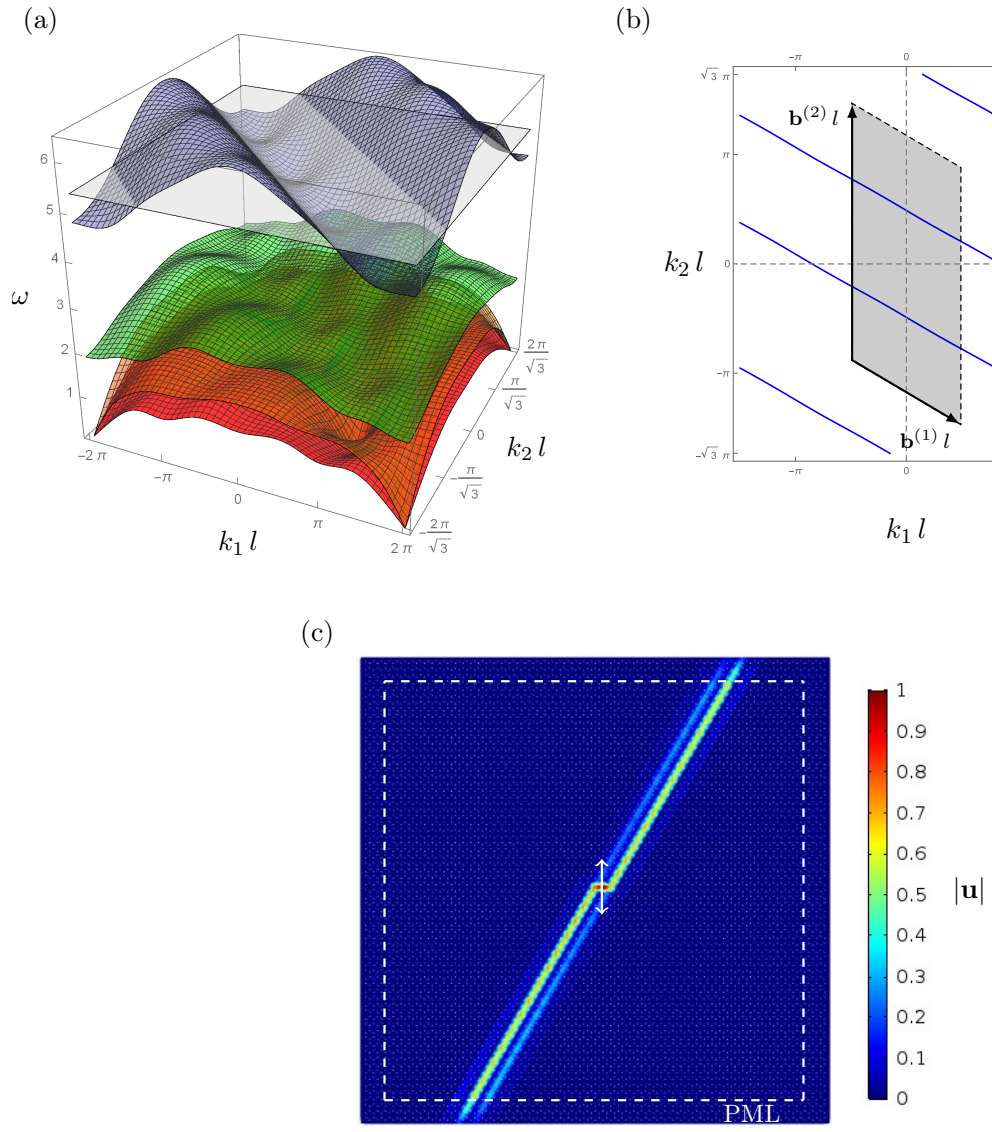

Figure 3.4: (a) Dispersion surfaces for a chiral triangular lattice. The masses are attached to a non-uniform distribution of gyroscopic spinners, determined by $\beta_1 = 0.5$ and $\beta_2 = 0.9$ (see Figure 3.3). (b) Slowness contours at $\omega = 5.36$ (indicated with the light grey plane in (a)). These contours are associated with the propagation of localised waves in the direction $(1/2, \sqrt{3}/2)$. The grey shaded region is the irreducible Brillouin zone. (c) Time harmonic analysis in a finite gyro-elastic lattice attached to a doubly periodic array of gyroscopes characterised by $\beta_1 = 0.5$ and $\beta_2 = 0.9$ and subjected to a harmonic force of $\omega = 5.36$ and unit amplitude. The position of the vertically acting force is indicated by the arrow.

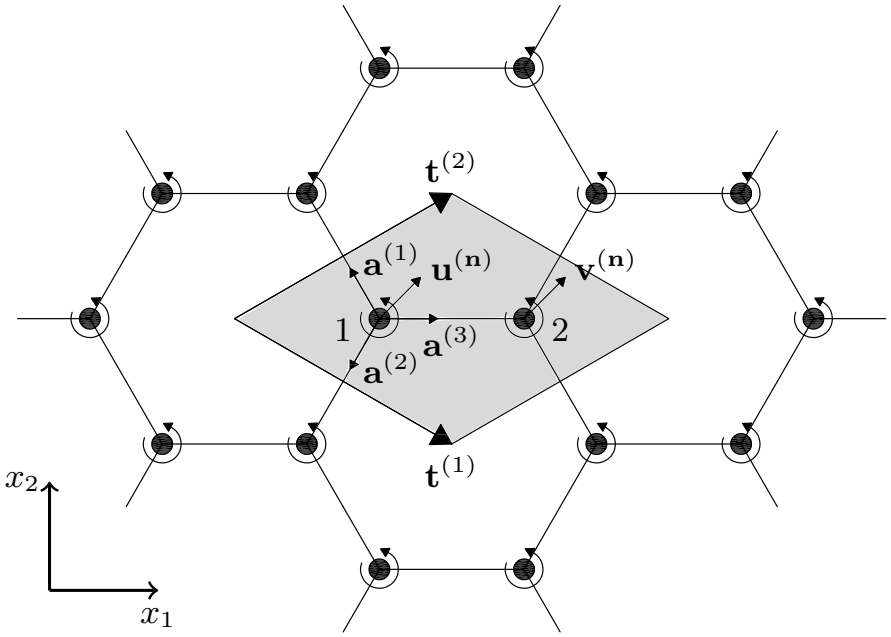

Figure 3.5: Hexagonal lattice with a uniform distribution of gyroscopic spinners, where $\mathbf{u}^{(\mathbf{n})}$ and $\mathbf{v}^{(\mathbf{n})}$ denote the displacements of the two lattice particles of the elementary cell, highlighted in grey.

properties.

3.2 Hexagonal chiral lattice

In this Section, we consider the dynamic properties of a structured hexagonal medium attached to gyroscopic spinners, shown in Figure 3.5 and we consider the influence of the choice of the gyroscopic spinners, represented through the spinner constant, on these properties.

3.2.1 Governing equations

In Figure 3.5, we indicate the elementary cell of the homogeneous hexagonal lattice with the grey rhombus, defined by the vectors

$$\mathbf{t}^{(1)} = (3l/2, -\sqrt{3}l/2)^{\mathrm{T}} \quad \text{and} \quad \mathbf{t}^{(2)} = (3l/2, \sqrt{3}l/2)^{\mathrm{T}}. \tag{3.19}$$

The position of each lattice particle is given by $\mathbf{x}^{(\mathbf{n})} = \mathbf{x}^{(\mathbf{0})} + n_1\mathbf{t}^{(1)} + n_2\mathbf{t}^{(2)}$, where $\mathbf{n} = (n_1, n_2)^{\mathrm{T}}$ is the multi-index and $\mathbf{x}^{(\mathbf{0})}$ is the position of a reference particle in the

lattice.

The elementary cell of the periodic structure consists of two particles, whose displacements are denoted by $\mathbf{u}^{(\mathbf{n})}$ and $\mathbf{v}^{(\mathbf{n})}$, see Figure 3.5. The equations of motion of the two lattice particles in the time-harmonic regime are given by:

$$-m\omega^2\mathbf{u}^{(\mathbf{n})} = c\sum_{j=1}^{3}\left[\mathbf{a}^{(j)}\cdot\left(\mathbf{v}^{(\mathbf{n}-\mathbf{e}_j)}-\mathbf{u}^{(\mathbf{n})}\right)\right]\mathbf{a}^{(j)} + \mathrm{i}\beta\omega^2\mathbf{R}\mathbf{u}^{(\mathbf{n})}\,, \tag{3.20a}$$

$$-m\omega^2\mathbf{v}^{(\mathbf{n})} = c\sum_{j=1}^{3}\left[\mathbf{a}^{(j)}\cdot\left(\mathbf{u}^{(\mathbf{n}+\mathbf{e}_j)}-\mathbf{v}^{(\mathbf{n})}\right)\right]\mathbf{a}^{(j)} + \mathrm{i}\beta\omega^2\mathbf{R}\mathbf{v}^{(\mathbf{n})}\,, \tag{3.20b}$$

where ω is the radian frequency, and the vectors $\mathbf{e}^{(1)} = (1,0)^{\mathrm{T}}$, $\mathbf{e}^{(2)} = (0,1)^{\mathrm{T}}$ and $\mathbf{e}^{(3)} = (0,0)^{\mathrm{T}}$ are used to specify the positions of the neighbouring particles. The unit vectors $\mathbf{a}^{(j)}$ in (3.20) define the directions of the lattice links (see Figure 3.5):

$$\mathbf{a}^{(1)} = \Big(-\frac{1}{2},\frac{\sqrt{3}}{2}\Big)^{\mathrm{T}}\,,\quad \mathbf{a}^{(2)} = \Big(-\frac{1}{2},-\frac{\sqrt{3}}{2}\Big)^{\mathrm{T}}\,,\quad \mathbf{a}^{(3)} = (1,0)^{\mathrm{T}}\,. \tag{3.21}$$

As discussed above, the contributions of the gyroscopic spinners lead to the last terms appearing in the right-hand sides of (3.20a) and (3.20b), where the matrix $\mathbf{R}$ is given in (3.13). The parameter β in (3.20) represents the spinner constant, which was obtained in [Brun, Jones and Movchan (2012)] (see Section 3.1.1) in modelling the interaction of the gyroscopic spinner with a truss system in the time-harmonic regime.

Floquet-Bloch analysis

The quasi-periodicity of the system is described by the Floquet-Bloch conditions (see Section 2.2.3), expressed in the form:

$$\mathbf{W}\left(\mathbf{r}+n_1\mathbf{t}^{(1)}+n_2\mathbf{t}^{(2)}\right) = \mathbf{W}\left(\mathbf{r}\right)\mathrm{e}^{\mathrm{i}\mathbf{k}\cdot\mathbf{T}\mathbf{n}}\,, \tag{3.22}$$

where $\mathbf{W} = (u_{x_1}, u_{x_2}, v_{x_1}, v_{x_2})^{\mathrm{T}}$ is the displacement vector, $\mathbf{r} = (x_1, x_2)^{\mathrm{T}}$ is the position vector, $\mathbf{k} = (k_1, k_2)^{\mathrm{T}}$ is the wavevector or Bloch vector, and the matrix for

the periodicity of the system is expressed as:

$$\mathbf{T} = [\mathbf{t}^{(1)}, \mathbf{t}^{(2)}] = l \begin{pmatrix} \frac{3}{2} & \frac{3}{2} \\ -\frac{\sqrt{3}}{2} & \frac{\sqrt{3}}{2} \end{pmatrix} . \tag{3.23}$$

By introducing (3.22) into (3.20), we obtain the following system of equations in matrix form:

$$\left[\mathbf{C} - \omega^2 (\mathbf{M} - \mathbf{A})\right] \mathbf{W} = \mathbf{0} , \tag{3.24}$$

where $\mathbf{M}$ is the diagonal mass matrix:

$$\mathbf{M} = \begin{pmatrix} m & 0 & 0 & 0 \\ 0 & m & 0 & 0 \\ 0 & 0 & m & 0 \\ 0 & 0 & 0 & m \end{pmatrix} , \tag{3.25}$$

$\mathbf{A}$ is the spinner matrix:

$$\mathbf{A} = \mathrm{i}\beta \begin{pmatrix} 0 & 1 & 0 & 0 \\ -1 & 0 & 0 & 0 \\ 0 & 0 & 0 & 1 \\ 0 & 0 & -1 & 0 \end{pmatrix} \tag{3.26}$$

and $\mathbf{C}$ is the stiffness matrix:

$$\mathbf{C} = c \begin{pmatrix} \frac{3}{2} & 0 & -1 - \frac{\mathrm{e}^{-\mathrm{i}\eta} + \mathrm{e}^{-\mathrm{i}\gamma}}{4} & \frac{\sqrt{3}\left(\mathrm{e}^{-\mathrm{i}\eta} - \mathrm{e}^{-\mathrm{i}\gamma}\right)}{4} \\ 0 & \frac{3}{2} & \frac{\sqrt{3}\left(\mathrm{e}^{-\mathrm{i}\eta} - \mathrm{e}^{-\mathrm{i}\gamma}\right)}{4} & -\frac{3\left(\mathrm{e}^{-\mathrm{i}\eta} + \mathrm{e}^{-\mathrm{i}\gamma}\right)}{4} \\ -1 - \frac{\mathrm{e}^{\mathrm{i}\eta} + \mathrm{e}^{\mathrm{i}\gamma}}{4} & \frac{\sqrt{3}\left(\mathrm{e}^{\mathrm{i}\eta} - \mathrm{e}^{\mathrm{i}\gamma}\right)}{4} & \frac{3}{2} & 0 \\ \frac{\sqrt{3}\left(\mathrm{e}^{\mathrm{i}\eta} - \mathrm{e}^{\mathrm{i}\gamma}\right)}{4} & -\frac{3\left(\mathrm{e}^{\mathrm{i}\eta} + \mathrm{e}^{\mathrm{i}\gamma}\right)}{4} & 0 & \frac{3}{2} \end{pmatrix} . \tag{3.27}$$

Here $\eta = \left(3k_1 - \sqrt{3}k_2\right) l/2$ and $\gamma = \left(3k_1 + \sqrt{3}k_2\right) l/2$. The matrices $\mathbf{A}$ and $\mathbf{C}$ are Hermitian. Also, we note that the determinant of $\mathbf{C}$ is zero for any value of the Bloch vector. This implies that the system is statically under-constrained (see [Zhang and Qiu (2014)]). However, in the dynamic case the inertial forces can balance external

loads. Typically, static honeycomb structures are designed as frames with rigid connections at the junctions [Gibson and Ashby (1997)]. Here, we have considered pin joints in order to solve the problem semi-analytically.

3.2.2 Dispersion properties

For non-trivial solutions of the homogeneous system (3.24) to exist, the following equation must hold:

$$\det\Big[\mathbf{C} - \omega^2\,(\mathbf{M} - \mathbf{A})\Big] = 0\,, \tag{3.28}$$

which represents the dispersion relation of the chiral system considered. Equation (3.28) is an algebraic equation of fourth order in ω^2 and it embeds the action due the gyroscopic motion of the spinners through the matrix $\mathbf{A}$.

We normalise (3.28) by introducing the non-dimensional quantities:

$$\tilde{\beta} = \frac{\beta}{m}\,, \quad \tilde{\omega} = \omega\sqrt{\frac{m}{c}} \quad , \quad \tilde{\mathbf{k}} = \mathbf{k}\,l$$

and the non-dimensional matrices:

$$\tilde{\mathbf{C}} = \frac{\mathbf{C}}{c} \quad \text{and} \quad \tilde{\mathbf{A}} = \frac{\mathbf{A}}{m}\,.$$

This leads to a normalized form of the dispersion relation:

$$\det\Big[\tilde{\mathbf{C}} - \tilde{\omega}^2\,\Big(\mathbf{I} - \tilde{\mathbf{A}}\Big)\Big] = 0\,. \tag{3.29}$$

In the following, the symbol "tilde" will be omitted for ease of notation. The above equations leads to a quartic equation in ω^2:

$$\begin{aligned}
&\omega^2\Big[2(\beta^2-1)^2\omega^6 + 12(\beta^2-1)\omega^4 \\
&+\Big((1+3\beta^2)\Big\{-2\cos\left(\frac{3k_1}{2}\right)\cos\left(\frac{\sqrt{3}k_2}{2}\right) - \cos(\sqrt{3}k_2)\Big\} + 3(7-3\beta^2)\Big)\omega^2 \\
&+3\Big\{2\cos\left(\frac{3k_1}{2}\right)\cos\left(\frac{\sqrt{3}k_2}{2}\right) + \cos(\sqrt{3}k_2)\Big\} - 9\Big] = 0\,.
\end{aligned}$$

In solving for ω^2, we note one of the solutions is always $\omega = 0$ for any value of the wavevector $\mathbf{k}$. This solution represents a rigid-body motion of the system, which is statically under constrained (see [Zhang and Qiu (2014)]) or kinematically undetermined, namely the system possesses internal degrees of freedom. In Section 3.4, it is shown that rigid-body motions are prevented if internal links are introduced, converting the hexagonal lattice into a heterogeneous triangular lattice.

We consider two groups of solutions depending on the spinner constant:

- $\beta < 1$: here (3.29) also admits three real and positive solutions in ω which yield three dispersion surfaces. The fourth solution is $\omega = 0$
- $\beta > 1$: two solutions for ω^2 are negative and hence only one dispersion surface is present.

The scenario $\beta = 1$ is a degenerate case and similar to [Brun, Jones and Movchan (2012)], the number of dispersion surfaces reduce to one and we do not consider this case here.

On the left of Figure 3.6 we show the dispersion surfaces, taken as the solutions of (3.29), for the chiral hexagonal lattice for different values of the spinner constant β. Accompanying each diagram on the left are the dispersion diagrams presented on the right, calculated along the path ΓMKΓ in the reciprocal lattice, shown in the inset of Figure 3.6(b). The points Γ, M and K are:

$$\Gamma = (0,0)\,, \quad \mathrm{M} = \left(\frac{2\pi}{3}, 0\right), \quad \mathrm{K} = \left(\frac{2\pi}{3}, \frac{2\pi}{3\sqrt{3}}\right),$$

(see [Cserti and Tichy (2004)]).

The vectors $\mathbf{b}^{(1)}$ and $\mathbf{b}^{(2)}$ describe the periodicity of the reciprocal lattice (see Section 2.2.3) and are given by

$$\mathbf{b}^{(1)} = \begin{pmatrix} \frac{2\pi}{3} \\ \\ \frac{-2\pi}{\sqrt{3}} \end{pmatrix} \quad \text{and} \quad \mathbf{b}^{(2)} = \begin{pmatrix} \frac{2\pi}{3} \\ \\ \frac{2\pi}{\sqrt{3}} \end{pmatrix}. \tag{3.30}$$

When there are no spinners attached to the lattice ($\beta = 0$), one solution is $\omega = \sqrt{3}$ for

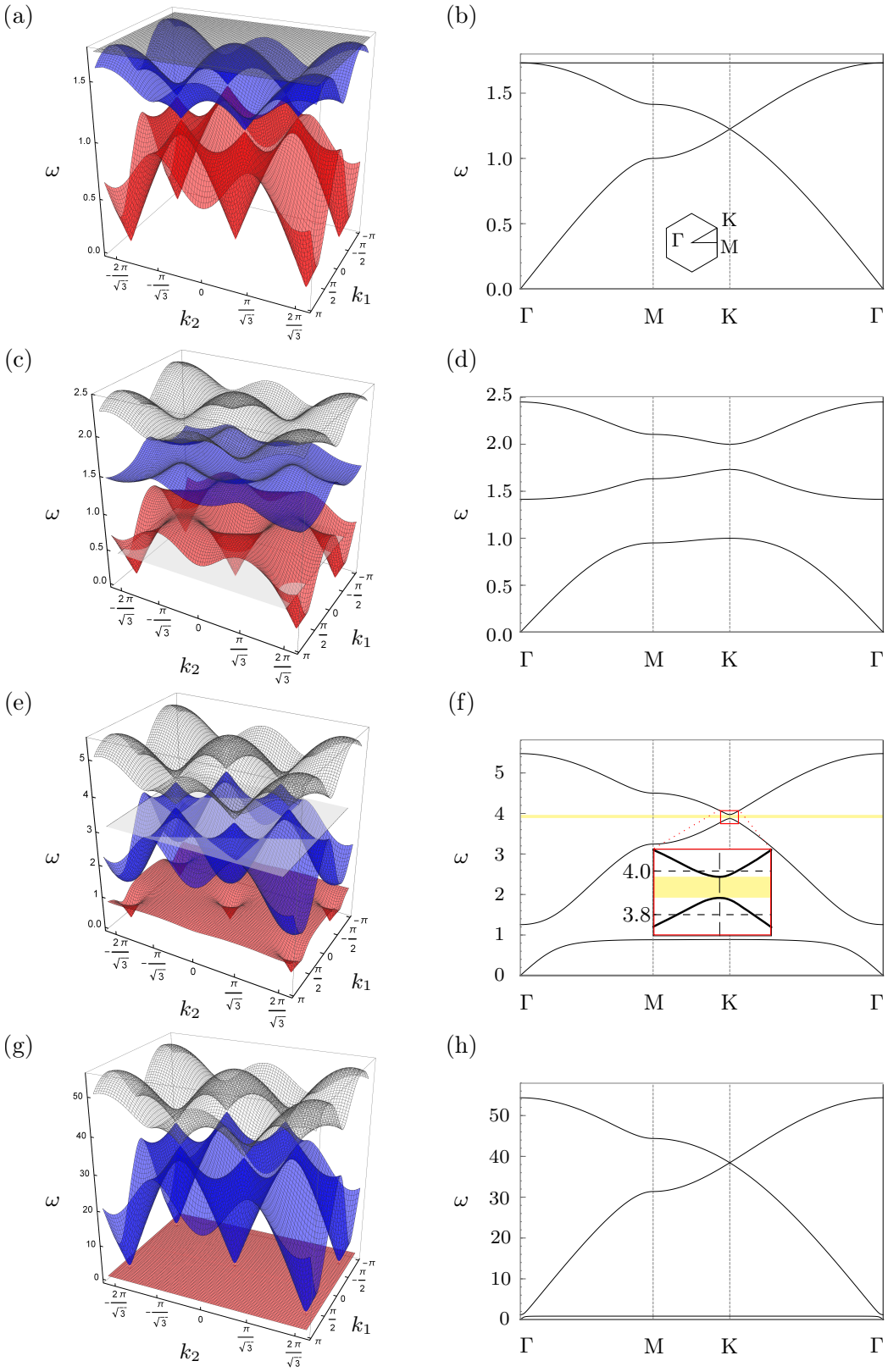

Figure 3.6: Dispersion surfaces (a, c, e, g) and corresponding cross-sections (b, d, f, h), determined for $\beta = 0$ (a, b), $\beta = 0.5$ (c, d), $\beta = 0.9$ (e, f), $\beta = 0.999$ (g, h). For $\beta < 1$, the discrete hexagonal system exhibits three dispersion surfaces; the fourth solution of the dispersion relation, given by $\omega = 0$, is not shown in the Figures for the sake of clarity. Note that the scales of the vertical axes are different, since the dispersion surfaces move to higher frequencies as $\beta \to 1$.

any value of the wavevector $\mathbf{k}$. The other two non-trivial solutions describe dispersion surfaces that intersect at a point of degeneracy known as a Dirac point, whose frequency is $\omega = \sqrt{3/2}$. We note that the dispersion diagrams in Figure 3.6(a),(b) for $\beta = 0$ are in agreement with [Cserti and Tichy (2004)]. The appearance of the Dirac points has been suggested to be linked to hidden symmetries [Hou and Chen (2015)] and mirror symmetries [He an Chan (2015)] of the medium. The physical interpretation of Dirac points is what is referred to as local neutrality, namely, at these points waves can propagate through a system without being disturbed by structure. Later we show how to use such points to generate topologically protected modes such as interfacial waves.

When $0 < \beta < 1$, the lowest non-zero dispersion surface decreases as β is increased, while the highest two dispersion surfaces increase. As a consequence, two finite stop-bands appear within the band diagram of the gyro-lattice. Furthermore, the highest dispersion surface is no longer $\mathbf{k}$-independent as in the case of $\beta = 0$. The width of the upper finite stop-band tends to zero as $\beta \to 1^{-}$, and a new Dirac point appears at a frequency larger than that for the case of $\beta = 0$. Figure 3.6(g), (h) shows the dispersion diagrams for $\beta = 0.999$; in this case, it is apparent that a new Dirac point is forming, and that the lowest non-zero dispersion surface is almost flat, except in a small proximity of point Γ.

In Figure 3.7(a), we show the dispersion surfaces for the case in which $\beta > 1$ ($\beta = 1.4$) and in Figure 3.7(b) the corresponding dispersion diagram along the path ΓMKΓ. We have only one dispersion surface in this case, as mentioned above, apart from $\omega = 0$. A similar phenomenon was observed for the triangular lattice with gyroscopic spinners [Brun, Jones and Movchan (2012), Carta et al. (2014)], where there is only one dispersion surface in the supercritical regime $\beta > 1$. In contrast to the triangular lattice, the dispersion surface of the hexagonal lattice, for $\beta > 1$, does not pass through the origin. Figure 3.8 shows that the dispersion surface decreases and becomes flatter as the spinner constant increases; in the limit when $\beta \to \infty$, it tends to zero for any wavevector $\mathbf{k}$.

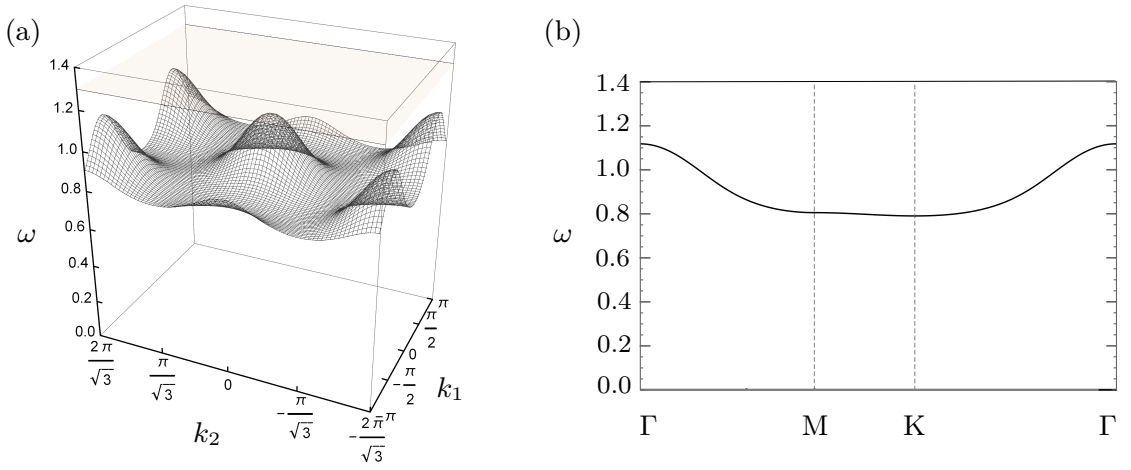

Figure 3.7: (a) Dispersion surfaces for $\beta = 1.4$ and (b) the dispersion curves determined by traversing the boundaries of the Brillouin zone defined by ΓMKΓ. For $\beta > 1$, the discrete hexagonal system possesses only one dispersion surface.

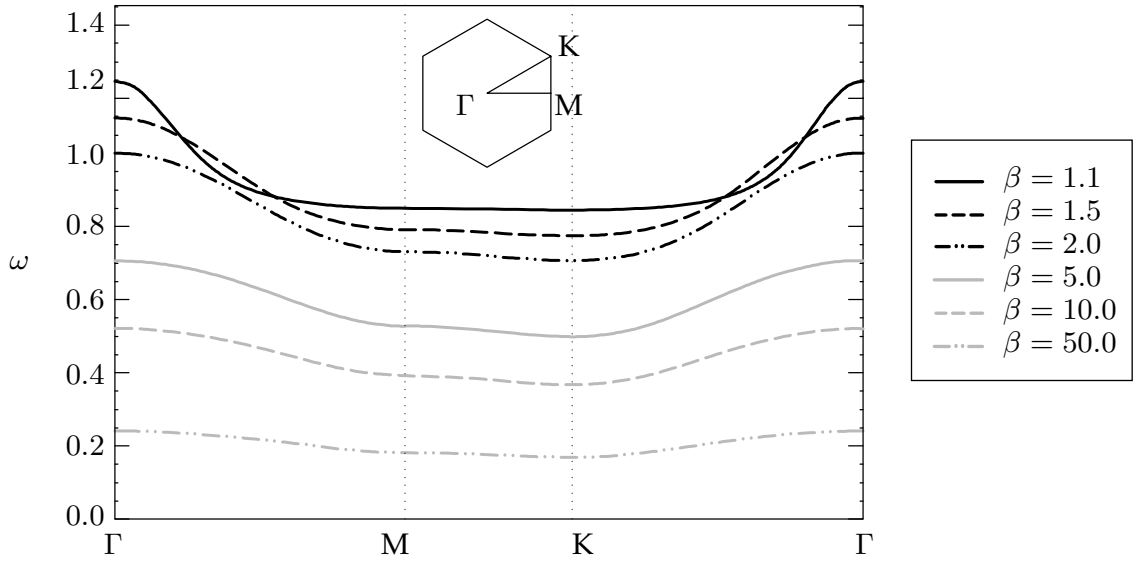

Figure 3.8: Dispersion diagrams for the hexagonal chiral lattice, computed for values of $\beta > 1$. The discrete hexagonal system is characterised by only one dispersion surface when $\beta > 1$; another real solution of the dispersion relation is $\omega = 0$ for any wavevector $\mathbf{k}$.

3.3 Numerical modelling of a gyro-elastic hexagonal lattice and interfacial waveforms

In this Section, we show the results of numerical simulations, when a time-harmonic displacement is applied to a particle in the hexagonal chiral lattice. The imposed displacement is $\mathbf{U}_0 \mathrm{e}^{-\mathrm{i}\omega t}$, where $|\mathbf{U}_0|$ is the amplitude and t is the time. The gyroscopic spinners attached to the particles are used to break the time-reversal symmetry and hence waves are expected to propagate along a preferential direction.

The time-harmonic response of the chiral lattice is analysed using *Comsol Multiphysics* (version 5.2a). The lattice is modelled as a system of massless rods connected by hinges, and point masses are incorporated at the junctions. In the finite element computations, the gyroscopic effect is taken into account by introducing a force proportional to the particle displacement at each lattice junction (see the last term on the right of the equations in (3.20)). In order to prevent rigid-body motions of the whole system, the displacements of the masses at the corners of the model are set equal to zero. In addition, PML (*Perfectly Matched Layers*) are attached to the sides of the model to avoid reflections of waves generated by the time-harmonic displacement. In this way, the system is modelled as a spatially infinite medium. PML are created by using viscous dampers, whose parameters are tuned to minimise the reflection coefficient [Carta et al. (2013), Carta et al. (2014)].

The cell containing the point with the imposed displacement is defined by the multi-index $\mathbf{n}^* = (n_1^*, n_2^*)^{\mathrm{T}}$. In this cell, we apply the condition

$$\delta_{j1}\mathbf{u}^{(\mathbf{n}^*)} + \delta_{j2}\mathbf{v}^{(\mathbf{n}^*)} = \mathbf{U}_0 \ , \tag{3.31}$$

where δ_{ij} is the Kronecker delta and $j = 1$ or 2 will correspond to a time-harmonic displacement applied to the node labelled 1 or 2, respectively, in the cell of Figure 3.5. The equations of motion for the nodes without imposed displacement are given by (3.20). Below, we give several computations based on a finite rectangular slab of a hexagonal lattice having the dimensions 150×110.

Validation of the numerical model against analytical results

Prior to investigating the capability of the gyro-elastic lattice in supporting interfacial waves with preferential directions, we validate the model against the analytical results obtained in Section 3.2. Here, the interfacial waves are considered as the waves that propagate along the interface created between two adjacent domains attached to different gyro-elastic lattices. In particular, we verify the vibrations supported by the medium agree with the slowness contours arising from the dispersion surfaces obtained from equation (3.29) for a range of frequencies and properties of the spinners.

The left panels of Figure 3.9 show the slowness contours for various frequencies and spinner constants. The right panels of this Figure show the response of the hexagonal lattice when subjected to the time-harmonic force, which is computed in *Comsol*.

The circular contours of Figure 3.9(a) show the lattice can have an isotropic response at a low frequency. At the frequency shown, when the chiral lattice is forced it produces an isotropic wave pattern, in the form of a vortex wave, owing to the action of the spinners as shown in Figure 3.9(b). In particular, the wave produced by the source is of the shear-type as the wavelength is small.

Figure 3.9(c) demonstrates that the chiral hexagonal lattice can possess dynamic anisotropy at high frequencies, previously investigated in the time-harmonic for gyro-elastic triangular lattices in [Carta et al. (2014)]. Figure 3.9(c) shows that the structure will support waves in three preferential directions aligned with the angles $\pi(2j+1)/6$, $j = 0, 1, 2$ measured anticlockwise in the lattice. In Figure 3.9(d), we see precisely the formation of such rays, along which the vibrations produced by the oscillating force are localised.

Finally in Figure 3.9(e), we give an example where one can expect highly localised deformation produced by the time-harmonic load. In fact, in this Figure, there are no slowness contours as the frequency has been chosen outside the structure's pass-band. The resulting displacement field shows a high intensity of deformation in the immediate vicinity of the load in Figure 3.9(f), and the intensity of these

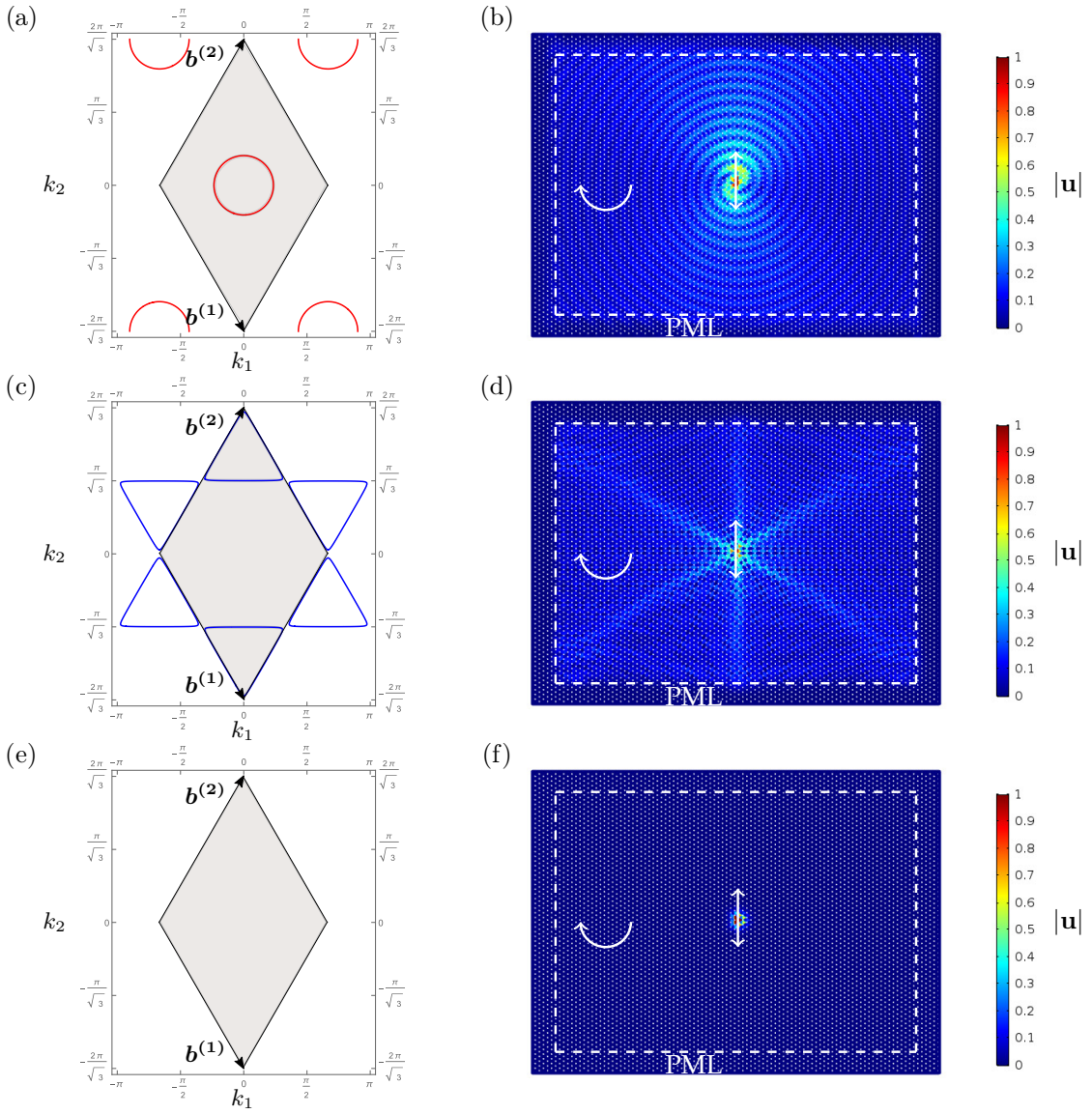

Figure 3.9: In the left panels we show the slowness contours for three different types of hexagonal gyro-elastic media. To the right of each slowness contour plot we provide the response of the medium computed in *Comsol*. This computation involves a finite hexagonal lattice subjected to a vertically acting time-harmonic point load (indicated by the white arrow). A region of PML is attached to aid simulate an infinite medium. The parameters for the computations are (a, b) $\omega = 0.5$, $\beta = 0.5$, (c, d) $\omega = 3.25$, $\beta = 0.9$ and (e, f) $\omega = 1.3$, $\beta = 1.4$. In all computations the spinner constant is chosen so that the gyroscopes attached to the lattice act in a clockwise direction.

displacements decay exponentially into the bulk of the lattice.

The above examples allow us to assert that the numerical model developed in *Comsol* is accurate. In particular, the PML supplied at the exterior of the computational domain is effective and reduces the reflections produced by the load in order that we can retrieve the anticipated response indicated by the slowness contours.

3.3.1 Excitations leading to waveforms with preferential directionality

In what follows, we show that localized interfacial waveforms can be supported in an inhomogeneous hexagonal lattice attached to gyroscopic spinners. In particular, the inhomogeneity of the lattice is brought by inserting gyroscopic spinners having different spinner constants, which are chosen equal to ± 0.9 in all examples considered in this Section. In addition, we demonstrate that the direction of these waveforms can be controlled by either altering the spin directions of the gyroscopic spinners or changing the frequency of the applied displacement.

In the first set of simulations, we divide the lattice domain into two different regions. The regions are distinguished by having gyroscopic spinners characterised by spinner constants of the same magnitude but of opposite sign. At specific frequencies, which can be predicted from the dispersion analysis described in Sections 3.2.2, interfacial waves propagate along the internal boundaries between the two regions.

Figure 3.10 shows a lattice divided by horizontal interface, where the spinners rotate as shown in the two magnifications presented. In the upper and lower regions, the gyroscopic spinners have the same spin rate ($|\beta| = 0.9$), but they spin in opposite directions, as indicated by the white circular arrows. At the central node of the domain, we impose a time-harmonic displacement, whose direction is represented by a white arrow. Figure 3.10 illustrates the displacement field calculated for the applied displacement of the radian frequency $\omega = 3.93$, which is inside of the stop-band highlighted in yellow in Figure 3.6(f), related to the problem concerning free

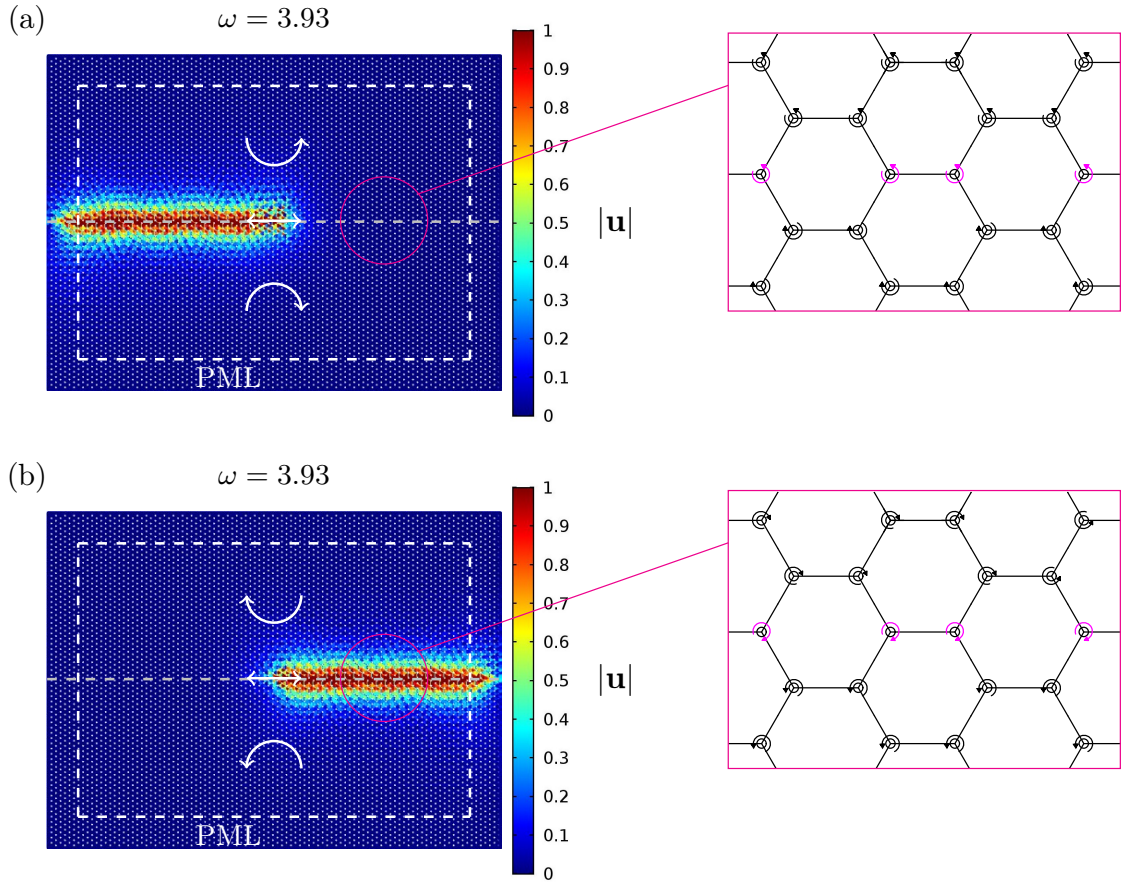

Figure 3.10: Total displacement in the inhomogeneous chiral lattices, with a horizontal interfaces. The interface is loaded by a time-harmonic displacement with frequency $\omega = 3.93$. The spin directions of the spinners in each sub-domain are indicated by the white circular arrows. The time-harmonic displacement (represented by a straight white arrow) is applied to the central node of the lattice. In these computations, the absolute value of the spinner constant is $|\beta| = 0.9$, their spin direction is (a) anticlockwise in the upper part and clockwise in the lower part of the lattice, and in (b) clockwise in the upper part and anticlockwise in the lower part of the lattice (see also Figure 3.6(f)). The region of PML (*Perfectly Matched Layers*) are indicated by the dashed white lines close to the exterior boundary. The interfaces between the sub-domains are shown as dashed grey lines. To the right, we provide a magnification of the interface, where the spinners on the interface are shown in pink.

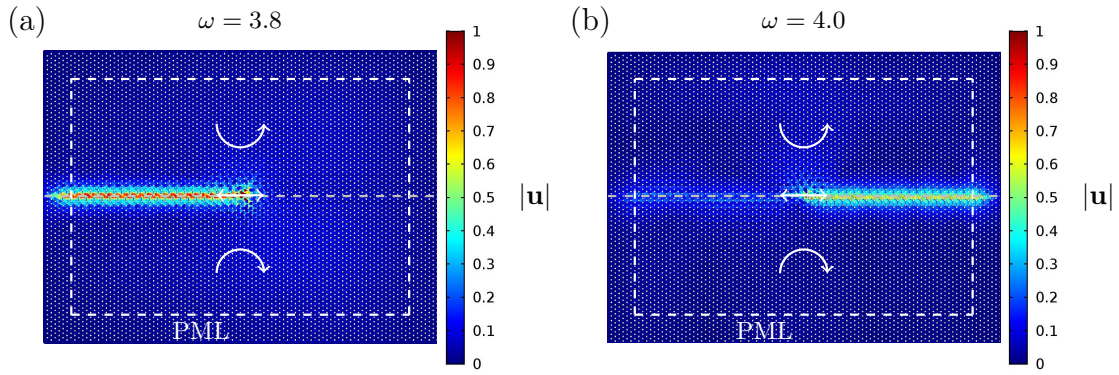

Figure 3.11: Displacement amplitude fields in the chiral lattice at different frequencies of the applied time-harmonic displacement and for different spin directions of the spinners (indicated by the white circular arrows) above and below the interface. In these computations, the absolute value of the spinner constant is $|\beta| = 0.9$, and the frequency of the applied displacement is (a) $\omega = 3.8$ and (b) $\omega = 4.0$ (see also Figure 3.6f). The arrangement of the gyroscopic spinners is reported in the caption for Figure 3.10(a).

vibrations in the homogeneous infinite system. From Figure 3.10(a), it is apparent that waves propagate along the interface between the two regions in one direction. In Figure 3.10(b) we show the direction of the interfacial wave can be reversed by swapping the spin directions of the spinners in the two regions and applying the same load along their interface.

Next, we demonstrate that the direction of the interfacial waveform can be reversed in the gyro-elastic material with a horizontal interface by only slightly adjusting the radial frequency of the load. In Figure 3.11(a), we illustrate the wave field obtained applying a displacement with radian frequency $\omega = 3.8$, which is below the lower limit of the stop-band highlighted in Figure 3.6(f). The wave propagates along the horizontal interface to the left of the interface. Figure 3.11(b) shows the interfacial waves generated by the applied displacement with the radian frequency $\omega = 4.0$. This frequency is above the upper limit of the stop-band highlighted in Figure 3.6(f). Here, it is clear that the interfacial wave propagates in the opposite direction to that observed in Figure 3.11(a). In particular, the interfacial waves identified in Figure 3.11, obtained for frequencies outside the highlighted stop-band in Figure 3.6(f), are more localised about the interface than those found in Figure 3.10, where the frequency is situated inside the stop-band.

Uni-directional interfacial waves can also be obtained for gyro-elastic lattices

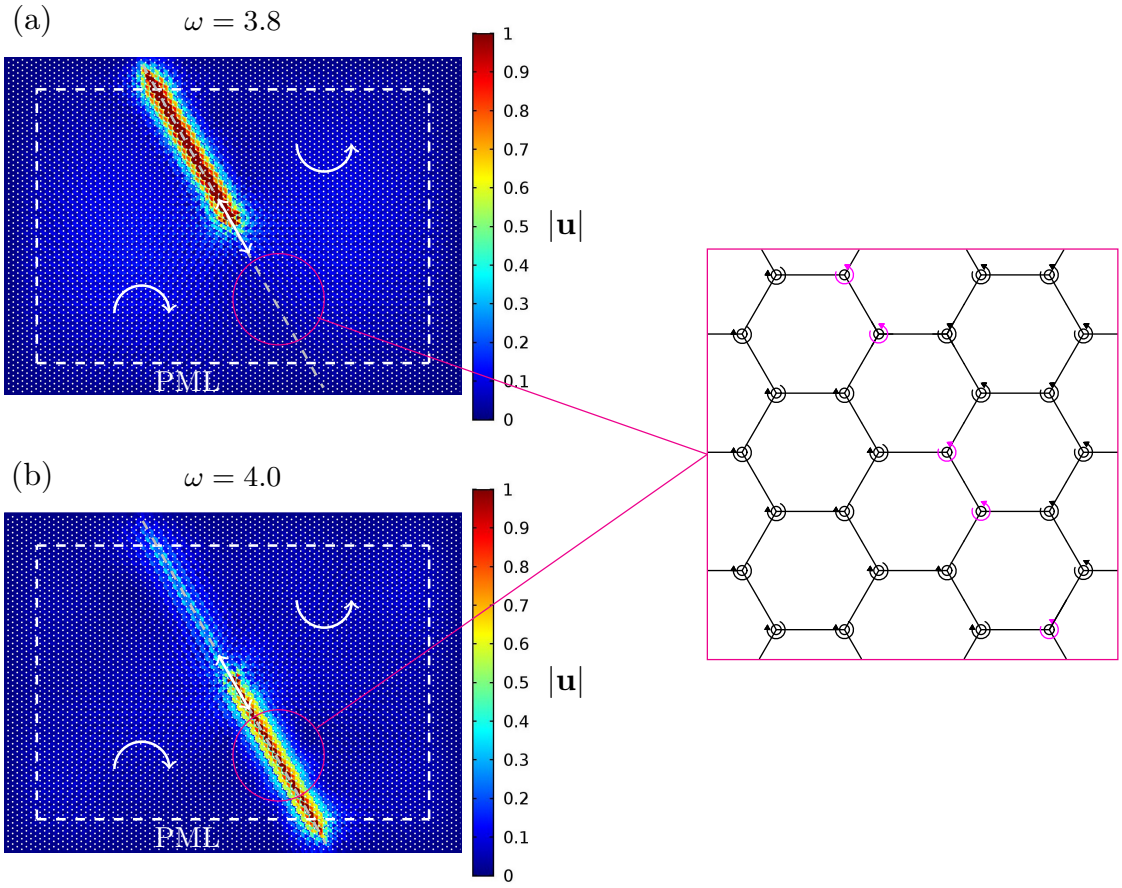

Figure 3.12: Computations showing the response of the hexagonal lattices. The particles are attached to an inhomogeneous distribution of spinners. The computational setup is described in the caption of Figure 3.11. The subdomains are divided by a sloped interface as indicated by the dashed grey line. The magnification highlights the arrangement of the spinners at the interface.

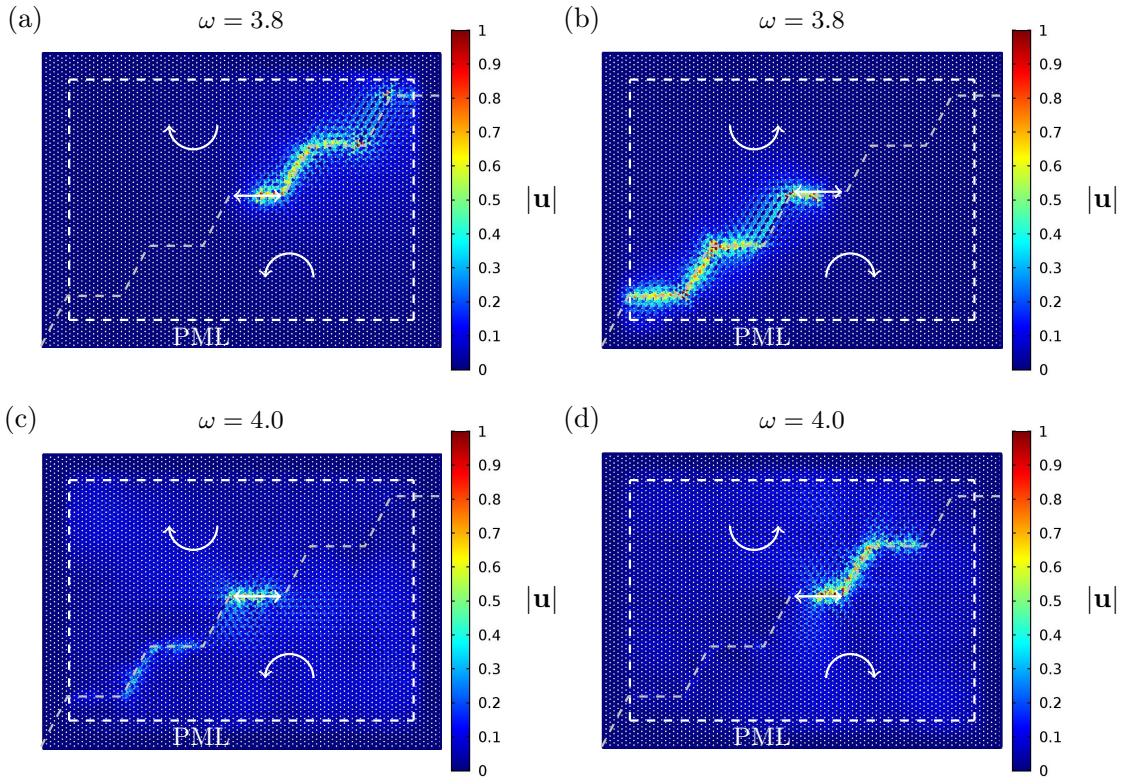

Figure 3.13: Unidirectional waveforms for an inhomogeneous lattice with an internal boundary containing several vertices. The domain is divided in two subdomains in which the constant spinner $|\beta| = 0.9$. The spin direction of the spinners in each subdomain differs, as indicated by the circular white arrows. The radian frequency of the interfacial point load (whose orientation is indicated by the white arrow) in (a)-(b) is $\omega = 3.8$ and in (c)-(d) $\omega = 4$ (see also Figure 3.6).

with different internal boundaries. In Figures 3.12, we show the case when interface runs obliquely through the lattice at an angle of 120° measured anticlockwise. From the examples shown in Figures 3.12, we see that an interfacial wave can propagate up along the interface in Figure 3.12(a), if the frequency of vibration is just below the stop-band highlighted in Figure 3.6(f). On the other hand an interfacial wave propagates down the slope when the load frequency is just above this stop-band (see Figure 3.12(b)).

In all the examples of Figures 3.10–3.12, we notice that the waveform appears to be exponentially localised to the interface and in each example the strength of the localisation appears to be uniform along the interface.

In Figure 3.13, we show how interfacial waves propagate along an internal boundary possessing vertices. The interface is taken as the staircase formation shown in Figure 3.13, that divides the domain into two subdomains. Figures 3.13(a) and

(b) show how the interfacial wave propagates along this interface for a frequency lower just below the stop-band highlighted in Figure 3.6(f). In Figure 3.13(a), the interfacial wave is able to propagate upward along the staircase interface and reach the right-hand boundary. There is some visible concentration in intensity of the wave at the vertices, where one can expect the wave to be scattered or reflected and this leads to the diminished intensity of the wave as it approaches the boundary. With interchanging the properties of the spinners either side of the boundary, as before, we are able to reverse the direction of this interfacial wave.

Figures 3.13(c) and (d) show the effect of adjusting the radian frequency of the load, so that it is situated just above the pass-band highlighted in Figure 3.6(f). Comparing (a) with (c) and (b) with (d) it is clear that the change in frequency provides a change in direction of the interfacial wave, but in this case the intensity of the displacements about the interface are much weaker.

Interfacial waveforms for closed interior boundaries

Next we give examples where we are able to generate interfacial waves along closed paths contained within the gyro-elastic hexagonal lattice.

The first example is presented in Figure 3.14. In this case, the interior boundary has been shown to have a hexagonal shape. Figures 3.14(a) and (b) show the displacement fields computed for two different values of the frequency of the imposed displacement, specified at the top of each Figure (see also Figure 3.6(f)); in both Figures 3.14(a) and (b), the spinners inside the hexagonal domain rotate clockwise, while the spinners in the ambient medium rotate anticlockwise. The comparison between Figures 3.14(a) and (b) emphasises the dependence of the preferential directionality of the medium on the frequency of the excitation, which can be predicted from the dispersion analysis discussed in Section 3.2.2. In Figure 3.14(a) and (b) the interfacial wave follows the internal boundary in an anticlockwise and clockwise direction, respectively. In addition, the intensity of the interfacial wave decreases as it tries to make a complete loop of the internal boundary, which can be attributed to the scattering of the wave when it attempts to pass through the

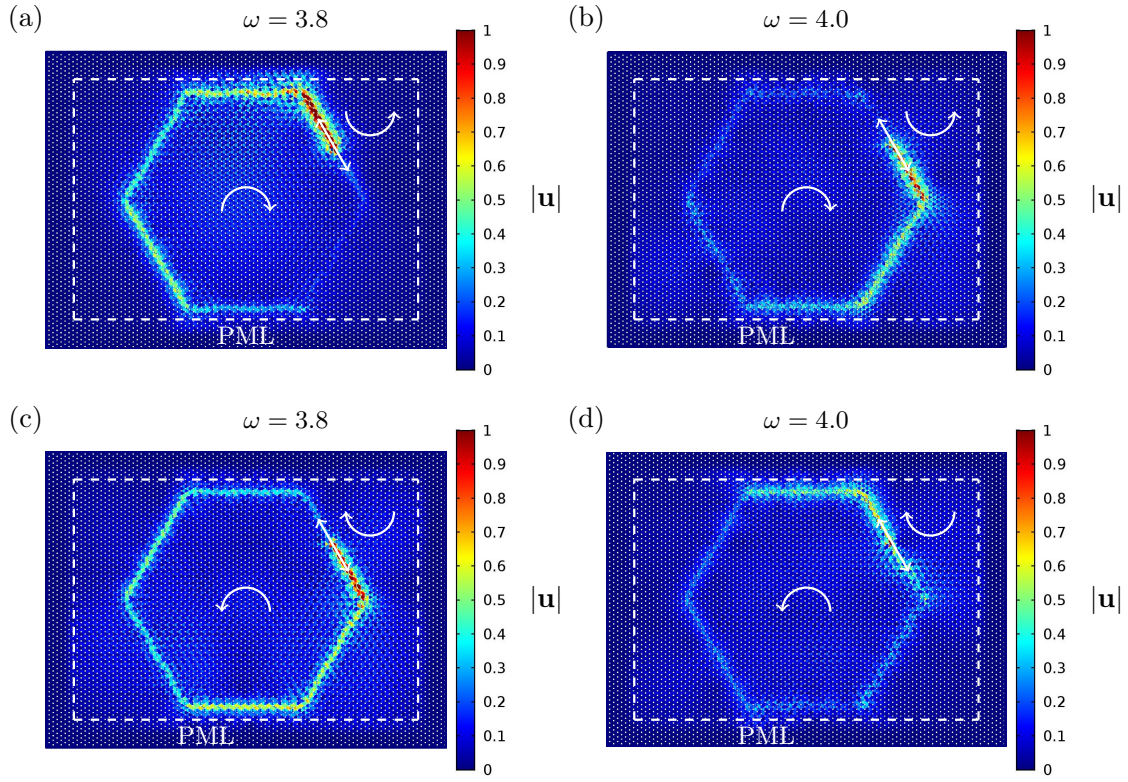

Figure 3.14: Interfacial waveforms with preferential directionality in a hexagonal lattice connected to a system of gyroscopic spinners. The lattice domain is divided into two regions: in the hexagonal region the spinners rotate (a,b) clockwise and (c,d) anticlockwise, while the ambient medium contains spinners which rotate in the opposite direction to those situated inside the hexagonal region. The absolute value of the spinner constant is $|\beta| = 0.9$ for all the gyroscopic spinners. At the interface, the spinners rotate in the same direction as in the exterior domain. A time-harmonic displacement, represented by the straight arrow, is applied to a node on the interface of these regions. The relative displacement amplitude fields are obtained for the applied displacement of frequency (a,c) $\omega = 3.8$ and (b,d) $\omega = 4.0$ (see also inset in Figure 3.6(f)). The Figures illustrate that the preferential direction of the interfacial waveform can be influenced by interchanging the direction of rotation of the spinners or by changing the frequency of the external excitation.

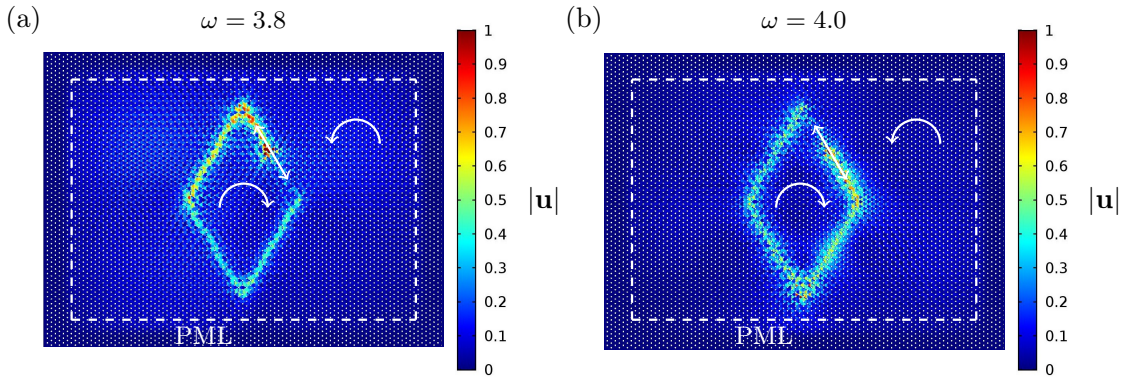

Figure 3.15: Another example showing the sensitivity of the preferential directionality of an interfacial waveform in a hexagonal lattice on spinners, containing a subdomain where the spinners rotate in the opposite direction to those in the ambient medium. The radian frequency of the applied displacement is (a) $\omega = 3.8$ and (b) $\omega = 4.0$ (see also Figure 3.6(f)). As in the previous simulations, the absolute value of the spinner constant is $|\beta| = 0.9$ throughout the domain.

vertices of the hexagonal boundary.

In Figures 3.14(c) and (d), the spinners inside the hexagonal lattice spin anticlockwise, while those in the ambient medium spin clockwise. Comparing Figures 3.14(c) and (a), and Figures 3.14(d) and (b), it is apparent that interchanging the directions of spin for the gyroscopes reverses the direction of the interfacial waveform, which is consistent with the phenomenon observed above.

The effect of uni-directional localisation shown in Figure 3.14 is not unique to the hexagonal subdomain within the inhomogeneous lattice. In Figure 3.15, the illustration of an interfacial waveform along the boundary of a different subset of an inhomogeneous hexagonal lattice is given, where the internal boundary is now a rhombus. In particular, Figures 3.15(a) and (b) are obtained for a radian frequency of the applied displacement equal to $\omega = 3.8$ and $\omega = 4.0$, respectively. These frequencies are indicated in the magnified inset of Figure 3.6(f). Once again, by changing the frequency of the external excitation, it is possible to alter the direction of the waveform.

We emphasize that, in all simulations presented in this Section, the results are found to be independent of the direction of the external excitation. We also observe that if the spin directions of the spinners on the interface are reversed, the wave pattern is not affected. Finally, it is interesting to note that interfacial waves propagating in the vertical direction were not observed in such a structure as there

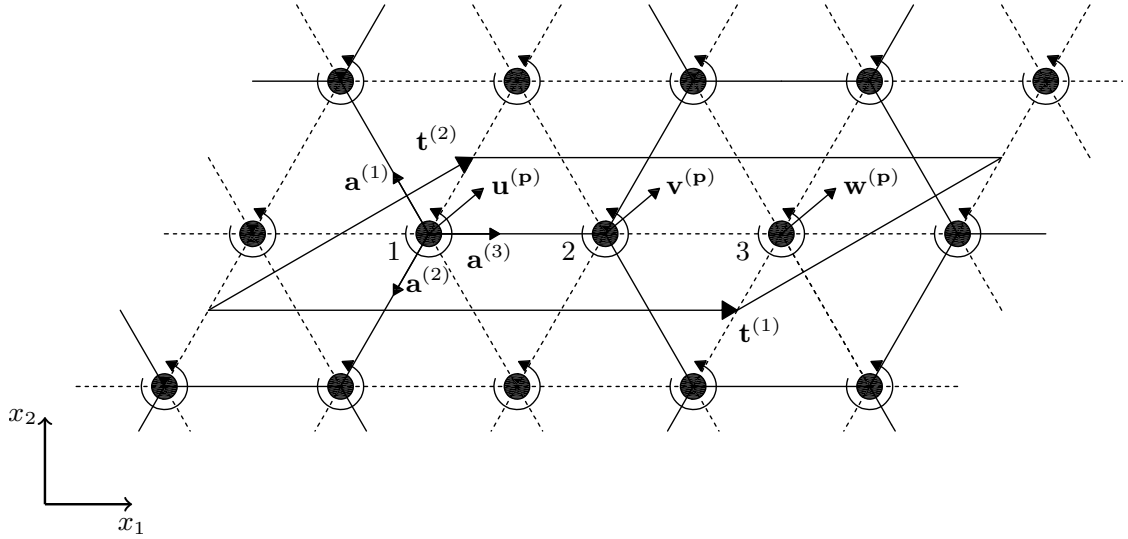

Figure 3.16: An inhomogeneous triangular lattice structure linked to a system of spinners. The elementary cell for this structure is shown, which contains 3 particles having displacements $\mathbf{u}^{(\mathbf{p})}$, $\mathbf{v}^{(\mathbf{p})}$ and $\mathbf{w}^{(\mathbf{p})}$. The lattice is composed of springs with stiffnesses c (solid lines) and c_ε (dashed lines), where $c_\varepsilon \ll c$. Springs possessing stiffness c_ϵ form the internal connections of the vertices of the hexagon in the lattice. Here the lattice basis vectors are taken as $\mathbf{t}^{(1)} = (3l, 0)^{\mathrm{T}}$ and $\mathbf{t}^{(2)} = (3l/2, \sqrt{3}l/2)^{\mathrm{T}}$.

are no links connecting two adjacent vertically aligned masses in the lattice.

3.4 A degenerating triangular chiral lattice

The hexagonal lattice described in Section 3.2 is statically under constrained and its dispersion diagram is characterised by a single acoustic branch for $\beta < 1$ (see Figure 3.6). In order to allow for propagation of both shear and pressure waves in the medium, we introduce internal links into the structure, which then becomes a triangular lattice. This lattice degenerates into the hexagonal lattice of Section 3.2 when the stiffness of these internal links tends to zero.

This triangular lattice is shown in Figure 3.16. It is composed of particles with mass m and two types of springs, each possessing length l and having stiffnesses c and c_ε. The stiffness c_ε is assumed to be small in comparison with c. As before, each mass is connected to a spinner that has a spinner constant β.

The elementary cell for this configuration is shown in Figure 3.16, where it can be seen that this cell contains three particles, whose displacements are denoted as $\mathbf{u}^{(\mathbf{p})}$, $\mathbf{v}^{(\mathbf{p})}$ and $\mathbf{w}^{(\mathbf{p})}$. In addition, the basis vectors $\mathbf{t}^{(1)} = (3l, 0)^{\mathrm{T}}$ and $\mathbf{t}^{(2)} = (3l/2, \sqrt{3}l/2)^{\mathrm{T}}$

are used to define the periodicity of the system. The unit vectors $\mathbf{a}^{(j)}$ introduced in (3.21) will also be utilised to define the directions of the links in the lattice. A particle's position in this lattice can be determined through $\mathbf{x}^{(\mathbf{p})} = \mathbf{x}^{(\mathbf{0})} + p_1\mathbf{t}^{(1)} + p_2\mathbf{t}^{(2)}$, where $\mathbf{p} = (p_1, p_2)^{\mathrm{T}}$ is a multi-index.

3.4.1 Governing equations of the heterogeneous triangular lattice

Following the algorithm outlined in Section 3.1.2, in the time-harmonic regime, the governing equations of the three particles in the elementary cell are

$$-m\omega^2\mathbf{u}^{(\mathbf{p})} = \sum_{j=1}^{3}\left[\mathbf{a}^{(j)}\cdot\left(c(\mathbf{v}^{(\mathbf{p}-\mathbf{q}_j)}-\mathbf{u}^{(\mathbf{p})})+c_\varepsilon(\mathbf{w}^{(\mathbf{p}+\mathbf{q}_j-\mathbf{e}_1)}-\mathbf{u}^{(\mathbf{p})})\right)\right]\mathbf{a}^{(j)}+\mathrm{i}\beta\omega^2\mathbf{R}\mathbf{u}^{(\mathbf{p})}\,, \tag{3.32a}$$

$$-m\omega^2\mathbf{v}^{(\mathbf{p})} = \sum_{j=1}^{3}\left[\mathbf{a}^{(j)}\cdot\left(c(\mathbf{u}^{(\mathbf{p}+\mathbf{q}_j)}-\mathbf{v}^{(\mathbf{p})})+c_\varepsilon(\mathbf{w}^{(\mathbf{p}-\mathbf{q}_j)}-\mathbf{v}^{(\mathbf{p})})\right)\right]\mathbf{a}^{(j)}+\mathrm{i}\beta\omega^2\mathbf{R}\mathbf{v}^{(\mathbf{p})}\,, \tag{3.32b}$$

$$-m\omega^2\mathbf{w}^{(\mathbf{p})} = c_\varepsilon\sum_{j=1}^{3}\left[\mathbf{a}^{(j)}\cdot\left(\mathbf{v}^{(\mathbf{p}+\mathbf{q}_j)}+\mathbf{u}^{(\mathbf{p}-\mathbf{q}_j+\mathbf{e}_1)}-2\mathbf{w}^{(\mathbf{p})}\right)\right]\mathbf{a}^{(j)}+\mathrm{i}\beta\omega^2\mathbf{R}\mathbf{w}^{(\mathbf{p})}\,, \tag{3.32c}$$

where $\mathbf{q}_1 = \mathbf{e}_1 - \mathbf{e}_2$, $\mathbf{q}_2 = \mathbf{e}_2$, $\mathbf{q}_3 = 0\mathbf{e}_1 + 0\mathbf{e}_2$ and $\mathbf{R}$ is the rotation matrix in (3.13). We note that (3.32a) and (3.32b) reduce to (3.20a) and (3.20b) if $c_\varepsilon = 0$, while in this case (3.32c) implies $\mathbf{w}^{(\mathbf{p})}$ vanishes for $\omega > 0$.

We proceed to analyse the Floquet-Bloch modes of the above system by introducing the quasi-periodicity conditions given in (3.22) and in (3.23), where $\mathbf{W} = (u_{x_1}, u_{x_2}, v_{x_1}, v_{x_2}, w_{x_1}, w_{x_2})^{\mathrm{T}}$ is the new displacement vector, $\mathbf{T}= [\mathbf{t}^{(1)}, \mathbf{t}^{(2)}]$ is constructed from the new lattice basis vectors and $\mathbf{p}$ replaces $\mathbf{n}$. In a similar way to that described in Section 3.2, we then arrive at a system of equations for $\mathbf{W}$ in the

form

$$\left[\mathbf{C}_\varepsilon - \omega^2 \left(\mathbf{M} - \mathbf{A}\right)\right] \mathbf{W} = \mathbf{0} \,, \tag{3.33}$$

where $\mathbf{M} = m\mathbf{I}_6$ ($\mathbf{I}_j$ is the $j \times j$ identity matrix), the spinner matrix

$$\mathbf{A} = \mathrm{i}\beta \,\mathrm{diag}\left(\left(\begin{array}{cc} 0 & -1 \\ 1 & 0 \end{array}\right), \left(\begin{array}{cc} 0 & -1 \\ 1 & 0 \end{array}\right), \left(\begin{array}{cc} 0 & -1 \\ 1 & 0 \end{array}\right)\right) \,, \tag{3.34}$$

and $\mathbf{C}_\varepsilon$ is a 6×6 stiffness matrix depending on the wavevector $\mathbf{k}$ given by

$$\mathbf{C}_\varepsilon = \left(\begin{array}{cc} \mathbf{C}_\varepsilon^{(1)} & \mathbf{C}_\varepsilon^{(3)} \\ \left(\overline{\mathbf{C}_\varepsilon^{(3)}}\right)^{\mathrm{T}} & \mathbf{C}_\varepsilon^{(2)} \end{array}\right), \tag{3.35}$$

with

$$\mathbf{C}_\varepsilon^{(1)} = \mathbf{C} + \frac{3}{2} c_\varepsilon \mathbf{I}_4 \,, \quad \mathbf{C}_\varepsilon^{(2)} = 3c_\varepsilon \mathbf{I}_2 \,, \tag{3.36}$$

and

$$\mathbf{C}_\varepsilon^{(3)} = \frac{c_\varepsilon}{4} \begin{pmatrix} -(4\mathrm{e}^{-\mathrm{i}\mu} + \mathrm{e}^{-\mathrm{i}\eta} + \mathrm{e}^{-\mathrm{i}\gamma}) & \sqrt{3}\,(-\mathrm{e}^{-\mathrm{i}\eta} + \mathrm{e}^{-\mathrm{i}\gamma}) \\ -\sqrt{3}\,(\mathrm{e}^{-\mathrm{i}\eta} - \mathrm{e}^{-\mathrm{i}\gamma}) & -3\,(\mathrm{e}^{-\mathrm{i}\eta} + \mathrm{e}^{-\mathrm{i}\gamma}) \\ -(4 + \mathrm{e}^{-\mathrm{i}\eta} + \mathrm{e}^{-\mathrm{i}\gamma}) & \sqrt{3}\,(\mathrm{e}^{-\mathrm{i}\eta} - \mathrm{e}^{-\mathrm{i}\gamma}) \\ \sqrt{3}\,(\mathrm{e}^{-\mathrm{i}\eta} - \mathrm{e}^{-\mathrm{i}\gamma}) & -3\,(\mathrm{e}^{-\mathrm{i}\eta} + \mathrm{e}^{-\mathrm{i}\gamma}) \end{pmatrix} . \tag{3.37}$$

Here $\mu = 3k_1 l, \eta = \left(3k_1 - \sqrt{3}k_2\right) l/2$, $\gamma = \left(3k_1 + \sqrt{3}k_2\right) l/2$, and $\varepsilon = c_\varepsilon / c$ is a small non-dimensional parameter. The bar in (3.35) denotes the complex conjugate.

Non-trivial solutions then follow from the roots of the determinant of the coefficient matrix in (3.33), which yields a polynomial of the sixth order in ω^2. We apply the same normalizations as in Section 3.2, except we introduce $\tilde{\mathbf{C}}_\varepsilon = \mathbf{C}_\varepsilon / c$ (where the "tilde" will again be omitted for convenience in what follows). For $\varepsilon \to 0$, we analyse the behaviour of eigenfrequencies as solutions associated with:

$$\det\left[\mathbf{C}_\varepsilon - \omega^2 \left(\mathbf{I} - \mathbf{A}\right)\right] = 0 \,. \tag{3.38}$$

3.4.2 Dispersive features of the chiral triangular lattice as it degenerates to a chiral hexagonal lattice

In this Section, we discuss the dispersion properties of the inhomogeneous chiral triangular structure. In particular, we determine the dispersion curves for this system in the reciprocal lattice space along the same path ΓΜΚΓ described in Section 3.2.2.

In Figure 3.17, we present dispersion diagrams based on (3.38). We note that the (3.38) does not allow for rigid-body motions in contrast to the hexagonal lattice of Section 3.2.2. When $0 \leq \beta < 1$, the relation (3.38) admits six positive solutions for ω, namely two acoustic branches and four optical branches. On the other hand, if $\beta > 1$, only three positive solutions of (3.38) exist (the other three solutions for ω^2 are negative). This can be observed, for instance, in Figure 3.17(a) and Figure 3.17(b), where dispersion curves based on (3.38) have been presented for $\beta = 0.8$ and $\beta = 1.2$, respectively; in both Figures, the ratio of the stiffnesses of the two types of links is $\varepsilon = 0.1$. Therefore, the inhomogeneous triangular lattice exhibits three additional wave modes compared with the hexagonal structure when $\beta < 1$ and two additional modes when $\beta > 1$.

For $\beta < 1$, Figures 3.17(a),(c),(e),(g) show the dispersion diagrams of the triangular lattice as the stiffness c_ε decreases to zero. In these Figures, we observe that when $\beta < 1$ there are three finite stop-bands. As ε decreases, the six dispersion curves move to lower frequencies and the widths of the lowest two finite stop-bands decrease and they disappear when $\varepsilon = 0$. In this limit there are only three dispersion curves in Figure 3.17(g). These curves represent the non-trivial branches associated with the dispersion relation (3.29) of the hexagonal lattice connected to gyroscopic spinners, described in detail in Section 3.2.2 (see also (3.32a)–(3.32c)).

Similar behaviour is observed for $\beta > 1$ and $\varepsilon \to 0$ in Figures 3.17(b), (d), (f) and (h). In this case, one finds three dispersion curves and two finite stop-bands. All curves move to lower frequencies as $\varepsilon \to 0$. The lowest two dispersion curves decrease and flatten with decrease of ε causing the lowest stop-band to shrink. These two curves approach zero and disappear as $\varepsilon \to 0$, thus retrieving the case of a hexagonal

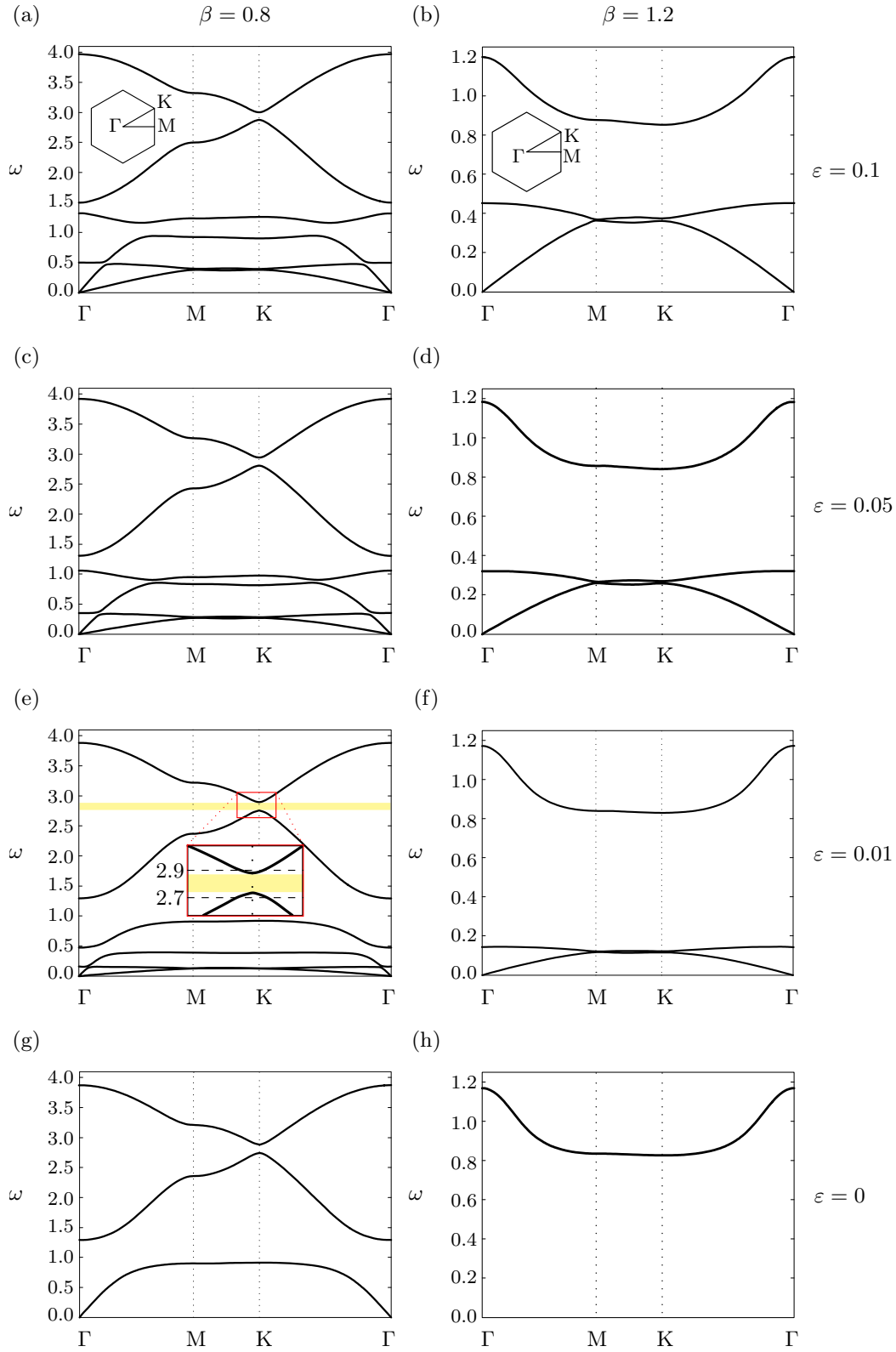

Figure 3.17: Dispersion diagrams for the chiral triangular lattice, determined for (a, c, e, g) $\beta = 0.8$ and (b, d, f, h) $\beta = 1.2$ and for decreasing values of ε: (a,b) $\varepsilon = 0.1$, (c,d) $\varepsilon = 0.05$, (e,f) $\varepsilon = 0.01$, (g,h) $\varepsilon = 0$. The discrete triangular system exhibits six (three) dispersion surfaces for $\beta < 1$ ($\beta > 1$). A magnified inset of the neighbourhood of point K is included in (e) for later use (see Section 3.4.3).

lattice connected to gyroscopic spinners when $\varepsilon = 0$ (see Figure 3.17(h)).

Figure 3.18 shows the dispersion diagrams for the triangular lattice, determined for a different value of the spinner constant, $\beta = 0.9$, and larger values for the stiffness of the internal links, proportional to ε. It is apparent that, in the low-frequency regime, the effective shear and pressure wave speeds increase with ε (identified from the slopes of the two acoustic branches near Γ), since the system becomes stiffer as ε is increased. At higher frequencies, the optical branches lift up as the stiffness of the internal links is increased. Moreover, for $\varepsilon \simeq 0.52$ the highest finite stop-band becomes a partial stop-band, as shown in Figure 3.18(d), so that waves can propagate in some directions and are evanescent in the other directions. When $\varepsilon \to 1$, two pairs of dispersion surfaces become closer to each other and they eventually coincide when $\varepsilon = 1$, forming a Dirac point. Figure 3.18(f) represents the dispersion diagram for a homogeneous triangular lattice (see, for instance, [Carta et al. (2014)]).

3.4.3 Uni-directional waveforms in the heterogeneous triangular lattice

Now, we show that the interfacial waveforms with preferential directionality can also be obtained in the heterogeneous triangular lattice by adjusting the gyroscopic spin directions in sub-domains of the lattice. In the numerical simulations presented below, performed in *Comsol Multiphysics*, the lattice domain is a 90×76.2 rectangle. The size of the domain is smaller than that used for the hexagonal lattice, since the model for the triangular lattice presents a higher complexity and hence requires a larger computational cost due to the additional degrees of freedom. Apart from the different size and the additional links, the finite element model developed for the triangular lattice is identical to that described in Section 3.3.1.

In Figure 3.19, we divide the lattice domain in two regions, where the gyroscopic spinners are characterised by spinner constants of the same magnitude ($|\beta| = 0.8$) but of opposite sign. We apply a time-harmonic displacement to a lattice particle situated on the horizontal interface between the two regions. In part (a), the radian frequency

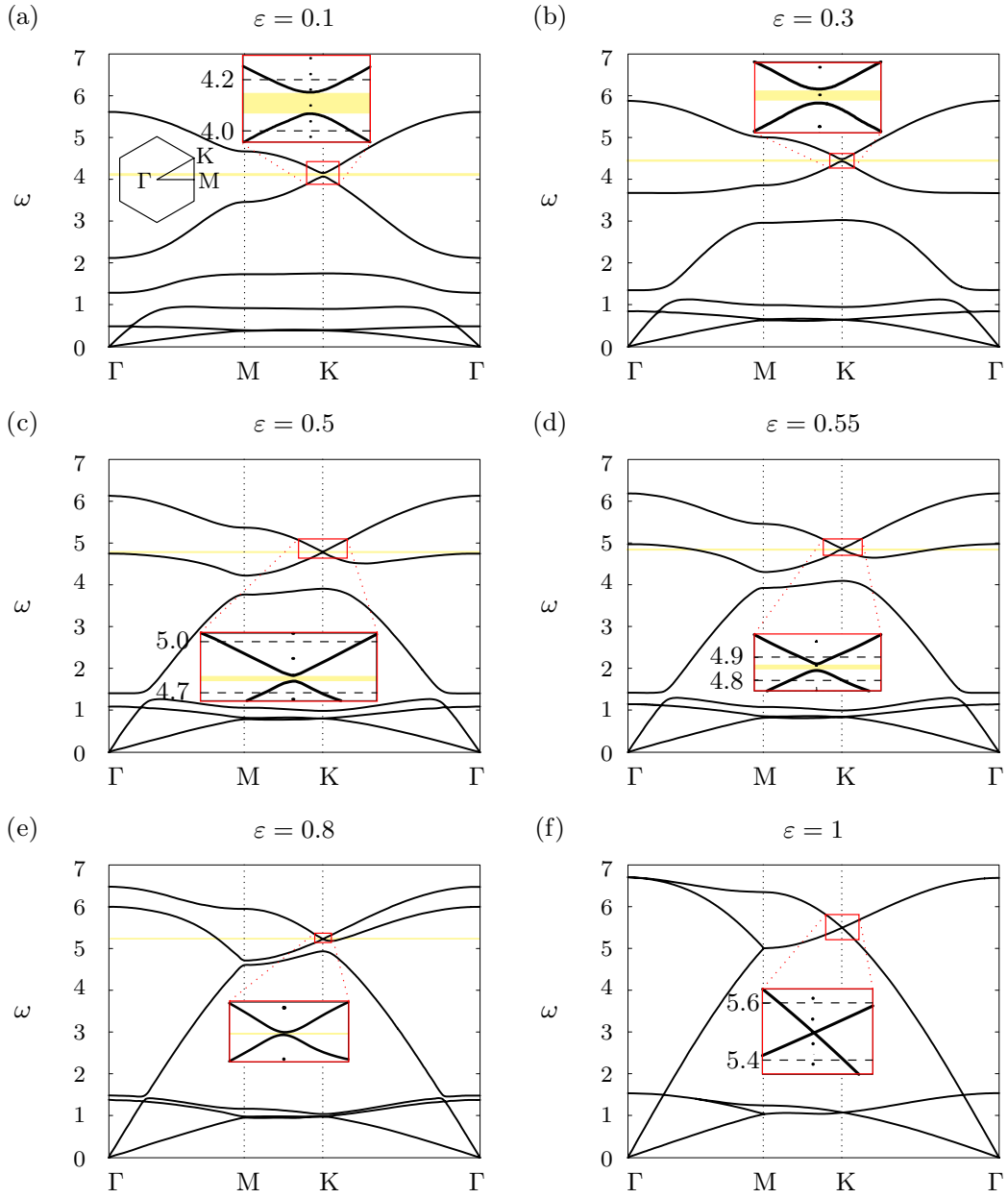

Figure 3.18: Dispersion diagrams for the chiral triangular lattice, calculated for $\beta = 0.9$ and for different values of ε, as specified. Magnified insets of the neighbourhood of point K are also presented.

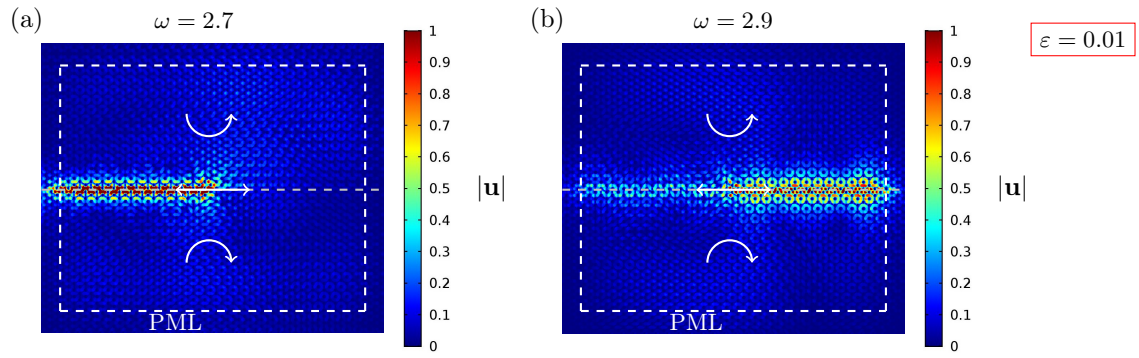

Figure 3.19: Elastic triangular lattice with soft internal links, whose domain is divided into two regions where the spinners rotate in opposite directions. A time-harmonic displacement is imposed on a node at the interface between the two regions. Interfacial waveforms are generated, whose direction depends on the frequency of the imposed displacement: (a) $\omega = 2.7$, (b) $\omega = 2.9$ (see also inset in Figure 3.17e). In the computations, the absolute value of the spinner constant is $|\beta| = 0.8$ and the links are very soft ($\varepsilon = 0.01$).

is $\omega = 2.7$, which is below the lower limit of the stop-band highlighted in yellow in Figure 3.17(e), corresponding to free vibrations in the analogous homogeneous infinite structure. Conversely, in part (b) the radian frequency of the external excitation is equal to $\omega = 2.9$, which lies above the upper limit of the stop-band highlighted in Figure 3.17(e).

Comparing Figures 3.19(a) and 3.19(b), we observe that uni-directional interfacial waves can be created in the heterogeneous triangular lattice with soft internal links. This is due to the non-trivial topology of the band diagram, characterised by the presence of (almost formed) Dirac points. As in the illustrations for the hexagonal lattice studied in Section 3.3.1 and presented in Figures 3.11(a) and 3.11(b), the wave directionality in the heterogeneous triangular lattice also depends on the frequency of the external excitation. The width of the region in Figure 3.19 where displacements are not zero is similar to that in Figure 3.11, although it seems larger due to the difference in size of the computational windows. We have verified that for the triangular lattice the direction of wave propagation can also be reversed by changing the spin directions of the gyroscopic spinners.

Figure 3.20 shows the same lattice structure as in Figure 3.19, but for $|\beta| = 0.9$. The stiffnesses of the internal links considered in Figures 3.20(a)-(f) are larger than the value chosen in Figures 3.19(a) and (b). Nonetheless, if the system exhibits a

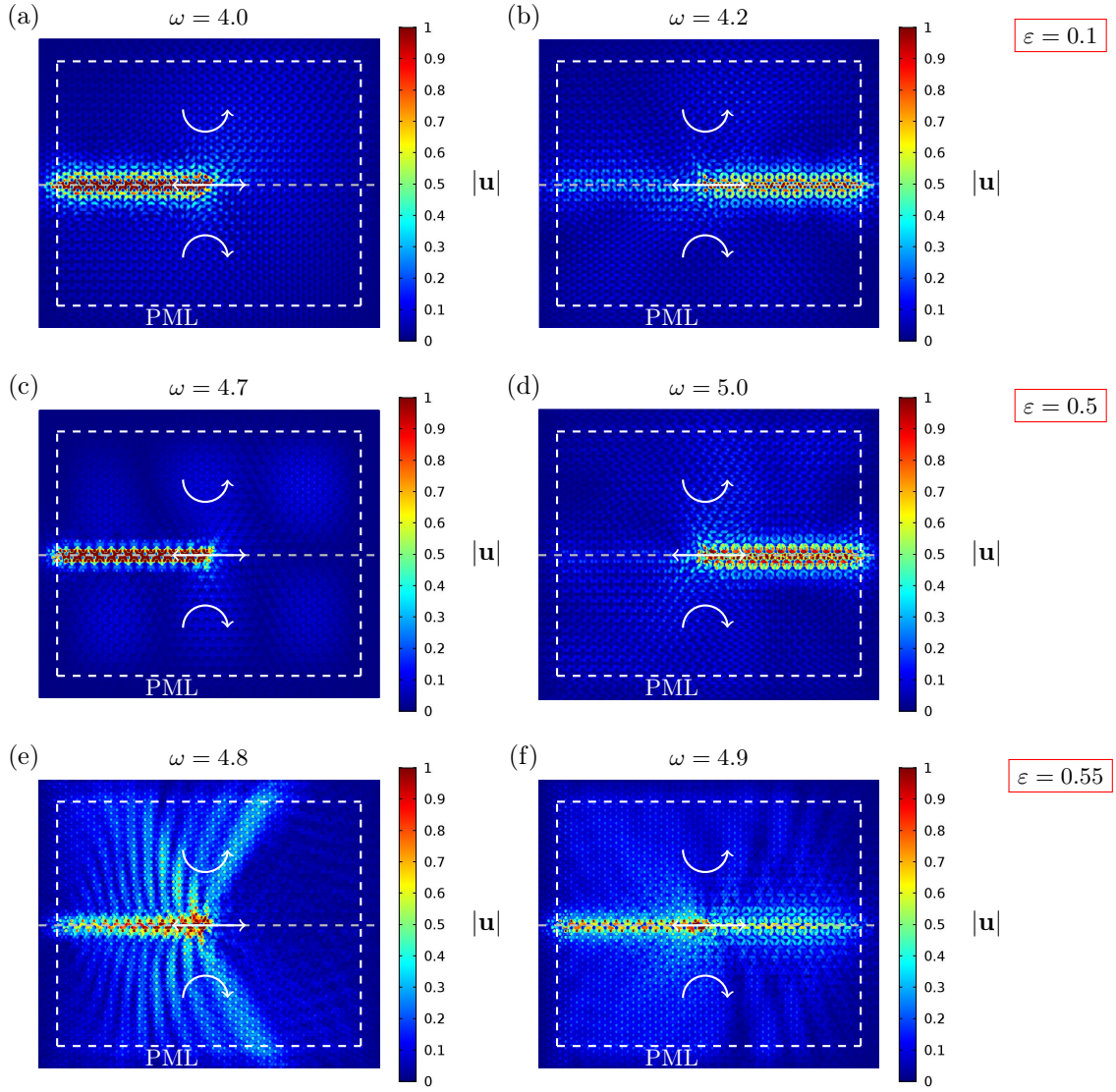

Figure 3.20: Computations showing the response of triangular lattices with internal links of different stiffness. Each lattice is attached to an inhomogeneous array of spinners. The computational setup is described in the caption of Figure 3.19, but in this case the absolute value of the spinner constant is $|\beta| = 0.9$. We consider three different values of the ratio ε of the stiffnesses of the links in the elementary cell of the lattice and for each ε we take two frequencies, one above and one below the stop-band highlighted in Figure 3.18. For $\varepsilon = 0.1$, the frequencies are $\omega = 4.0$ (part (a)) and $\omega = 4.2$ (part (b)); similarly, for $\varepsilon = 0.5$, $\omega = 4.7$ (part (c)) and $\omega = 5.0$ (part (d)); finally, for $\varepsilon = 0.55$, $\omega = 4.8$ (part (e)) and $\omega = 4.9$ (part (f)).

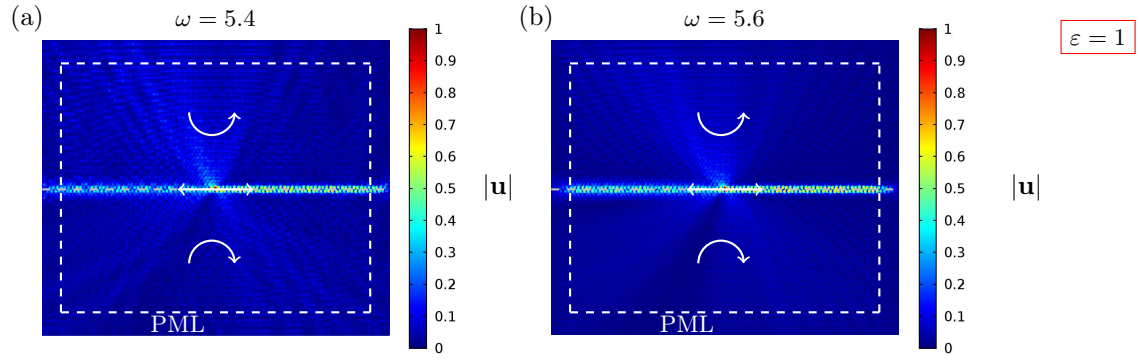

Figure 3.21: Displacement field in the homogeneous triangular lattice ($\varepsilon = 1$) produced by a time-harmonic displacement, having a frequency (a) lower and (b) higher than the frequency at the Dirac point (see Figure 3.18(f)). In both cases, the absolute value of the spinner constant is $|\beta| = 0.9$.

stop-band near the (almost formed) Dirac point, in particular for $\varepsilon = 0.1$ and $\varepsilon = 0.5$ (see Figures 3.18(a),(c)), uni-directional wave propagation can be realised in the triangular lattice (see Figures 3.20(a)-(d)). On the other hand, when the stop-band in the vicinity of the (almost formed) Dirac point is only partial (see Figure 3.18(d)), waves can also propagate in the bulk of the lattice (see Figures 3.20(e),(f)).

Now, we investigate the limit case when $\varepsilon = 1$, that is when the triangular lattice is homogeneous. The corresponding dispersion diagram, plotted in Figure 3.18(f), does not exhibit any finite width stop-bands and it shows the formation of a Dirac point. The response of the homogeneous triangular lattice under a time-harmonic displacement is shown in Figures 3.21(a) and 3.21(b) for the frequency $\omega = 5.4$ (below the Dirac point) and $\omega = 5.6$ (above the Dirac point), respectively. Wave localisation is observed on the interface between the two media where spinners rotate in opposite directions, but without preferential directionality. In addition, waves of small amplitude propagate within the bulk. These results demonstrate that preferential directionality can be realised if the system exhibits a total stop-band near the Dirac point.

Interfacial waveform in a close shape

Finally, we note that the interfacial waveforms following a closed path can be also generated for the inhomogeneous triangular chiral elastic lattice.

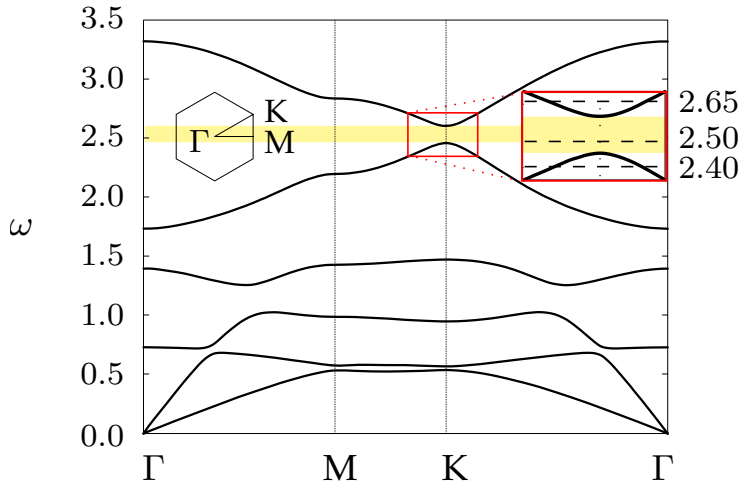

Figure 3.22: Dispersion diagrams for the chiral triangular lattice, calculated for $\beta = 0.7$ and for $\varepsilon = 0.2$, by going along the ΓMKΓ for the reciprocal lattice of a hexagonal lattice. Magnification of the almost formed Dirac point is shown in the inset.

Now we will consider a triangular lattice containing a bounded subset in which the properties of the spinners are different from those in the ambient lattice. The boundary of this subset defines the internal boundary of the system. The lattice is excited by a time harmonic displacement applied to a node along the internal boundary. In the example presented here, the internal boundary of the system is represented by an equilateral triangle of side length 55. The spinners are chosen to have the spinner constant $|\beta| = 0.7$. The inhomogeneity within the elastic lattice attached to the spinners is characterised by $\varepsilon = 0.2$. The dispersion curves are shown in Figure 3.22 along the path ΓMKΓ for the reciprocal lattice for the hexagonal system (see inset of the Figure).

The excitation frequencies chosen are $\omega = 2.50$, which is inside of the highest stop-band (indicated by the yellow horizontal strip in Figure 3.22), $\omega = 2.40$ and $\omega = 2.65$, situated in the immediate vicinity of the lower and upper limits, respectively, of the highest stop-band.

Figure 3.23 shows the displacement field for an applied displacement at frequency $\omega = 2.50$, taken inside of the stop-band. In Figure 3.23(a), the gyroscopic spinners are chosen to spin clockwise within the triangular domain and anticlockwise outside the domain. While the point force (whose position and direction of application are indicated by the white arrow) generates a highly localised wave around this internal

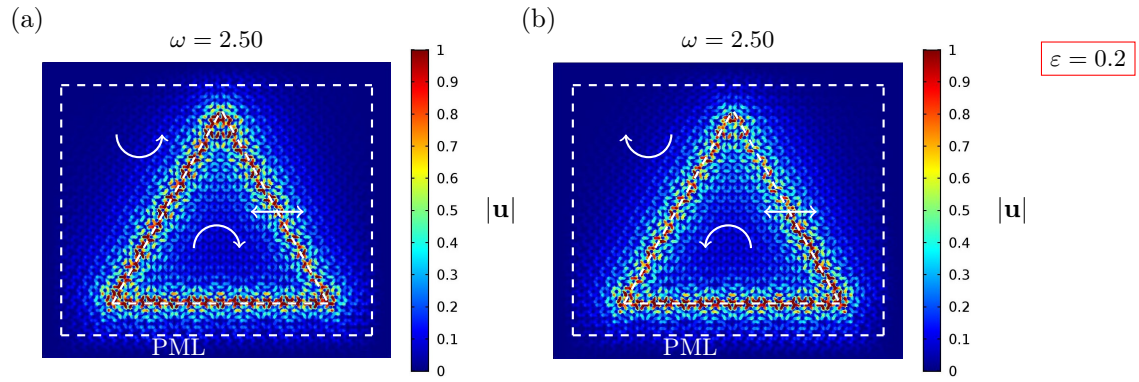

Figure 3.23: Displacement field for the elastic triangular lattice with soft internal links $\varepsilon = 0.2$. The domain is divided in two subdomains, separated by an equilateral triangle. The harmonic displacement is applied in an element at the interface between the two subdomain. The applied displacement generates an interfacial waveform, whose direction depends on the frequency of the perturbation. The frequency $\omega = 2.50$ is taken in the stop-band, see the inset in Figure 3.22. In (a) the triangular domain presents clockwise gyro-spinners and anticlockwise in the remaining lattice, whereas in (b) the gyro-spinners have an opposite distribution as indicated by the circular arrows. The spinner constant is $|\beta| = 0.7$.

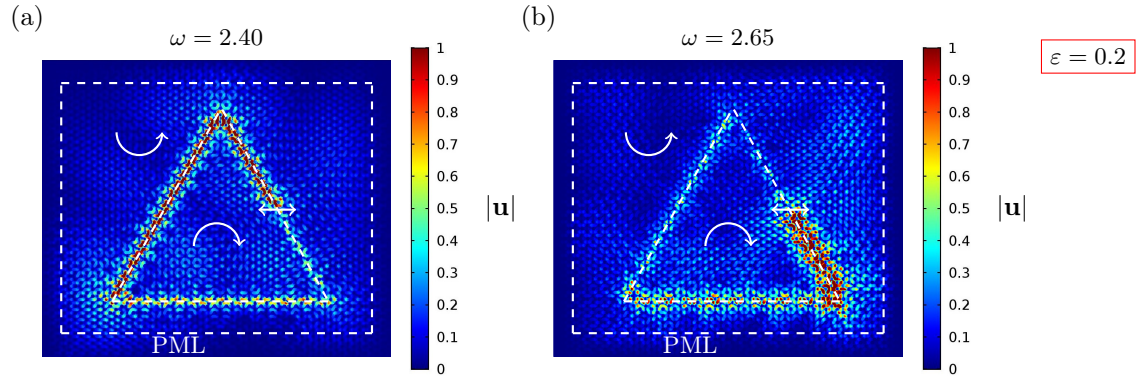

Figure 3.24: Response of the system with triangular subdomain (indicated by dashed lines), where inside the gyro-spinners are clockwise and outside anticlockwise, is shown in (a) and (b). The rotation directions of the spinners are indicated by the circular arrows and the spinner constant is $|\beta| = 0.7$. The absolute value of the displacement is shown for when the applied harmonic excitation has frequency (a) $\omega = 2.40$ and (b) $\beta = 2.65$.

boundary, it is possible to notice the width of the localisation slightly decreases as the running anti-clockwise from the applied load around the internal boundary. Given such an effect can be attributed to scattering produced by the wave passing through the vertices of the internal boundary, we conclude the wave runs anticlockwise around this boundary from the source.

On the other hand, in Figure 3.23(b) the spin direction of the spinners on the interior and exterior of the triangular subdomain have been interchanged and as expected this interfacial wave propagates in the opposite direction to that encountered in Figure 3.23(a) and this effect is clear.

Next we analyse the effect of loading the internal interface with frequencies just outside the stop-band in Figure 3.22. Figure 3.24(a) shows the response of the system when $\omega = 2.40$. In this case, a localised waveform propagates along the triangular interface in the anticlockwise direction. In Figure 3.24(b), when $\omega = 2.65$, for the same computational set up, the direction of the waveform is reversed. In both cases, once again the intensity of the waveform decreases as it passes through vertices of the triangle. The corners create some scattering as also seen in the case of a hexagonal elastic chiral lattice with an internal hexagonal boundary in Figure 3.14 and a rhomboidal boundary in Figure 3.15. It is clear from Figures 3.24(a) and (b) the waveforms have preferential directionality that is frequency dependent. We note that the directions of the waveforms may be reversed by interchanging the properties belonging to the spinners inside and outside the triangular subdomain similar to as in Figures 3.23(a) and (b), where the loading possesses a frequency situated in the stop-band.

3.5 Conclusions

In this Chapter, we have developed a novel approach to create uni-directional waveforms in discrete elastic periodic media without perturbing the structured system, such as in [Kariyado and Hatsugai (2015), Vila et al. (2017)]. This has been achieved by considering a hexagonal system of masses connected by elastic trusses

and by the introduction of gyroscopic spinners, which are linked to individual nodes of the structure. In the static regime, such a structure is statically under-constrained. In the time-harmonic regime, a comprehensive dispersion analysis of a hexagonal lattice connected to gyroscopic spinners has been presented and special features of the dispersive behaviour have been identified. The new aspects brought by the analysis of the novel hexagonal gyro-elastic lattice considered here include:

1. The ability to control the appearance of so-called Dirac points, or dispersion degeneracies possessed by the medium without chirality, by using the properties of the gyroscopic spinners. These also provide an effective tool for manipulating stop-bands in the vicinity of Dirac points that play a crucial role in the generating interfacial waveforms in the lattice system that is induced by the chirality brought by the spinners.

2. The generation of unidirectional interfacial waveforms with a tunable direction in lattice systems attached to inhomogeneous arrays of spinners. These interfacial waveforms have preferential directionality that is sensitive to the:

    - orientation of the spinners either side of the interface or
    - frequency of the applied load along the interface

3. The creation of new designs for lattice systems capable of supporting unidirectional interfacial waves running along closed contours.

The possibility to reverse the directionality of the interfacial waveforms by changing the frequency of the excitation is a counterintuitive novel aspect identified in this Chapter and this can be attributed by the change in the group velocity possessed by the lattice system in the vicinity of narrow high frequency stop bands linked to Dirac points.

Additionally, we have demonstrated that the above dynamic regimes are not only associated with a hexagonal lattice. In association with this, further novel aspects of the work presented show that:

4. Similar effects can be achieved when the lattice system is an inhomogeneous triangular elastic lattice. Here, the hexagonal elastic lattice represents the limit case of a triangular lattice with very soft internal links within hexagonal cells. Indeed, when gyroscopic spinners are attached to the triangular lattice, interfacial leaky waves can be generated at the boundaries of regions where spinners rotate in opposite directions.

5. We lose the effect of preferential unidirectionality when the triangular lattice is sufficiently close to the homogeneous structure, having an uniform distribution of elastic rods of equal stiffness, due to the emergence of partial stop bands as the internal link stiffness increases.

Chapter 4

Transient model of a gyro-elastic medium

In this Chapter, the transient analysis of gyro-elastic structured media, composed of periodically placed masses interconnected by elastic rods and attached to gyroscopic spinners, is presented. The motivation for this Chapter is to verify that the waveforms analysed in Section 3.3.1 and in [Garau et al. (2018)] can be realised. This will be investigated for several lattices subjected to different initial conditions and forcing terms.

In Section 4.1, the development of a novel linear asymptotic model, characterising the interaction between a single gyroscopic spinner and a mass embedded in a truss system, is presented in the transient regime. There, we extend the results of [Brun, Jones and Movchan (2012)]. Following this, in Section 4.2, numerical examples illustrating the motion of this system based on the results of Section 4.1 are given. This section also includes the independent verification of the linearised transient model via finite element simulations performed in *Comsol Multiphisics*. In Section 4.3, the results of Section 4.1 are exploited to investigate the transient behaviour of various lattice systems attached to arrays of gyroscopic spinners. This will include triangular and hexagonal gyro-elastic systems and we will show that the waveforms identified and discussed in Chapter 3 can be traced through transient computations, which will reveal new transient phenomena associated with the model of Section 4.1.

Finally, in Section 4.4, we give some conclusions based on the results of this Chapter.

4.1 Motion of the gyroscopic oscillator

As discussed in Chapter 3, the transient motion of a gyroscopic spinner is described by Euler's equations [Goldstein, Poole and Safko (2001)], which are non-linear time-dependent equations representing the angular momentum balance of a rigid gyroscopic body. When the gyroscope is considered to be connected to an elastic system, the non-linearity of the Euler equations poses difficulties in obtaining important information about the motion of the entire system. However, if the nutation angle of the gyroscope is small, the motion of the system can be described by a linearised model, which was presented for the first time in [Brun, Jones and Movchan (2012)] (see also Section 3.1.1). Even within this linearised setting, masses in a gyro-elastic medium can undergo a range of atypical trajectories that are geometrically non-linear and this behaviour depends on the properties of the system, which we investigate later.

In this Section, the transient motion of a single gyroscope that is hinged at its base and connected to a mass at its tip is studied. The gyroscope (see Figure 4.1(a)) is modelled as a rigid body that is constrained at the base. As an example, we consider the mass m, which is elastically constrained by a system of six extensional springs having stiffness c. We note that in the subsequent developments, one can consider more general arrangements for the truss. The effect of gravity will also be neglected throughout. We first state the main result of this section, concerning the linearised equation of motion for the mass.

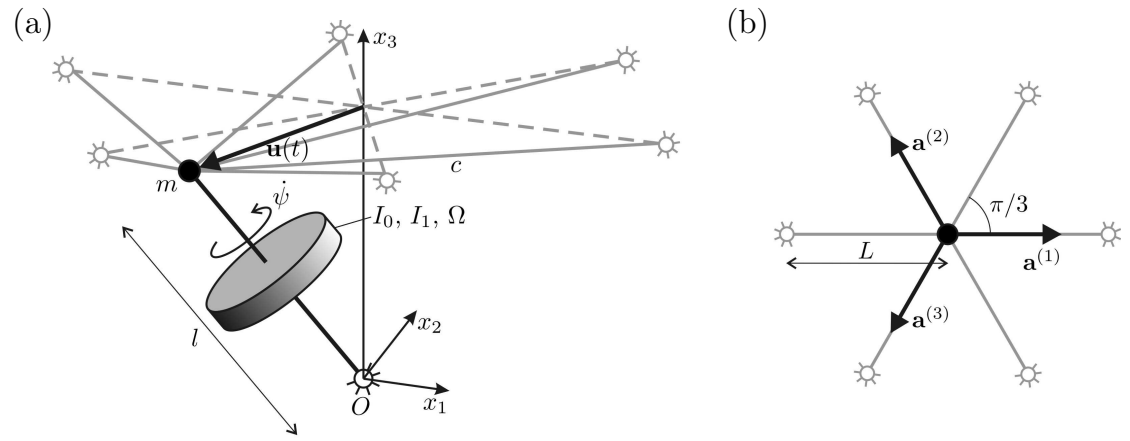

Figure 4.1: The gyroscopic oscillator. (a) A gyroscopic spinner hinged at its base and having a spin rate $\dot{\psi}$. At the top of the spinner a concentrated mass m is constrained by six non-inertial truss elements depicted in grey and having stiffness c. The mass displacement is $\mathbf{u}(t)$. The spinner has length l, moments of inertia I_0 and I_1, and gyricity Ω (see section 4.1.5). (b) Planar view in the reference configuration. The extensional springs have initial length L, and the basis vectors for the in-plane elastic system are $\mathbf{a}^{(1)}$, $\mathbf{a}^{(2)}$ and $\mathbf{a}^{(3)}$.

4.1.1 Main result: Linearised governing equations for the mass

Below, we show the dimensionless in-plane displacement $\mathbf{u} = (u_1, u_2)^{\mathrm{T}}$ of the mass in Figure 4.1 satisfies the linear equations:

$$\ddot{\mathbf{u}}(t) + \alpha\Omega\mathbf{R}\dot{\mathbf{u}}(t) + 3\mathbf{u}(t) = \mathbf{0}\,, \tag{4.1}$$

where

$$\alpha = \frac{I_1}{(\delta + I_0)} \quad \text{and} \quad \mathbf{R} = \begin{pmatrix} 0 & 1 \\ -1 & 0 \end{pmatrix}\,, \tag{4.2}$$

if the nutation angle θ of the gyroscope is small (see Figure 4.2). Here, I_0 and I_1 represent the dimensionless moments of inertia of the gyroscope about the principal axes of a coordinate system that follows the gyroscope as it precesses and nutates and δ is the ratio between the length of the gyroscope to the length of the elastic links inside the truss. The dimensionless parameter Ω appearing in (4.1) is known as the *gyricity* and is represented by the sum of the initial precession and spin rate

of the gyroscope. We note, if one sets $\Omega = \omega$, with ω being the eventual radian frequency of the system, in the time-harmonic regime we can retrieve a form of the gyroscopic forcing terms identified in [Brun, Jones and Movchan (2012)]. This case is investigated later for the study of complex gyro-elastic systems. In addition, here the parameter α results from the fact that the gyroscope also provides additional inertia terms to the system.

In (4.1) the matrix $\mathbf{R}$ provides the coupling of the in-plane components of the displacement of the mass, and the intensity of this is determined by the parameters α and Ω, characterising the gyroscope and its motion. The result (4.1) also illustrates that the gyricity Ω is a fundamental quantity in characterising how a gyroscopic spinner interacts with an elastic system and we refer to [Carta et al. (2018), Nieves et al. (2018)], where this quantity also appears in the modelling of other systems composed of spinners connected to Euler-Bernoulli beams. In the remaining part of this section, we derive (4.1), provide an analytical solution of motion of the system governed by (4.32) when initial conditions are supplied (see Section 4.2) and validate the model against the independent finite element package *Comsol* in Section 4.2.1.

4.1.2 Non-linear governing equations of the gyroscopic spinner

Here we derive a novel linearised model (4.1) that describes the interaction of a gyroscope connected to a mass embedded within a truss system (see Figure 4.1), [Carta et al. (2018)].

The generalised coordinates or Euler angles [Goldstein, Poole and Safko (2001)] that describe the motion of the gyroscopic spinner are denoted by ϕ, θ and ψ, and represent the precession, nutation and spin angle of the gyroscopic spinner, respectively, as defined in Chapter 3. They are shown in Figure 4.2.

We introduce both a fixed frame of reference $\mathcal{F}$, with basis $\{\mathbf{e}_1, \mathbf{e}_2, \mathbf{e}_3\}$ and coordinate system $Ox_1x_2x_3$, and a moving frame of reference $\mathcal{F}'$, which follows the gyroscopic spinner as it precesses and nutates (but not as it spins). The moving

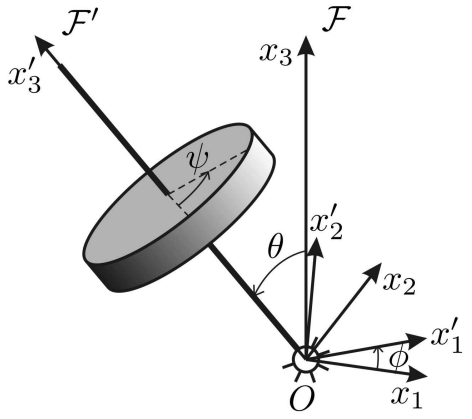

Figure 4.2: The Euler angles: precession ϕ, nutation θ and spin ψ of the gyroscopic spinner. In addition, the fixed frame $\mathcal{F}$ with coordinate system $Ox_1x_2x_3$ and the moving frame $\mathcal{F}'$ with coordinate system $Ox_1'x_2'x_3'$ are shown. The frame $\mathcal{F}'$ precesses with angle ϕ and nutates with angle θ.

frame $\mathcal{F}'$ has basis $\{\mathbf{e}_1', \mathbf{e}_2', \mathbf{e}_3'\}$ (which is time-dependent) and coordinate system $Ox_1'x_2'x_3'$. The basis in the moving frame can be written via the basis $\{\mathbf{e}_1, \mathbf{e}_2, \mathbf{e}_3\}$ in the fixed frame as

$$\begin{aligned}
\mathbf{e}_1' &= \cos(\phi(t))\mathbf{e}_1 + \sin(\phi(t))\mathbf{e}_2 \ , \\
\mathbf{e}_2' &= -\cos(\theta(t))\sin(\phi(t))\mathbf{e}_1 + \cos(\theta(t))\cos(\phi(t))\mathbf{e}_2 + \sin(\theta(t))\mathbf{e}_3 \ , \\
\mathbf{e}_3' &= \sin(\theta(t))\sin(\phi(t))\mathbf{e}_1 - \sin(\theta(t))\cos(\phi(t))\mathbf{e}_2 + \cos(\theta(t))\mathbf{e}_3
\end{aligned} \tag{4.3}$$

and we derive these identities below.

Angular momentum balance of the gyroscope in the fixed frame

In this section, we derive the form of the Euler equations written for the frame $\mathcal{F}$ and show they are

$$\begin{aligned}
M_1 &= I_0 \frac{\mathrm{d}}{\mathrm{d}t}[-\dot{\phi}\sin(\phi)\sin(\theta)\cos(\theta) + \dot{\theta}\cos(\phi)] + I_1 \frac{\mathrm{d}}{\mathrm{d}t}[\sin(\theta)\sin(\phi)(\dot{\phi}\cos(\theta) + \dot{\psi})] \ , \\
M_2 &= I_0 \frac{\mathrm{d}}{\mathrm{d}t}[\dot{\phi}\cos(\phi)\sin(\theta)\cos(\theta) + \dot{\theta}\sin(\phi)] - I_1 \frac{\mathrm{d}}{\mathrm{d}t}[\sin(\theta)\cos(\phi)(\dot{\phi}\cos(\theta) + \dot{\psi})] \ , \\
M_3 &= I_0 \frac{\mathrm{d}}{\mathrm{d}t}(\dot{\phi}\sin^2(\theta)) + I_1 \frac{\mathrm{d}}{\mathrm{d}t}[\cos(\theta)(\dot{\psi} + \dot{\phi}\cos(\theta))] \ ,
\end{aligned} \tag{4.4}$$

where M_j, $1 \leq j \leq 3$, represent external moments supplied to the gyroscope.

Angular momentum balance in a moving frame $\mathcal{F}'$

We note that for a rotating body, the angular momentum balance of the body can be written as

$$\mathbf{M}_{\mathrm{e}} = \frac{\mathrm{d}\mathbf{L}}{\mathrm{d}t} \ , \tag{4.5}$$

where $\mathbf{M}_{\mathrm{e}}$ is the vector representing the external moments imposed on the rotating body and $\mathbf{L}$ is the angular momentum of the body. In what follows, we use the above balance law to determine the equations of motion for the motion of the gyroscope in Figure 4.1. In this case, the quantities shown in the above equation can be written with respect to the basis in the moving system $\mathcal{F}'$ or $\mathcal{F}$. For simplicity we begin with the representation of these quantities in the frame $\mathcal{F}'$. We represent $\mathbf{L}$ as

$$\mathbf{L} = \mathbf{I}_{\mathrm{g}}\boldsymbol{\omega}_{\mathrm{g}} \ , \tag{4.6}$$

where $\mathbf{I}_{\mathrm{g}}$ is the moment of inertia tensor of the gyroscope and $\boldsymbol{\omega}_{\mathrm{g}}$ is the angular velocity vector of the gyroscope. We assume the gyroscope possesses axial symmetry in order that the $\mathbf{I}_{\mathrm{g}}$ is diagonal with respect to the frame $\mathcal{F}'$, i.e.

$$\mathbf{I}_{\mathrm{g}} = I_0(\mathbf{e}'_1 \otimes \mathbf{e}'_1 + \mathbf{e}'_2 \otimes \mathbf{e}'_2) + I_1\mathbf{e}'_3 \otimes \mathbf{e}'_3 \ , \tag{4.7}$$

where I_0 and I_1 are the principal moments of inertia about the x'_j-, $j = 1, 2$, and x'_3-axes, respectively. The angular velocity of the gyroscope $\boldsymbol{\omega}_{\mathrm{g}}$ is given by

$$\boldsymbol{\omega}_{\mathrm{g}} = \boldsymbol{\omega}_{\mathcal{F}'\mathcal{F}} + \dot{\psi}\,\mathbf{e}'_3 \ , \tag{4.8}$$

where

$$\boldsymbol{\omega}_{\mathcal{F}'\mathcal{F}} = \dot{\theta}\mathbf{e}'_1 + \dot{\phi}\sin(\theta)\mathbf{e}'_2 + \dot{\phi}\cos(\theta)\mathbf{e}'_3 \ , \tag{4.9}$$

is the angular velocity of the frame $\mathcal{F}'$ relative to the frame $\mathcal{F}$.

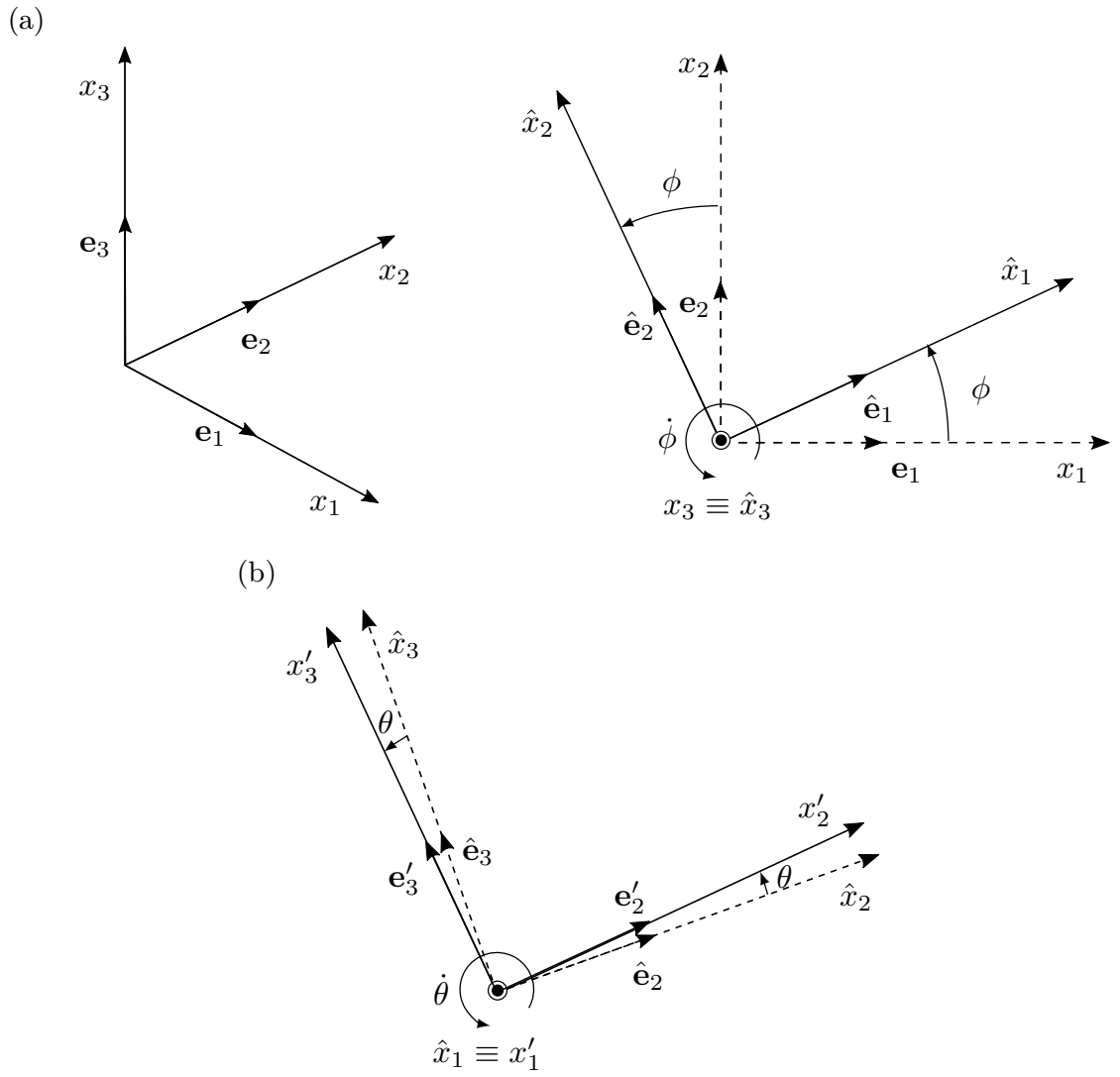

Figure 4.3: Coordinate transformations connecting (a) a frame $\hat{\mathcal{F}}$ with basis $\{\hat{\mathbf{e}}_1, \hat{\mathbf{e}}_2, \hat{\mathbf{e}}_3\}$ to the frame $\mathcal{F}$ with basis $\{\mathbf{e}_1, \mathbf{e}_2, \mathbf{e}_3\}$ and (b) the frame $\mathcal{F}'$ with basis $\{\mathbf{e}_1', \mathbf{e}_2', \mathbf{e}_3'\}$ to the frame $\hat{\mathcal{F}}$.

Derivation of the angular velocity vector of the gyroscope

Here we derive the expressions (4.8) and (4.9). To achieve this, we consider the angular velocities associated with the precession, nutation and spin of the gyroscope separately.

As the gyroscope undergoes precession through ϕ, measured in the x_1x_2-plane, the angular velocity attributed to this motion is described by the vector

$$\dot{\phi}\mathbf{e}_3. \tag{4.10}$$

To obtain the angular velocity associated with the nutation, it is convenient to introduce a coordinate transformation such that the new coordinate system $O\hat{x}_1\hat{x}_2\hat{x}_3$ in the frame $\hat{\mathcal{F}}$ that moves with the gyroscope as it precesses and which is obtained by a rotation of the coordinates $Ox_1x_2x_3$ through the angle ϕ anticlockwise about the x_3-axis (indicated in Figure 4.3(a) and compare with Figure 4.2). The basis of the new frame $\{\hat{\mathbf{e}}_1, \hat{\mathbf{e}}_2, \hat{\mathbf{e}}_3\}$ in $\hat{\mathcal{F}}$ can be written in terms of the basis for the fixed frame as

$$\hat{\mathbf{e}}_1 = \cos(\phi)\mathbf{e}_1 + \sin(\phi)\mathbf{e}_2 \ , \tag{4.11}$$

$$\hat{\mathbf{e}}_2 = -\sin(\phi)\mathbf{e}_1 + \cos(\phi)\mathbf{e}_2 \ , \tag{4.12}$$

$$\hat{\mathbf{e}}_3 = \mathbf{e}_3 \ . \tag{4.13}$$

In the new frame $\hat{\mathcal{F}}$, the gyroscope nutates in the $\hat{x}_2\hat{x}_3$ plane through angle θ. Thus the angular velocity vector associated with the nutation of the gyroscope and perpendicular to this plane is

$$\dot{\theta}(t)\hat{\mathbf{e}}_1 \ . \tag{4.14}$$

We note that the frame $\hat{\mathcal{F}}$ is an intermediate frame between $\mathcal{F}$ and $\mathcal{F}'$ and that the basis $\{\hat{\mathbf{e}}_1, \hat{\mathbf{e}}_2, \hat{\mathbf{e}}_3\}$ and $\{\mathbf{e}'_1, \mathbf{e}'_2, \mathbf{e}'_3\}$ are linked via

$$\mathbf{e}'_1 = \hat{\mathbf{e}}_1 \ , \tag{4.15}$$

$$\mathbf{e}'_2 = \cos(\theta)\hat{\mathbf{e}}_2 + \sin(\theta)\hat{\mathbf{e}}_3 \ , \tag{4.16}$$

$$\mathbf{e}'_3 = -\sin(\theta)\hat{\mathbf{e}}_2 + \cos(\theta)\hat{\mathbf{e}}_3 \ , \tag{4.17}$$

which corresponds the rotation of the coordinate axes $O\hat{x}_1\hat{x}_2\hat{x}_3$ through the angle θ anticlockwise about the $\hat{x}_1$ axis (illustrated in Figure 4.3(b), see also Figure 4.2). Note that using (4.11)–(4.13) and (4.15)–(4.17) we obtain (4.3). Moreover, in $\mathcal{F}'$, the gyroscope spins about the x'_3 axis. Therefore, the angular velocity vector connected with the spin rate is

$$\dot{\psi}(t)\mathbf{e}'_3 \ . \tag{4.18}$$

Combining (4.10), (4.14) and (4.18), we obtain the angular velocity vector $\boldsymbol{\omega}_{\mathrm{g}}$ of the gyroscope is

$$\boldsymbol{\omega}_{\mathrm{g}} = \dot{\phi}(t)\mathbf{e}_3 + \dot{\theta}(t)\hat{\mathbf{e}}_1 + \dot{\psi}(t)\mathbf{e}'_3 \ . \tag{4.19}$$

The first two terms in the above expression can also be identified with the angular velocity vector $\boldsymbol{\omega}_{\mathcal{F}'\mathcal{F}}$ (which undergoes precession and nutation with the gyroscope) that determines the angular velocity of the frame $\mathcal{F}'$ with respect to the fixed frame $\mathcal{F}$. We can use (4.11)–(4.13) and (4.15)–(4.17) to obtain (4.8).

Derivation of (4.4)

Next we substitute (4.7) and (4.8) into (4.6) and obtain the angular momentum of the gyroscope as

$$\mathbf{L} = I_0\dot{\theta}\mathbf{e}'_1 + I_0\dot{\phi}\sin(\theta)\mathbf{e}'_2 + I_1(\dot{\psi} + \dot{\phi}\cos(\theta))\mathbf{e}'_3 \ , \tag{4.20}$$

in terms of the basis in $\mathcal{F}'$. This can then be inserted into the angular momentum balance of the gyroscope in (4.5), and the first order time derivative of the angular momentum is computed taking into account that we must differentiate the components of $\mathbf{L}$ and the basis used in its representation (as it is time-dependent). In regards to the latter, we use the classical formula (see [Goldstein, Poole and Safko (2001)]), that relates the basis vector in $\mathcal{F}'$ to its time derivative:

$$\dot{\mathbf{e}}'_j = \boldsymbol{\omega}_{\mathcal{F}'\mathcal{F}} \times \mathbf{e}'_j \ . \tag{4.21}$$

In doing so, we arrive at the following form of the angular momentum balance of the gyroscope:

$$\mathbf{M}_{\mathrm{e}} = \mathbf{I}_{\mathrm{g}}\,\mathcal{A}_{\mathrm{g}} + \boldsymbol{\omega}_{\mathcal{F}'\mathcal{F}} \times \mathbf{L} \ , \tag{4.22}$$

with

$$\mathcal{A}_{\mathrm{g}} = \ddot{\theta}\mathbf{e}'_1 + (\ddot{\phi}\sin(\theta) + \dot{\phi}\dot{\theta}\cos(\theta))\mathbf{e}'_2 + (\ddot{\phi}\cos(\theta) - \dot{\phi}\dot{\theta}\sin(\theta) + \ddot{\psi})\mathbf{e}'_3 \ . \tag{4.23}$$

Here, the vector product on the right-hand side of (4.22), resulting from the differentiation of the time-dependent basis in $\mathcal{F}'$, can be calculated with (4.9) and (4.20) using the determinant of a matrix as follows:

$$\boldsymbol{\omega}_{\mathcal{F}'\mathcal{F}} \times \mathbf{L} = \begin{vmatrix} \mathbf{e}'_1 & \mathbf{e}'_2 & \mathbf{e}'_3 \\ \dot{\theta} & \dot{\phi}\sin\theta & \dot{\phi}\cos\theta \\ I_0\dot{\theta} & I_0\dot{\phi}\sin\theta & I_1(\dot{\phi}\cos\theta + \dot{\psi}) \end{vmatrix} ,$$

which can be written

$$\begin{aligned} \boldsymbol{\omega}_{\mathcal{F}'\mathcal{F}} \times \mathbf{L} &= \dot{\phi}\sin\theta \left[I_1(\dot{\phi}\cos\theta + \dot{\psi}) - I_0\dot{\phi}\cos\theta \right] \mathbf{e}'_1 \\ &\quad -\dot{\theta} \left[I_1(\dot{\phi}\cos\theta + \dot{\psi}) - I_0\dot{\phi}\cos\theta \right] \mathbf{e}'_2 \, . \end{aligned} \tag{4.24}$$

The explicit components of (4.22), obtained from (4.23) and the preceding equation, are

$$\begin{aligned} M'_1 &= I_0\ddot{\theta} + \dot{\phi}\sin(\theta)[-I_0\dot{\phi}\cos(\theta) + I_1(\dot{\phi}\cos(\theta) + \dot{\psi})] \, , \\ M'_2 &= I_0[\ddot{\phi}\sin(\theta) + 2\dot{\theta}\dot{\phi}\cos(\theta)] - I_1\dot{\theta}(\dot{\phi}\cos(\theta) + \dot{\psi}) \, , \\ M'_3 &= I_1(\ddot{\psi} + \ddot{\phi}\cos(\theta) - \dot{\phi}\,\dot{\theta}\sin(\theta)) \, , \end{aligned} \tag{4.25}$$

where M'_j, $1 \leq j \leq 3$, are the components of the external moment vector $\mathbf{M}_\mathrm{e}$ when written in terms of the basis $\{\mathbf{e}'_1, \mathbf{e}'_2, \mathbf{e}'_3\}$.

We denote by M_j, $1 \leq j \leq 3$, the components of the external moment vector $\mathbf{M}_\mathrm{e}$ when interpreted in terms of the basis of the fixed frame. From (4.3), they are:

$$\begin{pmatrix} M_1 \\ M_3 \\ M_3 \end{pmatrix} = \begin{pmatrix} \cos(\phi) & -\cos(\theta)\sin(\phi) & \sin(\theta)\sin(\phi) \\ \sin(\phi) & \cos(\theta)\cos(\phi) & -\sin(\theta)\cos(\phi) \\ 0 & \sin(\theta) & \cos(\theta) \end{pmatrix} \begin{pmatrix} M'_1 \\ M'_2 \\ M'_3 \end{pmatrix} .$$

We substitute (4.25) into the last relation and obtain

$$\begin{aligned} M_1 &= I_0\{-\sin(\theta)\cos(\theta)[\ddot{\phi}\sin(\phi)+\dot{\phi}^2\cos(\phi)]+\dot{\phi}\dot{\theta}\sin(\phi)[\sin^2(\theta)-\cos^2(\theta)-1] \\ &\quad +\ddot{\theta}\cos(\phi)\}+I_1\{(\dot{\phi}\cos(\theta)+\dot{\psi})[\dot{\theta}\cos(\theta)\sin(\phi)+\dot{\phi}\sin(\theta)\cos(\phi)] \\ &\quad +\sin(\theta)\sin(\phi)[\ddot{\phi}\cos(\theta)-\dot{\phi}\dot{\theta}\sin(\theta)+\ddot{\psi}]\}\ , \end{aligned} \tag{4.26}$$

$$\begin{aligned} M_2 &= I_0\{\sin(\theta)\cos(\theta)[\ddot{\phi}\cos(\phi)-\dot{\phi}^2\sin(\phi)]+\dot{\phi}\dot{\theta}\cos(\phi)[\cos^2(\theta)-\sin^2(\theta)-1] \\ &\quad +\ddot{\theta}\sin(\phi)\}-I_1\{(\dot{\phi}\cos(\theta)+\dot{\psi})[\dot{\theta}\cos(\theta)\cos(\phi)-\dot{\phi}\sin(\theta)\sin(\phi)] \\ &\quad +\sin(\theta)\cos(\phi)[\ddot{\phi}\cos(\theta)-\dot{\theta}\dot{\phi}\sin(\theta)+\ddot{\psi}]\}\ , \end{aligned} \tag{4.27}$$

$$\begin{aligned} M_3 &= I_0\{\ddot{\phi}\sin^2(\theta)-2\dot{\phi}\dot{\theta}\cos(\theta)\sin(\theta)\} \\ &\quad +I_1\{-\dot{\theta}\sin(\theta)(\dot{\psi}+\dot{\phi}\cos(\theta))+\cos(\theta)(\ddot{\psi}+\ddot{\phi}\cos(\theta)-\dot{\phi}\dot{\theta}\sin(\theta)\}\ . \end{aligned} \tag{4.28}$$

The terms in curly brackets can be written as first order derivatives in time of functions involving the Euler angles. Therefore, in the fixed coordinate system angular momentum balance for the gyroscope is as in (4.4).

4.1.3 External actions on the gyroscope

Here, we show that after incorporating the external moments supplied to the gyroscope by the lattice, that the angular momentum balance for the gyroscope is:

$$\begin{aligned} M_1 &= -l\sin(\theta)\cos(\phi)F_3-l\cos(\theta)F_2 \\ &= I_0\frac{\mathrm{d}}{\mathrm{d}t}[-\dot{\phi}\sin(\phi)\sin(\theta)\cos(\theta)+\dot{\theta}\cos(\phi)]+I_1\frac{\mathrm{d}}{\mathrm{d}t}[\sin(\theta)\sin(\phi)(\dot{\phi}\cos(\theta)+\dot{\psi})]\ , \end{aligned}$$

$$\begin{aligned} M_2 &= -l\sin(\theta)\sin(\phi)F_3+l\cos(\theta)F_1 \\ &= I_0\frac{\mathrm{d}}{\mathrm{d}t}[\dot{\phi}\cos(\phi)\sin(\theta)\cos(\theta)+\dot{\theta}\sin(\phi)]-I_1\frac{\mathrm{d}}{\mathrm{d}t}[\sin(\theta)\cos(\phi)(\dot{\phi}\cos(\theta)+\dot{\psi})]\ , \\ M_3 &= l\sin(\theta)\sin(\phi)F_2+l\sin(\theta)\cos(\phi)F_1 \\ &= I_0\frac{\mathrm{d}}{\mathrm{d}t}(\dot{\phi}\sin^2(\theta))+I_1\frac{\mathrm{d}}{\mathrm{d}t}[\cos(\theta)(\dot{\psi}+\dot{\phi}\cos(\theta))]\ , \end{aligned} \tag{4.29}$$

where l is the length of the gyroscope (see Figure 4.1(a)), and F_j, $1 \leq j \leq 3$, are the forces embedding the inertia of the mass and elastic restoring forces of the links (see below).

The position vector of the mass m can be written using the vector representing the position of the tip of the gyroscope $\boldsymbol{l}(t)$. This is defined as

$$\boldsymbol{l}(t) = l\,\mathbf{e}_3' \ ,$$

in the moving coordinate system. Using the transformation linking the basis of the moving frame $\mathcal{F}'$ and the global basis in $\mathcal{F}$ in 4.3 we can write this vector as

$$\boldsymbol{l}(t) = l\sin(\theta(t))\sin(\phi(t))\mathbf{e}_1 - l\sin(\theta(t))\cos(\phi(t))\mathbf{e}_2 + l\cos(\theta(t))\mathbf{e}_3 \ . \tag{4.30}$$

The mass displacement is

$$\mathbf{u}(t) = \boldsymbol{l}(t) - \boldsymbol{l}(0) \tag{4.31}$$

and it is assumed that $\boldsymbol{l}(0) = l\mathbf{e}_3$ at the initial time $t = 0$.

At the tip of the gyroscope acts the force

$$\mathbf{F} = -c\,\mathbf{h}[\mathbf{u}(t)] - m\ddot{\mathbf{u}}(t) \ , \tag{4.32}$$

which embeds the inertia term brought by the mass m and the elastic reaction of the extensional springs of stiffness c, described by the non-linear vectorial function $\mathbf{h}$. Using the basis vectors

$$\mathbf{a}^{(i)} = \cos\left((i-1)\frac{2\pi}{3}\right)\mathbf{e}_1 + \sin\left((i-1)\frac{2\pi}{3}\right)\mathbf{e}_2, \qquad i = 1,2,3 \ , \tag{4.33}$$

shown in Figure 4.1(b), the function $\mathbf{h}$ can be computed as

$$\mathbf{h} = \sum_{i=1}^{3}\left[(|\mathbf{u}(t) - L\mathbf{a}^{(i)}| - L)\frac{\mathbf{u}(t) - L\mathbf{a}^{(i)}}{|\mathbf{u}(t) - L\mathbf{a}^{(i)}|} + (|\mathbf{u}(t) + L\mathbf{a}^{(i)}| - L)\frac{\mathbf{u}(t) + L\mathbf{a}^{(i)}}{|\mathbf{u}(t) + L\mathbf{a}^{(i)}|}\right] \ , \tag{4.34}$$

where L is the initial length of the extensional springs (see Figure 4.1(b)). Here the unit vectors

$$\frac{\mathbf{u}(t) \pm L\mathbf{a}^{(i)}}{|\mathbf{u}(t) \pm L\mathbf{a}^{(i)}|} ,$$

represent the directional cosines that allow one to find the projection of the restoring forces provided by the elastic springs on to the $Ox_1x_2x_3$ axes.

The corresponding external moment produced by the truss system that acts on the gyroscope is

$$\mathbf{M}_{\rm e} = \boldsymbol{l} \times \mathbf{F} . \tag{4.35}$$

The vector product can be calculated using the determinant:

$$\mathbf{M}_{\rm e} = \begin{vmatrix} \mathbf{e}_1 & \mathbf{e}_2 & \mathbf{e}_3 \\ l\sin(\theta)\sin(\phi) & -l\sin(\theta)\cos(\phi) & l\cos(\theta) \\ F_1 & F_2 & F_3 \end{vmatrix} .$$

Thus, the external moments provided to the gyroscope by the truss system are:

$$\begin{aligned} \mathbf{M}_{\rm e} \;=\; & [-l\sin(\theta)\cos(\phi)F_3 - l\cos(\theta)F_2]\mathbf{e}_1 \\ & -[l\sin(\theta)\sin(\phi)F_3 - l\cos(\theta)F_1]\mathbf{e}_2 \\ & +[l\sin(\theta)\sin(\phi)F_2 + l\sin(\theta)\cos(\phi)F_1]\mathbf{e}_3 . \end{aligned} \tag{4.36}$$

Combining (4.4) with (4.36), the angular momentum balance in the fixed frame $\mathcal{F}$ then gives (4.29).

4.1.4 Normalisation

Next, we introduce the following normalisations:

$$\tilde{\boldsymbol{l}} = \frac{\boldsymbol{l}}{l} , \quad \tilde{t} = \sqrt{\frac{c}{m\gamma}}t , \quad \gamma = 1 + \frac{I_0}{ml^2} , \quad \delta = \frac{l}{L} , \quad \tilde{\mathbf{u}}(\tilde{t}) = \frac{\mathbf{u}(t)}{L} ,$$

$$\tilde{\mathbf{h}}[\tilde{\mathbf{u}}] = \frac{\mathbf{h}[\mathbf{u}]}{L} , \quad \tilde{\mathbf{F}} = \frac{\mathbf{F}}{cL} , \quad \tilde{\mathbf{M}}_{\rm e} = \frac{\mathbf{M}_{\rm e}}{cLl} , \quad \tilde{I}_j = \frac{I_j}{mlL} \quad (j = 0, 1) , \tag{4.37}$$

where the quantities with the symbol " ˜ " are dimensionless. In going forward, we will use the same notation for the Euler angles that depend on the normalised time $\tilde{t}$. Proceeding with the normalisation and considering that

$$\frac{\mathrm{d}}{\mathrm{d}t} = \frac{\mathrm{d}\tilde{t}}{\mathrm{d}t}\frac{\mathrm{d}}{\mathrm{d}\tilde{t}} = \sqrt{\frac{c}{m\gamma}}\frac{\mathrm{d}}{\mathrm{d}\tilde{t}} \,, \tag{4.38}$$

it is possible to write (4.29) as

$$\begin{aligned}
\tilde{M}_1 &= -\cos(\theta)\tilde{F}_2 - \cos(\phi)\sin(\theta)\tilde{F}_3 \\
&= \gamma^{-1}\tilde{I}_0\frac{\mathrm{d}}{\mathrm{d}\tilde{t}}[-\dot{\phi}\sin(\phi)\sin(\theta)\cos(\theta) + \dot{\theta}\cos(\phi)] + \gamma^{-1}\tilde{I}_1\frac{\mathrm{d}}{\mathrm{d}\tilde{t}}[\sin(\theta)\sin(\phi)(\dot{\phi}\cos(\theta) + \dot{\psi})] \,,
\end{aligned}$$

$$\begin{aligned}
\tilde{M}_2 &= \cos(\theta)\tilde{F}_1 - \sin(\phi)\sin(\theta)\tilde{F}_3 \\
&= \gamma^{-1}\tilde{I}_0\frac{\mathrm{d}}{\mathrm{d}\tilde{t}}[\dot{\phi}\cos(\phi)\sin(\theta)\cos(\theta) + \dot{\theta}\sin(\phi)] - \gamma^{-1}\tilde{I}_1\frac{\mathrm{d}}{\mathrm{d}\tilde{t}}[\sin(\theta)\cos(\phi)(\dot{\phi}\cos(\theta) + \dot{\psi})] \,, \\
\tilde{M}_3 &= \sin(\theta)\Big[\cos(\phi)\tilde{F}_1 + \sin(\phi)\tilde{F}_2\Big] \\
&= \gamma^{-1}\tilde{I}_0\frac{\mathrm{d}}{\mathrm{d}\tilde{t}}[\dot{\phi}\sin^2(\theta)] + \gamma^{-1}\tilde{I}_1\frac{\mathrm{d}}{\mathrm{d}\tilde{t}}[\cos(\theta)(\dot{\phi}\,\cos(\theta) + \dot{\psi})] \,.
\end{aligned}$$

In the following, we omit the symbol " ˜ " for ease of notation. Thus the angular momentum balance in normalised form is

$$\begin{aligned}
M_1 &= -\cos(\theta)F_2 - \cos(\phi)\sin(\theta)F_3 \\
&= \frac{I_0}{\gamma}\frac{\mathrm{d}}{\mathrm{d}t}[-\dot{\phi}\sin(\phi)\sin(\theta)\cos(\theta) + \dot{\theta}\cos(\phi)] \\
&\qquad + \frac{I_1}{\gamma}\frac{\mathrm{d}}{\mathrm{d}t}[\sin(\theta)\sin(\phi)(\dot{\phi}\cos(\theta) + \dot{\psi})] \,,
\end{aligned}$$

$$\begin{aligned}
M_2 &= \cos(\theta)F_1 - \sin(\phi)\sin(\theta)F_3 \\
&= \frac{I_0}{\gamma}\frac{\mathrm{d}}{\mathrm{d}t}[\dot{\phi}\cos(\phi)\sin(\theta)\cos(\theta) + \dot{\theta}\sin(\phi)] \\
&\qquad - \frac{I_1}{\gamma}\frac{\mathrm{d}}{\mathrm{d}t}[\sin(\theta)\cos(\phi)(\dot{\phi}\cos(\theta) + \dot{\psi})]
\end{aligned} \tag{4.39}$$

and

$$\begin{aligned} M_3 &= \sin(\theta)[\cos(\phi)F_1 + \sin(\phi)F_2] \\ &= \frac{I_0}{\gamma}\frac{\mathrm{d}}{\mathrm{d}t}[\dot{\phi}\sin^2(\theta)] + \frac{I_1}{\gamma}\frac{\mathrm{d}}{\mathrm{d}t}[\cos(\theta)(\dot{\psi} + \dot{\phi}\,\cos(\theta))] \,. \end{aligned} \tag{4.40}$$

Furthermore, (4.32) is updated with the normalisations (4.37) and (4.38) to

$$\mathbf{F} = -\mathbf{h}[\mathbf{u}(t)] - \gamma^{-1}\ddot{\mathbf{u}}(t) \,, \tag{4.41}$$

where quantities appearing in the above equation are dimensionless.

4.1.5 The linearised problem

We now assume that the nutation angle and its time derivatives satisfy

$$\left|\frac{\mathrm{d}^j\theta(t)}{\mathrm{d}t^j}\right| \leq \text{Const}\ \varepsilon \,, \qquad j = 0, 1, 2 \,,$$

where ε is a small dimensionless quantity such that $0 < \varepsilon \ll 1$. In addition, in what follows we assume all other quantities are $O(1)$ relative to ε.

Linearising (4.40) with respect to the nutation angle yields

$$\gamma\theta(F_2\sin(\phi) + F_1\cos(\phi)) + O(\varepsilon^3) = I_1(\ddot{\psi} + \ddot{\phi}) + O(\varepsilon^2) \,. \tag{4.42}$$

It also follows from (4.30) and (4.31) that $u_3 = O(\varepsilon^2)$.

Next we note that due to (4.31), $\mathbf{u} = O(\varepsilon)$ and we can use the Taylor expansion computed for $\mathbf{u} = \mathbf{0}$ to write

$$\begin{aligned} |\mathbf{u}(t) \pm \mathbf{a}^{(i)}| &= |\mathbf{a}^{(i)}| + \mathbf{u}(t)\cdot\nabla_{\mathbf{u}}(|\mathbf{u}(t) \pm \mathbf{a}^{(i)}|)\Big|_{\mathbf{u}=\mathbf{0}} + O(\varepsilon^2) \\ &= 1 \pm \mathbf{a}^{(i)}\cdot\mathbf{u}(t) + O(\varepsilon^2) \,, \end{aligned} \tag{4.43}$$

where we have considered the fact that:

$$\begin{aligned}\nabla_{\mathbf{u}}(|\mathbf{u}(t)\pm\mathbf{a}^{(i)}|) &= \left(\frac{\partial}{\partial u_1}|\mathbf{u}(t)\pm\mathbf{a}^{(i)}|,\frac{\partial}{\partial u_2}|\mathbf{u}(t)\pm\mathbf{a}^{(i)}|,\frac{\partial}{\partial u_3}|\mathbf{u}(t)\pm\mathbf{a}^{(i)}|\right)^{\mathrm{T}}\\ &= \frac{\mathbf{u}(t)\pm\mathbf{a}^{(i)}}{|\mathbf{u}(t)\pm\mathbf{a}^{(i)}|}\ .\end{aligned} \tag{4.44}$$

Using (4.43), the function $\mathbf{h}[\mathbf{u}(t)]$ in (4.34) can be linearised so that

$$\begin{aligned}\mathbf{h}[\mathbf{u}(t)] &= \sum_{i=1}^{3}\left[(|\mathbf{u}(t)-\mathbf{a}^{(i)}|-1)\frac{\mathbf{u}(t)-\mathbf{a}^{(i)}}{|\mathbf{u}(t)-\mathbf{a}^{(i)}|}+(|\mathbf{u}(t)+\mathbf{a}^{(i)}|-1)\frac{\mathbf{u}(t)+\mathbf{a}^{(i)}}{|\mathbf{u}(t)+\mathbf{a}^{(i)}|}\right]\\ &= 2\sum_{i=1}^{3}\mathbf{a}^{(i)}(\mathbf{a}^{(i)}\cdot\mathbf{u}(t))+O(\varepsilon^2)\ ,\end{aligned}$$

and then (4.41) becomes

$$\mathbf{F}=-\mathbf{K}\mathbf{u}(t)-\gamma^{-1}\ddot{\mathbf{u}}(t)+O(\varepsilon^2)\ , \tag{4.45}$$

where $\mathbf{K}$ is the stiffness matrix characterising the action of the springs. We note in (4.45) that $F_3=O(\varepsilon^2)$. As a result, in going forward we neglect the $\mathbf{e}_3$ component of the motion for the mass and set $\mathbf{F}=(F_1,F_2)^{\mathrm{T}}$ and $\mathbf{u}=(u_1,u_2)^{\mathrm{T}}$. Moreover, the stiffness matrix $\mathbf{K}$ in (4.45) takes the form

$$\mathbf{K}=2\sum_{j=1}^{3}\mathbf{a}^{(j)}\otimes\mathbf{a}^{(j)}=3\mathbf{I}_2\ , \tag{4.46}$$

where $\mathbf{I}_2$ is the 2×2 identity matrix.

We now derive the form of the in-plane forces acting on the mass. Due to the smallness of F_3 its contribution to M_1 and M_2 in eqs. (4.39) can be neglected. Accordingly, after introducing the normalised forms of the displacements u_1 and u_2, we rewrite eqs. (4.39) as

$$\begin{aligned}F_1 &= \frac{1}{\gamma\cos(\theta)}\Big[I_0\frac{\mathrm{d}}{\mathrm{d}t}\Big(\frac{\dot{u}_1}{\delta}\cos(\theta)+\dot{\theta}\sin^2(\theta)\sin(\phi)\Big)\\ &\qquad +\frac{I_1}{\delta}\frac{\mathrm{d}}{\mathrm{d}t}((\dot{\phi}\cos(\theta)+\dot{\psi})u_2)\Big]+O(\varepsilon^3)\ ,\end{aligned}$$

$$F_2 = \frac{1}{\gamma\cos(\theta)}\Big[I_0\frac{\mathrm{d}}{\mathrm{d}t}\Big(\frac{\dot{u}_2}{\delta}\cos(\theta) - \dot{\theta}\sin^2(\theta)\cos(\phi)\Big) - \frac{I_1}{\delta}\frac{\mathrm{d}}{\mathrm{d}t}((\dot{\phi}\cos(\theta)+\dot{\psi})u_1)\Big] + O(\varepsilon^3)\ . \tag{4.47}$$

Carrying out the linearisation with respect to the nutation angle once more shows that

$$\begin{aligned} F_1 &= \frac{I_0}{\gamma\delta}\ddot{u}_1 + \frac{I_1}{\gamma\delta}[(\ddot{\psi}+\ddot{\phi})u_2 + (\dot{\psi}+\dot{\phi})\dot{u}_2] + O(\varepsilon^3)\ , \\ F_2 &= \frac{I_0}{\gamma\delta}\ddot{u}_2 - \frac{I_1}{\gamma\delta}[(\ddot{\psi}+\ddot{\phi})u_1 + (\dot{\psi}+\dot{\phi})\dot{u}_1] + O(\varepsilon^3)\ . \end{aligned} \tag{4.48}$$

The last two equalities lead to

$$F_j = O(\varepsilon)\ , \tag{4.49}$$

for $j = 1, 2$ (see (4.31)). Returning to (4.42), we have

$$0 = I_1(\ddot{\psi}+\ddot{\phi}) + O(\varepsilon^2)\ , \tag{4.50}$$

which implies that, to leading order, the sum of the precession and spin rates is independent of time. Therefore, we define

$$\Omega = \dot{\psi}(0) + \dot{\phi}(0) = \dot{\psi}(t) + \dot{\phi}(t)\ . \tag{4.51}$$

From here on, Ω is referred to as the *gyricity* of the gyroscopic spinner. Here the gyricity is given in normalised form; the normalisation factor is $\sqrt{m\gamma/c}$, and the dimension is radians per unit time. We note that although the gyricity is constant throughout the motion of the spinner, the spin and precession rates can change with time and in general are not constant. This fact is further illustrated in Section 4.2.

Finally, by combining (4.48) with (4.46) and (4.45), to leading order one obtains the governing equation (4.1).

4.2 Numerical validation of model for gyroscopic oscillator

In the small nutation regime, the motion is governed by (4.1), where the skew-symmetric matrix $\mathbf{R}$ describes the chiral effect induced by the gyroscopic spinner.

One can construct the solution of (4.1) through a modal analysis by studying the existence of solutions in the form

$$\mathbf{u}(t) = \mathbf{A}e^{\mathrm{i}\omega t} \,, \tag{4.52}$$

where the constant amplitude vector $\mathbf{A}$ and the radian frequency ω should be determined. Substituting the first and second time derivatives of (4.52):

$$\begin{aligned} \dot{\mathbf{u}}(t) &= \mathrm{i}\omega\mathbf{A}e^{\mathrm{i}\omega t} \,, \\ \ddot{\mathbf{u}}(t) &= -\omega^2\mathbf{A}e^{\mathrm{i}\omega t} \,, \end{aligned}$$

in (4.1) yields

$$-\omega^2\mathbf{A}e^{\mathrm{i}\omega t} + \mathrm{i}\omega\alpha\Omega\mathbf{R}\mathbf{A}e^{\mathrm{i}\omega t} + 3\mathbf{A}e^{\mathrm{i}\omega t} = \mathbf{0} \,.$$

Following further simplifications, we obtain the homogeneous system

$$((3-\omega^2)\mathbf{I} + \mathrm{i}\omega\alpha\Omega\mathbf{R})\mathbf{A} = \mathbf{0} \,,$$

where $\mathbf{I}$ is the 2×2 identity matrix, or in the expanded form we have

$$\begin{pmatrix} -\omega^2+3 & \mathrm{i}\alpha\Omega\omega \\ -\mathrm{i}\alpha\Omega\omega & -\omega^2+3 \end{pmatrix} \mathbf{A} = \mathbf{0} \,. \tag{4.53}$$

Non-trivial solutions $\mathbf{A}$ of this system are obtained by analysing when the determinant

of the preceding Hermitian matrix vanishes:

$$(3-\omega^2)^2-(\alpha\Omega\omega)^2=0\ . \tag{4.54}$$

The positive solutions of the equation above are

$$\omega_\pm=\frac{1}{2}\left[\pm\alpha\Omega+\sqrt{(\alpha\Omega)^2+12}\right]\ . \tag{4.55}$$

The non-trivial vector $\mathbf{A}$ is written in the form

$$\mathbf{A}(\omega)=\begin{pmatrix}1\\ \mathrm{i}\dfrac{3-\omega^2}{\alpha\Omega\omega}\end{pmatrix}\ . \tag{4.56}$$

Next, some numerical illustrations are considered that illustrate the behaviour of the solution obtained for the system. The frequencies (4.55) are plotted as functions of the gyricity Ω in Figure 4.4, where it can be seen that one frequency is monotonically increasing while the other is monotonically decreasing. When the gyricity is zero, there is a double eigenfrequency for the system; in this case, the body does neither spin nor precess during its motion. In addition, in Figure 4.4 the vertical dashed line for the gyricity $\Omega=6$ is shown, where the two eigenfrequencies are: $\omega_+=2.6375$ and $\omega_-=1.1375$. These values will be used in the numerical results presented below.

In general, the motion of the system can be written as a linear combination of modes of the form (4.52), so that the solution $\mathbf{u}$ of (4.1) is

$$\mathbf{u}(t)=c_1\mathbf{A}(\omega_+)e^{\mathrm{i}\omega_+t}+c_2\overline{\mathbf{A}(\omega_+)}e^{-\mathrm{i}\omega_+t}+c_3\mathbf{A}(\omega_-)e^{\mathrm{i}\omega_-t}+c_4\overline{\mathbf{A}(\omega_-)}e^{-\mathrm{i}\omega_-t}\ , \tag{4.57}$$

where the constant coefficients c_1, c_2, c_3 and c_4 are determined from the initial conditions for the system.

The mode corresponding to the eigenfrequency $\omega_+=2.6375$, obtained for $\Omega=6$, is shown in Figure 4.5 (assuming $L=l=1\mathrm{m}$ and hence $\delta=l/L=1$). In this case, the mass moves anticlockwise along a circular trajectory with normalised

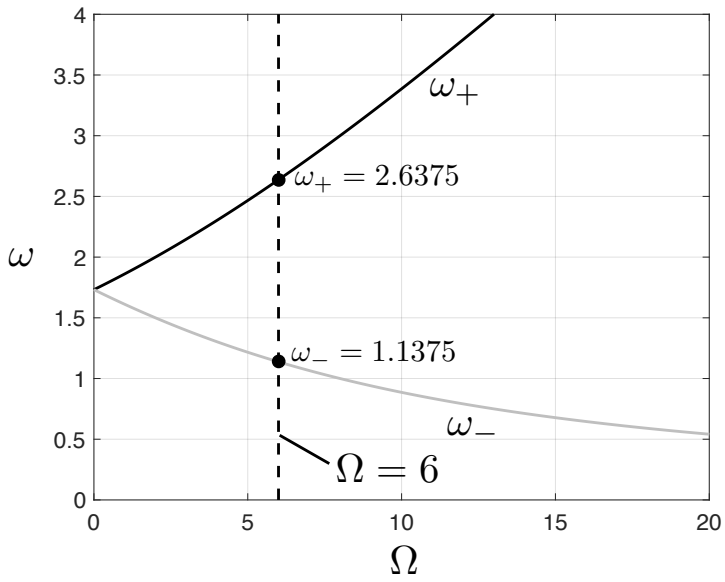

Figure 4.4: Eigenfrequencies of the gyroscopic oscillator in Figure 4.1 as a function of the gyricity Ω. Computations are based on (4.55), with the parameter $\alpha = 0.25$. The dashed line indicates the case $\Omega = 6$, considered in Figures 4.5 and 4.6. The values of $\omega_\pm$ in (4.55) when $\Omega = 6$ are also shown.

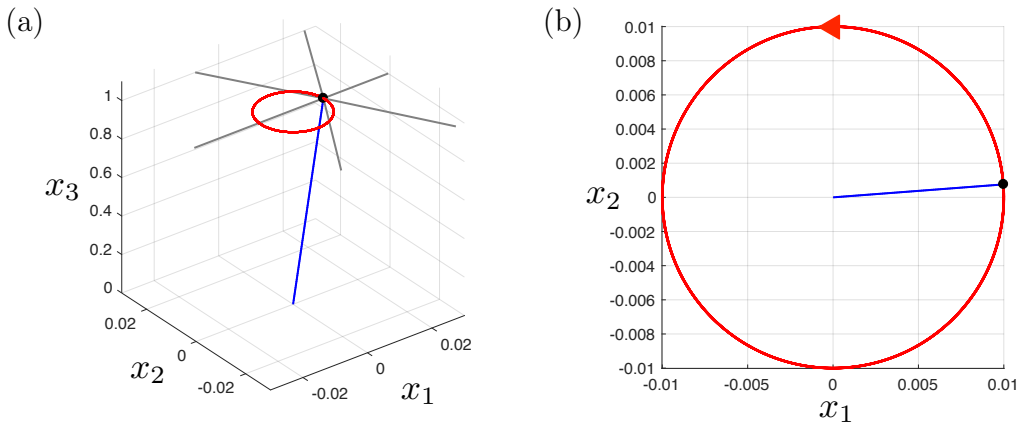

Figure 4.5: Eigenmode of the gyroscopic oscillator shown in Figure 4.1. The result corresponds to gyricity $\Omega = 6$, $\alpha = 0.25$ and initial conditions (4.58)–(4.60). (a) The linearised motion of the mass m in the time interval $0 \leq t \leq 2.42$ is given in red. Note the different scales used for the plane (x_1, x_2) and the axis x_3. (b) Planar view of the trajectory traced by the mass m, where the direction of the motion of the mass is indicated with the arrow.

displacement magnitude 0.01. The time period to complete this loop of this trajectory is $2\pi/\omega_+ = 2.3823$. This eigenmode of the system corresponds to the frequency ω_+ and the choice of the initial conditions:

$$\mathbf{u}(0) = \begin{pmatrix} 0.01 \\ 0 \end{pmatrix} , \quad \dot{\mathbf{u}}(0) = \begin{pmatrix} 0 \\ 0.0264 \end{pmatrix} . \tag{4.58}$$

These conditions are associated with the following initial conditions for the precession and nutation of the gyroscope:

$$\phi(0) = \pi/2 , \quad \dot{\phi}(0) = 2.6375 , \quad \theta(0) = 0.01 , \quad \dot{\theta}(0) = 0 , \tag{4.59}$$

obtained by solving the system composed of equations. In addition, we specify the initial condition on the spin

$$\psi(0) = 0 , \quad \dot{\psi}(0) = \Omega - \dot{\phi}(0) = 3.3625 , \tag{4.60}$$

where use of the selected value of gyricity and the initial data for the precession rate enforces the last condition (4.59) on the spin rate. In this example, the initial conditions of the Euler angles can be found from matching (4.58) to the displacement components given by

$$u_1(t) = \sin(\theta(t)) \sin(\phi(t)) , \qquad u_2(t) = -\sin(\theta(t)) \cos(\phi(t)) ,$$

and their associated velocities:

$$\dot{u}_1(t) = \dot{\theta}(t) \cos\theta(t) \sin\phi(t) + \dot{\phi}(t) \cos\phi(t) \sin\theta(t) ,$$

$$\dot{u}_2(t) = -\dot{\theta}(t) \cos\theta(t) \cos\phi(t) + \dot{\phi}(t) \sin\phi(t) \sin\theta(t) ,$$

at $t = 0$.

For the mode corresponding to $\omega_- = 1.1375$, the mass m moves clockwise on a

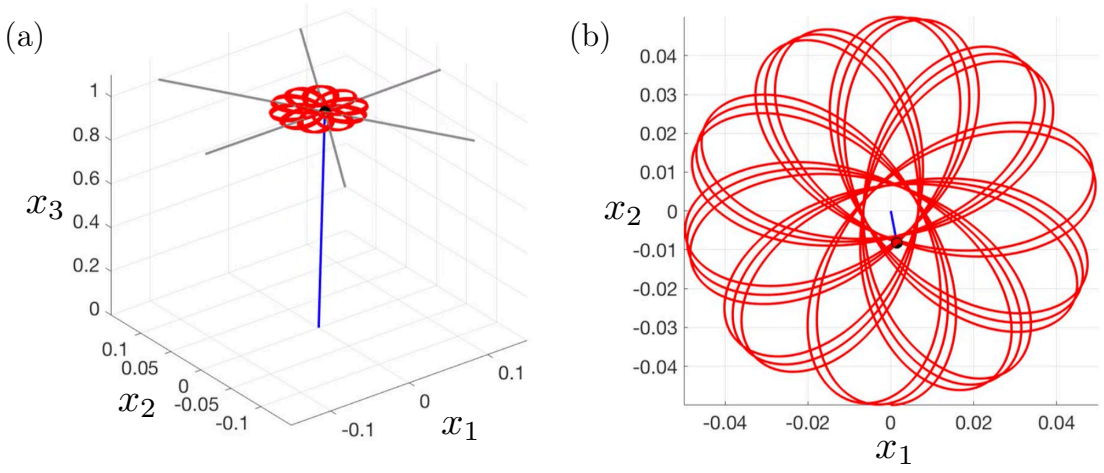

Figure 4.6: Eigenmode of the gyroscopic oscillator shown in Figure 4.1. The result corresponds to the same parameters of Figure 4.5, but initial conditions (4.61)–(4.63). (a) The linearised motion of the mass m in the time interval $0 \leq t \leq 47.5$ is given in red. (b) Planar view of the trajectory traced by the mass m.

circular trajectory, with a normalised period $2\pi/\omega_- = 5.5239$. It is noted that in association with the eigenmodes the precession and spin rates of the spinner are constant and these quantities sum to give the prescribed value of the gyricity, in this case $\Omega = 6$.

As an illustration showing a more general motion of the system that combines the modes corresponding to both frequencies $\omega_\pm$, the initial conditions are set as

$$\mathbf{u}(0) = \begin{pmatrix} 0 \\ -0.05 \end{pmatrix} , \quad \dot{\mathbf{u}}(0) = \begin{pmatrix} 0.05 \\ 0 \end{pmatrix} . \tag{4.61}$$

These can be linked to the following initial conditions for the generalised coordinates of the gyroscope:

$$\phi(0) = 0 , \quad \dot{\phi}(0) = 1 , \quad \theta(0) = 0.05 , \quad \dot{\theta}(0) = 0 , \tag{4.62}$$

and

$$\psi(0) = 0 , \quad \dot{\psi}(0) = \Omega - \dot{\phi}(0) = 5 . \tag{4.63}$$

As shown in Figure 4.6, the trajectory traced by the mass is non-circular and is

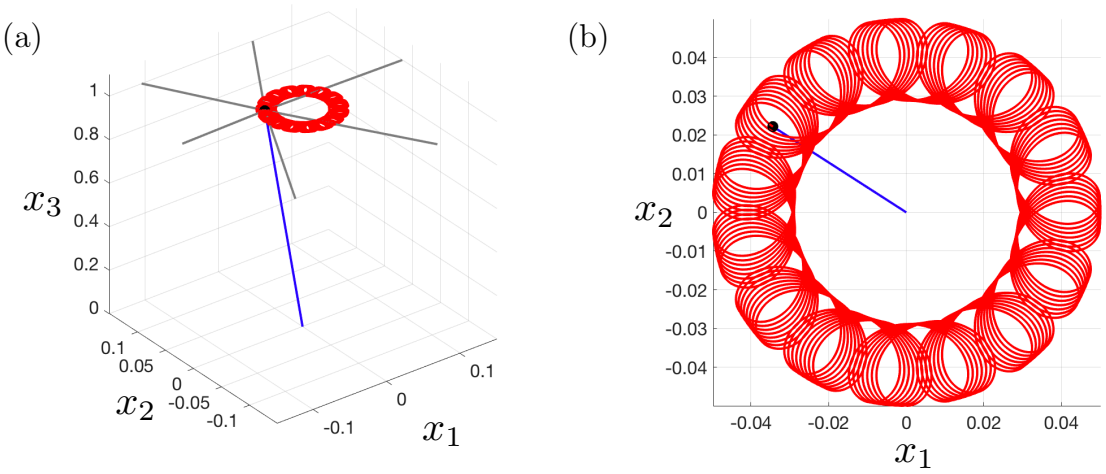

Figure 4.7: Eigenmode of a single gyroscopic spinner. The gyroscopic spinner is hinged at its base and connected to a mass m at its tip. The mass is also constrained by a system of six extensional springs. The spinner is represented by the blue line and the mass m by the black dot. The six grey lines indicate the springs attached to the mass. (a) Representation of the system with the trajectory of the mass shown in red. (b) Planar view of the system showing a magnification of the path traced by the mass.

contained inside an annulus with the origin as its centre and its inner and outer radii approximately equal to 0.007 and 0.05, respectively. This motion results from the combination of both eigenmodes of the system in accordance with (4.57). For the behaviour of the system shown in Figure 4.6, we note the precession rate of the spinner is not constant and hence its spin rate is also dependent on time. However, as shown in Section 4.1.5 the sum of these quantities is constant (and $\Omega = 6$).

The behaviour of the system can allow for a variety of trajectories for the mass. As an additional example of this, we refer to Figure 4.7, which was computed for the parameters and initial conditions as in the example of Figure 4.6, except that $\alpha = 1$.

4.2.1 Finite element simulation

Here, we compare the analytical results based on (4.1) with the numerical outcomes obtained from a finite element simulation developed in *Comsol Multiphysics 5.3*.

A non-linear transient analysis has been performed based on the numerical model shown in Figure 4.8. The gyroscope is implemented as a solid rigid body and the mass m as a cylindrical rigid element of small size and six truss elements represent

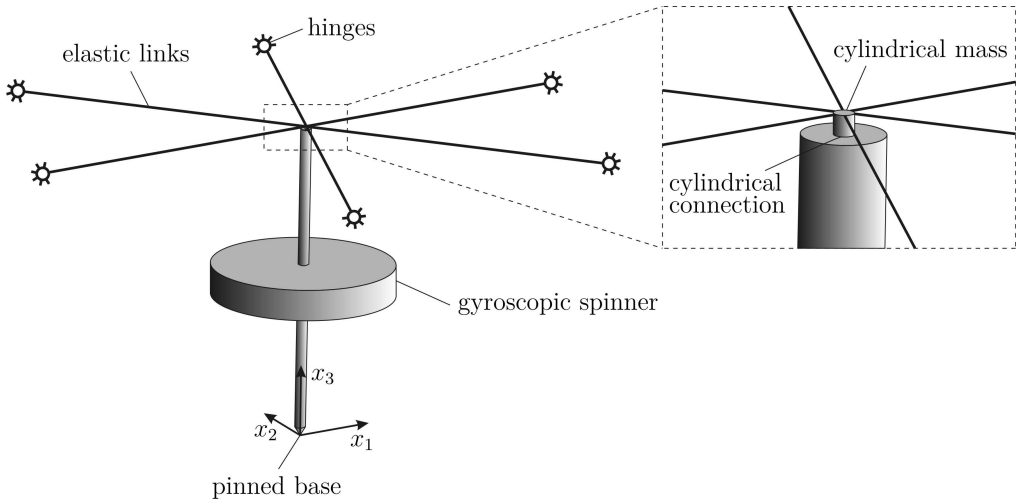

Figure 4.8: The geometry of the model implemented in *Comsol*, consisting of a gyroscopic spinner (represented by a rigid solid) that is pinned at the base and whose tip is connected to a mass m (represented by a small cylinder), that is also connected to an array of 6 extensional springs (shown as lines). The gyroscope has moments of inertia 63.7 kg m^2 about the $x_{1,2}$-axes and 10.0 kg m^2 about the x_3-axis, respectively; the length $l = 1$ m. The initial spin and precession rates are $\dot{\psi} = \dot{\phi} = 250$ rad/s. The mass at the tip of the gyroscope is $m = 100$ kg. Each rod has longitudinal stiffness $c = 1000$ N m^{-1} and length $L = 1$ m.

the extensional springs. The values of the material and geometrical parameters are given in the caption of Figure 4.8. The normalised values are the following: $I_0 = 0.637$, $I_1 = 0.1$, $\gamma = 1.637$ and $\alpha = 0.061$.

The following initial conditions have been imposed:

$$\phi(0) = \theta(0) = \psi(0) = 0 \ , \quad \dot{\theta}(0) = 0.040 \ , \quad \dot{\phi}(0) = \dot{\psi}(0) = 101.15, \tag{4.64}$$

which correspond to the gyricity $\Omega = 202.30$ and

$$\mathbf{u}(0) = \begin{pmatrix} 0 \\ \\ 0 \end{pmatrix} \ , \quad \dot{\mathbf{u}}(0) = \begin{pmatrix} 0 \\ \\ -0.040 \end{pmatrix} \ . \tag{4.65}$$

The results of the transient simulation are shown in Figure 4.9 together with the analytical ones (based on (4.1) and (4.57)). It is evident that the numerical results obtained from a non-linear transient simulation in *Comsol* are in excellent agreement with the analytical predictions. The results confirm the correctness of the analytical approach and the validity of the proposed linearisation.

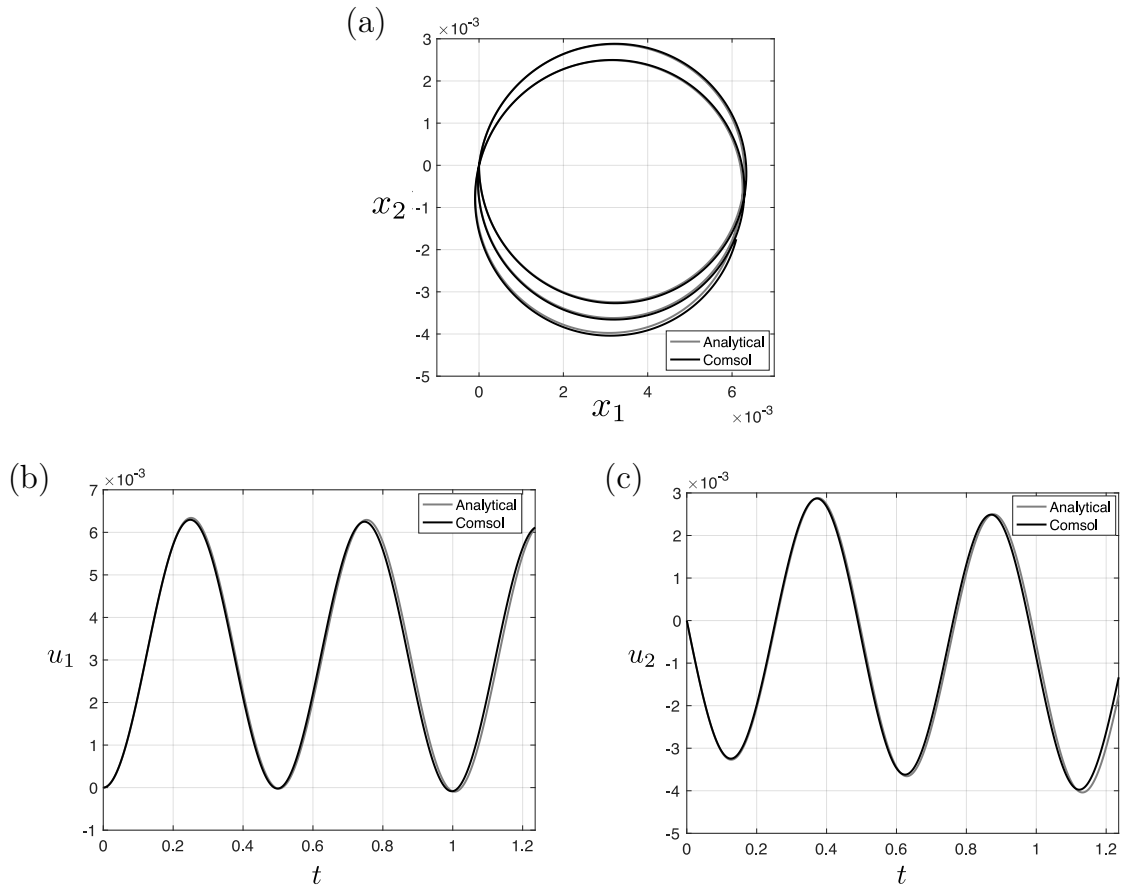

Figure 4.9: (a) The trajectory traced by the mass in the system shown in Figure 4.8, resulting from a transient analysis in *Comsol*. Displacement (b) u_1 and (c) u_2 of the mass m as a function of time.

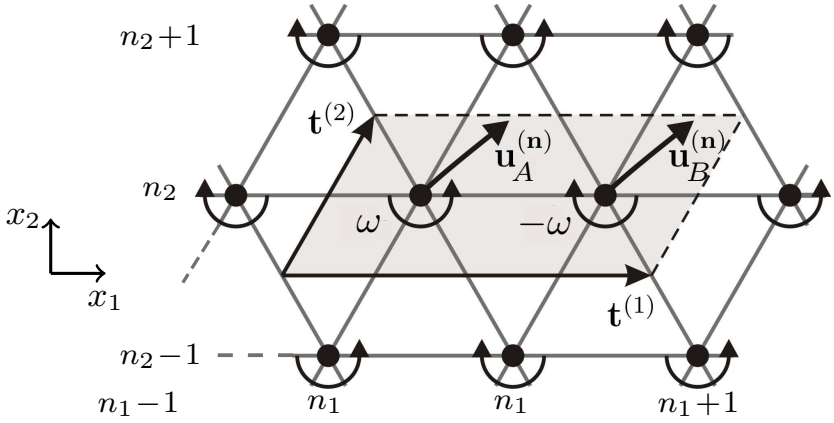

Figure 4.10: Infinite triangular elastic lattice attached to an array of gyroscopic spinners. Masses m at the nodal points are connected by extensional springs of stiffness c and length L. The unit cell of the periodic system is indicated in grey and it is defined by the vectors $\mathbf{t}^{(1)} = (2, 0)^{\mathrm{T}}$ and $\mathbf{t}^{(2)} = (1/2, \sqrt{3}/2)^{\mathrm{T}}$. Nodal points are identified by the multi-index $\mathbf{n} = (n_1, n_2)$. The gyricity Ω has magnitude ω and alternates in sign switching from A to B.

Once again, the motion shown in Figure 4.9 demonstrates the coupling effect induced by the spin and precession rates of the gyroscope. Despite of the fact that the initial conditions (4.65) excite the motion only in direction x_2, both displacement components u_1 and u_2 vary sinusoidally with similar amplitude.

4.3 Transient analysis of gyro-elastic lattices

In this Section, we extend the theoretical results of Section 4.1 to model the interaction of masses, placed at the junctions of various lattice systems that are connected to inhomogeneous arrays of gyroscopes in the transient regime. Inhomogeneity will be associated to a non-constant distribution of the parameter α or the gyricity constant Ω. In addition, for some of the examples considered below, the gyricity constant in the gyro-elastic lattice will be chosen as:

$$|\Omega| = \omega \ , \tag{4.66}$$

where ω is the radian frequency of vibrations of the lattice particles (see [Brun, Jones and Movchan (2012), Carta et al. (2014), Carta et al. (2017a), Garau et al. (2018)] and Chapter 3 where such cases are analysed in the time-harmonic regime). On

the other hand, for some of the problems considered, we provide examples where the gyricity will be taken as a parameter independent of the radian frequency of the lattice. In those cases, we will also find that the desired dynamic effects can be retrieved.

The steady-state analyses presented in [Carta et al. (2017a)], [Garau et al. (2018)] and Chapter 3 have shown that the gyro-elastic lattice may lead to special waveforms due to the dynamic chirality conferred by the spinners to the lattice. Here, several possibilities are investigated that show these special waveforms appear in the transient regime. In addition, the transient analysis may bring new interesting dynamic features, that cannot be revealed through a steady-state analysis. Moreover, in some cases the response of the gyro-elastic systems will be studied for different initial conditions or when subjected to fully transient loads.

4.3.1 Highly localised waveforms

We consider a periodic triangular lattice as shown in Figure 4.10, composed of masses m periodically constrained by elastic links having stiffness c and length L. Each mass is attached to a gyroscopic spinner that spins about its axis parallel to $0x_3$; the spinners have normalised parameters α_A or α_B, and alternating gyricities equal to ω or $-\omega$, where ω is the radian frequency of the lattice, as shown in Figure 4.10. The unit cell of the periodic system contains two nodal points, and the normalised lattice basis vectors are $\mathbf{t}^{(1)} = (2,0)^{\mathrm{T}}$ and $\mathbf{t}^{(2)} = (1/2, \sqrt{3}/2)^{\mathrm{T}}$. Each unit cell is identified by the multi-index $\mathbf{n} = (n_1, n_2)^{\mathrm{T}}$ and the displacements of the two nodes within each cell are indicated with $\mathbf{u}_A^{(\mathbf{n})}$ and $\mathbf{u}_B^{(\mathbf{n})}$.

Following the theoretical model developed in Section 4.1 and assuming nearest neighbour interactions only, the linearised governing equations of the lattice are

$$\begin{aligned}
\ddot{\mathbf{u}}_A^{(n_1,n_2)} \;=\; & \Big[\mathbf{a}^{(1)}\cdot\Big(\mathbf{u}_B^{(n_1,n_2)} + \mathbf{u}_B^{(n_1-1,n_2)} - 2\mathbf{u}_A^{(n_1,n_2)}\Big)\,\mathbf{a}^{(1)} \\
& +\; \mathbf{a}^{(2)}\cdot\Big(\mathbf{u}_B^{(n_1-1,n_2+1)} + \mathbf{u}_B^{(n_1,n_2-1)} - 2\mathbf{u}_A^{(n_1,n_2)}\Big)\,\mathbf{a}^{(2)} \\
& +\; \mathbf{a}^{(3)}\cdot\Big(\mathbf{u}_A^{(n_1,n_2+1)} + \mathbf{u}_A^{(n_1,n_2-1)} - 2\mathbf{u}_A^{(n_1,n_2)}\Big)\,\mathbf{a}^{(3)}\Big] \\
& -\; \alpha_A\omega\mathbf{R}\dot{\mathbf{u}}_A^{(n_1,n_2)}\,,
\end{aligned} \tag{4.67}$$

$$\begin{aligned}\ddot{\mathbf{u}}_B^{(n_1,n_2)} &= \Big[\mathbf{a}^{(1)}\cdot\Big(\mathbf{u}_A^{(n_1+1,n_2)}+\mathbf{u}_A^{(n_1,n_2)}-2\mathbf{u}_B^{(n_1,n_2)}\Big)\mathbf{a}^{(1)}\\ &+\ \mathbf{a}^{(2)}\cdot\Big(\mathbf{u}_A^{(n_1,n_2+1)}+\mathbf{u}_A^{(n_1+1,n_2-1)}-2\mathbf{u}_B^{(n_1,n_2)}\Big)\mathbf{a}^{(2)}\\ &+\ \mathbf{a}^{(3)}\cdot\Big(\mathbf{u}_B^{(n_1,n_2+1)}+\mathbf{u}_B^{(n_1,n_2-1)}-2\mathbf{u}_B^{(n_1,n_2)}\Big)\mathbf{a}^{(3)}\Big]\\ &+\ \alpha_B\omega\mathbf{R}\dot{\mathbf{u}}_B^{(n_1,n_2)}\ ,\end{aligned}\tag{4.68}$$

where the basis vectors $\mathbf{a}^{(j)}$, $j=1,2,3$, shown in Figure 4.1(b), were given in (4.33). The last terms appearing in the right-hand sides of eqs. (4.67) and (4.68) represent the influence of two different gyroscopes in the unit cell having gyricities of equal magnitude but opposite sign, i.e. $\Omega_A=-\Omega_B=\omega$.

We note a slightly different form of the above equations were discussed in the time-harmonic regime in Section 3.1.2, Chapter 3, in connection with the generation of highly localised Gaussian beams in the gyro-elastic lattice. Here we show this phenomena can be achieved in the gyro-elastic medium considered in the transient regime. Before doing this, we first derive the dispersion. relations of the system and identify the frequencies where it is possible to attain such dynamic phenomena,

4.3.2 Floquet-Bloch waves and dispersion relation

To identify waves in the lattice, we follow the general procedure outline in Section 2.4 of Chapter 2. We look for the solutions to (4.67) and (4.68) in the form

$$\mathbf{u}_j^{(\mathbf{n})}=\mathbf{U}_j^{(\mathbf{n})}e^{\mathrm{i}\omega t}\ ,\quad j=A,B\ .\tag{4.69}$$

The amplitudes $\mathbf{U}_j^{(\mathbf{n})}$, $j=A,B$, satisfy the Floquet-Bloch conditions

$$\mathbf{U}_j^{(\mathbf{n}+\mathbf{a})}=\mathbf{U}_j^{(\mathbf{n})}e^{\mathrm{i}\mathbf{k}\cdot\mathbf{T}\mathbf{a}}\ ,\qquad \mathbf{T}=[\mathbf{t}^{(1)},\mathbf{t}^{(2)}]=\begin{pmatrix}2 & \dfrac{1}{2}\\ 0 & \dfrac{\sqrt{3}}{2}\end{pmatrix},\tag{4.70}$$

where $\mathbf{k} = (k_1, k_2)^{\mathrm{T}}$ is the Bloch or wave vector. Combining this with the equation of motion for the masses (4.67) and (4.68), the dispersion relation becomes:

$$\det[\mathbf{C} - \omega^2(\mathbf{I}_4 - \mathbf{S})] = 0 \ , \tag{4.71}$$

where $\mathbf{I}_4$ is the 4×4 identity matrix and the matrix characterising the effect of the spinners is

$$\mathbf{S} = \mathrm{i}\ \mathrm{diag}\left(\alpha_1 \mathbf{R}, -\alpha_2 \mathbf{R}\right) \ .$$

In addition, in (4.71) the stiffness matrix $\mathbf{C}$ is given by

$$\mathbf{C} = \begin{pmatrix} \mathbf{C}^{(1)} & \mathbf{C}^{(2)} \\ \overline{\mathbf{C}^{(2)}} & \mathbf{C}^{(1)} \end{pmatrix} \ ,$$

where

$$\mathbf{C}^{(1)} = \begin{pmatrix} 3 - \frac{1}{2}\cos(\zeta) & -\frac{\sqrt{3}}{2}\cos(\zeta) \\ -\frac{\sqrt{3}}{2}\cos(\zeta) & 3\Big(1 - \frac{1}{2}\cos(\zeta)\Big) \end{pmatrix}$$

and

$$\mathbf{C}^{(2)} = \begin{pmatrix} -e^{-\mathrm{i}(\zeta+\xi)}\left(2\cos(\zeta+\xi) + \frac{1}{2}\cos(\xi)\right) & \frac{\sqrt{3}}{2}e^{-\mathrm{i}(\zeta+\xi)}\cos(\xi) \\ \frac{\sqrt{3}}{2}e^{-\mathrm{i}(\zeta+\xi)}\cos(\xi) & -\frac{3}{2}e^{-\mathrm{i}(\zeta+\xi)}\cos(\xi) \end{pmatrix} \ ,$$

with $\xi = \frac{k_1}{2} - \frac{\sqrt{3}k_2}{2}$ and $\zeta = \frac{k_1}{2} + \frac{\sqrt{3}k_2}{2}$.

Generation of localised waveforms in the transient regime

In [Carta et al. (2017a)] and Chapter 3, it was demonstrated that waveforms localised in a single line can be created at specific frequencies in a gyro-elastic lattice with two types of spinners, shown in Figure 4.10. This phenomenon is associated with the dispersion properties of the structured medium reported in Chapter 3. There, this phenomena is realised in the system due to the influence of the gyroscopic forces brought by the array of gyroscopes, whose magnitudes depend on the spinner constant of the gyroscopes and the lattice radian frequency.

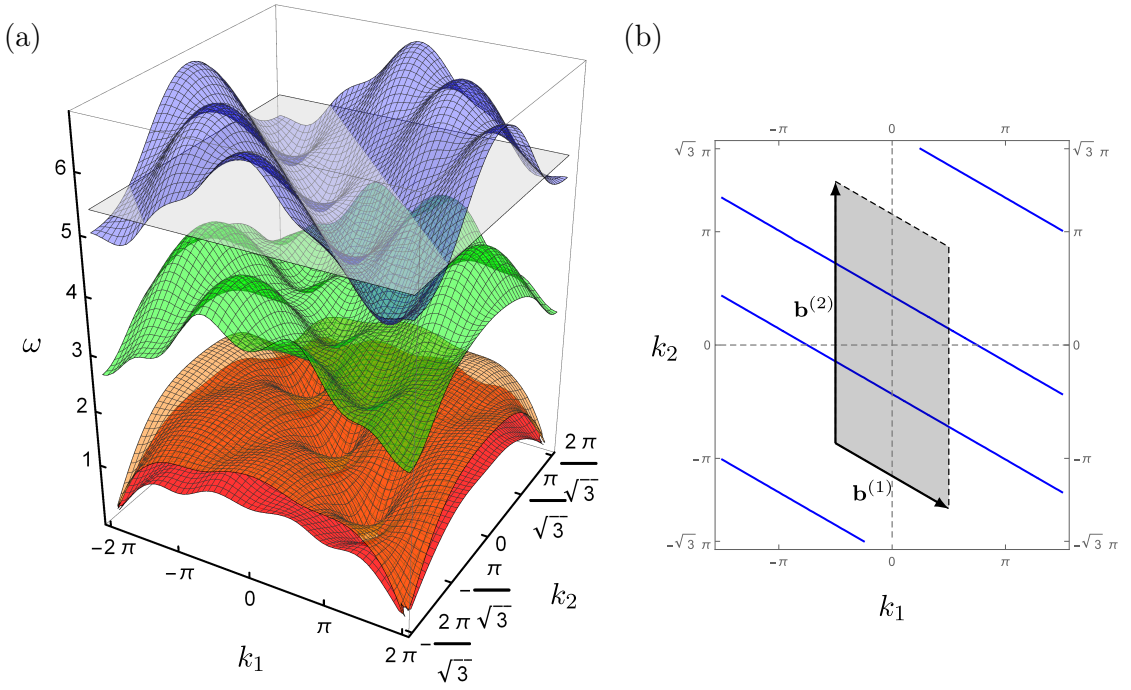

Figure 4.11: Dispersion properties of the gyro-elastic lattice in Figure 4.10. The computations are given for $\alpha_A = 0.8$ and $\alpha_B = 0.9$. (a) Dispersion surfaces. (b) Slowness contours at $\omega = 1.72\,\pi = 5.39$. These contours are associated with the propagation of localised waves in the direction $(1/2, \sqrt{3}/2)$. The grey region represents the first Brillouin zone.

In this Chapter, we have shown the influence of gyroscopic forces depends on the gyricity Ω of the gyroscopic spinner, which is a parameter that can be chosen freely, independent of the lattice radian frequency. In what follows, we develop the theory in accordance with [Carta et al. (2017a)] and Chapter 3, where the gyricity satisfies (4.66). However, we will show that it is possible to obtain highly localised waveforms in the case when the gyricity does not satisfy (4.66) (with some obvious modifications).

In Figure 4.11, the dispersion properties obtained from (4.71) are reported, where $\alpha_A = 0.8$ and $\alpha_B = 0.9$. The slowness contours at $\omega = 1.717\,\pi = 5.394$ are given in Figure 4.11(b). The first Brillouin zone is also indicated, defined by the reciprocal vectors

$$\mathbf{b}^{(1)} = (\pi, -\pi/\sqrt{3})^{\mathrm{T}}, \qquad \mathbf{b}^{(2)} = (0, 4\pi/\sqrt{3})^{\mathrm{T}}\,. \tag{4.72}$$

The slowness contours are associated with wave propagation in the direction normal to the contour lines, namely the direction associated with the vector $(1/2, \sqrt{3}/2)$.

In Figure 4.12, we show the results of a transient analysis, which is performed on a finite lattice with dimensions $100 \times 50\sqrt{3}$. A *Matlab* code has been implemented in order to solve the equations of motion (4.67) and (4.68) on the 5000 unit cells of Figure 4.12. The system is initially at rest and the exterior lattice nodes are clamped. A wave is produced by a concentrated load, acting at the central node indicated by a yellow dot in Figure 4.12; the node is of type A (see Figure 4.10). The applied force is $\mathbf{P}\sin(\omega t)$, where the amplitude vector $\mathbf{P} = (0, 0.96)^{\mathrm{T}}$.

In Figure 4.12 the displacement magnitude $|\mathbf{u}|$ is given at three different time instants (a) $t = 12.80$, (b) $t = 127.35$ and (c) $t = 235.58$. These snapshots are representative of the evolution of the localised wave form. It is evident that the wave is highly localised along the direction predicted by the dispersion properties in Figure 4.11, namely perpendicular to the straight slowness contours at $\omega = 1.72\pi$.

A deeper inspection of the numerical results, evidenced by the inset on the left of Figure 4.12(c), reveals that, while the force is applied to a node of type A (see Figure 4.10), the wave is mainly localized in the lattice nodes of type B. The transient analysis shows that there is an initial stage $0 \leq t \leq 13$, in which the wave propagates from the node where the force is applied to the neighboring nodes, without an evident preferential direction, as in Figure 4.12(a), and a second stage where two highly localized waves are generated departing from the two nodes of type B adjacent to the node where the force is applied, as demonstrated in Figure 4.12(b) and (c). An additional simulation, reported in Figure 4.13, shows that also in the case in which the force is applied to a node of type B the wave is highly localized on these type of nodes. This is in agreement with the steady-state results reported in [Carta et al. (2017a)], which show that waves tend to propagate along the lines where the parameter α is larger. However, with reference to the computation of Figure 4.11, a steady-state analysis does not give any information about the initial range when the wave moves from point A to point B. Moreover, such an analysis does not give any indication about the wave speed, which can be instead obtained from the present transient simulations in Figures 4.12 and 4.13. In particular, the two cases show that the localised waves can be achieved in the elastic system in a relatively short finite

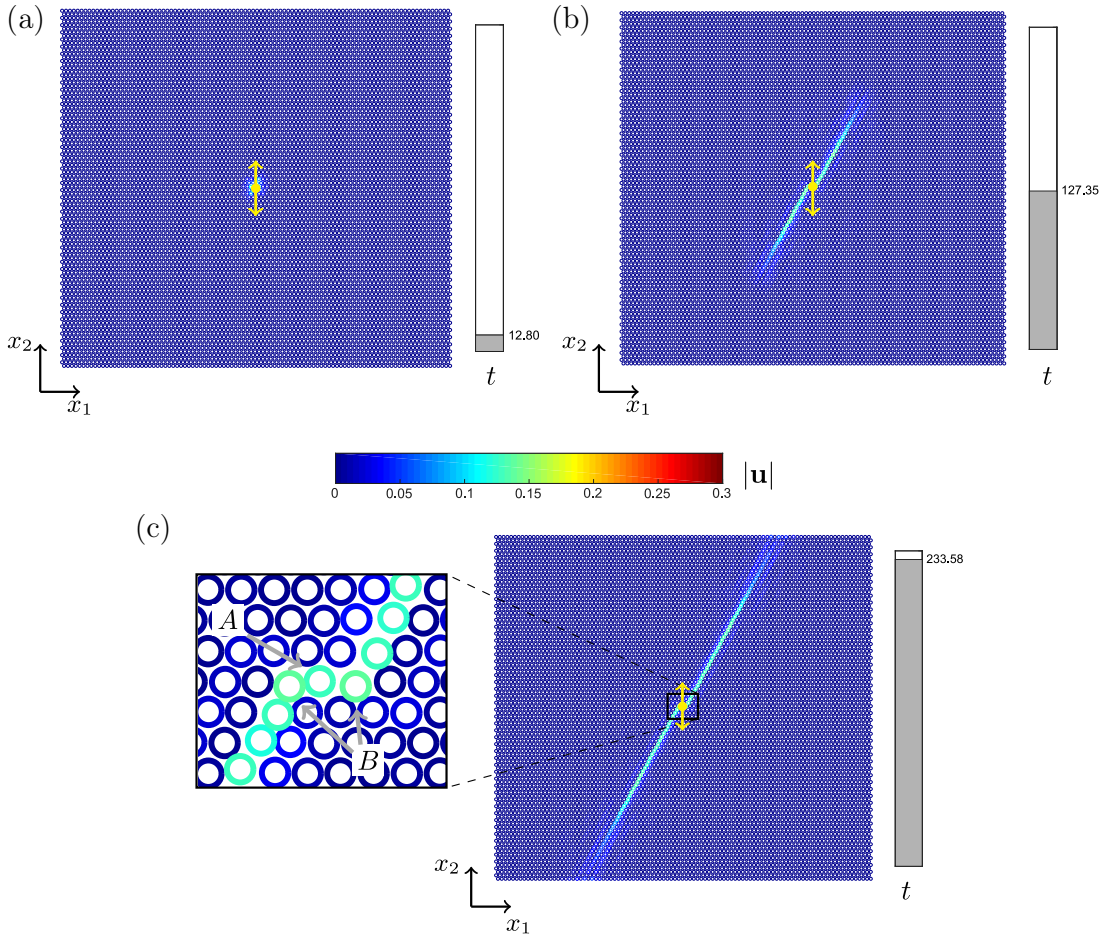

Figure 4.12: Transient dynamic analysis in a finite gyro-elastic lattice composed of 5000 unit cells with spinners possessing $\alpha_A = 0.8$, $\alpha_B = 0.9$ and gyricities $\Omega_A = -\Omega_B = \omega = 1.72\pi$. The force indicated with a yellow arrow is applied in node of type A, as shown in the magnification of (c). The displacement magnitude $|\mathbf{u}|$ is given at the normalised time (a) $t = 12.80$, (b) $t = 127.35$ and (c) $t = 233.58$.

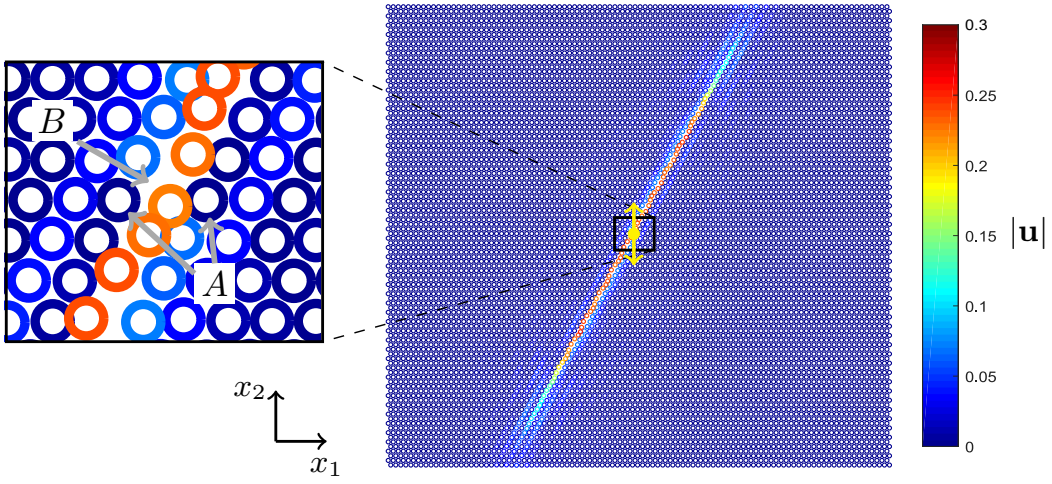

Figure 4.13: Transient dynamic analysis in a finite gyro-elastic lattice whose properties are described in the caption of 4.12. The force indicated with a yellow arrow is applied in node of type B, shown in the magnification. The displacement magnitude $|\mathbf{u}|$ is given at the normalised time $t = 233.56$.

time interval.

Next, we investigate if localised waveforms can be generated in a gyro-elastic lattice possessing uniform gyricity that does not satisfy (4.66). In this scenario, in the last terms in the right-hand sides of (4.67) and (4.68), ω is replaced by Ω_G. Figure 4.14(a) shows the dispersion surfaces for the geometry described in Figure 4.10 and gyricity $\Omega_G = 3$. The surfaces are intersected by a grey plane with frequency $\omega = 1.15\pi$, whose slowness contours are shown in Figure 4.14(b). These contours can be computed with the dispersion analysis presented in Section 4.3.2 with obvious modifications. Once again, it can be seen that the slowness contours in Figure 4.14(b) are straight lines associated with waves that propagate in the direction $(1/2, \sqrt{3}/2)$. In Figure 4.14(c)-(e), the response of the system when subjected to the sinusoidal load $\mathbf{P}\sin(\omega t)$ is reported at different instants of time. The forcing amplitude vector is $\mathbf{P} = (0, 1)^T$. There, a clear localised waveform can be observed that propagates in the direction parallel to the inclined rows of the lattice.

This response is realised in a similar way to that encountered in the example of Figure 4.12. However, as evidenced by the magnification of Figure 4.14(e), the load is able to excite more neighbouring nodes, as seen in the interval $0 \leq t \leq 20$, of which in Figure 4.14(c) we report an example. As a consequence, this also leads to

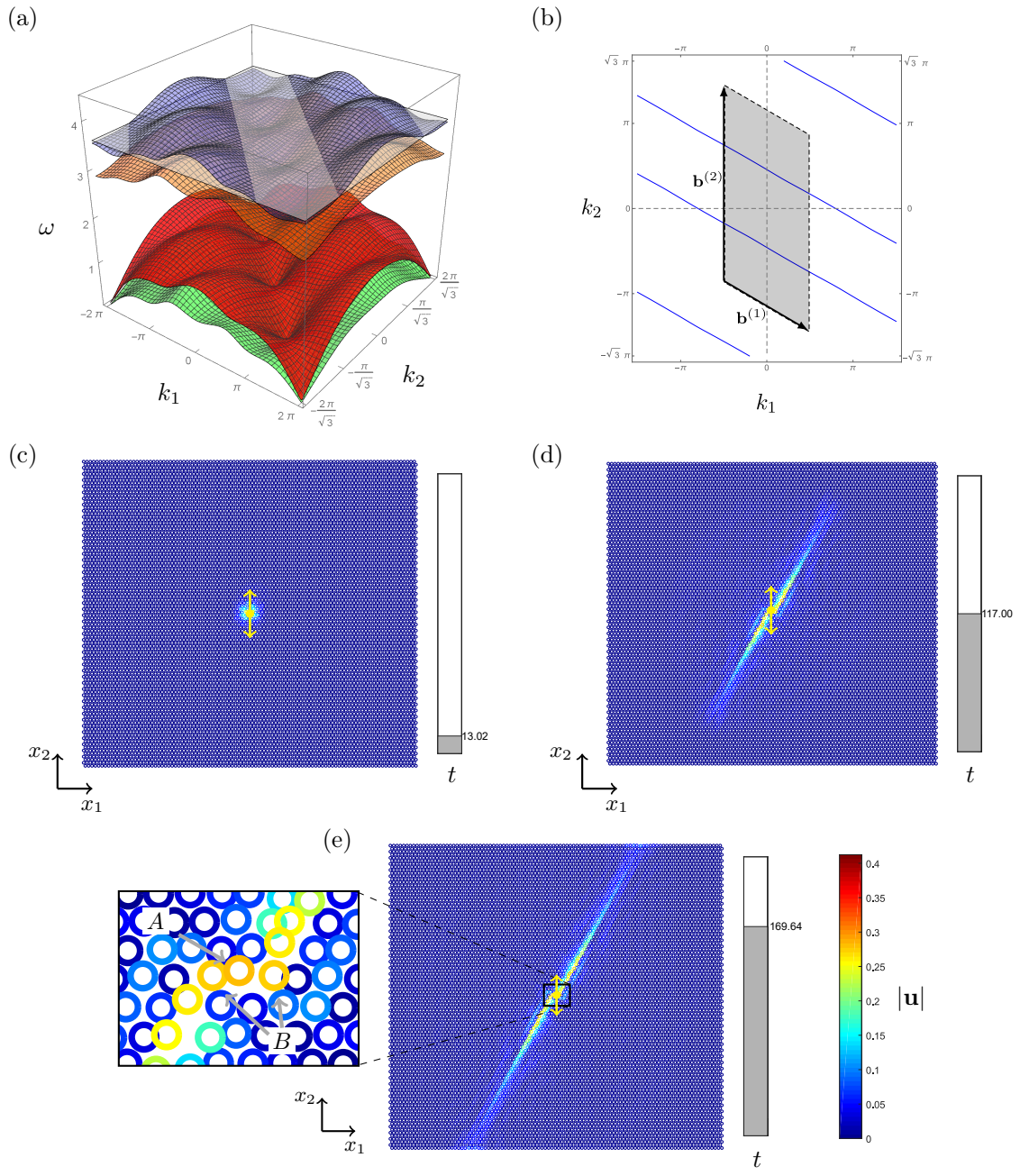

Figure 4.14: Dispersion analysis based on a modification of the results in 4.3, where in (a) the dispersion surfaces for gyricity $\Omega_G = 3$ and in (b) the slowness contours at $\omega = 1.15\pi$ are shown. The grey region represents the first Brillouin zone. The transient dynamic analysis in a finite gyro-elastic lattice composed of 5000 unit cells with spinners possessing $\alpha_A = 0.8$, $\alpha_B = 0.9$ gives the displacement magnitude $|\mathbf{u}|$ at the normalised time (c) $t = 13.02$, (d) $t = 117.00$ and (e) $t = 169.64$.

more than one localised wave and they propagate parallel to each other, which is clearly seen in Figure 4.14(d). These additional localised waves appear along the first and the second neighbouring inclined rows to the load that contain the nodes of type B. The intensity of the displacements produced by these waveforms are greater along the nearest neighbouring inclined rows.

The results of Figures 4.14(c)-(e) demonstrate that highly localised waves can be achieved in a gyro-elastic medium without the requirement (4.66) on the gyricity.

Finally, we concluded the analysis of these waves by asking a natural question: "Can the localised waveforms be realised in a gyro-elastic lattice subjected to different initial configurations?"

To answer this question, we consider non-zero initial conditions in a neighbourhood of the load. The initial conditions of the system are now modified inside a 10×10 rectangle centred at the point where the load is applied in the lattice (see the black dot and the black rectangle in Figure 4.15). In this rectangular region, each node is given an initial displacement of 0.02 and initial velocity 0.05 in the horizontal and vertical directions. All other nodes in the system are considered to be initially at rest.

A snapshot of the lattice within the initial stage of its response is shown in Figure 4.15(a). Once more, a clearly visible highly localised wave can be seen propagating along the nodes of the type B, see Figure 4.15(b)-(f). Accompanying this, a vortex-type transient wave propagates outward from the load. The displacements produced by this wave are small in comparison with the dominant dynamic feature in Figure 4.15(c)-(f). Hence, in the Figures 4.15(a)-(e) the maximum displacement associated with the colour bar has been truncated to highlight the effects of the vortex wave. In Figure 4.15(f), the behaviour of the lattice at a much later time is shown. It is seen that the effects of the transient vortex wave are negligible and, in accordance with the slowness contours of Figure 4.11(b), the highly localised waveform predicted by the dispersion analysis is achieved.

Figure 4.15 demonstrates the effect of the non-homogeneous distribution of the initial conditions on the evolution of the system's motion. There the motion can be

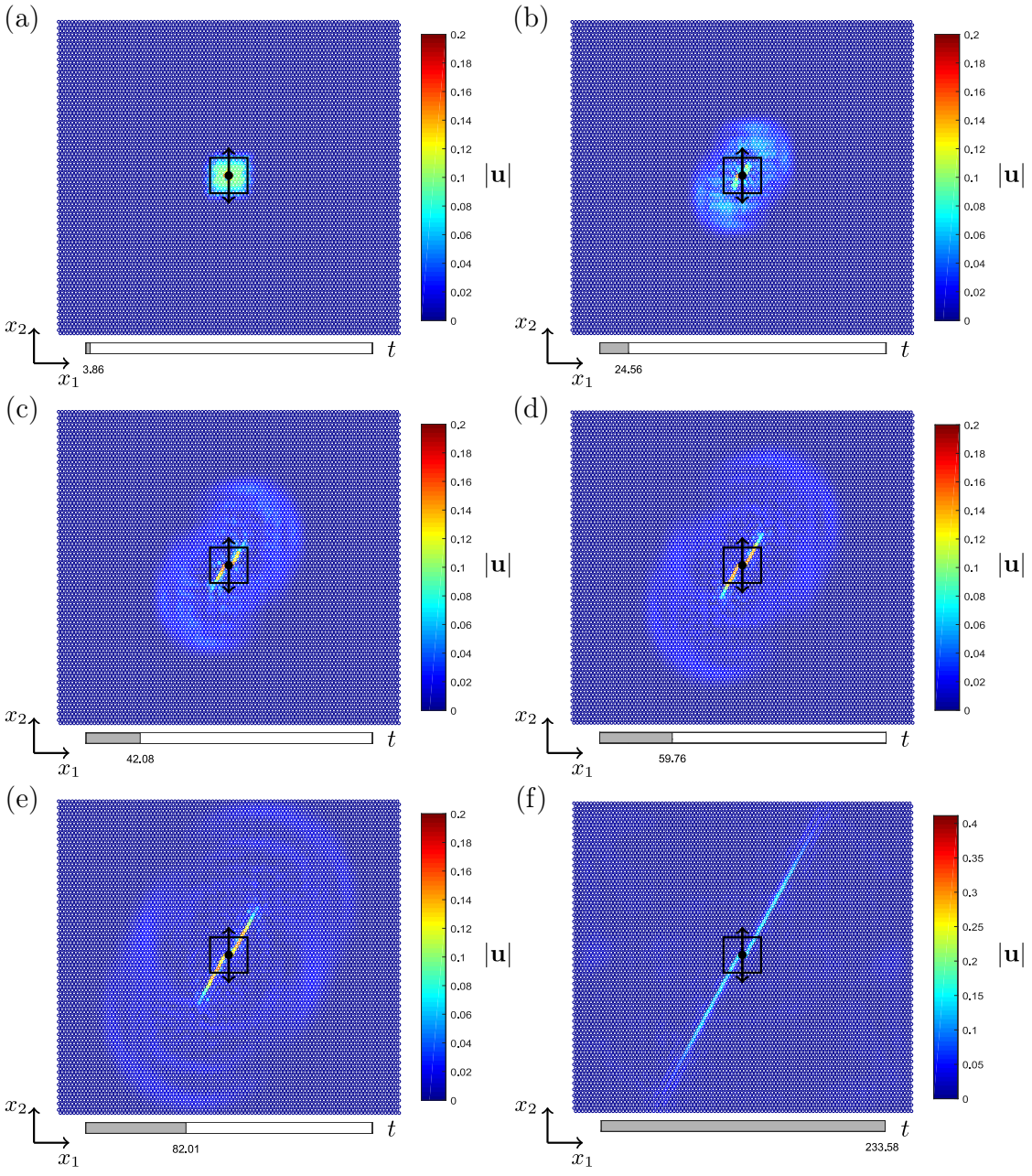

Figure 4.15: Transient dynamic analysis in a finite gyro-elastic lattice subject to non-homogeneous initial conditions within the black rectangles, centred on the position of the applied force (the black dot). The lattice is composed of 5000 unit cells with spinners possessing $\alpha_A = 0.8$, $\alpha_B = 0.9$ and gyricities $\Omega_A = -\Omega_B = \omega = 1.72\pi$. The displacement magnitude $|\mathbf{u}|$ is given at the normalised time (a) $t = 3.86$, (b) $t = 24.56$, (c) $t = 42.08$, (d) $t = 59.76$, (e) $t = 82.01$ and (f) $t = 233.58$.

described in three stages. For $0 \leq t \leq 4$, the intensity of the deformations created by the non-homogeneous initial conditions is visible within the prescribed rectangle of Figure 4.15(a) and they decrease with time inside this interval. During this period there is also visible deformation created by load at the centre of the lattice. The second stage of the lattice motion occurs for $4 \leq t \leq 25$, where the deformations created by the initial lattice configuration and the source interact. In this period, no preferential direction of the deformation is observed, see Figure 4.15(b). The third stage takes place for $t > 25$, where the waveform possessing preferential directions expected from the dispersion analysis (see Figure 4.11) becomes clearly visible, for instance see Figure 4.15(c). In this stage, nodes of the type B to the left and right of the load are excited and begin to generate the highly localised waveform similar to the scenario of the lattice with homogeneous initial conditions. The evolution of the highly localised waveform can be seen in Figures 4.15(c)-(e). As this evolves, the influence of the initial conditions can still be seen as the vortex wave propagates outwardly from the load and interacts with the upper and lower lattice boundaries at approximately $t = 82$, Figure 4.15(e). After some time, the effects of the transient vortex wave diminish and a highly localised wave continues to propagate in the medium (see Figure 4.15(f)).

The example presented in Figures 4.15 demonstrate that changing the initial conditions of the system will produce different transient effects but the waveforms predicted by the theoretical model of [Carta et al. (2017a)] in the time-harmonic regime are still realisable.

4.3.3 Interfacial waves in a hexagonal elastic lattice attached to gyroscopic spinners

Here, we consider a hexagonal lattice connected to an inhomogeneous array of spinners that divides the lattice into subdomains. In particular, our aim is to analyse the transient behaviour of interfacial waveforms that can appear when the boundaries between subdomains are excited at selected frequencies.

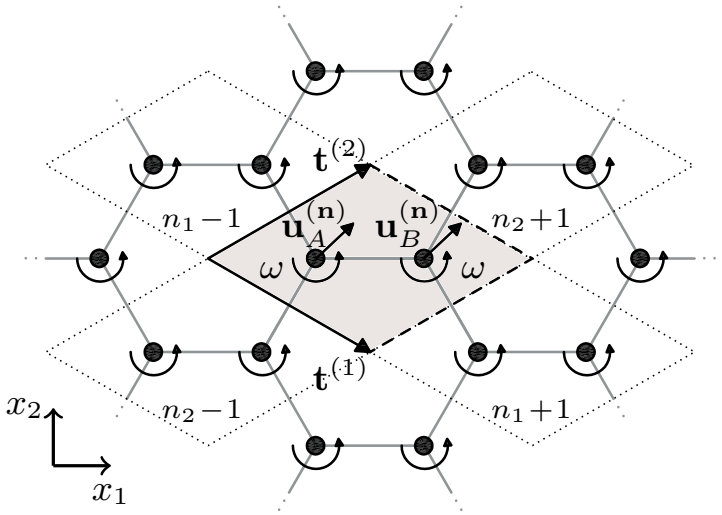

Figure 4.16: An infinite lattice composed of elastic links connecting a periodic hexagonal array of masses. The junctions are also attached to a uniform array of gyroscopic spinners characterised by the material parameter α and having gyricity ω, which is the radian frequency of the entire system. The elementary cell is defined by the vectors $\mathbf{t}^{(1)} = (3/2, -\sqrt{3}/2)^{\mathrm{T}}$ and $\mathbf{t}^{(2)} = (3/2, \sqrt{3}/2)^{\mathrm{T}}$.

In order to achieve this goal, we first introduce the model of a homogeneous gyro-elastic hexagonal lattice shown in Figure 4.16. Similar to Section 3.3 of Chapter 3, we define the elementary cell of the lattice with the basis vectors $\mathbf{t}^{(1)} = (3/2, -\sqrt{3}/2)^T$ and $\mathbf{t}^{(2)} = (3/2, \sqrt{3}/2)^T$. The multi-index $\mathbf{n}$ is used again to identify the elementary cells in the lattice. In this system, the gyricity is uniform and is set equal to the radian frequency of vibration in the lattice. The displacements $\mathbf{u}_j^{(\mathbf{n})}$, $j = A, B$, of the nodes in the cell with index $\mathbf{n}$ satisfy the dynamic equations:

$$\ddot{\mathbf{u}}_A^{(\mathbf{n})} = \sum_{j=1}^{3} \mathbf{a}^{(j)} \cdot \{\mathbf{u}_B^{(\mathbf{n}-\mathbf{p}_j)} - \mathbf{u}_A^{(\mathbf{n})}\}\mathbf{a}^{(j)} - \alpha\omega\mathbf{R}\dot{\mathbf{u}}_A^{(\mathbf{n})} \,, \tag{4.73}$$

$$\ddot{\mathbf{u}}_B^{(\mathbf{n})} = \sum_{j=1}^{3} \mathbf{a}^{(j)} \cdot \{\mathbf{u}_A^{(\mathbf{n}+\mathbf{p}_j)} - \mathbf{u}_B^{(\mathbf{n})}\}\mathbf{a}^{(j)} - \alpha\omega\mathbf{R}\dot{\mathbf{u}}_B^{(\mathbf{n})} \,, \tag{4.74}$$

with $\mathbf{p}_1 = (0,0)^{\mathrm{T}}$, $\mathbf{p}_2 = (1,0)^{\mathrm{T}}$ and $\mathbf{p}_3 = (0,1)^{\mathrm{T}}$. The last terms in the preceding right-hand sides represent the dynamic contribution of the uniform array of spinners to the lattice system.

A detailed dispersion analysis of the system was carried out in Section 3.2.2 of Chapter 3 (see also [Garau et al. (2018)]). In addition, a detailed explanation of how to obtain interfacial waves in inhomogeneous gyro-elastic lattice systems was

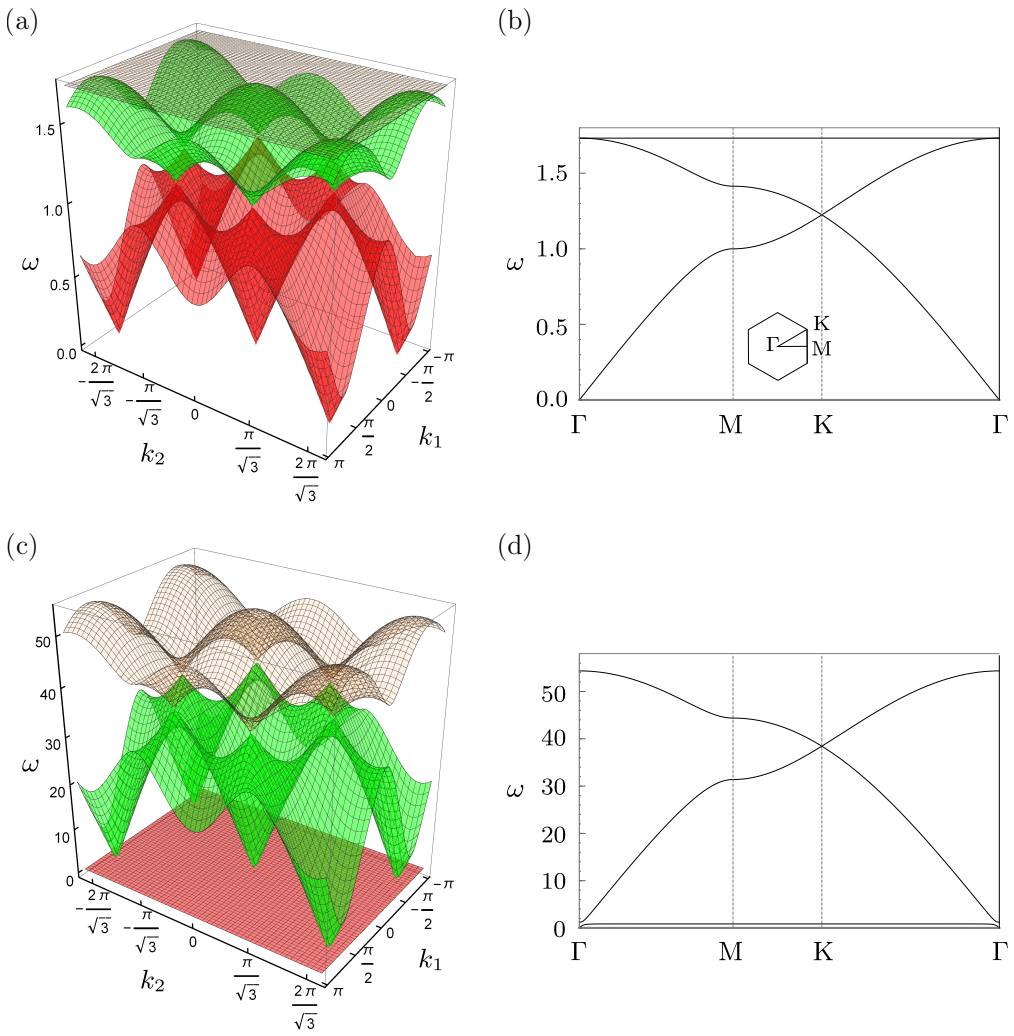

Figure 4.17: Dispersion properties of the hexagonal gyro-elastic lattice of Figure 4.16 with (a)-(b) $\alpha = 0$, (c)-(d) $\alpha = 0.9999$. (b) and (d) show the dispersion surface along the path ΓMKΓ, (see the inset of (b)).

described. Below, we briefly recall some of these results in describing the set up of the subsequent transient simulations.

In connection with the results of Section 3.2.2, it can be noticed that the considered structure admits dispersive degeneracies such as Dirac cones when $\alpha = 0$, corresponding to the case of an ordinary hexagonal lattice without spinners shown in Figures 4.17(a) and (b). The Dirac Point is at $\mathrm{K} = (2\pi/3, 2\pi/(3\sqrt{3}))$ and $\omega = \sqrt{3/2}$. Here, for $\alpha \to 1^-$ another Dirac cone appears at a higher frequency. Such a case is shown in Figures 4.17(c) and (d) for $\alpha = 0.999$. Actually, in this case the Dirac cone has not formed yet and an extremely narrow stop band is opened at the reciprocal lattice point $\mathrm{K} = (2\pi/3, 2\pi/(3\sqrt{3}))$, in the vicinity of the vertex of the Dirac cone

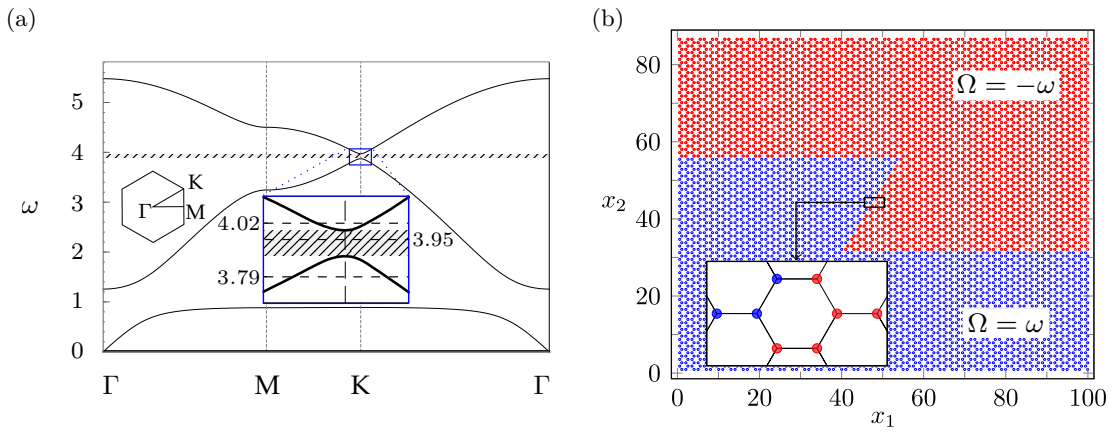

Figure 4.18: (a) Dispersion curves of the hexagonal gyro-elastic lattice of Figure 4.16 along the path ΓMKΓ are given for $\alpha = 0.9$. The narrow stop band in the high-frequency regime is highlighted in the inset, which also includes the frequencies of the external excitation used in the numerical simulations. (b) Computational domain for the example of Section 4.3.4, involving a rectangular slab of a hexagonal lattice connected to gyroscopic spinners. The lattice is divided into two subdomains defined by the gyricities of the spinners, taken as $\Omega = -\omega$ ($\Omega = \omega$) for the red (blue) nodes. The parameter $\alpha = 0.9$ is uniform throughout the medium.

appearing for $\alpha \to 1^-$.

4.3.4 Uni-directional interfacial waves in hexagonal chiral media with distributed gyricity

Here, we show that by using an inhomogeneous distribution of gyricities one can generate interfacial waveforms with preferential directionality in the transient regime as discussed in Chapter 3 and [Garau et al. (2018)]. We demonstrate how to obtain such an effect in the transient regime for the case $\alpha = 0.9$. The dispersion diagram for this value of α is shown in Figure 4.18(a). We note that the curves admit a narrow stop band in the interval $3.865 < \omega < 3.963$. In addition, in this figure we indicate the frequencies $\omega = 3.79$ and 4.02 for the harmonic excitation of the lattice, where one will encounter interfacial waves propagating in opposite directions.

We consider the system shown in Figure 4.18(b). A rectangular slab of lattice, with dimensions $100 \times 50\sqrt{3}$, is divided in two subdomains, having a zig-zag interface. Inside this lattice the parameter $\alpha = 0.9$ and we distribute the gyricity of the spinners such that in the lower portion of the lattice $\Omega = \omega$ (nodes shown in blue in Figure 4.18(b)), while in the upper portion of the lattice $\Omega = -\omega$ (nodes shown in red in

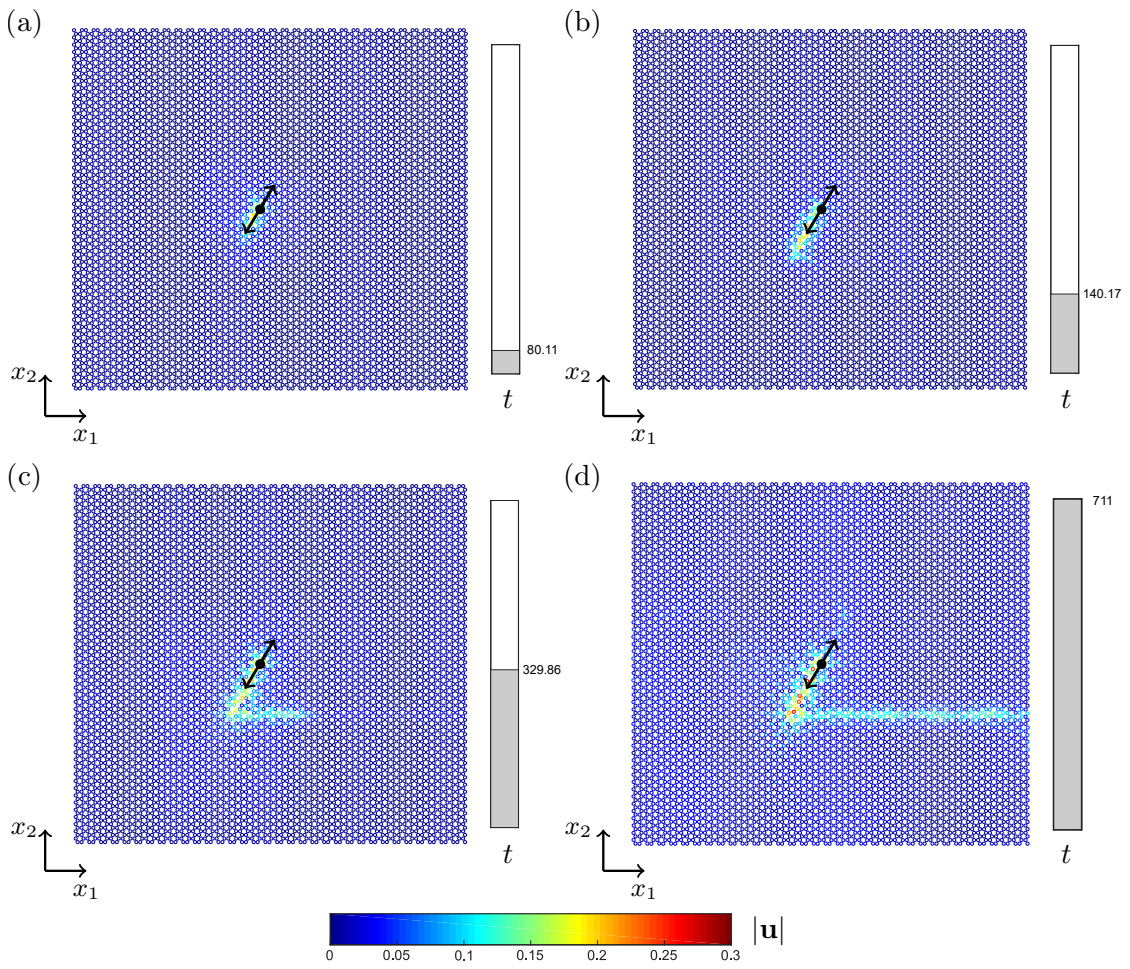

Figure 4.19: Interfacial waves produced by a point force varying sinusoidally in time and applied at the interfacial node indicated with a black dot. The geometrical and material parameters are given in Figure 4.18. The displacement magnitude $|\mathbf{u}|$ is given for $\omega = 3.79$ at the instants (a) $t = 80.11$, (b) $t = 140.17$, (c) $t = 329.86$ and (d) $t = 711$.

Figure 4.18(b)).

A *Matlab* code has been implemented to solve the equations analogous to (4.73) and (4.74) (taking into account the inhomogeneity of the spinner array) on the 4332 nodes of the lattice of Figure 4.18(b). The system is assumed to be initially at rest and the lattice nodes along the exterior of the slab are clamped. At the node indicated with a black dot in Figure 4.19, we apply the harmonic force $\mathbf{P}\sin(\omega t)$. Here, $\mathbf{P} = 0.29\,(1/2, \sqrt{3}/2)^{\mathrm{T}}$, so that the force is aligned with the interface. The forcing frequency ω is chosen to coincide with either $\omega = 3.79$ or $\omega = 4.02$, indicated in the dispersion diagram of Figure 4.18(a) for the infinite homogeneous medium with $\alpha = 0.9$.

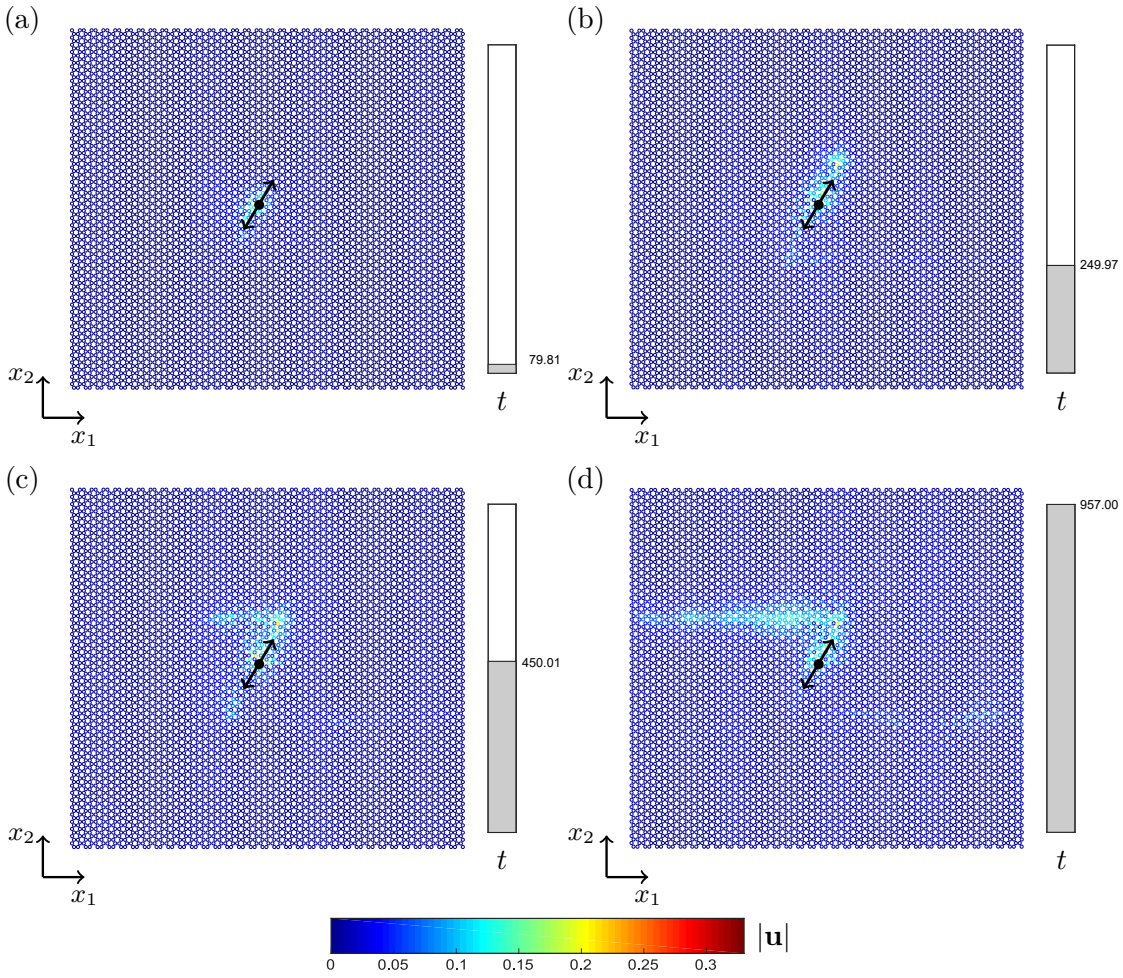

Figure 4.20: Interfacial waves produced by a point force varying sinusoidally in time and applied at the interfacial node indicated with a black dot. The geometrical and material parameters of the lattice are given in Figure 4.18. The displacement magnitude $|\mathbf{u}|$ is given for $\omega = 4.02$ at the instants (a) $t = 79.81$, (b) $t = 249.97$, (c) $t = 450.01$ and (d) $t = 957.00$.

For $\omega = 3.79$ the displacement magnitude is shown in Figure 4.19 at different times of the transient simulation. In the Figure, one can clearly see that a localised wave has appeared and begins to propagate downward from the location of the point source, following the internal interface (see Figure 4.19(a)). We report that the propagation of the wave is hindered when it attempts to by-pass the lower vertex of the internal interface after the instant shown in Figure 4.19(b). As the wave passes through the vertex it then begins to move along the lower portion of the internal interface towards the right-hand boundary (see Figure 4.19(c)). The interfacial wave reaches the right-hand boundary at approximately $t = 711$ (see Figure 4.19(d)). It is evident that the intensity of the interfacial waveform before the vertex is greater than after the vertex. This can be attributed to the scattering of waves with small amplitudes when the wave attempts to traverse the lower vertex of the interface.

In Figure 4.20, the results of the transient simulation of the lattice subjected to a force with radian frequency $\omega = 4.02$ along the zig-zag interface is shown. The wave propagates along the interface, but in the direction opposite to that in Figure 4.19. The transient analysis shows a different velocity of propagation of the two interfacial waves at the frequencies $\omega = 3.79$ and $\omega = 4.02$, where the speed of propagation is higher in the first case, which can be seen by comparing the time taken for the waves to reach the boundaries (compare Figure 4.19(d) with Figure 4.20(d)). Once more, as the wavefront tries to pass through the corner, it produces some scattering into the bulk of the lattice, which is also evidenced by the lower amplitude of the displacement in the upper horizontal part of the interface. Here, unlike in Figures 4.19(a)-(c), the interfacial wave initially propagates in both directions along the inclined part of the interface (see Figure 4.20(a)–(c)). As the motion of the system evolves in time, the intensity of those waves travelling down the inclined part of the interface decreases and the preferential direction of the wave becomes evident (see Figure 4.20(d)).

It is worth mentioning that the effects shown here are independent of the position of the load. In Figure 4.21, we show the displacement amplitude when the load is applied on the upper horizontal edge of the interface. In particular, we considered

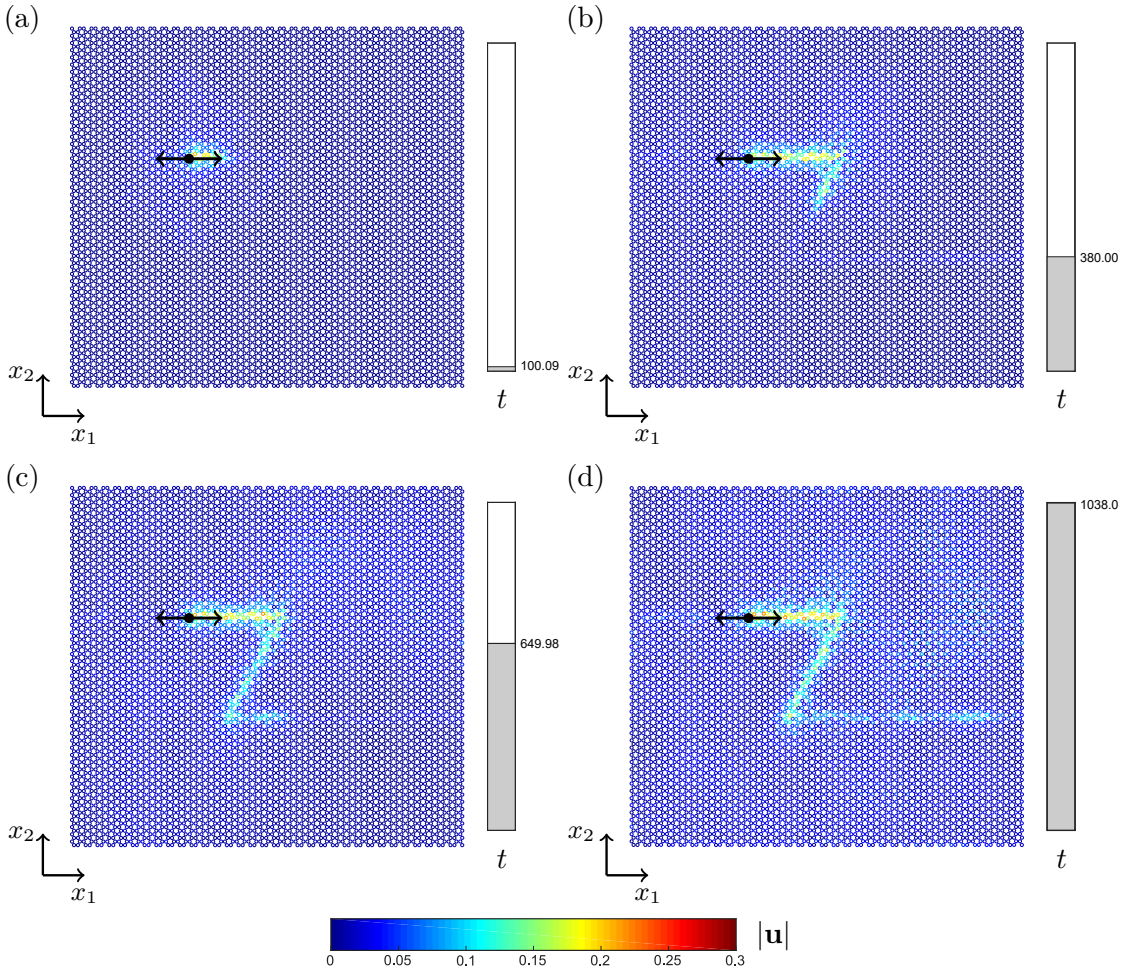

Figure 4.21: Interfacial waves are produced by a concentrated load applied at the point indicated with the black dot. The geometrical and material parameters of the lattice are given in Figure 4.18. Displacement magnitude $|\mathbf{u}|$ is given for $\omega = 3.79$, at the instants (a) $t = 100.09$, (b) $t = 380.00$, (c) $t = 649.98$ and (d) $t = 1038.00$.

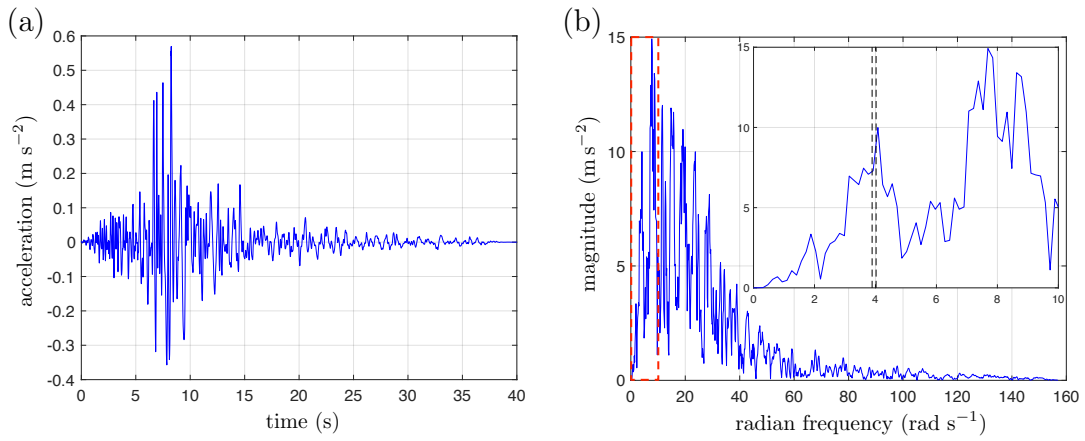

Figure 4.22: (a) Accelerations produced by the accelerogram NORTHR_ORR090.AT2 as a function of time. (b) The Fast Fourier Transform of the data in (a), a magnification of the magnitude of frequency spectrum in the frequency interval [0,10] (highlighted by the red dashed box) is presented on the inset of the figure. There, the frequencies 3.82 and 4.02, corresponding to the interfacial wave frequencies of Figure 4.18, are shown by vertical dashed black lines.

a harmonic force $\mathbf{P}\sin(\omega t)$, with $\mathbf{P} = 0.29\,(1,0)^{\mathrm{T}}$ and $\omega = 3.79$, applied at the node indicated with a black dot in the figure. As for the case in Figure 4.19, the interfacial wave propagates to the right of the load and, after passing the two corners, towards the right boundary of the lattice slab. The generation and propagation of the interfacial waves for this case can be observed in Figure 4.21, where we report some frames of the transient simulation, that clearly show how in passing the vertices of the internal interface causes a reduction of the wave intensity (compare Figure 4.21(b), (c) and (d)).

Finally, we investigate the response of the inhomogeneous gyro-elastic medium when subjected to a transient load along the interface. In what follows, we consider a gyro-elastic lattice with $cLm^{-1} = 1\mathrm{m\ s}^{-2}$ and $L = \gamma^{-1}$ m. In this way, the magnitude of the loading and the radian frequency of the structure in the physical and dimensionless settings coincide.

The load is chosen to represent the acceleration history measured by an accelerogram (labelled NORTHR ORR090.AT2) that recorded the famous seismic event in Northridge, 1994. The data for this event was captured within a 40s period. The real signal is shown in Figure 4.22(a). For the simulation below, we have implemented a load that repeats the signal generated by this earthquake after every 40 time

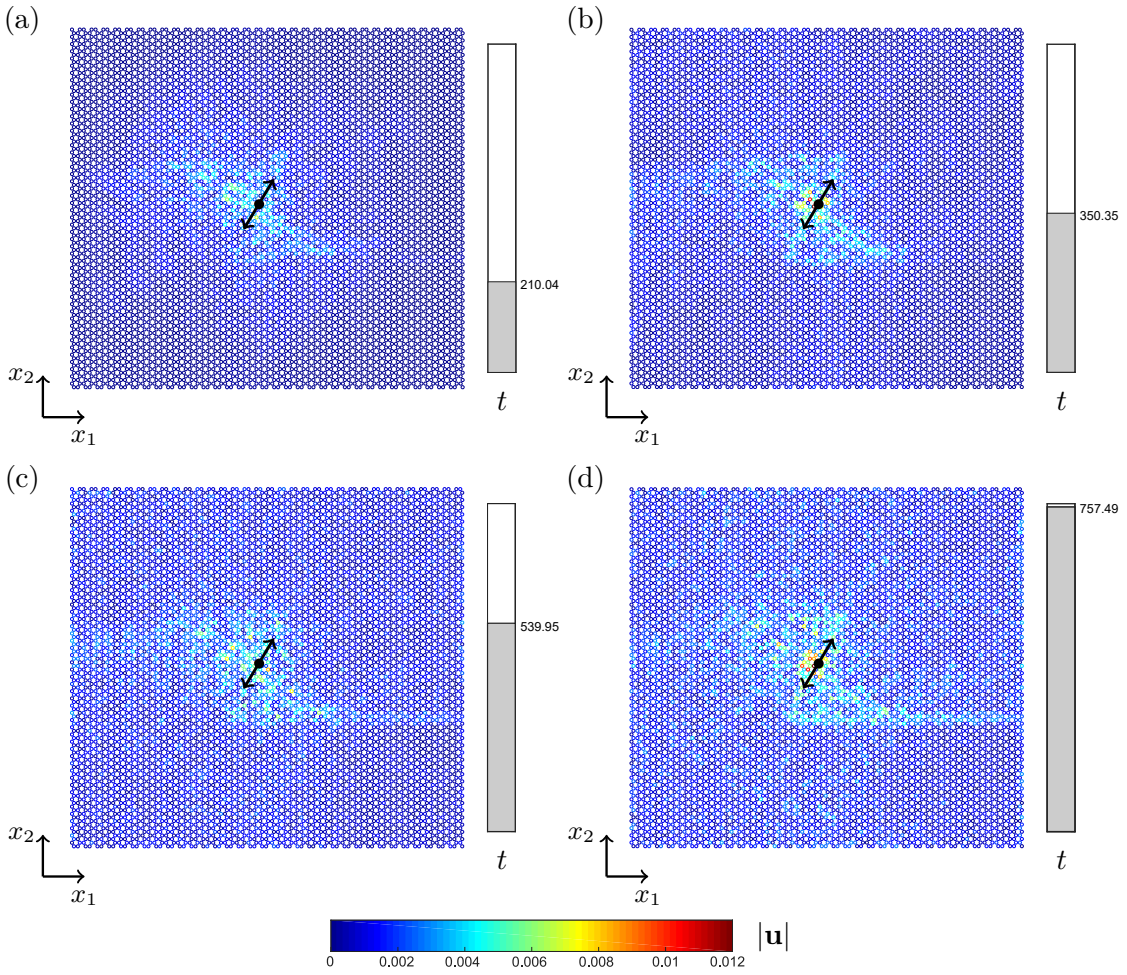

Figure 4.23: Response of an inhomogeneous gyro-elastic lattice with a zig-zag interface subject to transient loading. The geometrical and material parameters of the lattice are given in Figure 4.18. The displacement magnitude $|\mathbf{u}|$ is given for (a) $t = 210.04$, (b) $t = 350.35$, (c) $t = 539.95$ and (d) $t = 757.49$.

units. In Figure 4.22(b), the frequency spectrum (in rad s^{-1}) obtained using the Fast Fourier Transform of the signal data is given. The frequency spectrum indicates that the load is the superposition of multiple frequency components, with the largest amplitudes in the frequency interval $[0, 30]$, which includes some of the pass bands of the lattice structure, reported in Figure 4.18(a). Hence, we may anticipate multiple harmonic wave components to be excited by such a load.

As in the examples of Figures 4.19 and 4.20, we apply the load along the zig-zag interface, at the node indicated with the black dot in Figure 4.23, and this acts parallel to the inclined part of the internal boundary. Figure 4.23 shows how the behaviour of the lattice evolves in time as a result of the load with multiple frequency content. As

expected, many waves are created by the load that propagate in multiple directions within the time interval $0 \leq t \leq 250$. A snapshot representative of this phenomena in this interval is shown in Figure 4.23(a). Following this interval, these processes are accompanied by an interfacial wave that begins to propagate downward along the interface in the lattice from the load, as shown in Figures 4.23(b). While less localised than in the examples shown in Figures 4.19 and 4.20, a propagating interfacial wave can be seen propagating to the right-boundary of the lattice in Figure 4.23(c) and (d), which is the most prominent dynamic feature of these snapshots. There is also some evidence of an interfacial wave that attempts to move along the interface in the opposite direction. This occurs until $t = 350$, see Figure 4.23(b). However, this wave does not reach the left-boundary of the lattice in the computational time window shown. One possible explanation for this is based on the results of Figures 4.19 and 4.20, associated with the harmonic excitation of the gyro-elastic hexagonal lattice. There, it was revealed that the interfacial wave travels faster to the right boundary.

The example presented in Figure 4.23 indicates that multiple waves can be generated by a transient source, including waveforms occurring at special frequencies. The frequency spectrum of the load chosen here contains information about such frequencies, but they are not the dominant frequencies composing the signal (see inset of Figure 4.22(b)). Nevertheless, here we have shown that the interfacial waveform obtained at selected frequencies are still realisable and represent a significant dynamic effect in transient loading configurations.

4.4 Conclusions

Here, we have derived:

1. A new asymptotic transient model that describes the influence of a single gyroscopic spinner on a mass attached to a truss system of elastic rods. The derived force attributed to the spinner shows this mechanical element couples the in-plane displacements of the mass within the truss as in [Brun, Jones and Movchan (2012)]. It also brings to light physical parameters that are significant

in influencing the behaviour of the system, including gyricity, representing the initial spin and precession rates of the gyroscopes (see [Carta et al. (2018), Nieves et al. (2018)] where this quantity appears in the modelling interactions between gyroscopes and beams). This marks the first occasion where this parameter has been observed to influence dynamic regimes associated with such lattice systems.

For the considered gyro-elastic system, we note the linearised model has been obtained using the assumption that the nutation angle of the spinner is a small quantity. This derivation does not require the assumption that the spin and precession rates are independently constant as in [Brun, Jones and Movchan (2012)] and embeds the consideration of the moving coordinate characterising the gyroscope's motion. For simple configurations, an analytical solution to this model can be derived and this has been shown to give an excellent agreement with the solution based on the method of finite elements, despite the fact the dimensionality of both models is different. Additionally:

3. The gyricity present in the transient model is an input parameter that has potential important applications in designing new lattice systems with remarkable effects. In particular, the model derived here generalises the work of [Brun, Jones and Movchan (2012)], which is linked to subclass of lattice systems appearing when the gyricity of the spinners is chosen to coincide with the steady-state frequency of the lattice.

The model has also been extended to study the dynamics of elastic lattices attached to gyroscopes, with the focus given to special dynamic regimes possessed by the medium, previously identified in [Carta et al. (2017a), Garau et al. (2018)] and in Chapter 3 for the time-harmonic regime. In the transient regime, we have that highly localised waveforms and uni-directional interfacial waves can propagate through a lattice attached to anisotropic arrays of spinners. The transient analysis allows us to:

4. Obtain a comprehensive description of the time evolution of these waveforms.

Moreover, such results are important in the design and validation of potential future experiments in the application of gyro-elastic lattices.

5. Study the response of gyro-elastic lattices subjected to different initial conditions and transient loads. In such cases, the gyricity was taken equal to the lattice radian frequency in order to retrieve previously known results from [Brun, Jones and Movchan (2012), Carta et al. (2017a), Garau et al. (2018)]. In these transient studies, we have shown that certain initial configurations do not influence the eventual steady state response of the system and when transient loads are applied, we cannot ignore effects brought by different frequency components contained in the loading signal. However, we have also shown in the latter case that the special waveforms found in [Brun, Jones and Movchan (2012), Carta et al. (2017a), Garau et al. (2018)] remain a significant effect in the dynamic response of the gyro-elastic lattices considered.

6. Consider the influence of the gyricity on the response of the gyro-elastic lattices. In particular, we have shown that the special dynamic regimes identified in [Carta et al. (2017a)] can appear when the gyricity differs from the lattice radian frequency. As a result of this observation, the model developed here demonstrates the potential for the design of a new range of gyro-elastic lattices, where the gyricity plays a fundamental role in achieving special dynamic properties.

Chapter 5

Applications of gyro-elastic media to topological protection and cloaking

The analysis presented in Chapters 3 and 4, demonstrate that a gyro-elastic lattice can be used to generate special dynamic phenomena including interfacial waves and highly localised waveforms. Here, we further investigate the properties of these systems with a view to applications. In particular, using a gyro-elastic structured medium we propose designs of two advanced devices:

1. a structured topological insulator, which is investigated in Section 5.1, that supports highly localised waves on its exterior and prevents waves from entering the bulk and

2. a discrete cloaking device for a lattice system, which is developed in Section 5.2, that is capable of preventing significant interactions of vibrations with defects situated within a structured medium, effectively hiding the defect to an external observer.

The efficiency of these devices will be investigated in the transient regime, using the model developed in Chapter 4.

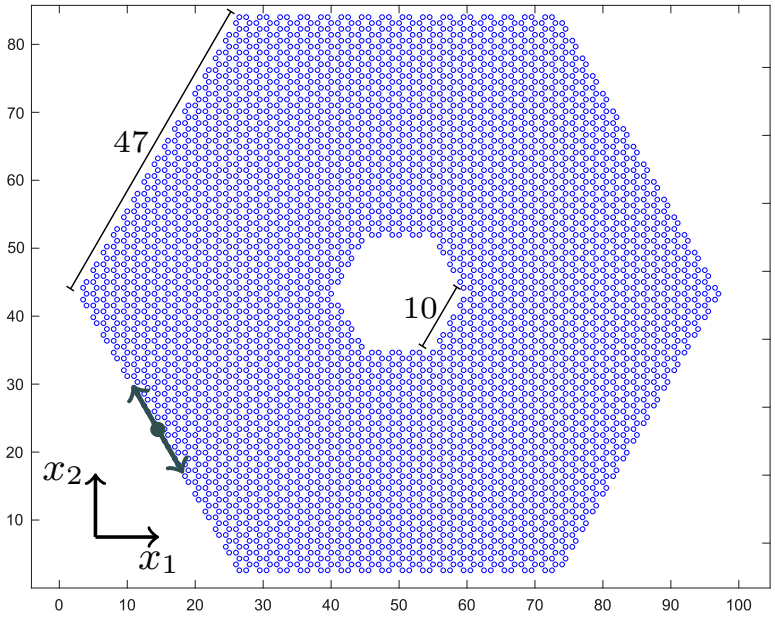

Figure 5.1: Geometry of the domain analysed in Section 5.1. The parameters of the gyroscopic spinners are $\Omega = \omega = 3.95$ and $\alpha = 0.9$.

5.1 Topological protection

Here, we investigate the capability of a gyro-elastic lattice in supporting edge waves. To this end, we perform the transient analysis of a gyro-elastic hexagonal lattice arranged as in Figure 5.1, containing a hexagonal cavity. The unit cell of the gyro-elastic lattice is as in Figure 4.16 of Chapter 4. We use the governing equations (4.73) and (4.74) of Chapter 4 to model this lattice. While the elementary cell in Figure 4.16, Chapter 4, can be used to replicate the interior of the geometry presented in Figure 5.1, we note that for the nodes along the internal and exterior boundaries the periodicity of the system is broken. The nodes along these boundaries are connected to nodes within the interior of this lattice, but in comparison to the latter the external nodes are subjected to fewer elastic restoring forces as they are connected to fewer elastic links (see Chapter 2). Hence the motion of such nodes are governed by (4.73) and (4.74) in Chapter 4 with some obvious modifications.

The gyricity and the parameters, characterising the motion and type of spinners, are uniform and taken as $\Omega = \omega$ and $\alpha = 0.9$, respectively. The lattice is assumed to be at rest initially and it is excited on the external boundary at the point indicated

in Figure 5.1 with the sinusoidal force $\mathbf{P}\sin(\omega t)$. In this case, $\mathbf{P} = A(1/2, -\sqrt{3}/2)^{\mathrm{T}}$, with $A = 7.7\times10^{-2}$ and $\omega = 3.95$. This frequency is within the narrow high-frequency stop band indicated in Figure 4.18, Chapter 4.

In Figure 5.2, we show some snapshots of the response of the lattice system of Figure 5.1 at various times. They illustrate that the external force generates a wave that propagates along the external boundary of the domain in the clockwise direction. This displacement is ten times larger than the maximum displacement inside the rest of the system and the displacement is concentrated near the external boundary of the lattice. In order to better visualise the displacement field in the whole domain, in Figure 5.2, we have truncated the total displacement scale at $|\mathbf{u}| = 0.1$. In the bulk of the lattice, and in particular on the internal hexagonal boundary, the displacements are negligibly small with respect to the values attained on the external hexagonal boundary. Accordingly, an object placed in the cavity of the domain would be protected from a dynamic disturbance produced by forcing at this frequency on the exterior of the lattice.

We note in this simulation, the masses of the system rotate in the plane of the lattice in the anti-clockwise direction, yet the edge wave propagates along the exterior boundary in the clockwise direction. This counter-intuitive phenomenon is typical with wave motion in discrete gyro-elastic media. Similar effects may also be observed in Chapters 3 and 4 where it was shown that the slight adjustment of the frequency may induce waveforms propagating in different directions, regardless of the preferential spin of the gyroscopes.

5.2 Cloaking

In the example considered here, we show that one can design a structured gyro-elastic medium that can act as an efficient cloaking device to hide a defect in a discrete lattice (see Figure 5.3(a)). The cloak possesses an inner and outer hexagonal annulus, each of which is split into two domains, as shown in Figure 5.3(b). Throughout the cloak the quantity $\alpha|\Omega|$, characterising the magnitude of the effective input of the

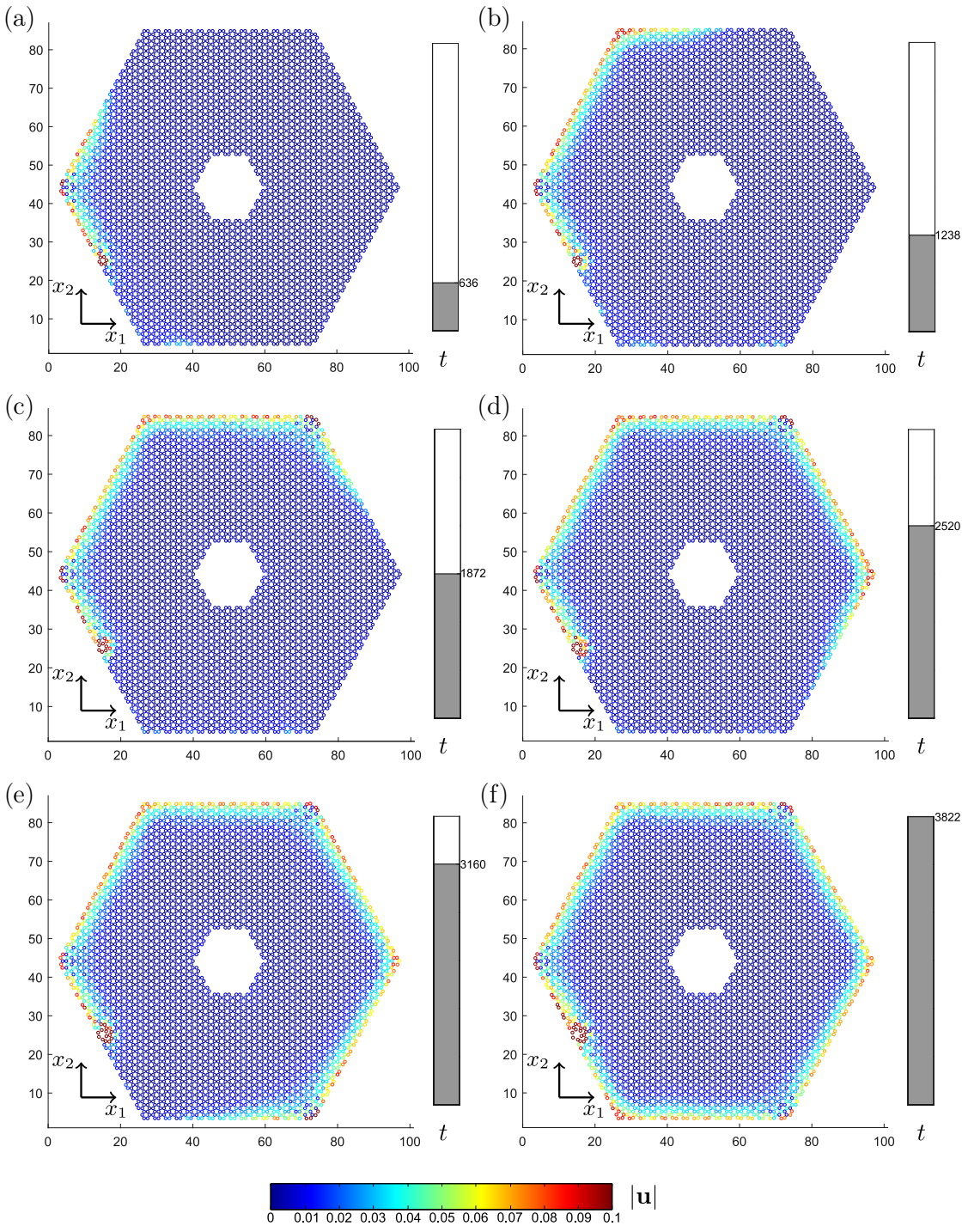

Figure 5.2: A selection of snapshots from the numerical computation that illustrates the response of the gyro-elastic lattice in Figure 5.1 excited on the external boundary. The displacement magnitude $|\mathbf{u}|$ is given at times t indicated on the bar on the right of each figure.

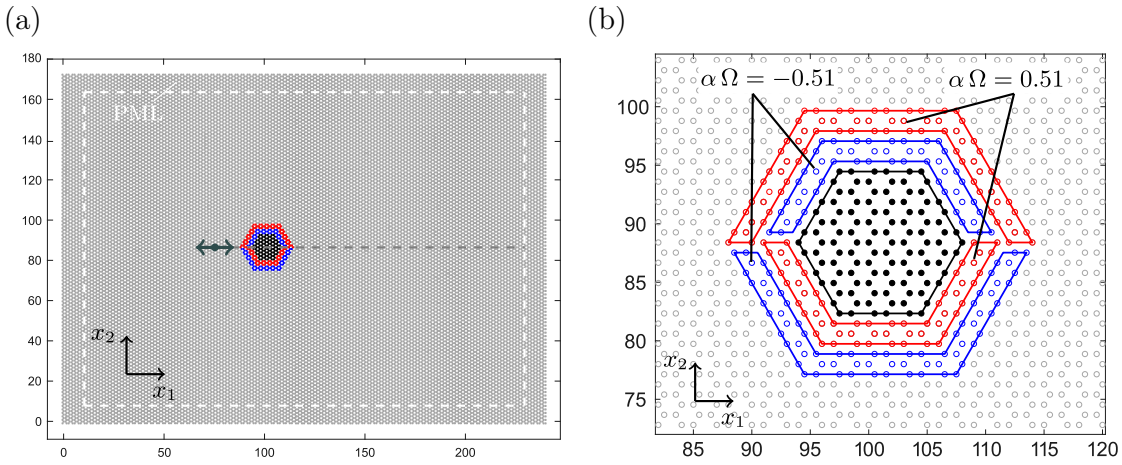

Figure 5.3: (a) A hexagonal lattice containing a defect (black hexagonal region), coated by a gyro-elastic cloak (red and blue regions). Along the exterior boundary of the lattice Perfectly Matched Layers are used, whose interior boundary is represented by a white dashed line. The position of the external excitation is indicated by a black arrow. (b) A magnification of the cloaked defect. The region bounded by the red (blue) lines contains lattice nodes connected to gyroscopic spinners with product $\alpha\Omega = 0.51$ ($\alpha\Omega = -0.51$). The defect is represented by the black solid circles, connected by links of stiffness equal to 12, whereas the stiffness of the links in the ambient medium is 1.

gyroscopes to the cloak, is uniform. The value of $\alpha\Omega$ in each subdomain of the cloak is indicated in the Figure 5.3(b).

In *Comsol*, we used the Structural Mechanics module and the transient forcing terms due to the gyroscopic spinners (see (4.32) in Chapter 3) were implemented as additional forces to the junctions of the truss inside the cloak.

We remark that the design of the cloaking device is similar to that proposed in [Brun, Jones and Movchan (2012)]. However, here we are considering a discrete medium, while in [Brun, Jones and Movchan (2012)] a homogenised continuum was implemented in the design and simulations.

We consider a rectangular slab of hexagonal lattice with dimensions $241.5 \times 199\sqrt{3}/2$ (with the length of all links set to unity). We study the dynamic response of this lattice in three scenarios:

(i) when there is no defect and hence the lattice is homogeneous;

(ii) when the lattice contains a defect, represented by the black hexagon in Figure 5.3(a) and (b), and

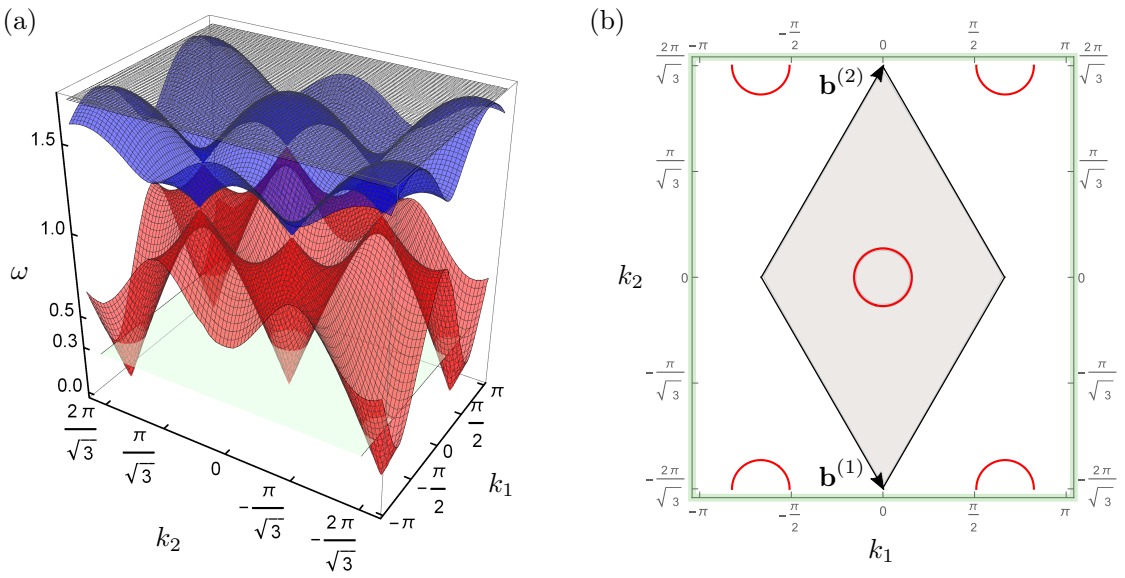

Figure 5.4: (a) Dispersion surfaces for an infinite hexagonal lattice having the material properties of the medium exterior to the cloak and the defect in Figure 5.3. A light green plane is used to indicate the frequency $\omega = 0.3$, chosen for the computations as the frequency of the applied displacement and in (b) the corresponding slowness contours are reported.

(iii) when the defect is coated by the gyro-elastic cloak, marked in red and blue in Figure 5.3(a) and (b).

As demonstrated below, without the cloak the defect would create noticeable effects, such as scattering and shielding, when interacting with waves propagating in the ambient medium. Conversely, when the cloak designed as in Figure 5.3(b) is inserted, these effects are reduced, especially in particular directions, reconstructing the wave pattern as if the defect was not present.

In all the computations presented here, the lattice is assumed to be initially at rest. Perfectly Matched Layers (PML) are used to minimise the reflections produced at the edges of the lattice. Elastic waves are generated by an applied displacement, indicated by a black arrow in Figure 5.3(a). The imposed displacement is positioned at $(75, 50\sqrt{3})$ (represented by the black dot in Figure 5.3(a)) and is expressed by $\mathbf{Q}\sin(\omega t)$, where $\mathbf{Q} = (0.5, 0)^{\mathrm{T}}$ and $\omega = 0.3$. We note that the chosen value of the frequency ω is relatively low and corresponds to an almost isotropic response of the analogous infinite medium for the material situated on the exterior of the defect, indicated in grey in Figure 5.3. In Figure 5.4(a), we show the dispersion surfaces for

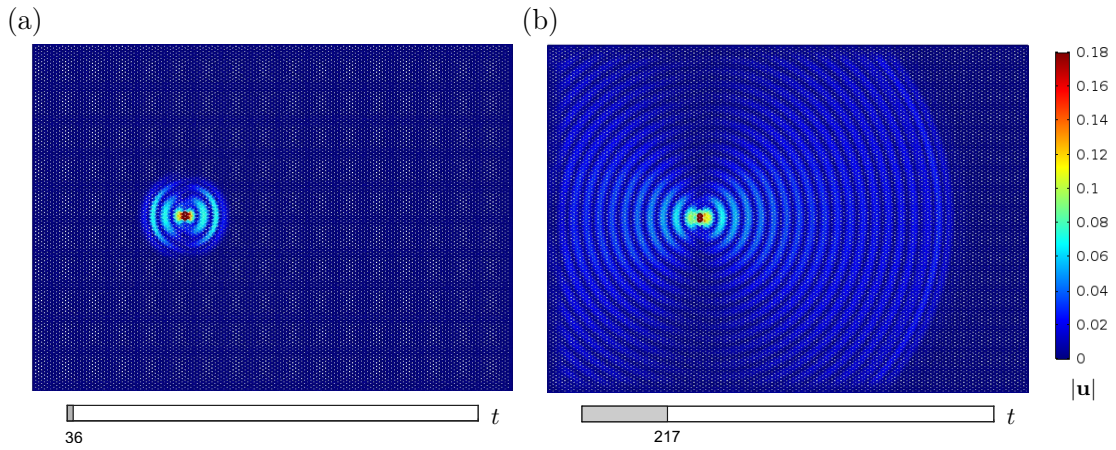

Figure 5.5: Displacement fields of the homogeneous hexagonal lattice produced by the applied displacement. The response of the lattice is shown at (a) $t = 36$ and (b) $t = 217$.

the infinite homogeneous hexagonal lattice (without defects or gyroscopic spinners) corresponding to the material properties for the medium outside the cloak and defect in Figure 5.3. The light green plane is associated with the radian frequency $\omega = 0.3$, of the sinusoidal displacement, and intersects the lowest surface. The slowness contours connected with this frequency are shown in Figure 5.4(b), that indicate the imposed lattice loading will excite a dynamically isotropic response.

We start by considering the case (i), in which the lattice is homogeneous. Figure 5.5 shows the response of the medium by the external excitation at two different times. Waves with a circular front propagate outward from the applied displacement and shadow regions can be observed in the vertical directions relative to the excitation, Figure 5.5(a). Physically, this is expected, due to the microstructure of hexagonal lattice. Additionally, we observe that the wave pattern in the lattice is not affected by interactions with the exterior boundaries due to the presence of the PML, as shown in Figure 5.5(b).

Next, we consider the case (ii) when a defect is situated in the lattice. The defect is represented by a region of nodes that are connected to each other by links stiffer than those in the ambient medium. The region of the defect, indicated by the black hexagon in Figure 5.3(b), has side length equal to 7. Figure 5.6 shows the response of the system for different time instants. The outgoing waves from the applied displacement reach the defect at $t = 36$, shown in Figure 5.6(a). Until this time, the

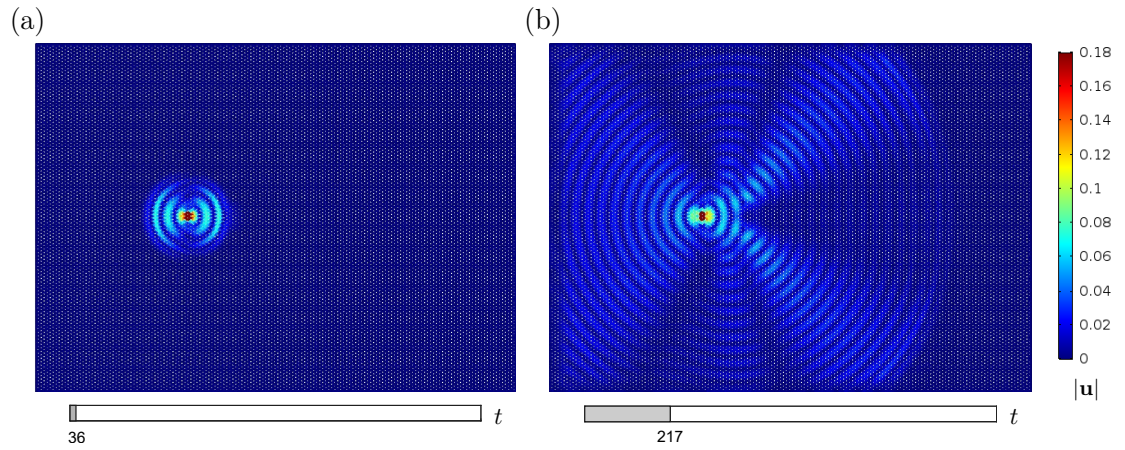

Figure 5.6: Displacement field produced by the applied displacement in the hexagonal lattice containing a stiff inclusion. The response of the lattice is shown at (a) $t = 36$ and (b) $t = 217$ of the transient simulation.

wave pattern is similar to the field produced in the homogeneous lattice (compare with Figure 5.5(a)). After $t = 36$, the left-most vertex of the defect also begins to act as a source, creating scattered waves that interact with the waves generated by the imposed displacement. The resulting wave pattern is shown in Figure 5.6(b) at $t = 217$. A clear shadow can be seen to develop on the right of the defect, in addition to other shadows created in the vertical direction. Furthermore, there are scattered waves produced by the left-most vertex of the defect that propagate at $\pm 60°$ and $\pm 90°$ to the positive horizontal direction relative to this vertex shown in Figure 5.6(b).

In Figure 5.7, we illustrate the results of the transient analysis at different time instants for the lattice with the coated defect. Until $t = 24$, the displacement pattern of the system is similar to that of the homogeneous lattice. After this instant, waves begin to interact with the gyro-elastic cloak. For $24 < t < 93$, we see scattering due to the left-most vertex of the cloak in the vertical directions and waves being re-routed through the coating around the defect. In this time interval, the displacements in the defect are visibly small, as we can see in Figure 5.7(b). After $t = 93$, the right-most vertices of the cloak begin to act as sources, producing elastic waves with circular fronts propagating away from the cloak in several directions, see Figure 5.7(c). Here, the cloak acts like a resonator, keeping the displacements in the defect region very

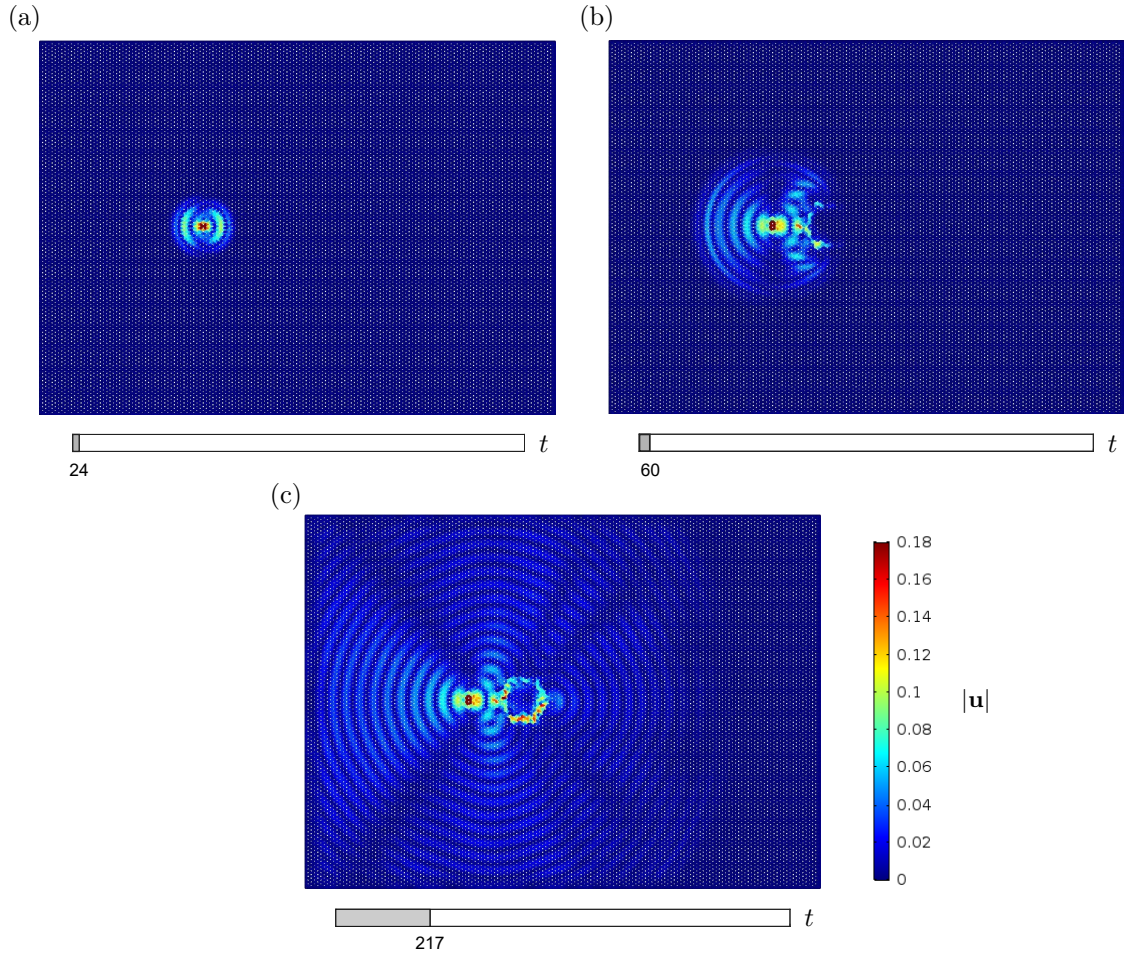

Figure 5.7: Displacement field produced by the applied displacement when the hexagonal lattice contains the defect that is coated by gyro-elastic cloak (see Figure 5.3). The response of the lattice is shown at (a) $t = 24$, (b) $t = 60$ and (c) $t = 217$.

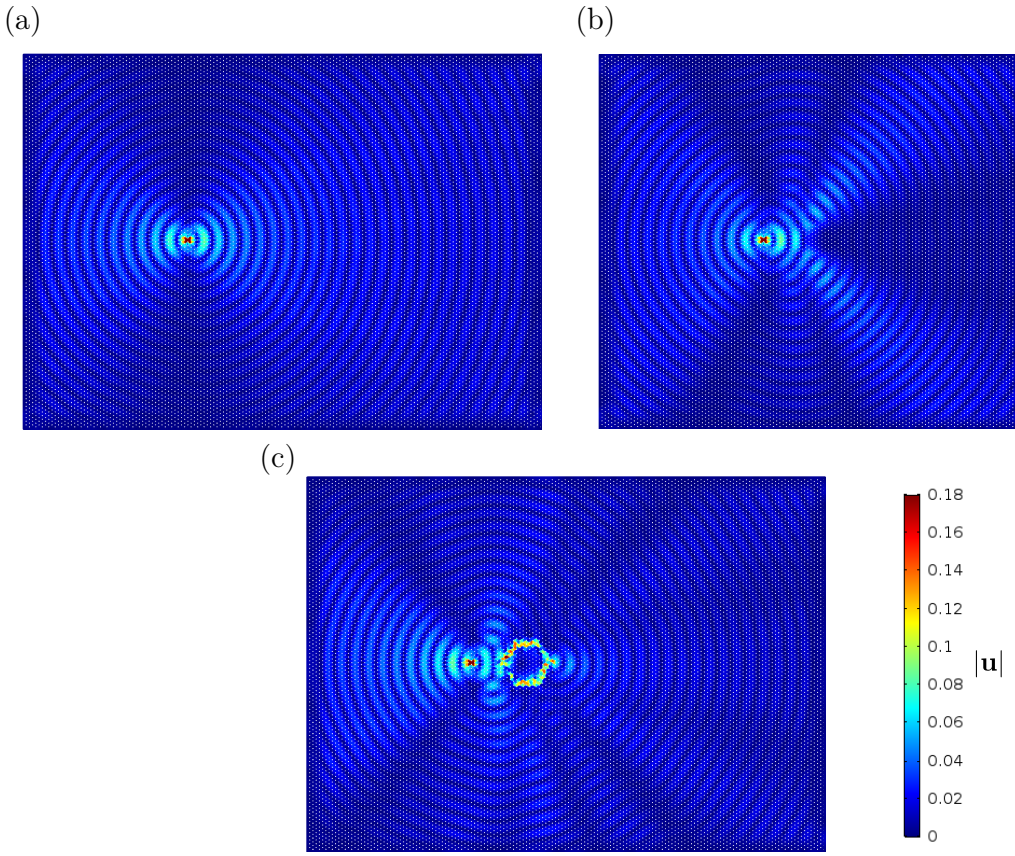

Figure 5.8: The displacement field produced by a point excitation when the hexagonal lattice (a) is homogeneous, (b) contains the defect and (c) contains the defect that is coated by the gyro-elastic cloak (see Figure 5.3). The figures show the response of the lattices at $t = 1353$.

small. Accordingly, the gyroscopic spinners inside the cloak re-route the incoming waves around the defect, leaving the cloak interior almost undisturbed.

The waves generated by the vertices of the cloak lead to a visibly excellent reconstruction of the cylindrical wave pattern observed in the homogeneous medium to the right of the cloak. We note that as this reconstruction occurs, the gyro-elastic medium undergoes large deformations in comparison to the far field generated in the ambient lattice by the source (see for example Figure 5.7(c)).

For the sake of comparison in Figure 5.8, we present the response of the medium for all three cases (i)-(iii) for a large value of time. Especially, we notice from Figure 5.8(c) that the coating is capable of reconstructing the wave pattern to the right of the defect in Figure 5.8(a) for case (i), where there would be otherwise a shadow produced by the defect, as visible in Figure 5.8(b). In addition, we see that there

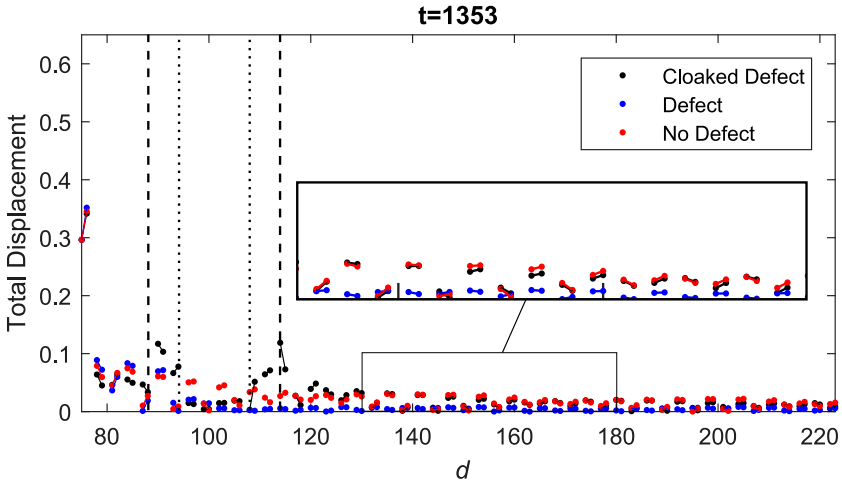

Figure 5.9: Total displacement of the hexagonal lattice subjected to a harmonic excitation, computed along the grey dashed line shown in Figure 5.3, for the case when the structure (i) is homogeneous, (ii) contains the defect and (iii) contains the defect that is coated by the gyro-elastic cloak. The location of the defect along this line is indicated by the vertical dotted lines and the gyro-elastic cloak is contained in the region between the dashed and dotted lines. A magnification of the results obtained for $130 \leq d \leq 180$ is also presented for the sake of comparison.

exist narrow regions in oblique directions where the cloaking device is less efficient in reconstructing the wave field as in the case of the homogeneous lattice.

In order to illustrate the efficiency of the cloak quantitatively, we determine the total displacements of the lattice nodes for a given time and along the horizontal dashed grey line of Figure 5.3(a). Along this line, the distance between two lattice nodes alternates between being equal to one or two lattice units. The total displacements along this line are calculated for all three computations presented in Figure 5.8 and they are plotted in Figure 5.9. The results for the case of the lattice with the defect show a significant reduction in the amplitude of the displacement field to the right of the defect, when compared with the results of the homogeneous lattice. On the other hand, the introduction of the cloak allows for a good reconstruction of the displacement field to the right of the cloak itself, to the extent that in some regions the results for the coated defect and the homogenous case are indistinguishable. In scenario (iii), we also note large displacements in the gyro-elastic cloak, which re-routes the external waves around the defect, and very small displacements in the defect region.

Figure 5.10 shows the total displacements along the dashed line at different time

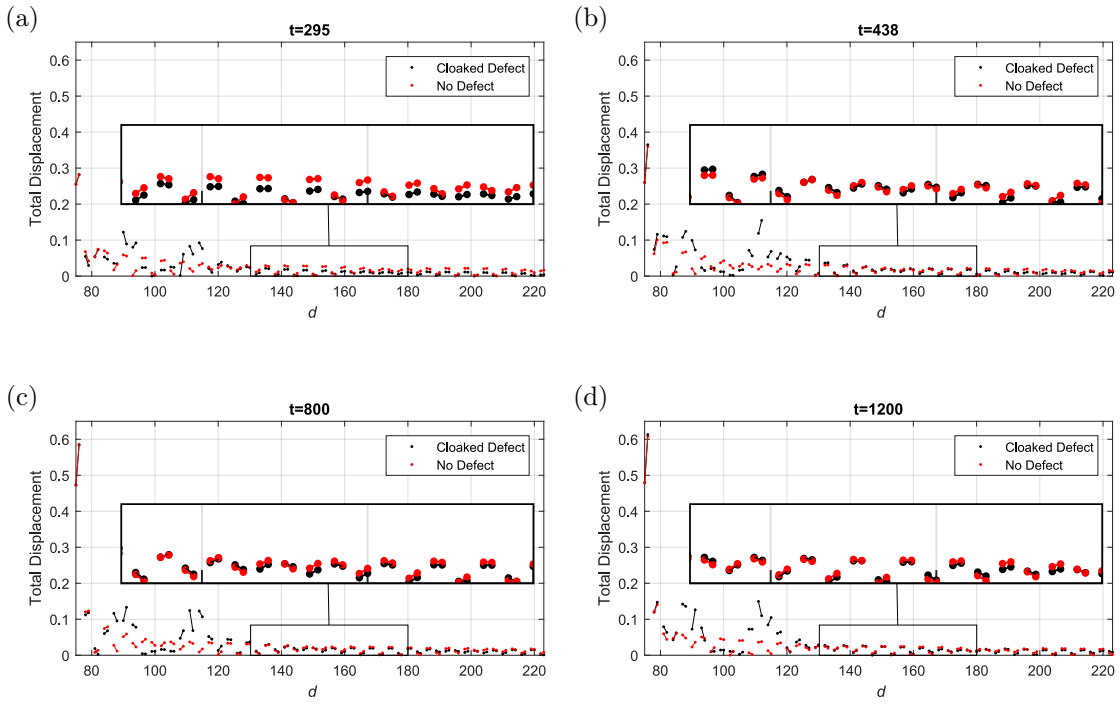

Figure 5.10: Total displacements for the hexagonal lattice subjected to a harmonic excitation, computed along the grey dashed line shown in Figure 5.3 for the cases when the structure is homogeneous and when it contains the defect that is coated by the gyro-elastic cloak. The time instants shown are (a) $t = 295$, (b) $t = 438$, (c) $t = 800$ and (d) $t = 1200$. A magnification of the results obtained for $130 \leq d \leq 180$ is also presented for the sake of comparison.

instants in the transient computations for scenarios (i) and (iii). We note until $t = 438$, the displacement fields produced in both scenarios do not match very well in both amplitude and phase. An example of this is shown in Figure 5.10(a). The Figure 5.10(b) shows how at $t = 438$ the total displacements for case of the cloaked defect reproduces approximately the displacement field for the case of the homogeneous lattice. At $t > 438$, in the region on the right of the cloak, the total displacements for the scenarios (i) and (iii) agree very well and move together in phase, as shown in the examples of Figures 5.10(c) and (d).

Finally, we recall that in the illustrations of Figure 5.8, the quantity $\alpha|\Omega|$, within the gyro-elastic cloak, is uniform. Thus, we remark that the proposed design in Figure 5.3, corresponds a structure embedding a wide class of arrays of gyroscopes, with uniform distributions of the gyricity magnitude $|\Omega|$ and physical properties characterised by α, for which the cloaking effect identified here is achievable.

Next, we demonstrate the effect of varying the $\alpha|\Omega|$ on the ability of the cloak to reconstruct the field behind the defect as if the defect were no longer present.

5.2.1 Dependency of the efficiency of the cloak on the quantity $\alpha|\Omega|$

Here, we analyse the effect of changing the parameter $\alpha|\Omega|$ on efficiency of the cloak in the transient regime.

We examine the response of the hexagonal lattice when the defect is coated by one of two choices of the gyro-elastic cloak determined by either $\alpha|\Omega| = 0.495$ or $\alpha|\Omega| = 0.519$. We replicate the arrangement in the sign of the product $\alpha\Omega$ as in Figure 5.3.

The results for $\alpha|\Omega| = 0.495$ are shown in Figure 5.11(a) at the instant $t = 1325$, computed along the dashed horizontal line of Figure 5.3(a). We notice that the quality of the reconstruction of the field is not as good as in the Figure 5.9 (see the magnification of Figure 5.11(a), where the total displacement for case (iii) clearly differs from case (i)). Nevertheless, Figure 5.11(b) demonstrates that by employing

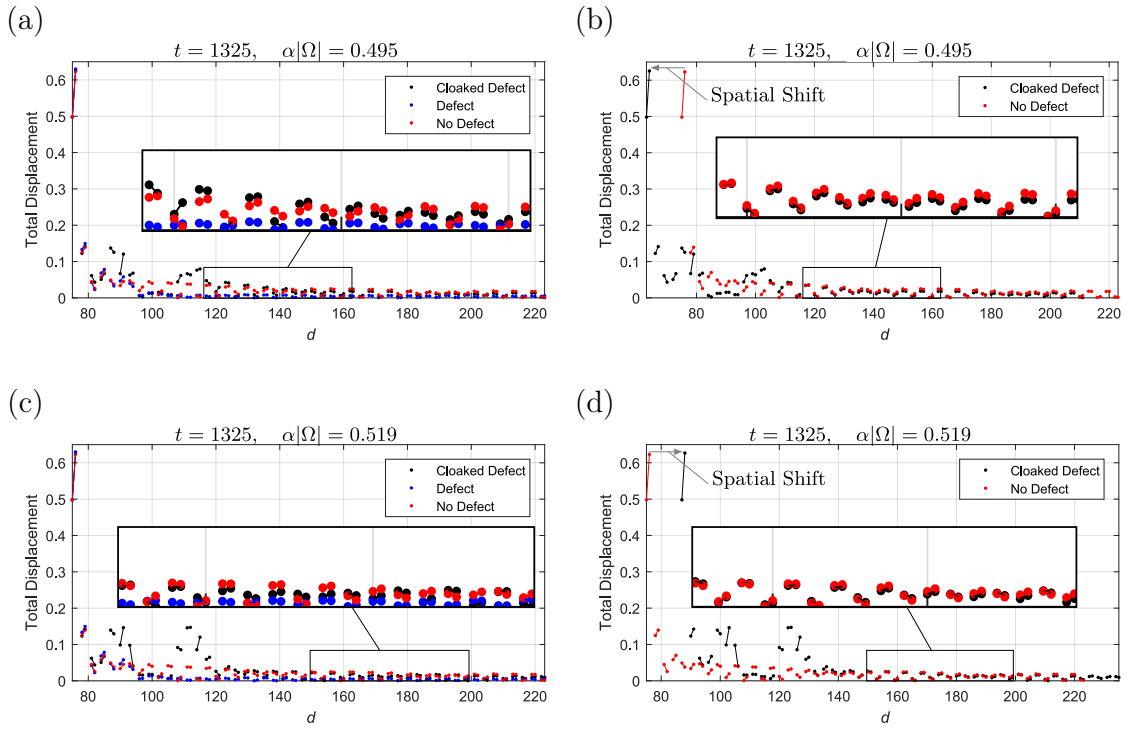

Figure 5.11: Displacement magnitude of the nodal points intersecting the dashed grey line in Figure 5.3 as a function of the position d for (a) and (b) when $\alpha|\Omega| = 0.495$ and (c) and (d) when $\alpha|\Omega| = 0.519$. In (b) and (d), the displacements for the case of the cloaked defect in (a) and (c) have been spatially shifted to the left and right, respectively. The results are given at the normalised time $t = 1325$.

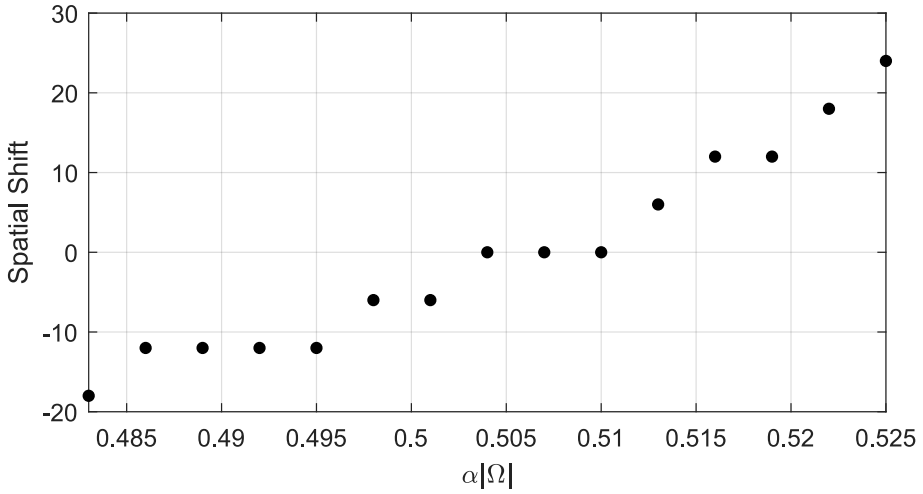

Figure 5.12: The spatial shift is shown as a function of the quantity $\alpha|\Omega|$.

a spatial shift in the data for the cloaked configuration of 12 lattice units to the left, it is possible to retrieve an excellent match.

Considering the case for $\alpha|\Omega| = 0.519$ in Figure 5.11(c), once more we show that the reconstruction of the field is not as good as in Figure 5.9. However, by once again introducing a shift of 12 units to the right for the data obtained from the cloaked configuration, we retrieve an almost perfect reconstruction of the field as shown in Figure 5.11(d).

Concerning the spatial shift that can be applied in order to obtain a good reconstruction of the field behind the defect, this is further examined in Figure 5.12 as a function of $\alpha|\Omega|$. The spatial shift is a monotonically increasing function of $\alpha|\Omega|$. For $0.504 \leq \alpha|\Omega| \leq 0.51$, no spatial shift is required. For $\alpha|\Omega|$ below (above) this interval, a negative (positive) spatial shift is needed to demonstrate the capability of the cloak in reconstructing the field.

Finally, Figures 5.13(a) and (b) show the response for the lattice with the cloaked defects possessing different $\alpha|\Omega|$. It can be concluded that apart from some clear preferential directions, Figures 5.13(a) and (b) present a clear reconstruction of the field in Figure 5.8(a) behind the defect.

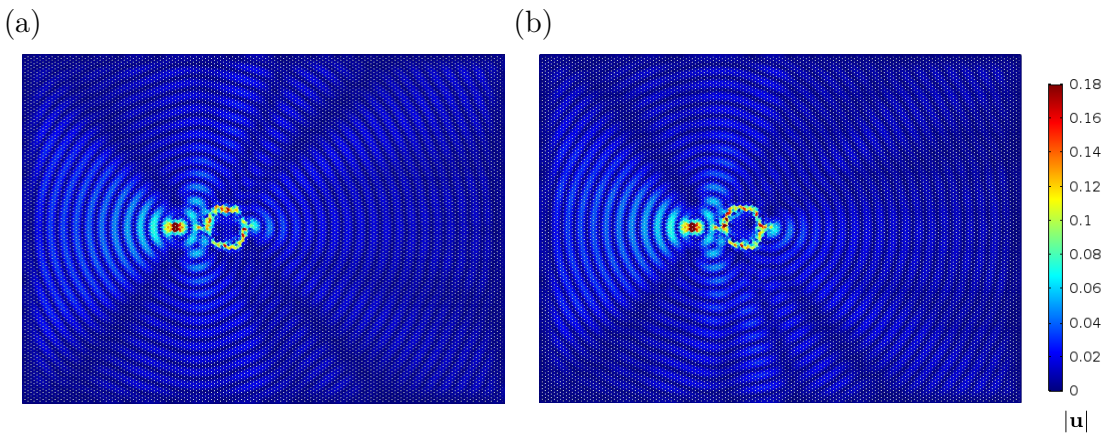

Figure 5.13: The response of the hexagonal lattice containing the cloaked defect, where for the cloak (a) $\alpha|\Omega| = 0.495$ and (b) $\alpha|\Omega| = 0.519$. The snapshots shown are taken at $t = 1325$.

5.3 Conclusion

In this chapter, two important applications of a gyro-elastic system have been developed. The first application shows that a gyro-elastic medium can be used to construct a robust topological insulator that when excited on the exterior boundary, at a given frequency, confines vibrations to this boundary, leaving the interior of the structure almost undisturbed. The second application concerns the design of a structured gyro-elastic cloak that is capable of being used as an efficient cloaking device in a lattice system. In particular, the design of the cloak embeds the product of two input parameters, concerning the type of gyroscope used and the gyricity of the gyroscope, that can be tuned to achieve the cloaking effects in addition to the apparent distance between the source and the external observer. We note that this may also be used to cloak defects within the lattice at different loading frequencies.

Chapter 6

Waves and dynamic fracture in discrete flexural structures

Another important area of study in the dynamics of structures involves determining how waves influence failure processes in such systems. In the previous Chapters, a variety of wave propagation phenomena in gyro-elastic structures were identified, but under the assumption that these structures are able to withstand such vibrations without failing.

In this Chapter, we consider waves in a discrete flexural system and identify how these processes can initiate and sustain failure propagation within these structures. The modelling of periodic flexural materials is a useful tool in understanding the behaviour of structures commonly found in civil engineering, such as buildings, bridges, rooftops, pipeline systems and many more. The need to understand the response of these structures, as shown in Figure 6.1, is greater when failure initiates and propagates through the system. The analysis presented in this Chapter introduces a simplified model that may represent the failure of a long bridge or a rooftop, involving a supported mass-beam system, whose supports undergo sequential failure with a constant speed due to vibration.

This Chapter is organised as follows. In Section 6.1, we present an analytical description of the problem concerning failure propagation in the mass-beam structure subjected to a sinusoidal load. This section also includes the reduction of the problem

(a) (b)

Figure 6.1: (a) The demolition of a bridge in Guangxi, China. The excavator in this picture was used to initiate a failure at one end of the bridge. The Figure shows the resulting periodic failure process propagating through the structure, where the supporting columns fail sequentially. An alternative view of this process is presented in (b).

to a functional equation of the Wiener-Hopf type using the Fourier transform. The characterisation of the dispersive nature of this particular discrete system is given in Section 6.2. The results of Section 6.2 are then used in Section 6.3 to solve the Wiener-Hopf equation. We also identify the dynamic properties of the system during the steady propagation of the failure modes in Section 6.4. In Section 6.5, we present numerical simulations which support the analytical results of Sections 6.1–6.4. We give some conclusions in Section 6.6.

6.1 Model of failure within a discrete periodic flexural structure

Here, we introduce the model of the supported mass-beam system shown in Figure 6.2 composed of massless Euler-Bernoulli beams connecting periodically placed masses, that undergoes failure. The failure is represented by the sequential removal of links supporting the masses along the central chain, aligned with the horizontal axis, that occurs with a constant speed.

In [Nieves, Mishuris and Slepyan (2016), Nieves, Mishuris and Slepyan (2017)], the failure process was investigated under the assumption that the supporting beams are removed if the masses along it achieve a positive displacement. The steady regimes achieved in this case are referred to here as "*pure steady-state regimes*" and assumed to be driven by a remote mechanical sinusoidal load.

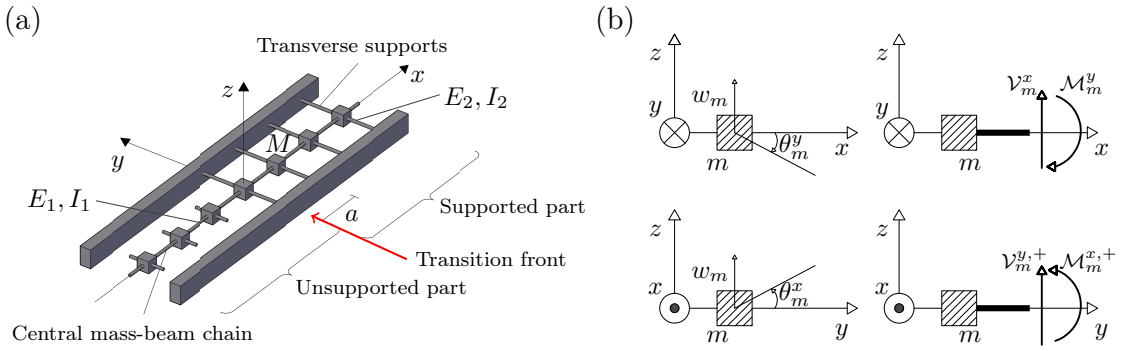

Figure 6.2: (a) A heterogeneous discrete structure composed of point masses connected by beams. (b) The convention adopted for positive direction of the displacement w_m and rotations θ^x_m and θ^y_m associated with the m^{th} mass. The positive directions for the internal bending moments $\mathcal{M}^y_m$, $(\mathcal{M}^{x,+}_m)$ and shear forces $\mathcal{V}^x_m$, $(\mathcal{V}^{y,+}_m)$ in the m^{th} beam directed from the m^{th} mass in the positive x-direction (y-direction) are also indicated.

In terms of applications, it is realistic to consider the case when the supporting links break if a positive or negative critical displacement is reached. As we show in this Chapter, along with the *pure steady-state regimes* observed in [Nieves, Mishuris and Slepyan (2016), Nieves, Mishuris and Slepyan (2017)], the imposed fracture criterion yields additional regimes that can be predicted and verified numerically. These regimes correspond to the case when, at each consecutive failure in the system, a change in the sign of the bending moments and shear forces in the supporting beams can be observed. These regimes are investigated in detail here and are referred to as "*alternating generalised strain regimes*".

6.1.1 Description of the problem

We consider a structure composed of a mass-beam chain, as shown in Figure 6.2(a). This structure is formed from periodically placed point masses, connected longitudinally (along x-axis) by massless Euler-Bernoulli beams having Young's Modulus E_1 and second moment of area I_1. Each junction node has mass M and corresponds to an index $m \in \mathbb{Z}$. All masses have negligible moments of inertia. This chain is assumed to be partially supported by transverse Euler-Bernoulli beams (parallel to the y-axis), having Young's modulus E_2 and second moment of area I_2. These beams connect the masses to an interface where the beams are clamped. All beams have length a.

Inside the structure, failure is assumed to propagate with an uniform speed V as a result of the breakage of the transverse connections to the interfaces within the structure. The front of the failure or transition front represents a moving interface between the supported and unsupported parts of the medium (see Figure 6.2(a)). A failure in the transverse breakage occurs when the *absolute value* of the displacement w_p of the p^{th} mass (where $m = p$ corresponds to the position of the transition front in the structure, see Figure 6.2(a), that depends on time) reaches a critical value w_c. Thus we assume for bonds to remain intact

$$|w_j(t)| < w_c, \quad j \geq p, \quad p \in \mathbb{Z} \tag{6.1}$$

and when the condition $w_p = \pm w_c$ is fulfilled, the transverse links at the p^{th}-mass break and the transition front advances a distance a in the structure to the $(p+1)^{th}$ node. These conditions in the analytical model considered neglect the possibility that a breakage can occur ahead of the transition front, which leads to non-uniqueness in the failure front and non-steady failure of the supports. In the numerical illustrations discussed later, such scenarios will be taken into account.

Under the conditions (6.1), we consider the case when the *generalised strains* (moments and shear forces) inside the transverse links can alternate in sign during the failure process.

6.1.2 Governing equations for the masses in the flexural structure

At a given time t, the position of the interface in the structure is given by $m = \lfloor Vt/a \rfloor$, where $\lfloor x \rfloor$ denotes the integer part of x.

Here, the inequality $m \geq \lfloor Vt/a \rfloor$ corresponds to masses located in the supported part of the structure and $m < \lfloor Vt/a \rfloor$ are those in the unsupported region of the structure (see Figure 6.2(a)). In the medium shown in Figure 6.2, the masses experience forces and moments supplied by the beam connections. Hence, the motion

of each mass involves both displacement and rotation. In what follows, we neglect the influence of gravity and assume the masses do not undergo rotations about the x-axis.

Therefore, the equations for the balance of linear and angular momentum for the m^{th} mass, $m \in \mathbb{Z}$, are

$$M\frac{\mathrm{d}^2 w_m(t)}{\mathrm{d}t^2} = \mathcal{V}_m^x(0,t) - \mathcal{V}_{m-1}^x(a,t) + H(x-Vt)(\mathcal{V}_m^{y,+}(0,t) - \mathcal{V}_m^{y,-}(a,t)) + Q_m(t), \quad (6.2)$$

$$\mathcal{M}_m^y(0,t) = \mathcal{M}_m^y(a,t), \quad (6.3)$$

where H is the Heaviside function

$$H(x) = \begin{cases} 1\,, & \text{if } x \geq 0\,, \\ 0\,, & \text{otherwise}\,, \end{cases}$$

and the term $Q_m(t)$, $m \in \mathbb{Z}$ represents an external load or force applied to the structure at each nodal point. Later we will link this external action to a remote sinusoidal load that helps to propagate the failure in the medium.

In (6.2) and (6.3), $\mathcal{M}_m^y(\tilde{x},t)$ and $\mathcal{V}_m^x(\tilde{x},t)$, denote the y-component of the moment vector and the shear forces in the m^{th} horizontal beam, respectively, at time t and position $\tilde{x}$ along the beam, where $0 < \tilde{x} < a$, (see Figure 6.2(b)). Additionally, $\mathcal{V}_j^{y,+}(y_+,t)$ and $\mathcal{V}_j^{y,-}(y_-,t)$ correspond to the shear forces in the transverse beam located at $0 < y < a$ and $-a < y < 0$, respectively, for $x = ja$ where $j \geq \lfloor Vt/a \rfloor$ (see Figure 6.2 for the convention adopted with these forces). Here, the notation $\tilde{y}_+ = y$ ($\tilde{y}_- = y + a$) represents the local coordinate for the transverse beam located at $y > 0$ ($y < 0$).

In what follows, we show that equations (6.2) and (6.3) can be written as a finite difference problem involving the generalised coordinates w_m and θ_m, $m \in \mathbb{Z}$,

describing the motion of each mass (see Figure 6.2(b)):

$$6\left\{2[2w_m(t) - w_{m-1}(t) - w_{m+1}(t)] - a[\theta^y_{m+1}(t) - \theta^y_{m-1}(t)]\right\} + 24rw_m(t)H(m - Vt/a) + \frac{Ma^3}{E_1I_1}\frac{\mathrm{d}^2w_m(t)}{\mathrm{d}t^2} = \frac{a^3}{E_1I_1}Q_m(t) \quad (6.4)$$

and

$$3[w_{m+1}(t) - w_{m-1}(t)] + a[\theta^y_{m+1}(t) + \theta^y_{m-1}(t) + 4\theta^y_m(t)] = 0\,, \quad (6.5)$$

where the contrast parameter $r = E_2I_2/E_1I_1$. We also show the rotation θ^x_m for $m = 0$ about the x-axis can be neglected.

Derivation of the governing equations (6.4) and (6.5)

We follow the approach of Section 2.2 of Chapter 2 and construct the governing equations for the structure of Figure 6.2, taking into account that the connections linking the masses are flexural massless elements.

The displacements W_m and $W^{\pm}_j$, along the horizontal and transverse beams, respectively, can be found by solving the Euler-Bernoulli equations:

$$\frac{\mathrm{d}^4W_m}{\mathrm{d}\tilde{x}^4}(\tilde{x}, t) = 0\,, \quad 0 < \tilde{x} < a\,, m \in \mathbb{Z}$$

and

$$\frac{\mathrm{d}^4W^{\pm}_j}{\mathrm{d}\tilde{y}^4_{\pm}}(\tilde{y}_{\pm}, t) = 0\,, \quad 0 < \tilde{y}_{\pm} < a\,, j > \lfloor Vt/a \rfloor\,, j \in \mathbb{Z}\,,$$

for $t > 0$, where the local coordinates $\tilde{x} = x - am$, $\tilde{y}_+ = y$ and $\tilde{y}_- = y + a$. The function W_m satisfies the boundary conditions

$$W_m(0, t) = w_m(t)\,, \quad \frac{\mathrm{d}W_m}{\mathrm{d}\tilde{x}}(0, t) = -\theta^y_m(t)\,,$$

$$W_m(a, t) = w_{m+1}(t)\,, \quad \frac{\mathrm{d}W_m}{\mathrm{d}\tilde{x}}(a, t) = -\theta^y_{m+1}(t)\,,$$

which represent the connection of the m^{th} beam to the masses at its ends. The

function W_m^+ is subject to the conditions

$$W_m^+(0,t) = w_m(t) \ , \quad \frac{\mathrm{d}W_m^+}{\mathrm{d}\tilde{y}}(0,t) = \theta_m^x(t) \ , \quad W_m^+(a,t) = 0 \ , \quad \frac{\mathrm{d}W_m^+}{\mathrm{d}\tilde{y}}(a,t) = 0 \ ,$$

whereas W_m^- satisfies

$$W_m^-(0,t) = 0 \ , \quad \frac{\mathrm{d}W_m^-}{\mathrm{d}\tilde{y}}(0,t) = 0 \ , \quad W_m^-(a,t) = w_m(t) \ , \quad \frac{\mathrm{d}W_m^-}{\mathrm{d}\tilde{y}}(a,t) = \theta_m^x(t) \ ,$$

where here the homogeneous conditions represent the clamping of the beam to the rigid interfaces. Thus, it can be concluded from the above that

$$\begin{aligned} W_m(\tilde{x},t) = &-[a(\theta_m^y(t) + \theta_{m+1}^y(t)) - 2(w_m(t) - w_{m+1}(t))]\frac{\tilde{x}^3}{a^3} \\ &+[a(2\theta_m^y(t) + \theta_{m+1}^y(t)) - 3(w_m(t) - w_{m+1}(t))]\frac{\tilde{x}^2}{a^2} - \theta_m^y(t)\tilde{x} + w_m(t) \ , \end{aligned} \tag{6.6}$$

and

$$W_m^+(\tilde{y}_+,t) = [a\theta_m^x(t) + 2w_m(t)]\frac{\tilde{y}_+^3}{a^3} - [2a\theta_m^x(t) + 3w_m(t)]\frac{\tilde{y}_+^2}{a^2} + \theta_m^x(t)\tilde{y}_+ + w_m(t) \ , \tag{6.7}$$

$$W_m^-(\tilde{y}_-,t) = [a\theta_m^x(t) - 2w_m(t)]\frac{\tilde{y}_-^3}{a^3} - [a\theta_m^x(t) - 3w_m(t)]\frac{\tilde{y}_-^2}{a^2} \ . \tag{6.8}$$

Next, it remains to compute the moments and shear forces produced by the beams, which requires computing second and third order derivatives of these displacement functions. Note, in the considered phase transition problem, the transverse supports fail at the connections to rigid interface. In this case, behind the transition front, the transverse beams are attached to the masses at one end and are free at the other. At the free end, the bending moments and shear forces are zero. Hence, the displacements along these beams can be shown to be linear functions. Consequently, they do not contribute to the linear and angular momentum balance of the masses behind the transition front (for instance, see (6.2)).

The bending moments in the transverse beams applied about the x-axis can be calculated via

$$\mathcal{M}_m^{x,\pm}(\tilde{y}_\pm, t) = E_2 I_2 \frac{\mathrm{d}^2 W_m^\pm}{\mathrm{d}\tilde{y}_\pm^2}(\tilde{y}_\pm, t) \ .$$

Hence, using (6.7) and (6.8),

$$\mathcal{M}_m^{x,\pm}(\tilde{y}_\pm, t) = \pm \frac{E_2 I_2}{a^3} w_m(t)[2\tilde{y}_\pm - a] \ . \tag{6.9}$$

The angular momentum balance about the y-axis for a mass in the supported region then gives

$$\mathcal{M}_m^{x,+}(0,t) - \mathcal{M}_m^{x,-}(a,t) = 0 \ ,$$

where the right-hand side is zero as it is assumed all masses have negligible moments of inertia. This together with (6.7) and (6.8) implies $\theta_m^x = 0$ in the supported region, justifying the assumption the masses do not rotate about the x-axis.

The shear forces in the transverse beams then have the form

$$\mathcal{V}_m^{y,\pm}(\tilde{y}_\pm, t) = -E_2 I_2 \frac{\mathrm{d}^3 W_m^\pm}{\mathrm{d}\tilde{y}_\pm^3}(\tilde{y}_\pm, t)$$

and using (6.7) and (6.8) leads to

$$\mathcal{V}_m^{y,\pm}(y_\pm, t) = \mp \frac{12 E_2 I_2}{a^3} w_m(t) \ . \tag{6.10}$$

Here, (6.9) and (6.10), show if the sign of the mass displacement alternates between each instant of fracture then the sign of the generalised strains, i.e. bending moments and shears forces, in the links that fail will alternate in sign.

The internal bending moments and shear forces in the m^{th} beam aligned with the horizontal axis, (see Figure 6.2) are computed via

$$\mathcal{M}_m^y(\tilde{x}, t) = -E_1 I_1 \frac{\mathrm{d}^2 W_m}{\mathrm{d}\tilde{x}^2}(\tilde{x}, t) \quad \text{and} \quad \mathcal{V}_m^x(\tilde{x}, t) = -E_1 I_1 \frac{\mathrm{d}^3 W_m}{\mathrm{d}\tilde{x}^3}(\tilde{x}, t) \ , \tag{6.11}$$

respectively. Insertion of (6.6) into these relations yields

$$\mathcal{M}^y_m(\tilde{x},t)=-\frac{2E_1I_1}{a^3}[a^2\theta^y_m(t)+a(a-3\tilde{x})(\theta^y_m(t)+\theta^y_{m+1}(t))-3(2\tilde{x}-a)(w_{m+1}(t)-w_m(t))]\,, \tag{6.12}$$

$$\mathcal{V}^x_m(\tilde{x},t)=\frac{6E_1I_1}{a^3}[a(\theta^y_m(t)+\theta^y_{m+1}(t))-2(w_m(t)-w_{m+1}(t))]\,, \tag{6.13}$$

which are written in terms of the generalised coordinates describing the motion of the m^{th} mass and where w_m is the displacement and θ^y_m is the rotation about the y-axis of the m^{th} mass. Combining (6.10), (6.12) and (6.13) with (6.2) and (6.3), we obtain (6.4) and (6.5).

6.1.3 Derivation of the Wiener-Hopf equation

In (6.4) and (6.5), we introduce the normalisations

$$\tilde{t}=t\sqrt{\frac{E_1I_1}{Ma^3}}\,,\quad \tilde{v}=V\sqrt{\frac{Ma}{E_1I_1}},\quad \tilde{w}_m(\tilde{t})=\frac{w_m(t)}{a},\quad \tilde{Q}_m(\tilde{t})=\frac{a^2}{E_1I_1}Q_m(t),$$

where the symbol “tilde" will be omitted in the following for ease of notation. In this case, the dimensionless governing equations for the system are then

$$6\,\{2[2w_m(t)-w_{m-1}(t)-w_{m+1}(t)]-[\theta^y_{m+1}(t)-\theta^y_{m-1}(t)]\} + 24rw_m(t)H(m-vt)+\frac{\mathrm{d}^2w_m(t)}{\mathrm{d}t^2}=Q_m(t)\,, \tag{6.14}$$

and

$$3[w_{m+1}(t)-w_{m-1}(t)]+[\theta^y_{m+1}(t)+\theta^y_{m-1}(t)+4\theta^y_m(t)]=0\,. \tag{6.15}$$

Since we consider the case of alternating generalised strains, we look for the displacements and the rotations as functions of the moving coordinate $\eta=m-vt$ as follows

$$w_m(t)=(-1)^m w(\eta),\quad \theta^y(t)=(-1)^m\theta^y(\eta)\,, \tag{6.16}$$

where $w(\eta)$ and $\theta(\eta)$ play the role of envelope functions (see [Mishuris, Movchan and

Slepyan (2009)]). In addition, we assume the load takes the form $Q_m(t) = (-1)^m Q(\eta)$.

We introduce the Fourier transforms with respect to the variable η for the quantities $w^{\rm F}$, $\theta^{y{\rm F}}$ as

$$\{w^{\rm F}, \theta^{y{\rm F}}\} = \int_{-\infty}^{\infty} \{w(\eta), \theta^y(\eta)\} e^{{\rm i}k\eta} d\eta \ ,$$

where k is the dimensionless wavenumber. Later, we will also use the shift property of the Fourier transform:

$$\{(w(\eta+n))^{\rm F}, (\theta^y(\eta+n))^{\rm F}\} = e^{-{\rm i}nk}\{w^{\rm F}, \theta^{y{\rm F}}\} \ , \qquad n \in \mathbb{Z} \ , \tag{6.17}$$

and the formula

$$\left\{\left(\frac{{\rm d}^j w}{{\rm d}\eta^j}(\eta)\right)^{\rm F}, \left(\frac{{\rm d}^j \theta^y}{{\rm d}\eta^j}(\eta)\right)^{\rm F}\right\} = (0 + {\rm i}k)^j \{w^{\rm F}, \theta^{y{\rm F}}\} \ , \qquad j \geq 0, \quad j, n \in \mathbb{Z} \ , \tag{6.18}$$

(see [Slepyan (2002b)]). Here

$$0 + {\rm i}kv = \lim_{\varepsilon \to +0} (\varepsilon + {\rm i}kv) \ , \tag{6.19}$$

in (6.18) appears as a result of the causality principle discussed in [Slepyan (2002b)], and represents the passing from the transient regime to the steady-state regime in the Laplace transform.

The following "half" transforms are also used:

$$w_\pm(k) = \int_{-\infty}^{\infty} w(\eta) e^{{\rm i}k\eta} H(\pm\eta) d\eta \ , \quad \pm {\rm Im}\ k > 0 \ , \qquad w^{\rm F} = w_+ + w_- \ , \tag{6.20}$$

where w_+ (w_-) corresponds to a function analytic in the upper (lower) half of the complex plane defined by k (see [Slepyan (2002b), Hochstadt (2011)]), i.e. w_+ (w_-) possess no singularities and can be represented by a convergent powers series at any point of the upper (lower) complex plane. We assume a priori that the displacements and rotations in the medium are bounded and as a result one can show from the

(6.20) that $w_{\pm} \to 0$ as $\mathrm{Im}(k) \to \pm\infty$.

After substitution of (6.16) into (6.14) and (6.15), we obtain

$$6\left\{2[2w(\eta)+w(\eta-1)+w(\eta+1)]+[\theta^y(\eta+1)-\theta^y(\eta-1)]\right\} + 24rw(\eta)H(\eta)+v^2\frac{\mathrm{d}^2w(\eta)}{\mathrm{d}\eta^2}=Q(\eta) \quad (6.21)$$

and

$$-3[w(\eta+1)-w(\eta-1)]+[4\theta^y(\eta)-\theta^y(\eta+1)-\theta^y(\eta-1)]=0\,. \quad (6.22)$$

The Fourier transform of (6.22) with respect to the moving coordinate η leads to

$$\theta^{y\mathrm{F}}=-\frac{3\mathrm{i}\sin(k)}{2-\cos(k)}w^{\mathrm{F}} \quad (6.23)$$

and together with the Fourier transform of (6.21) we then obtain

$$h_1(k,0+\mathrm{i}kv)w_+ + h_2(k,0+\mathrm{i}kv)w_-= Q^{\mathrm{F}}\,, \quad (6.24)$$

where Q^{F} is the Fourier transform of the load Q and

$$h_j(k,Y)=\Omega_j^2(k+\pi)+Y^2\,, \quad j=1,2, \quad (6.25)$$

$$\Omega_1(k)=\sqrt{\frac{48\sin^4(k/2)}{2+\cos(k)}+24r}\,, \qquad \Omega_2(k)=\sqrt{\frac{48\sin^4(k/2)}{2+\cos(k)}}\,. \quad (6.26)$$

Note that the expressions (6.26) correspond to dispersion relations for the problem in [Nieves, Mishuris and Slepyan (2016), Nieves, Mishuris and Slepyan (2017)], where the fracture was considered for the pure steady-state failure regimes.

6.2 Characterisation of waves in the structure

As in [Slepyan (2002b)], the dispersive properties of the structure can be determined from the zeros of h_j, $j=1,2$, in (6.24). We will see later that the zeros of h_j,

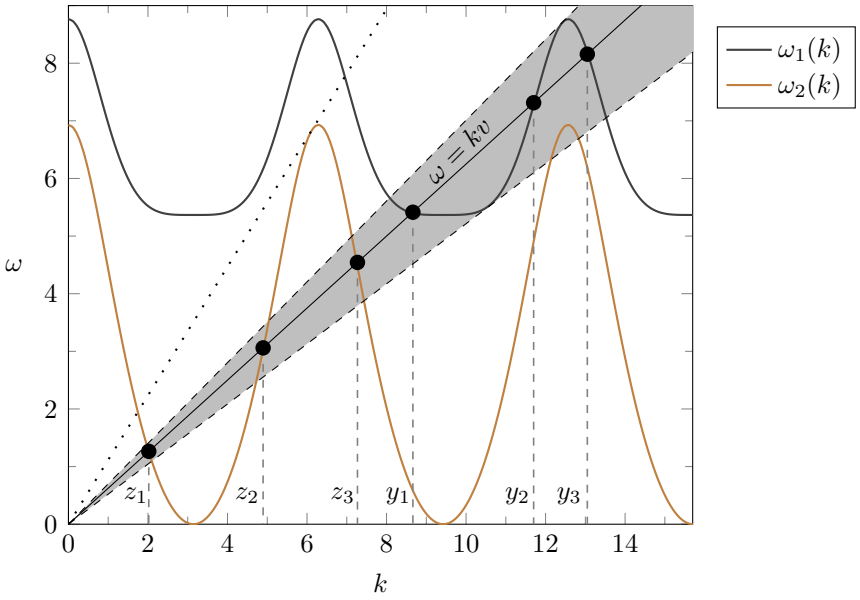

Figure 6.3: Dispersion diagrams for equations (6.27) and (6.28) are shown as functions of the wavenumber k for $r = 1.2$. The ray $\omega = kv$ intersects the dispersion curves at points, shown as dots, with the k-coordinates y_1, y_2, y_3 and z_1, z_2, z_3 that are solutions of h_1 and h_2, respectively. The dotted inclined line has the gradient $v_1 = 1.117$ and represents the upper bound of the alternating generalised strain failure regime. The dashed inclined lines represent the bounds for the speeds of possible transmission regimes, where waves propagating ahead of the transition front can occur. The occurrence of such regimes can increase with decrease of the failure speed. Outside these intervals, failure regimes where evanescent waves propagate ahead of the transition front are encountered.

$j = 1, 2$, define simple poles linked to waves propagating in the medium as it fails. In replacing Y by $\mathrm{i}\omega$ in (6.25) and rearranging for ω we obtain the dispersion relations

$$\omega_1(k) = \Omega_1(k + \pi) = \sqrt{\frac{48\cos^4(k/2)}{2 - \cos(k)} + 24r}\,, \tag{6.27}$$

for the waves ahead of the transition front and

$$\omega_2(k) = \Omega_2(k + \pi) = \sqrt{\frac{48\cos^4(k/2)}{2 - \cos(k)}}\,, \tag{6.28}$$

for waves behind the transition front.

Waves inside the structure are assumed to propagate as a result of either the external action from a remote load or through dissipation from the transition front. These waves can be identified from the functions in (6.25). In Figure 6.3, we give a representative example showing the dispersion curves ω_1 and ω_2 as functions of the wave number k, based on (6.27)–(6.28), along with the line $\omega = kv$.

Characterisation of the waves. Intersections of the line defined by $\omega = kv$ with the curve based on the relation ω_1 in (6.27) represent waves propagating ahead of the transition front ($\eta \geq 0$). Those intersection points of this line with ω_2, given by (6.28), correspond to waves behind the transition front ($\eta < 0$).

By computing the group velocity of the wave defined by $v_g = d\omega/dk$ at each intersection point, it is possible to determine the direction of propagation of the wave. For any intersection point of the curve given by ω_1 with the line $\omega = kv$ where $v_g < v$ or $v_g > v$ indicates a wave propagating in the supported region towards or away from the transition front, respectively. In a similar way, any intersection of the curve provided by ω_2 with the ray $\omega = kv$ where $v_g > v$ or $v_g < v$ indicates a wave propagating in the unsupported region towards or away from the transition point, respectively.

Roots of the functions h_j***,*** $j = 1, 2$***.*** Here we describe, in general, possible roots of the functions h_j, $j = 1, 2$, which will determine the waves inside the structure. These roots are associated with the intersections of the rays $\omega = kv$ and the curves corresponding to the functions ω_j, $j = 1, 2$.

For the failure process with speed v to occur, it is required that there exists one intersection point of the line $\omega = kv$ with the curve ω_2 where $v_g > v$. Such a point defines a wave that can propagate behind and deliver energy to the transition front. Hence, for the analytical model presented here, we consider the speed range $0 < v \leq v_1 = 1.117$. Here, the upper bound determines the maximum speed for which the failure process can occur under the alternating generalised strain regime. This upper bound is the slope of the dotted inclined line in Figure 6.3.

Zeros of h_1*.* The function $h_1(k, \mathrm{i}kv)$ has one, three or more pairs of simple zeros at the points $k = \pm y_1, \pm y_2, \ldots, \pm y_{2b+1}$, with $b \in \mathbb{Z}$, $b \geq 0$.

Here b depends on the speed v. Prior to taking the limit in (6.19), according to [Slepyan (2002b)], these zeros are located in the complex plane and possess a small imaginary part. The sign of the imaginary part is then determined by comparing the group velocity v_g with the failure speed v. For the points

1. with $k = \pm y_1, \ldots, \pm y_{2b+1}$, the group velocity $v_g < v$ and

2. with $k = \pm y_2, \ldots, \pm y_{2b}$, the group velocity $v_g > v$.

If $v_g < v$ ($v_g > v$), these points are located in the upper (lower) part of the complex plane defined by k. Thus in the limit (6.19), we have $k = \pm y_1 + \mathrm{i}0, \ldots, \pm y_{2b+1} + \mathrm{i}0$ and $k = \pm y_2 - \mathrm{i}0, \ldots, \pm y_{2b} - \mathrm{i}0$.

Here, the points with $v_g < v$ can represent waves produced by a load situated far ahead of the transition front. In the loading problem considered in the next section, the points with $v_g > v$ will be associated with transmitted waves that propagate ahead of the transition front in the steady-state failure process. These waves can appear for particular failure speeds and an example of an interval of such speeds is shown in the shaded region in Figure 6.3. In this case, the boundaries of this region correspond to the failure speeds $v = 0.5214$ and $v = 0.703$.

Zeros of h_2. The function $h_2(k, \mathrm{i}kv)$ can have three, five or more pairs of simple zeros at $k = \pm z_1, \pm z_2, \pm z_3, \ldots, \pm z_{2l+1}$, $l \in \mathbb{Z}$, $l \geq 1$. Again l is a parameter which depends on the speed v. For

1. $k = \pm z_1, \pm z_3, \ldots, \pm z_{2l+1}$, we have $v_g < v$,

2. $k = \pm z_2, \pm z_4, \ldots, \pm z_{2l}$, it holds that $v_g > v$.

Again, in the limit in (6.19), we receive $k = \pm z_1 + \mathrm{i}0, \ldots, \pm z_{2l+1} + \mathrm{i}0$ and $k = \pm z_2 - \mathrm{i}0, \ldots, \pm z_{2l} - \mathrm{i}0$. In the next section, we consider the problem of the loading of the structure and the wave numbers with a negative or positive imaginary part will correspond to (i) feeding waves generated by the load (with $v_g > v$) or (ii) reflected waves ($v_g < v$), respectively, that appear behind the transition front during the steady failure regime.

6.3 The Wiener-Hopf equation and fracture criterion

Here, we identify solution of (6.24), which involves the use of the Wiener-Hopf technique. We rewrite (6.24) in the form

$$w_+ + \frac{\Psi_+(k)}{\Psi_-(k)} L(k) w_- = \frac{Q^{\mathrm{F}}}{h_1(k, 0 + \mathrm{i}kv)} \,, \tag{6.29}$$

with

$$\Psi_+(k) = \frac{\displaystyle\prod_{i=1}^{l} (0 - \mathrm{i}(k - z_{2i}))(0 - \mathrm{i}(k + z_{2i}))}{(1 - \mathrm{i}k)^{2(l-b)} \displaystyle\prod_{j=1}^{b} (0 - \mathrm{i}(k - y_{2j}))(0 - \mathrm{i}(k + y_{2j}))} \,, \tag{6.30}$$

$$\Psi_-(k) = \frac{(1 + \mathrm{i}k)^{2(l-b)} \displaystyle\prod_{j=0}^{b} (0 + \mathrm{i}(k - y_{2j+1}))(0 + \mathrm{i}(k + y_{2j+1}))}{\displaystyle\prod_{i=0}^{l} (0 + \mathrm{i}(k - z_{2i+1}))(0 + \mathrm{i}(k + z_{2i+1}))} \,, \tag{6.31}$$

where $\prod_{j=1}^{0} = 1$ and

$$L(k) = \frac{\Psi_-(k)}{\Psi_+(k)} \frac{h_2(k, 0 + \mathrm{i}kv)}{h_1(k, 0 + \mathrm{i}kv)} \,. \tag{6.32}$$

Here, the function $L(k)$ has none of zeros or poles that have been shifted from the real line owing to the ratio involving $\Psi_\pm$.

One can check that the function $L(k)$ also satisfies for $k \in \mathbb{R}$

$$\mathrm{Re}(L(k)) = \mathrm{Re}(L(-k)) \quad \text{and} \quad \mathrm{Im}(L(k)) = -\mathrm{Im}(L(-k)) \,. \tag{6.33}$$

In addition, the functions $\Psi_\pm$ have the asymptotes:

$$\Psi_\pm(k) = 1 + \frac{2\mathrm{i}(b - l)}{k} + O\Big(\frac{1}{k^2}\Big) \tag{6.34}$$

and so $L(k) \to 1$ as $k \to \pm\infty$. Further, the index or winding number of the function

$L(k)$ is zero. The latter implies the function $L(k)$ for $k \in \mathbb{R}$ determines a contour in the complex plane that does not loop around the origin.

Then, as a result of the above conditions satisfied by $L(k)$, this function can be written using the Cauchy-type factorisation in the form:

$$L(k) = L_+(k)L_-(k) \ , \quad L_\pm(k) = \exp\left(\pm\frac{1}{2\pi \mathrm{i}}\int_{-\infty}^{\infty}\frac{\ln L(\xi)}{\xi - k}\,d\xi\right) \ , \quad \pm\mathrm{Im}(k) > 0 \ . \tag{6.35}$$

In this representation, the function L_+ (L_-) is analytic in the upper (lower) half of the complex plane defined by k. We note, for $k \to \infty$, (6.35) gives the asymptote:

$$L_\pm(k) = 1 \pm \frac{\mathrm{i}}{2\pi k}\int_{-\infty}^{\infty}\ln L(\xi)\,d\xi + O\Big(\frac{1}{k^2}\Big) \ . \tag{6.36}$$

Then, (6.29) can be written in the form of the Wiener-Hopf equation

$$\frac{1}{L_+(k)\Psi_+(k)}w_+ + \frac{1}{\Psi_-(k)}L_-(k)w_- = \frac{Q^{\mathrm{F}}}{L_+(k)\Psi_+(k)h_1(k, 0 + \mathrm{i}kv)} \ . \tag{6.37}$$

6.3.1 The solution of the Wiener-Hopf equation

As in [Slepyan (2002b)], non-trivial solutions of (6.37) correspond to singular points of the right-hand side. Such singular points occur when

$$L_+(k)\Psi_+(k)h_1(k, 0 + \mathrm{i}kv) = 0 \ .$$

As $L(k)$ has no real zeros and, referring to Section 6.2 and (6.30), we note the above left-hand side is only zero when $k = \pm y_{2j+1} - \mathrm{i}0$, $0 \le j \le b$, and $k = \pm z_{2j} - \mathrm{i}0$, $1 \le j \le l$. The points $k = \pm y_{2j+1} - \mathrm{i}0$, $0 \le j \le b$, correspond to the action of a remote force ahead of the transition front as they are associated with the inequality $v_g < v$. On the other hand, the points $k = \pm z_{2j} - \mathrm{i}0$, $1 \le j \le l$, represent the loading from behind the transition front (with $v_g > v$).

Here, we assume that the loading of the structure takes the form of an oscillatory mechanical load. This load is situated at some point far from the transition front on

the negative x-axis with frequency $\omega_0 = vk_f$, where we note in addition $\omega_0 = \omega_2(k_f)$. Here k_f, corresponds to a feeding wave that causes the failure to propagate with constant speed v (see Section 6.5.2 for the description of how k_f is chosen). Following [Slepyan (2002b)], this allows one to rewrite the right-hand side of (6.37) as

$$\begin{aligned}\frac{1}{L_+(k)\Psi_+(k)}w_+ + \frac{L_-(k)}{\Psi_-(k)}w_- &= \frac{Ce^{\mathrm{i}\phi}}{0-\mathrm{i}(k-k_f)} + \frac{\overline{C}e^{-\mathrm{i}\phi}}{0-\mathrm{i}(k+k_f)} \\ &\quad + \frac{Ce^{\mathrm{i}\phi}}{0+\mathrm{i}(k-k_f)} + \frac{\overline{C}e^{-\mathrm{i}\phi}}{0+\mathrm{i}(k+k_f)}\,, \end{aligned} \tag{6.38}$$

where ϕ is the phase of the feeding wave and C is a constant to be linked to the amplitude of the feeding wave. Here the right-hand side represents the action of a sinusoidal load in the medium. This equation can be rearranged so that

$$\begin{aligned}&\frac{1}{L_+(k)\Psi_+(k)}w_+ - \left[\frac{Ce^{\mathrm{i}\phi}}{0-\mathrm{i}(k-k_f)} + \frac{\overline{C}e^{-\mathrm{i}\phi}}{0-\mathrm{i}(k+k_f)}\right] \\ &\qquad = \frac{Ce^{\mathrm{i}\phi}}{0+\mathrm{i}(k-k_f)} + \frac{\overline{C}e^{-\mathrm{i}\phi}}{0+\mathrm{i}(k+k_f)} - \frac{L_-(k)}{\Psi_-(k)}w_-\,, \end{aligned} \tag{6.39}$$

where the left-hand side is an analytic function in the upper half of the complex defined by k ("+" function) and the right-hand side is an analytic function in the lower half ("−" function). According to this equation, these functions coincide for $k \in \mathbb{R}$ and are equal to a function, say $J(k)$. Owing to (6.39), we can construct $J(k)$ as an entire function in complex plane by analytic continuation so that it is holomorphic at finite points in the complex plane except possibly at infinity. Moreover, both the left- and right-hand sides of (6.39) tend to zero if k tends to infinity in any direction in upper and lower halves of the complex plane, respectively, (see also (6.35), (6.36) and (6.20)). Hence, the entire function tends to zero at infinity in any direction of the complex plane. Using Liouville's theorem we can claim $J(k) \equiv 0$ in the complex plane. Hence, we can find the solutions $w_\pm$ in the form:

$$w_+ = L_+(k)\Psi_+(k)\left[\frac{Ce^{\mathrm{i}\phi}}{0-\mathrm{i}(k-k_f)} + \frac{\overline{C}e^{-\mathrm{i}\phi}}{0-\mathrm{i}(k+k_f)}\right]\,, \tag{6.40}$$

$$w_- = \frac{\Psi_-(k)}{L_-(k)}\left[\frac{Ce^{\mathrm{i}\phi}}{0+\mathrm{i}(k-k_f)} + \frac{\overline{C}e^{-\mathrm{i}\phi}}{0+\mathrm{i}(k+k_f)}\right]\,. \tag{6.41}$$

6.3.2 The fracture criterion and uniqueness of the solution

In terms of the moving coordinate system, the condition (6.1) can be re-interpreted for the amplitude function $w(\eta)$ as

$$w(0) = w_c, \quad \text{and} \quad w'(+0) < 0 \, . \tag{6.42}$$

The first of these conditions can be satisfied by computing the limits (see Slepyan [Slepyan (2002b)])

$$w(\eta)\Big|_{\eta=0} = \lim_{k \to \mathrm{i}\infty} -\mathrm{i}k \, w_+ = \lim_{k \to -\mathrm{i}\infty} \mathrm{i}k \, w_- \, , \tag{6.43}$$

using (6.40) and (6.41). In doing this we obtain

$$w_c = 2\mathrm{Re}(Ce^{\mathrm{i}\phi}) \, , \tag{6.44}$$

which allows for the unique determination of ϕ if the feeding wave amplitude, and consequently C, are known. With regard to the second condition in (6.42), we construct the asymptote of w_+ in (6.40) as $k \to \mathrm{i}\infty$, which in terms of the physical variables represents the expansion

$$w(\eta) = w(+0) + \eta w'(+0) + O(\eta^2) \, , \quad \text{for } \eta \to +0 \, .$$

Combining (6.34) and (6.40) we also have

$$\begin{aligned} w_+ \;\; = \;\; & -\frac{2\mathrm{Re}(Ce^{\mathrm{i}\phi})}{\mathrm{i}k} - \frac{2}{k^2}\Big[k_f \mathrm{Im}(Ce^{\mathrm{i}\phi}) \\ & + \mathrm{Re}(Ce^{\mathrm{i}\phi}) \left\{ 2(b-l) + \frac{1}{2\pi} \int_{-\infty}^{\infty} \ln L(\xi) d\xi \right\} \Big] + O\left(\frac{1}{k^3}\right) \, , \end{aligned} \tag{6.45}$$

for $k \to \mathrm{i}\infty$. Owing to the fact that

$$\int_0^{\infty} \eta e^{\mathrm{i}k\eta} dk = \frac{1}{(0 - \mathrm{i}k)^2} \, ,$$

(see [Slepyan (2002b)]) we obtain from (6.45) that the second condition in (6.42) is satisfied if

$$k_f \mathrm{Im}(Ce^{\mathrm{i}\phi}) + \mathrm{Re}(Ce^{\mathrm{i}\phi}) \left\{ 2(b-l) + \frac{1}{2\pi} \int_{-\infty}^{\infty} \ln L(\xi) d\xi \right\} < 0 \,. \tag{6.46}$$

This allows for ϕ to be uniquely determined as a solution of (6.44).

6.4 Dynamic loading and waves in the steady-state fracture regimes

We discuss the dynamic behaviour of the structure, subjected to a sinusoidal load, during the alternating generalised strain failure process. In particular, concerning the wave radiation processes associated with the moving transition front, we discuss the reflected and transmitted waves emitted from this point.

First we analyse the response of the unsupported medium when subjected to an oscillating point force, that will be used to define the feeding wave later.

6.4.1 An oscillating point force in an infinite mass-beam chain

Here, we derive the amplitude associated with the outgoing waves generated by point force in an unsupported mass-beam chain. The force is assumed to have frequency ω_0 and amplitude P_0. According to the derivation of the governing equations in Section 6.1.2, the problem may be written as

$$\begin{aligned} \frac{Ma^3}{E_1 I_1} \frac{\mathrm{d}^2 w_m(t)}{\mathrm{d}t^2} &= -6 \left\{ 2[2w_m(t) - w_{m-1}(t) - w_{m+1}(t)] - a[\theta^y_{m+1}(t) - \theta^y_{m-1}(t)] \right\} \\ &\quad + \frac{a^3}{E_1 I_1} P_0 \sin(\omega_0 t) \delta_{m,0} \end{aligned} \tag{6.47}$$

and

$$3[w_{m+1}(t) - w_{m-1}(t)] + a[\theta^y_{m+1}(t) + \theta^y_{m-1}(t) + 4\theta^y_m(t)] = 0 \,. \tag{6.48}$$

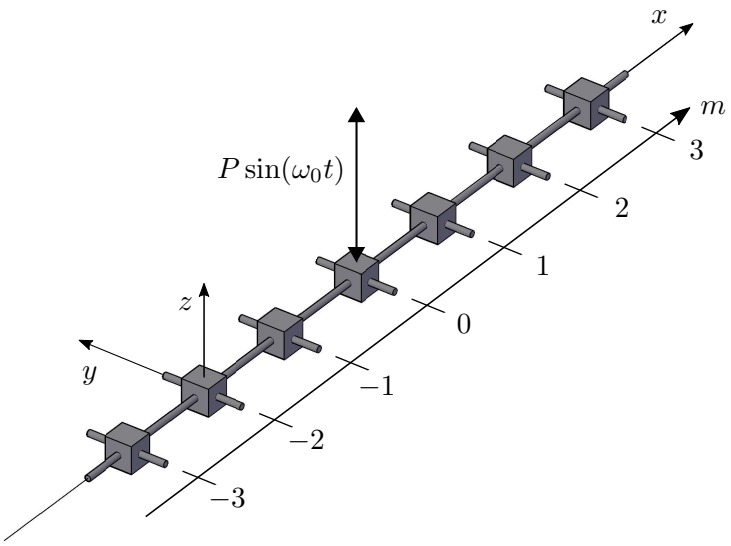

Figure 6.4: The unsupported mass-beam chain subjected to a harmonic load.

Here the Kronecker delta $\delta_{i,j}$ has been used to represent the position of the force in the structure.

In what follows, for $m \to \infty$ we show the amplitude A of the wave produced by the point source is given as

$$A = \frac{P_0}{2k_f R_0(k_f, \omega_0)} \, . \tag{6.49}$$

Derivation of (6.49)

We consider the complex solution of this problem, i.e. we look for the solutions as

$$w_m(t) = \mathrm{Re}(\mathfrak{w}_m(t)) \, , \quad \theta^y_m(t) = \mathrm{Re}(\vartheta^y_m(t)) \, , \tag{6.50}$$

which allows us to consider the problem in terms of complex functions $\mathfrak{w}_m$ and ϑ^y_m:

$$\begin{aligned} \frac{Ma^3}{E_1 I_1} \frac{\mathrm{d}^2 \mathfrak{w}_m(t)}{\mathrm{d}t^2} &= -6 \left\{ 2[2\mathfrak{w}_m(t) - \mathfrak{w}_{m-1}(t) - \mathfrak{w}_{m+1}(t)] - a[\vartheta^y_{m+1}(t) - \vartheta^y_{m-1}(t)] \right\} \\ &\quad - \frac{a^3}{E_1 I_1} \mathrm{i} P_0 e^{\mathrm{i}\omega_0 t} \delta_{m,0} \end{aligned} \tag{6.51}$$

and

$$3[\mathfrak{w}_{m+1}(t) - \mathfrak{w}_{m-1}(t)] + a[\vartheta^y_{m+1}(t) + \vartheta^y_{m-1}(t) + 4\vartheta^y_m(t)] = 0\,. \tag{6.52}$$

Here we non-dimensionalise (6.51) and (6.52) by introducing

$$\omega_0 = \sqrt{\frac{E_1 I_1}{Ma^3}}\tilde{\omega}_0\ , \quad P_0 = \frac{E_1 I_1}{a^2}\tilde{P}_0\ , \quad \mathfrak{w}_m = a\tilde{\mathfrak{w}}_m\ ,$$

and we will also assume the solutions take the form

$$\tilde{\mathfrak{w}}_m(t) = (-1)^m \mathcal{W}_m e^{\mathrm{i}\omega_0 t}\ , \qquad \theta^y_m(t) = (-1)^m \Theta^y_m e^{\mathrm{i}\omega_0 t}\ . \tag{6.53}$$

We drop the “tilde" representing dimensionless quantities in going forward and derive the system

$$-\omega_0^2 \mathcal{W}_m(t) = -6\left\{2[2\mathcal{W}_m + \mathcal{W}_{m-1} + \mathcal{W}_{m+1}] + [\Theta^y_{m+1} - \Theta^y_{m-1}]\right\} - \mathrm{i}P_0\delta_{m,0} \tag{6.54}$$

and

$$-3[\mathcal{W}_{m+1} - \mathcal{W}_{m-1}] + 4\Theta^y_m - \Theta^y_{m+1} - \Theta^y_{m-1} = 0\ , \tag{6.55}$$

where all variables in the above equations are dimensionless. In the following, the discrete Fourier transforms are used

$$\mathcal{W}^F = \sum_{m=-\infty}^{\infty} \mathcal{W}_m e^{\mathrm{i}km} \qquad \text{and} \qquad \Theta^{y,F} = \sum_{m=-\infty}^{\infty} \Theta^y_m e^{\mathrm{i}km}\ .$$

We take the discrete Fourier transform of (6.54) and (6.55) to obtain

$$[-24(1+\cos(k)) + \omega_0^2]\mathcal{W}^F + 12\mathrm{i}\sin(k)\Theta^{y,F} - \mathrm{i}P_0 = 0 \tag{6.56}$$

and

$$6\mathrm{i}\sin(k)\mathcal{W}^F + 2(2-\cos(k))\Theta^{y,F} = 0\,. \tag{6.57}$$

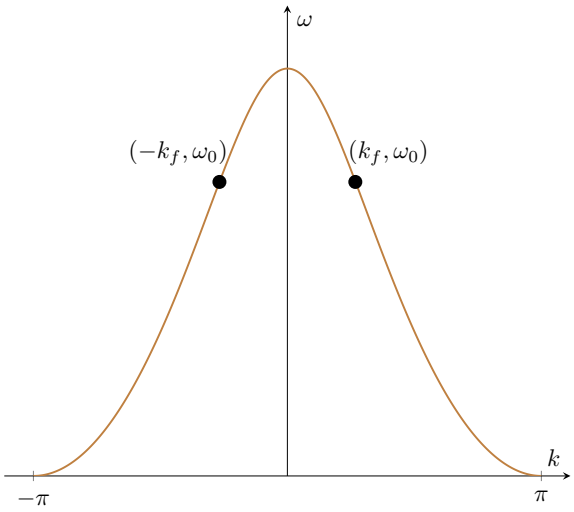

Figure 6.5: Dispersion curve ω_2 for $k \in [-\pi, \pi]$.

Combining (6.56) and (6.57) we have

$$\mathcal{W}^F = -\frac{\mathrm{i}P_0}{h_2(k, \mathrm{i}\omega_0)} \, .$$

Evaluation of displacements produced by the point load. Applying the inverse discrete Fourier transform yields

$$\mathcal{W}_m = -\frac{\mathrm{i}}{2\pi} \int_{-\pi}^{\pi} \frac{P_0 e^{-\mathrm{i}km}}{h_2(k, \mathrm{i}\omega_0)} dk \, . \tag{6.58}$$

For outgoing waves from the source to exist we require that $\omega_0 < \sqrt{48}$, representing the pass band of the structure (see Figure 6.3 and Figure 6.5). In this case, in the interval $-\pi < k < \pi$ the chosen load frequency can be linked with two wave numbers $\pm k_f \pm \mathrm{i}0$ (for the signs of the imaginary parts see [Slepyan (2002b)] and Section 6.2), that define the waves propagating in the medium. These wavenumbers are singular points of the kernel in the above integral. This is then rewritten as

$$\mathcal{W}_m = -\frac{\mathrm{i}}{2\pi} \int_{-\pi}^{\pi} \frac{P_0 e^{-\mathrm{i}km}}{(0 + \mathrm{i}(k - k_f))(0 - \mathrm{i}(k + k_f)) R_0(k, \omega_0)} dk \, , \tag{6.59}$$

where the function R_0 is defined

$$R_0(z, \omega_0) = \frac{h_2(z, \mathrm{i}\omega_0)}{(0 + \mathrm{i}(z - k_f))(0 - \mathrm{i}(z + k_f))} \, , \tag{6.60}$$

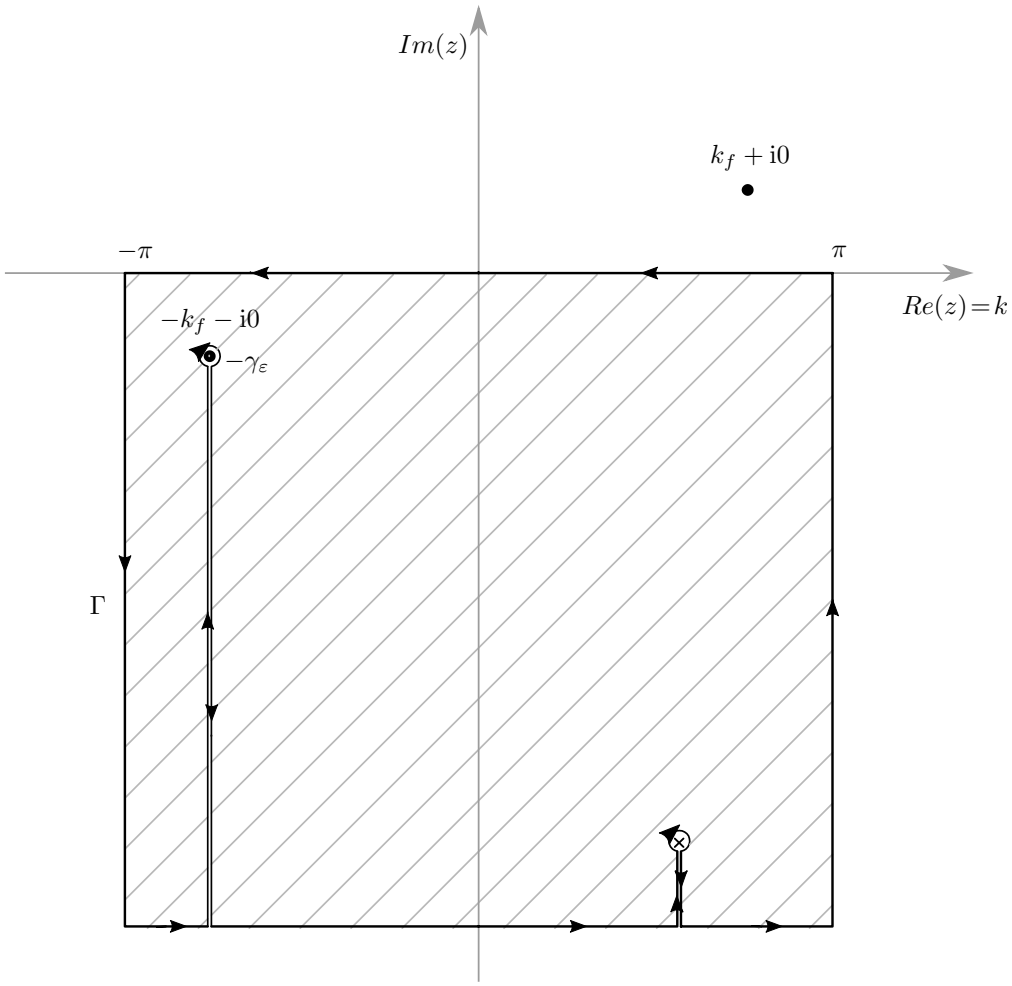

Figure 6.6: Contour Γ used in the inverse Fourier transform (6.58) for the problem of an unsupported Euler-Bernoulli beam structure loaded by a point source. Here points marked with a "$\times$" represent poles of the kernel in (6.61) with non-negligible negative imaginary part and correspond to evanescent modes in the medium for $m \to \infty$.

and has no real zeros in $[-\pi, \pi]$.

We want to obtain an expression from (6.58) for the waves that are outgoing with respect to the load and corresponding to $m \to \infty$. In this case, to compute (6.58), we use contour integration over a contour Γ shown in Figure 6.6, which takes into account the kernel function may have poles at complex values of k with non-negligible negative imaginary parts. These poles contribute to evanescent features observed in the structure localised to the load and that decay exponentially fast with $m \to \infty$. Note that for this contour, by Cauchy's Theorem we have

$$\int_\Gamma \frac{P_0 e^{-\mathrm{i}zm}}{(0 + \mathrm{i}(z - k_f))(0 - \mathrm{i}(z + k_f))R_0(z, \omega_0)} dz = 0 \,. \tag{6.61}$$

Owing to the continuity of the integrand and its 2π-periodicity with respect to the real part of z, the integrals over the vertical line segments shown in Figure 6.6 sum to zero. Additionally, if $m \to \infty$ the integrals along the horizontal segments remote from the real axis decay exponentially. Hence, when $m \to \infty$, the above relation leads to the asymptote

$$\begin{aligned}&\int_{-\pi}^{\pi} \frac{P_0 e^{-\mathrm{i}km}}{(0+\mathrm{i}(k-k_f))(0-\mathrm{i}(k+k_f))R_0(k,\omega_0)}dk \\ &\sim \quad -\int_{\gamma_\varepsilon(-k_f-\mathrm{i}0)} \frac{P_0 e^{-\mathrm{i}zm}}{(0+\mathrm{i}(z-k_f))(0-\mathrm{i}(z+k_f))R_0(z,\omega_0)}dz\ ,\end{aligned}$$

where $\gamma_\varepsilon(k_f - 0)$ is the circle oriented anti-clockwise, with centre at $k_f - \mathrm{i}0$ and radius ε chosen sufficiently small so that it does not overlap with the real axis. Using the Residue theorem we obtain:

$$\begin{aligned}&\int_{-\pi}^{\pi} \frac{P_0 e^{-\mathrm{i}km}}{(0+\mathrm{i}(k-k_f))(0-\mathrm{i}(k+k_f))R_0(k,\omega_0)}dk \\ &\sim \quad -2\pi\mathrm{i}\,\mathrm{Res}\Big(\frac{P_0 e^{-\mathrm{i}zm}}{(0+\mathrm{i}(z-k_f))(0-\mathrm{i}(z+k_f))R_0(z,\omega_0)}, z = k_f - \mathrm{i}0\Big)\ .\end{aligned}$$

Thus given the residue corresponds to a simple pole at $k = k_f - \mathrm{i}0$, under the assumption $m \to \infty$ we have

$$\frac{1}{2\pi}\int_{-\pi}^{\pi} \frac{P_0 e^{-\mathrm{i}km}}{(0+\mathrm{i}(k-k_f))(0-\mathrm{i}(k+k_f))R_0(k,\omega_0)}dk \sim \frac{\mathrm{i}P_0 e^{\mathrm{i}k_f m}}{2k_f R_0(-k_f,\omega_0)}\ , \qquad \text{for } m \to \infty \tag{6.62}$$

where it has been used that

$$R_0(-k_f,\omega_0) = \lim_{z\to -k_f} R_0(z,\omega_0) = -\frac{1}{2k_f}\frac{dh_2}{dk}(k,\mathrm{i}\omega_0)\Big|_{k=-k_f}\ ,$$

owing to L'Hopital's Rule. Next, we note for fixed ω_0, the function $h_2(k,\mathrm{i}\omega_0)$ is an even function of k. Hence, $R_0(k_f,\mathrm{i}\omega_0) = R_0(-k_f,\mathrm{i}\omega_0)$ and we derive from combining (6.53), (6.50), (6.59) and (6.62) that

$$w_m(t) \sim \frac{P_0}{2k_f R_0(k_f,\omega_0)}\cos((k_f+\pi)m + \omega_0 t) \quad \text{for} \quad m \to \infty\ .$$

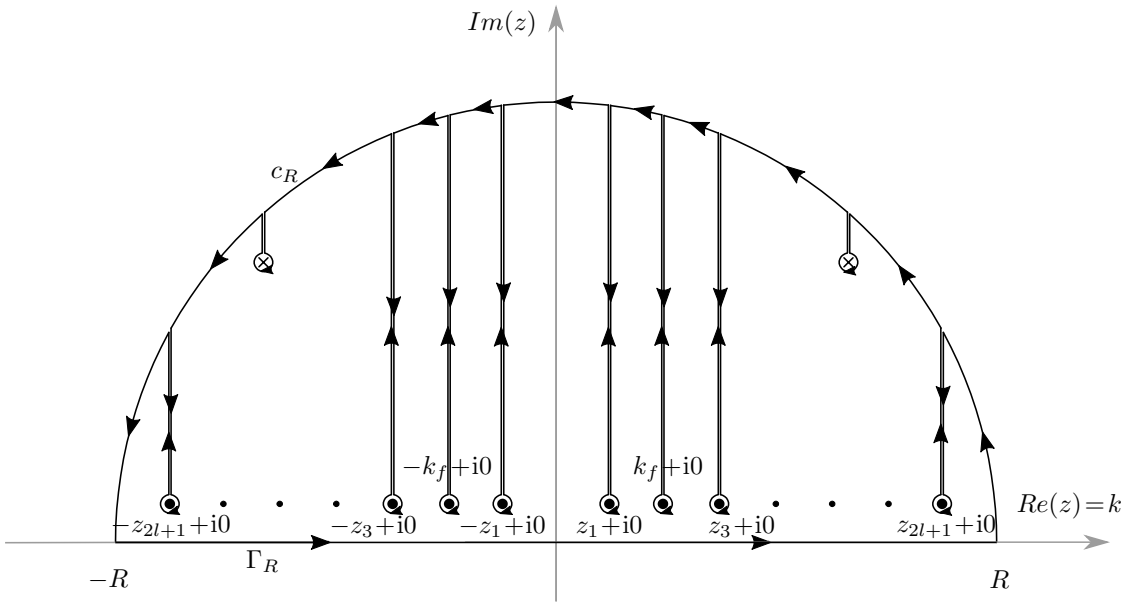

Figure 6.7: Contour Γ_R used in the inverse Fourier transform (6.64) in the problem of dynamic failure of a supported Euler-Bernoulli structure.

As noted above, the information obtained from the problem considered here will enable us to impose a feeding wave with a given amplitude generated by a remote load in the problem concerning the failure of the supported medium. Hence from the preceding equation we see that such an amplitude can take the form as in (6.49).

6.4.2 The feeding wave

We assume a sinusoidal load acts at some point far from the origin on the negative x-axis (see Figure 6.2) inside the structure. The load has amplitude P_0 and frequency ω_0. Using the results of the previous section, we assume the remote load generates a wave incident on the moving interface with the form

$$w_f(\eta) = \frac{P_0}{2k_f R_0(k_f, \omega_0)} \cos(k_f \eta - \phi) \ , \tag{6.63}$$

where ϕ is the feeding wave phase, $\eta = m - \omega_0 t/k_f$, with $\omega_0/k_f = v$ being the phase speed of the outgoing wave.

We now determine the expression for the constant C in the solution (6.40), (6.41) by considering the fracture criterion at the point $\eta = 0$. We note that the form of the feeding wave based on (6.63) can also be found if one considers the complex

residues of the simple poles at $k = \pm k_f$ for the inverse Fourier transform of w_-. This is derived under the assumption $\eta \to -\infty$, corresponding to a remote distance far behind the transition front and using

$$w(\eta) = \frac{1}{2\pi} \int_{-\infty}^{\infty} w_-(k) e^{-\mathrm{i}k\eta} dk \ , \qquad \text{for } \eta < 0 \ . \tag{6.64}$$

The right-hand side can again be computed using a contour integral and we briefly give the details here. We now consider the integral over the contour Γ_R shown in Figure 6.7, that is oriented anti-clockwise. Here, we have chosen a path that once again avoids the simple poles of the integrand that correspond to $k = \pm z_{2j+1} + \mathrm{i}0$, $0 \le j \le l$, identified in Section 6.2 and $k = \pm k_f + \mathrm{i}0$. In addition, the integrand above may contain other singular points corresponding to complex values of k with non-negligible positive imaginary part. Again, these points give rise to evanescent modes in the medium behind the transition front that exponentially decay for $\eta \to -\infty$. For the considered contour, we have by Cauchy's Theorem

$$\int_{\Gamma_R} w_-(z) e^{-\mathrm{i}z\eta} dz = 0 \ .$$

Due to the continuity of the integrand, the integrals over the straight line segments sum to zero. Moreover, for $\eta \to -\infty$ the integral over the circular arc c_R is exponentially small, in addition to those terms corresponding to evanescent modes. Hence, for $\eta \to \infty$ and $R \to \infty$, we can assert

$$\begin{aligned} \int_{-\infty}^{\infty} w_-(k) e^{-\mathrm{i}k\eta} dk \ \sim \ & \int_{\gamma_\varepsilon(k_f + \mathrm{i}0)} w_-(z) e^{-\mathrm{i}z\eta} dz + \int_{\gamma_\varepsilon(-k_f + \mathrm{i}0)} w_-(z) e^{-\mathrm{i}z\eta} dz \\ & + \sum_{j=0}^{l} \left\{ \int_{\gamma_{\varepsilon_j}(z_{2j+1} + \mathrm{i}0)} w_-(z) e^{-\mathrm{i}z\eta} dz + \int_{\gamma_{\varepsilon_j}(-z_{2j+1} + \mathrm{i}0)} w_-(z) e^{-\mathrm{i}z\eta} dz \right\} , \end{aligned} \tag{6.65}$$

where $\gamma_r(\zeta) := \{z : |z - \zeta| < r\}$ and ε, ε_j, $j = 0, \ldots, l$ are chosen sufficiently small. Each integral on the right-hand side produces a residue owing to the simple pole at

the centre of the domain of integration. Thus, we may write

$$w(\eta) \sim w_f(\eta) + \sum_{j=0}^{l} w_r^{(j)}(\eta) \ ,$$

where using (6.64), the feeding wave

$$w_f(\eta) = \mathrm{i}\ \mathrm{Res}(w_-(z)e^{-\mathrm{i}z\eta}, z = k_f + \mathrm{i}0) + \mathrm{i}\ \mathrm{Res}(w_-(z)e^{-\mathrm{i}z\eta}, z = -k_f + \mathrm{i}0) \quad (6.66)$$

and $w_r^{(j)}$, $0 \leq j \leq l$, are the waves reflected by the interface, given by:

$$w_r^{(j)}(\eta) = \mathrm{i}\ \mathrm{Res}(w_-(z)e^{-\mathrm{i}z\eta}, z = z_{2j+1} + \mathrm{i}0) + \mathrm{i}\ \mathrm{Res}(w_-(z)e^{-\mathrm{i}z\eta}, z = -z_{2j+1} + \mathrm{i}0) \ , \quad (6.67)$$

for $j = 0, \ldots, l$. We analyse the reflected waves further in Section 6.4.4. For now, we focus on determining the constant C in the expression for the feeding wave.

Using (6.66) and (6.41), we calculate the residues at the simple poles $k = k_f + \mathrm{i}0$ and obtain:

$$w_f = \left[\frac{\Psi_-(k_f)}{L_-(k_f)} C e^{\mathrm{i}(\phi - k_f\eta)} + \frac{\Psi_-(-k_f)}{L_-(-k_f)} \overline{C} e^{-\mathrm{i}(\phi - k_f\eta)}\right] . \quad (6.68)$$

Noting that

$$\Psi_\pm(-k) = \overline{\Psi_\pm(k)}, \quad L_\pm(-k) = \overline{L_\pm(k)} \ , \quad (6.69)$$

we obtain

$$w_f = 2\mathrm{Re}\left[\frac{\Psi_-(k_f)}{L_-(k_f)} C e^{\mathrm{i}(\phi - k_f\eta)}\right] . \quad (6.70)$$

Comparing with (6.63), we see that C should be chosen as

$$C = \frac{L_-(k_f) P_0}{4k_f R_0(k_f, \omega_0)\Psi_-(k_f)} \ . \quad (6.71)$$

6.4.3 Criterion for steady-state failure propagation in the alternating generalised strain regime

For the crack to propagate steadily, it is required that amplitude of the feeding wave reaches or exceeds the critical displacement, i.e.

$$w_f(-0) \geq w_c \, .$$

Using this condition, (6.44) and (6.71) yields the criterion

$$\mathcal{P} \geq \mathcal{P}_{\min} \, , \tag{6.72}$$

for the failure to propagate steadily in the alternating generalised strain regime, where

$$\mathcal{P} = P_0/w_c \qquad \text{and} \qquad \mathcal{P}_{\min} := \min \mathcal{P} = \frac{2k_f R_0(k_f, \omega_0)|\Psi_-(k_f)|}{|L_-(k_f)|} \, . \tag{6.73}$$

Figure 6.8, shows the plot of $\mathcal{P}_{\min}$ in (6.73) for a representative range of load frequencies. The computations are performed for $r = 0.4$, corresponding to a structure with soft supports, which will be investigated further in Section 6.5. For a given choice of the load frequency, the grey solid and dashed lines, based on (6.73) in Figure 6.8, predict the $\mathcal{P}_{\min}$ required for a fracture process with speed $v = \omega/k_f$ to propagate through the flexural system. Here k_f is determined from the dispersion diagram. The grey solid curve corresponds to regimes with a higher fracture speed than those connected with the grey dashed curve. These curves are associated with the $\mathcal{P}_{\min}$ for the alternating generalised strain regime.

For illustrative purposes, we also plot the results of [Nieves, Mishuris and Slepyan (2016), Nieves, Mishuris and Slepyan (2017)] with black curves and these predict the appearance of pure steady-state modes, where the sign of the bending moments and shear forces are uniform at each instant of the failure process.

Accompanying these analytical computations is a verification of the predictions

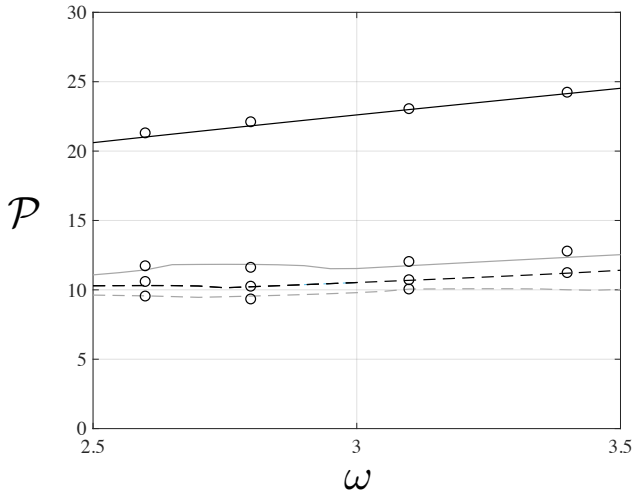

Figure 6.8: The plot of $\mathcal{P}_{\min}$ in a typical range of loading frequencies ω. Black curves are associated with the pure steady-state regimes identified in [Nieves, Mishuris and Slepyan (2016), Nieves, Mishuris and Slepyan (2017)] and the grey curves are computed using (6.72) and (6.73). The circles are results obtained from numerical simulations implemented in *Matlab* (discussed in Section 6.5), where a sufficiently large system loaded by a sinusoidal load is considered and these failure regimes are identified. For a given frequency in this interval, each curve provides the $\mathcal{P}_{\min}$ for the failure to propagate with a speed $v = \omega/k_f$. The speed is different for each curve and in this case the speeds form a monotonically increasing sequence, with the grey dashed curve associated with the lowest failure speed and the solid black curve corresponding to the highest possible failure speed.

based on numerical simulations for a sufficiently large finite structure implemented in *Matlab* (and described in detail in Section 6.5). There is an excellent agreement between the analytical results, which are based on an infinitely long medium, and the results of the *Matlab* computations based on a finite medium.

6.4.4 Dynamic features for the alternating generalised strain regime

Here, we give the representation of the envelope functions for the reflected and transmitted waves encountered during the failure process based on (6.40) and (6.41). The expressions for the associated waveforms in the structure may then be determined by combining the results presented here with (6.16).

Reflected waves behind the transition front.

The reflected waves can be derived from the residues of the poles $k = \pm z_{2j+1} + \mathrm{i}0$, $1 \leq j \leq l$, of the function w_- in (6.41) as shown in Section 6.4.2. Using (6.41) and

(6.67) derived there, we obtain:

$$\begin{aligned} w_r^{(s)} &= -\frac{\mathrm{i}\Psi_-^r(z_{2s+1})}{L_-(z_{2s+1})}\left[\frac{Ce^{\mathrm{i}\phi}}{z_{2s+1}-k_f}+\frac{\overline{C}e^{-\mathrm{i}\phi}}{z_{2s+1}+k_f}\right]e^{-\mathrm{i}z_{2s+1}\eta} \\ &\quad +\frac{\mathrm{i}\Psi_-^r(-z_{2s+1})}{L_-(-z_{2s+1})}\left[\frac{Ce^{\mathrm{i}\phi}}{z_{2s+1}+k_f}+\frac{\overline{C}e^{-\mathrm{i}\phi}}{z_{2s+1}-k_f}\right]e^{\mathrm{i}z_{2s+1}\eta}\,, \end{aligned} \tag{6.74}$$

for $j=0,\ldots,l$, where

$$\Psi_-^r(z_{2s+1}) = \frac{(-1)^{b-l+1}(1+\mathrm{i}z_{2s+1})^{2(l-b)}}{2\mathrm{i}z_{2s+1}}\frac{\prod_{j=0}^{b}(z_{2s+1}^2-y_{2j+1}^2)}{\prod_{\substack{0\le i\le l\\ i\neq s}}(z_{2s+1}^2-z_{2i+1}^2)}\,,$$

Upon noticing that (6.74) contains two terms that are a complex conjugate pair, due to the previous relation and (6.69), we can write functions $w_r^{(s)}$, $0\le s\le l$ as real waves in the form

$$w_r^{(s)} = A_r^{(s)}\cos(z_{2s+1}\eta-\psi_r^{(s)})\,,$$

with amplitude $A_r^{(s)}$ given by

$$A_r^{(s)} = \frac{4|C||\Psi_-^r(z_{2s+1})|}{|L_-(z_{2s+1})||z_{2s+1}^2-k_f^2|}\sqrt{z_{2s+1}^2\cos^2(\phi+\psi_c)+k_f^2\sin^2(\phi+\psi_c)}\,,$$

where the phase shift $\psi_r^{(s)}$ given as

$$\psi_r^{(s)} = \arg\Big(-\frac{\mathrm{i}\Psi_-^r(z_{2s+1})(z_{2s+1}\cos(\phi+\psi_c)+\mathrm{i}k_f\sin(\phi+\psi_c))}{(z_{2s+1}^2-k_f^2)L_-(z_{2s-1})}\Big)\,,\quad \psi_c=\arg(C)\,.$$

Waves transmitted ahead of the transition front.

Lastly, we determine the form of the waves transmitted ahead of the transition front. This is calculated by analysing the formula

$$w(\eta) = \frac{1}{2\pi}\int_{-\infty}^{\infty} w_+(k)e^{-\mathrm{i}k\eta}dk\,,\qquad \text{for } \eta>0 \tag{6.75}$$

assuming $\eta\to\infty$.

As in Section 6.4.2, this can be computed with a contour integration, in a similar

way to as in Figure 6.7, except the contour should be transformed downward and avoid the poles $k = y_{2j} - \mathrm{i}0$, $1 \le j \le b$, and the additional complex poles with non-negligible negative imaginary part that w_+ may possess. The latter give rise to evanescent modes propagating in the supported region that decay exponentially for $\eta \to \infty$. Note that at $k = \pm k_f - \mathrm{i}0$, has removable singularities, as k_f coincides with one of the collection of zeros at $z_{2j} - \mathrm{i}0$, $1 \le j \le l$ that $w_+(k)$ possesses (see (6.41) and (6.30)). From (6.75), in a similar way to Section 6.4.2, we can then obtain that

$$w(\eta) \sim \sum_{j=1}^{b} w_{tr}^{(j)}(\eta) \qquad \text{for} \quad \eta \to \infty \ ,$$

where $w_{tr}^{(j)}(\eta)$ are the transmitted waves ahead of the propagating interface given as

$$w_{tr}^{(j)} = -\mathrm{i}\mathrm{Res}(w_+(z)e^{-\mathrm{i}z\eta}, z = y_{2j} - \mathrm{i}0) - \mathrm{i}\mathrm{Res}(w_+(z)e^{-\mathrm{i}z\eta}, z = -y_{2j} - \mathrm{i}0) \ .$$

Using (6.40) and (6.30) the preceding residues at the poles $k = \pm y_{2j} - \mathrm{i}0$ can be calculated to give

$$\begin{aligned} w_{tr}^{(j)} \ &= \ \mathrm{i}L_+(y_{2j})\Psi_+^{tr}(y_{2j}) \left[\frac{Ce^{\mathrm{i}\phi}}{y_{2j} - k_f} + \frac{\overline{C}e^{-\mathrm{i}\phi}}{y_{2j} + k_f} \right] e^{-\mathrm{i}y_{2j}\eta} \\ &\quad -\mathrm{i}L_+(-y_{2j})\Psi_+^{tr}(-y_{2j}) \left[\frac{Ce^{\mathrm{i}\phi}}{y_{2j} + k_f} + \frac{\overline{C}e^{-\mathrm{i}\phi}}{y_{2j} - k_f} \right] e^{\mathrm{i}y_{2j}\eta} \ , \end{aligned} \tag{6.76}$$

with

$$\Psi_+^{tr}(y_{2j}) = \frac{(-1)^{l-b}}{2\mathrm{i}y_{2j}(1 - \mathrm{i}y_{2j})^{2(l-b)}} \frac{\prod_{i=1}^{l}(y_{2j}^2 - z_{2i}^2)}{\prod_{\substack{1 \le i \le b \\ i \ne j}} (y_{2j}^2 - y_{2i}^2)} \ .$$

Here, the above and (6.69) show that (6.76) is again the sum of two functions that are complex conjugate to each other. Therefore the transmitted waves can be written as a real waves as follows:

$$w_{tr}^{(s)} = A_{tr}^{(s)} \cos(y_{2s}\eta - \psi_{tr}^{(s)}) \ ,$$

where the amplitude $A_{tr}^{(s)}$ has the form

$$A_{tr}^{(s)} = \frac{4|C||\Psi_+^{tr}(y_{2s})||L_+(y_{2s})|}{|y_{2s}^2 - k_f^2|}\sqrt{y_{2s}^2\cos^2(\phi+\psi_c) + k_f^2\sin^2(\phi+\psi_c)}\,.$$

The phase shift $\psi_{tr}^{(s)}$ is

$$\psi_{tr}^{(s)} = \arg\Big(\frac{\mathrm{i}\Psi_+^{tr}(y_{2s})L_+(y_{2s})[y_{2s}\cos(\phi+\psi_c) + \mathrm{i}k_f\sin(\phi+\psi_c)]}{y_{2s}^2 - k_f^2}\Big)\,.$$

Note, if $b = 0$, then there are no propagating waves transmitted to the intact structure.

6.5 Numerical simulations modelling the failure process

In this section, we implement a numerical scheme in *Matlab* that models the behaviour of a finite flexural structure subjected to a sinusoidal load. In addition, using the numerical scheme we also trace the propagation of failure inside this structure as a result of the action of the load. The scheme is based on the normalised governing equations (6.14) and (6.15) for the system, which are solved using the `ode45` routine of *Matlab*.

We use the results from the analysis of the alternating generalised strain fracture regime presented in Section 6.1, to show that we can predict:

(i) when such regimes occur,

(ii) the speed with which the fracture propagates in such regimes,

(iii) the behaviour of the structure in these particular regimes.

6.5.1 The numerical model

A finite structure composed of 3800 nodes, connected by massless beams, is considered. As the numerical scheme is based on the dimensionless equations (6.14) and (6.15), the

dimensionless length and flexural stiffness of the connecting beams can be taken equal to unity. Therefore, the position of each mass is then given by $x = n$, $1 \leq n \leq 3800$. The system is initially at rest. We consider this structure composed of a region supported by transverse links and a region where the masses along the central axis of the structure are unsupported by such links. The supported region is characterised by the heterogeneity parameter r. The nodes corresponding to $0 \leq x \leq 1999$ constitute the unsupported part of the structure, behind the interface, and the remaining 1800 nodes (corresponding to $2000 \leq x \leq 3800$) represent the system in the supported region. Therefore, the interface between these two media is initially at $n = 2000$.

The external applied force is taken as a sinusoidal force having the form $P_0 \sin(\omega_0 t)$, where P_0 and ω_0 are the dimensionless load amplitude and frequency. This load is situated at node $x = 1800$. We can choose the value of ω_0 based on the frequency ω of the unforced problem for the unsupported structure of infinite extent in the x direction. To generate feeding waves in the unsupported structure capable of reaching the transition front, the load frequency ω_0 should be chosen in the interval $0 < \omega_0 < \sqrt{48}$, representing the passband for the analogous infinite medium. Below, we consider $\omega_0 = 3.1$ and 5.9 representing frequencies located in the middle and close to the upper limit of the passband, producing waves capable of exciting the microstructure. In the numerical scheme, the right end of the structure is clamped at $x = 3800$, whereas the node at $x = 1$ is free. The structure's size has been chosen to minimise effects due to reflections produced by the ends.

As discussed in Section 6.4.2, the feeding waves generated by the load help to initiate and propagate the failure process. Fracture regimes in two different types of structure are examined here:

Case 1: A structure whose supporting transverse links are "softer" than those along the central axis of the structure ($r = 0.4$).

Case 2: A structure with transverse supports that are much stiffer than the beams along its central axis ($r = 3.4$).

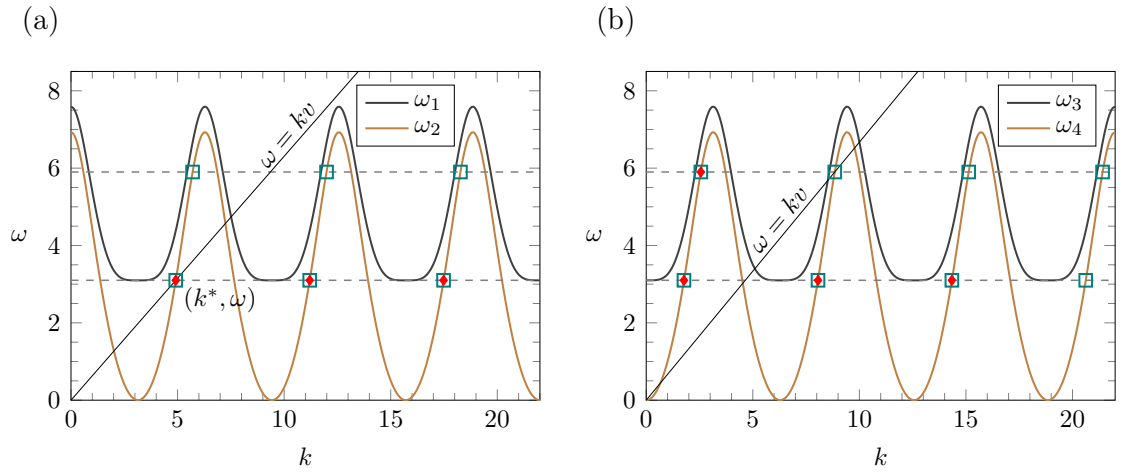

Figure 6.9: Dispersion relations for $r = 0.4$. (a) The dispersion curves ω_1 and ω_2 for the case of the alternating generalised strain regime for fracture propagation (see (6.27) and (6.28)). (b) The dispersion curves ω_3 and ω_4 for the pure steady-state regimes that are associated with the conditions (6.77) (see [Nieves, Mishuris and Slepyan (2016), Nieves, Mishuris and Slepyan (2017)]). The loading frequencies $\omega_0 = 3.1$ and 5.9 are shown as dashed horizontal lines. The squares represent the intersection points of lower curves with these lines, where the wave group velocity v_g exceeds the wave phase velocity v. The slope of the ray $\omega = kv$ that passes through the intersection points indicates possible steady-state speeds. Those intersection points with the red diamonds are associated with failure regimes observed in the *Matlab* numerical simulations.

6.5.2 Case 1 - soft supports

Here we show that it is possible to encounter two fracture regimes. The first involves the regime where the failure will propagate if (6.1) is violated at the transition front. The second concerns the regime defined by

$$w_j(t) < w_c, \quad j \geq p, \quad p, j \in \mathbb{Z}\,, \tag{6.77}$$

where p represents the node number where the interface is located at a given time t. This was studied in detail in [Nieves, Mishuris and Slepyan (2016), Nieves, Mishuris and Slepyan (2017)]. For these regimes, the sign of the generalised strains at the instant of each fracture in the structure remains constant. We refer to the regimes associated with (6.77) as the *pure steady-state regimes*.

We first show that speeds associated with the failure regimes observed can be predicted from the dispersion curves (6.27), (6.28) and those identified in [Nieves, Mishuris and Slepyan (2016), Nieves, Mishuris and Slepyan (2017)].

Failure speed predictions.

A list of steady-state speeds for the considered fracture regimes can be determined using the dispersion curves discussed in Section 6.2. Figure 6.9(a) shows the dispersion curves (6.27), (6.28) plotted as functions of the wave number k for the case $r = 0.4$. In addition, the horizontal dashed lines represent the loading frequencies ω_0 chosen for the *Matlab* computations.

For the case $\omega_0 = 3.1$, the horizontal dashed line in Figures 6.9(a) and (b) associated with this frequency intersect the curves given by $\omega_2(k)$ and $\omega_4(k)$ infinitely many times. Since we require a feeding wave to reach the transition front inside the structure, we need the group velocity v_g of this wave to be greater than the fracture speed v i.e. the slope of the line $\omega = kv$. For $k > 0$, we have indicated these intersection points, using squares that represent possible feeding waves, where this criterion is satisfied in Figure 6.9(a) and (b).

Without loss of generality, we take the first of these points (k^*, ω), shown in Figure 6.9(a), along the line $\omega = 3.1$ with the smallest wavenumber. We connect this point to the origin by a ray whose slope is defined by $v = \omega/k^*$ (see Figure 6.9(a)). This slope predicts a possible steady-state speed of failure inside the structure. In the case of $\omega = 3.1$ in Figure 6.9(a), such an intersection point is given by $(k^*, \omega) = (4.915, 3.1)$ and the slope of the corresponding ray is 0.6307. That particular intersection point corresponds to an alternating generalised strain failure regime with speed $v = 0.6307$ initiated by the sinusoidal load of frequency $\omega = 3.1$.

Owing to the 2π-periodicity of the function $\omega_2(k)$, a decreasing sequence of possible speeds can be deduced in the form

$$v = \frac{\omega}{k^* + 2\pi n}\,, \quad n \geq 0, n \in \mathbb{Z}\,.$$

As an example, for the case $\omega = 3.1$ in Figure 6.9(a), this list takes the form

$$v = 0.6307,\ 0.2768,\ 0.1773,\ 0.1304,\ 0.1032,\ \ldots\,. \tag{6.78}$$

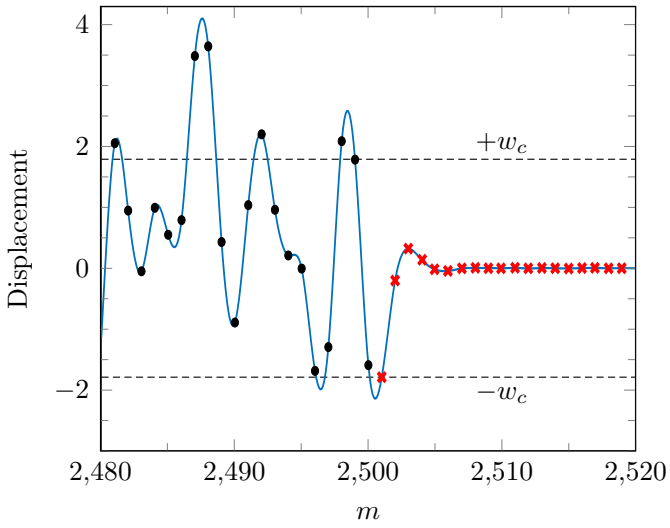

Figure 6.10: Displacement profile attained by the central axis of the harmonically excited flexural system that is undergoing a steady failure with the alternating generalised strain mode. The frequency and amplitude of the external load is $\omega_0 = 3.1$ and $\mathcal{P} = 13.115$, respectively. The heterogeneity parameter of the structure $r = 0.4$. The speed of failure for this particular regime is 0.6307. Masses along the unsupported structure are represented by black dots and those masses supported by transverse links are marked with crosses. The limits $\pm w_c$, with $w_c = 1.7919$, of the critical displacement for every mass in the supported region is indicated by horizontal dashed lines.

The intersection points connected with these speeds are shown along the line defined by $\omega = 3.1$ in Figure 6.9(a) by squares.

In the *Matlab* simulations we can also identify pure steady-state regimes corresponding to the case when the failure propagation occurs as a result of the violation of (6.77) at the transition front. In this scenario, following [Nieves, Mishuris and Slepyan (2016), Nieves, Mishuris and Slepyan (2017)], the dispersion relations are given by $\omega_{j+2}(k) = \Omega_j(k)$, $j = 1, 2$, (see (6.25)) and are shown in Figure 6.9(b). Repeating the procedure outlined above, we can obtain the speeds in the pure steady-state regime. For $\omega = 3.1$, the list of predicted speeds for this regime is:

$$v = 1.7484,\ 0.3848,\ 0.2162,\ 0.1503,\ 0.1152,\ \ldots\ .$$

Predictions for the potential steady-state speeds at different load frequencies can be calculated in a similar way.

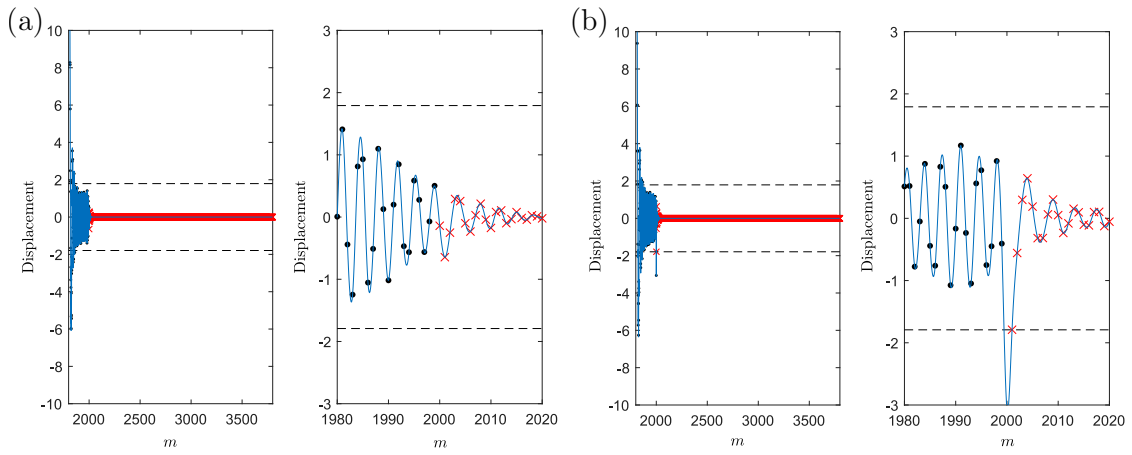

Figure 6.11: Response of the partially supported Euler-Bernoulli beam structure at (a) $t = 59.875$ prior to the first breakage and (b) $t = 63.7056$, corresponding to the failure of the transverse supports at the interface initiating the failure process. The computations are based on a transient analysis undertaken for the parameters described in Figure 6.10.

Results of the transient analysis and identification of failure regimes.

Here, for $r = 0.4$ and $\omega = 3.1$, we analyse the failure processes in the finite structure for various load amplitudes. We show that the failure processes discussed here and in [Nieves, Mishuris and Slepyan (2016), Nieves, Mishuris and Slepyan (2017)] both can appear as a result of the action of the load.

Figure 6.10 shows a result of the transient computation presented here when one of the alternating generalised strain failure regimes is initiated in the finite medium. As mentioned earlier, for a given load frequency, the appearance of these regimes is dependent on the applied load amplitude. In Figure 6.10, we show the dynamic response of the structure when the speed of this failure regime is maximal. There, as predicted by the analytical results in Sections 6.1–6.4, the transition front propagates with a constant speed as a result of feeding waves from the load providing energy to the front. This allows the front to reach the critical displacement for the failure of the supports. During the steady propagation, waves are radiated outward from the transition front when the failure of the supporting beams is achieved.

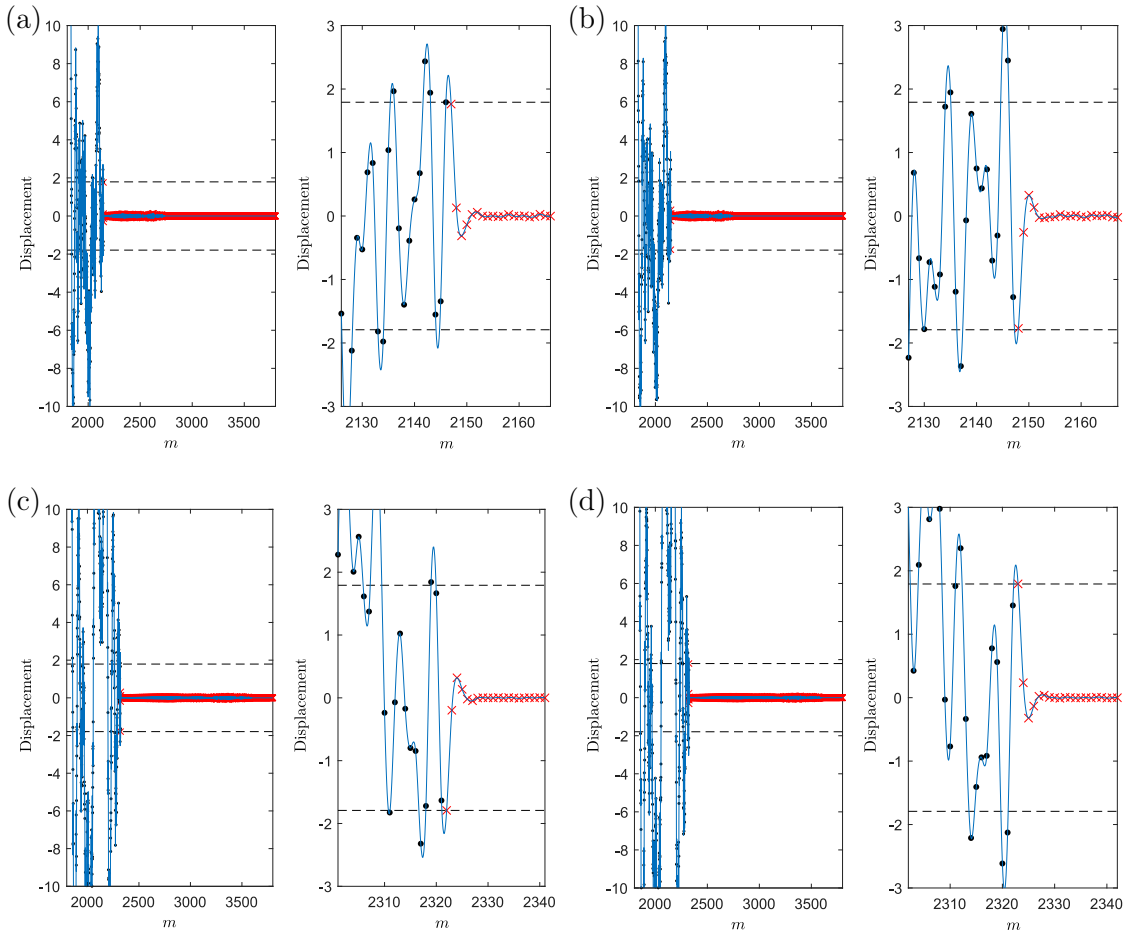

Figure 6.12: The profile of the structure subjected to a harmonic load undergoing failure at (a) $t = 294.2496$, where the transverse supports break at $m = 2147$ and (b) the next failure to occur at $t = 295.8689$ at $m = 2148$ fail. In (c) $t = 571.6862$, where the failure occurs at $m = 2321$, whereas (d) corresponds to the next instant in time when the failure occurs at $t = 573.2804$ and $m = 2322$. In cases (a) and (b), the failure process has yet to reach the steady-state regime whereas in (c) and (d) this regime has been reached and the front propagates with a constant speed. For (a) and (c) ((b) and (d)), the failure occurs when the displacement at the interface equals -1.7919 (+1.7919). The computations are based on a transient analysis undertaken for the parameters described in Figure 6.10

Illustration: Dynamic behaviour of the structure undergoing the alternating generalised strain failure regime

Figures 6.11 and 6.12 illustrates the evolution of this failure process and the behaviour of the structure resulting from the transient analysis. We show six representative time instants of the motion in the system. The structure is subjected to an oscillating load with amplitude $\mathcal{P} = 13.115$. This load initiates and sustains the alternating generalised strain failure process.

In the left-hand frame of Figures 6.11(a), (b) and 6.12 (a)-(d), we provide a global view of the structure where the position of the point force is placed at node 1800 on the left of the frame. The right panel of each of these shows the local view of the transition front during the simulation. The horizontal dashed lines depict the critical values of the displacement. Crosses in these figures represent the masses supported in the medium by beams and the dots are the unsupported masses. The snapshots show several instances where the failure of the supports in the medium occurs (corresponding to the crosses intersecting with the horizontal dashed lines in the right panels of each figure, that represent the limits ± 1.7919).

The applied load produces elastic waves, which excite the structure. Initially, the force causes the masses in the unsupported region to oscillate and this force generates waves propagating towards the interface, positioned at the 2000^{th} mass. At approximately after $t = 47$, see Figure 6.11(a), the mass at the interface starts to oscillate within the limits defined by the critical displacement and the first breakage is achieved at approximately $t = 63.71$, see Figure 6.11(b). This occurs when the smallest critical value of displacement of -1.7919 is reached. After this time, we see the transition front propagate through the structure.

After the first instant of failure in the structure, the failure process continues with the subsequent breakage of consecutive pairs of transverse supports in the medium. First we note the process undergoes a transient behaviour before settling to the steady state regime. Figures 6.12(a) and (b), show the behaviour of the medium during this phase, where transient waves with significant amplitude are transmitted

into the supported region. The amplitude of these transmitted waves diminishes until the steady-state fracture regime is achieved. About $t = 316.49$, in Figure 6.12(c), the steady propagation of the transition front reaches an average speed of 0.6307. Figure 6.12(d) shows the failure in the structure at the next time instant. We note that in the steady state process, the sign of the mass displacements alternate local to the transition front between consecutive instants of fracture (see Figure 6.12(c) and (d)). Additionally, no vibrations are transmitted into the supported part of the structure. Behind the transition front, one can find the superposition of the feeding wave and a single wave reflected by this moving interface.

Later we show that in the transient regime the failure process can occur non-steadily before reaching such states. In particular, we will also demonstrate that dynamic response of the structured medium is different when undergoing an alternating generalised strain failure mode when compared with a pure steady failure mode.

Transient behaviour of the transition front

The failure of the finite structure resulting from the harmonic load was performed for a large interval of load amplitudes. We denote by m^* the index of the mass where the transition front is initially located. For the simulations $m^* = 2000$. The index $m_i = m - m^* + 1$ refers to the index of a mass in the supported region where the failure of the transverse beams at time t_i, $i \geq 1$, $i \in \mathbb{Z}$, occurs. Simultaneously, as the length of the beams along the central axis is equal to unity, m_i also represents the position of the failure in the supported region measured with respect to the initial position of the transition front.

Figure 6.13(a) shows several examples of the failure position as a function of time t for various load amplitudes where steady failure regimes can be observed in the simulations. Since the results are based on a transient simulation, we can expect some effects in the initial period of the failure process. For instance, for $\mathcal{P} = 11.496$ in Figure 6.13(b) we see a visible oscillatory behaviour in the transition front speed

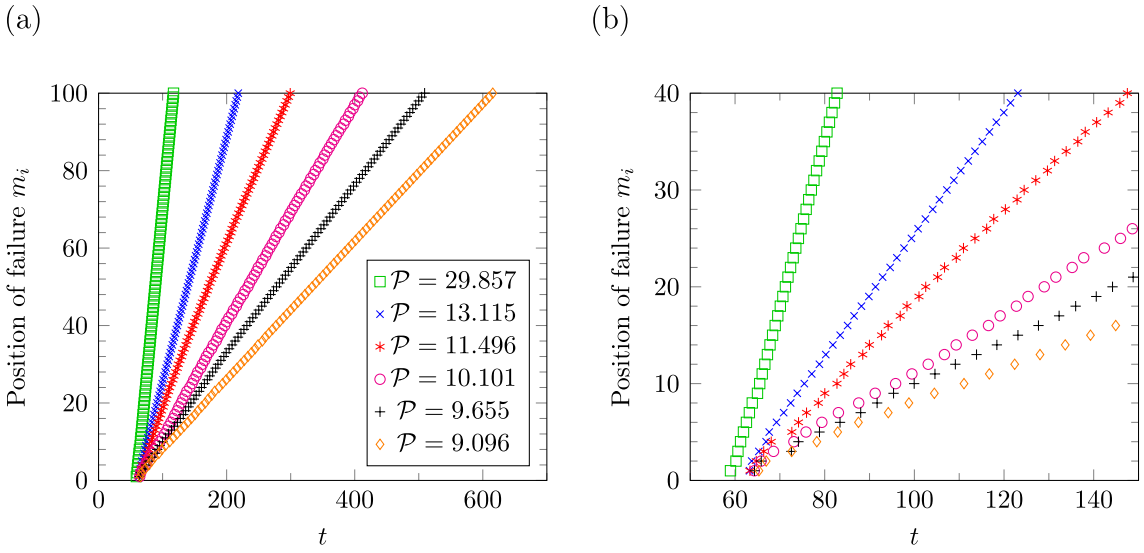

Figure 6.13: For $r = 0.4$ and $\omega_0 = 3.1$, we show the behaviour of the transition front as a function of time for various load amplitudes $\mathcal{P}$. (a) The position of failure inside the supported part of the structure as a function of time. (b) A magnification of the initial data of the computations in (a).

initially. Similar behaviour can also be seen for the computations based on the other load amplitudes.

After these initial periods, the transition process settles and the position of failure appears to behave as a linear function of time, representing that the steady-state failure phenomenon has been achieved. After the transient failure process, we can calculate the average failure speed from the data shown. The average speed $\bar{v}$ is then computed as the slope of the line of best fit for this data. In this case, the average speeds obtained are $\bar{v} = 0.1773, 0.2162, 0.2768, 0.3848, 0.6307, 1.7484$, that agree with the analytical predictions for the possible failure speeds of Section 6.5.2. As expected from physical considerations, Figure 6.13 shows that as the load amplitude is increased, a higher failure speed is achieved.

Actually, one can observe further oscillations in the failure speed when it appears to have settled to a uniform state. We define the instantaneous speed v_i for the fracture process as

$$v_i = \frac{m_i - m_{i-1}}{t_i - t_{i-1}}, \text{ if } i \geq 2 \, . \tag{6.79}$$

Using the notion of the instantaneous speed, we also can understand how quickly the failure process settles to the steady-state limit.

In Figure 6.14(a), we show the instantaneous speed plotted as function of the

failure position m_i. Here, the instantaneous speed data presented corresponds to cases considered in Figure 6.13. To demonstrate the speed of convergence to the steady-state failure process, each set of data for the instantaneous front speed has been normalised by the analytical prediction for the speed v_{pred} that was attained in Figure 6.13 (see Section 6.5.2). In this case, convergence to the steady-state speed is represented by the convergence to unity in Figure 6.14. It is observed that the instantaneous speeds, for nearly all the load amplitudes, oscillate about the predicted speed in each case (see the magnification in Figure 6.14(b)). In fact, Figure 6.14(b) shows that there exist micro-oscillations in speed of the failure front not necessarily seen in Figures 6.13(a) and (b). In addition, these oscillations in the transition front speed are not part of the analytical model studied in Section 6.1–6.4, where the speed of the front is assumed to be uniform.

Larger oscillations in the transition front speed are attained with larger values of the amplitude $\mathcal{P}$. The speed of convergence of these regimes appears to be a non-monotonic function of the load amplitude.

In Figure 6.14(c), we show a special case ($\mathcal{P} = 10.101$) where the instantaneous speed of the front does not converge to unity in the steady failure process, but instead settles to two distinct speeds (given by v_i/v_{pred} approximately equal to 0.79 and 1.39 after the 118^{th} failure event). Although there is an apparent jump in the instantaneous speed of the failure, the average speed $\bar{v}$ is in fact equal to the predicted value 0.2768. Moreover, the corresponding data representing the failure position as a function of time in Figure 6.13(a) exhibits a straight line that is commonly associated with the steady-state failure propagation.

Dependency of the average failure speed on the load amplitude

In the Figure 6.15, we show the average fracture speed $\bar{v}$ as a function of the normalised oscillating force amplitude $\mathcal{P}$. There we see six plateaus corresponding to the steady-state speeds reached by the transition front observed in Figures 6.13 and 6.14. These include the speeds $\bar{v} = 0.1773, 0.2768, 0.6307$, which correspond to alternating generalised strain regimes, and $\bar{v} = 0.2162, 0.3848, 1.7484$ that are the

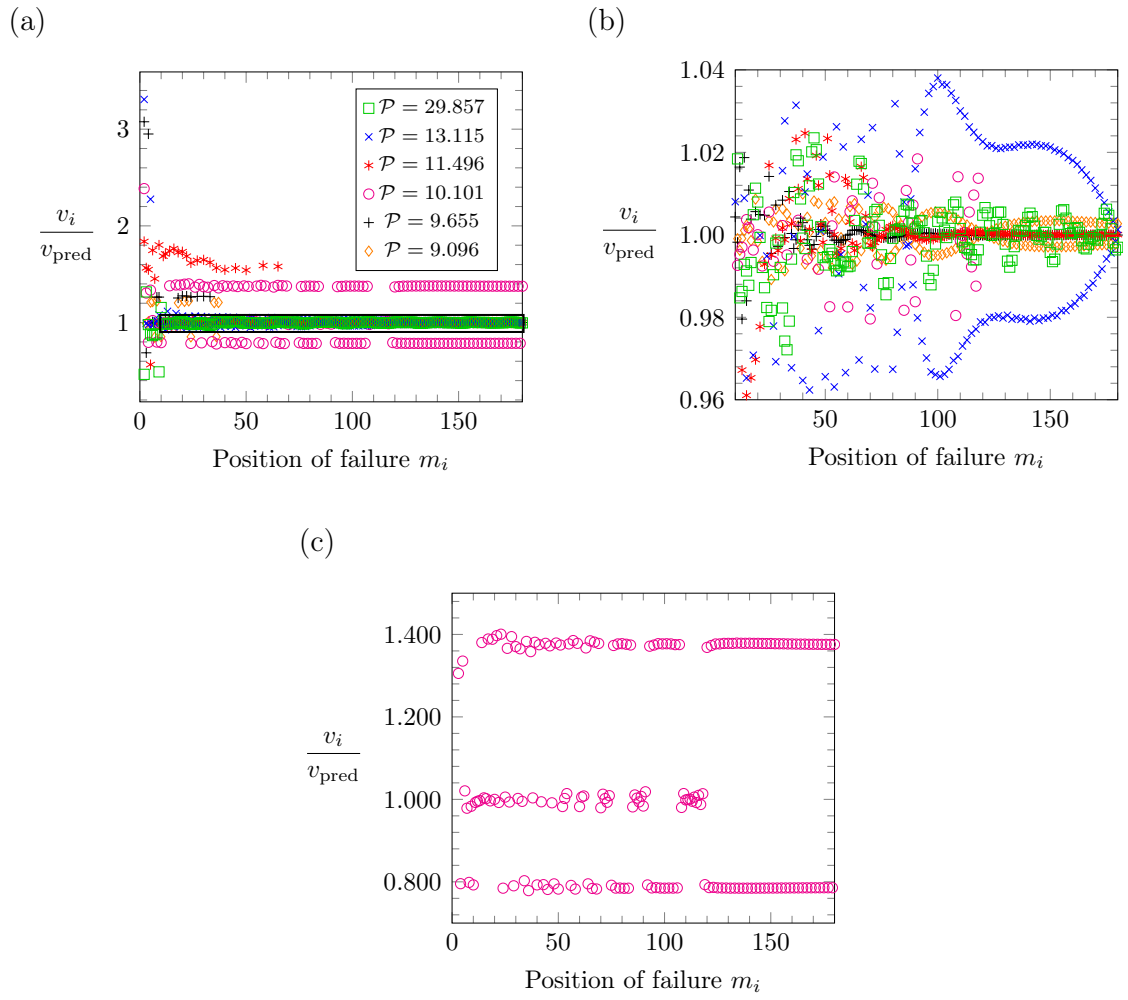

Figure 6.14: (a) The normalised instantaneous speeds computed via (6.79) (and normalised by the respective predicted steady-state speeds based on the dispersion diagrams in Section 6.2) as a function of the position of failure. (b) Magnification of the black box in (a). (c) A magnification of the normalised instantaneous speed distribution as a function of the position of failure for the case $\mathcal{P} = 10.101$. The computations are performed for $r = 0.4$ and $\omega_0 = 3.1$.

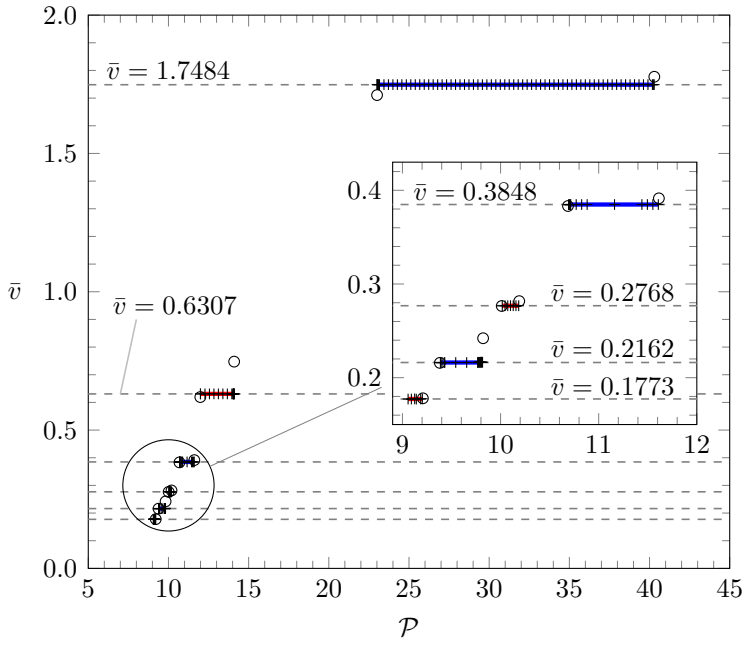

Figure 6.15: The average failure speed shown as a function of the quantity $\mathcal{P}$, for $\omega_0 = 3.1$ and $r = 0.4$. The circles and crosses represent the fracture behaviour for different regimes recorded from *Matlab* simulations. Specifically, the crosses are associated with the steady-state propagation of the transition front and the circles indicate non steady-state propagation regimes. The dashed horizontal lines are for the predicted steady-state speeds that follow from the dispersion curve analysis in Section 6.5.2. Here, the plateaus for the steady-state speeds are shown as red for the alternating generalised strain regimes and blue for the pure steady-state regimes.

speeds associated with the pure steady-state regimes.

From Figure 6.15, we can conclude:

- The average speed is a monotonically increasing function of the load amplitude.
- There exist several plateaus, highlighted in red and blue indicating alternating generalised strain regimes and pure steady-state regimes, respectively, where speeds predicted by the analytical model are realised.
- Only a finite collection of speeds predicted by the analytical model are realised and lower speeds exist for narrow intervals of the load amplitude or are never realised.
- Between any two pure steady-state regimes, corresponding to the fracture process associated with criteria (6.1), there exists a plateau of finite width at the failure speed associated with the alternating generalised strain failure regime.

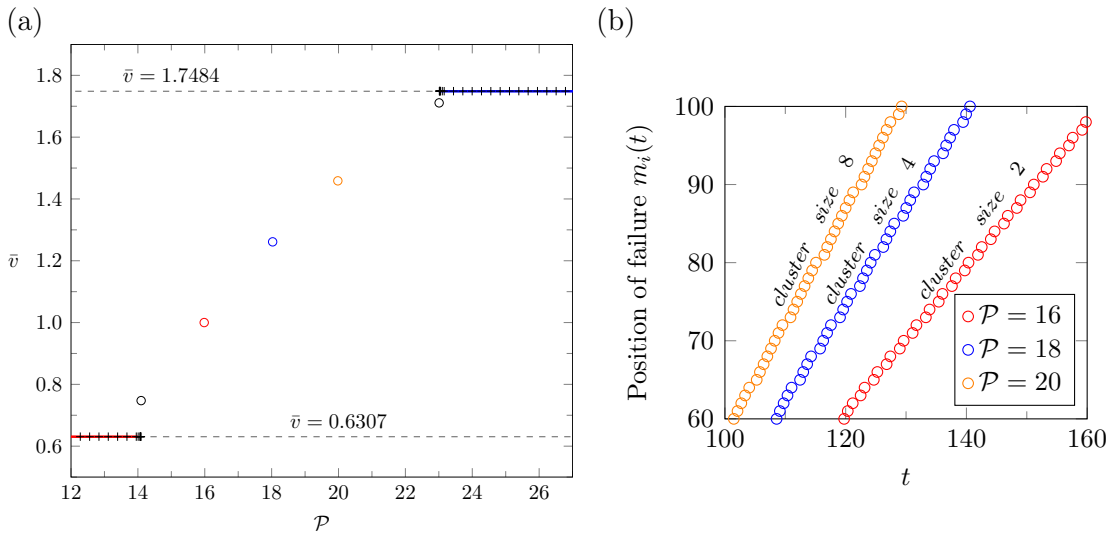

Figure 6.16: (a) Magnified view of Figure 6.15, with three additional results obtained for the load amplitudes $\mathcal{P} = 16$, 18, 20 (red, blue and orange circles). (b) Clustering phenomenon of the transition front.

- The size of plateaus for each steady-state regime corresponding to the alternating generalised strain fracture process increases with the load amplitude. The same behaviour is observed for the plateaus corresponding to the pure steady-state regimes.

- Outside the plateaus, the fracture propagates non-uniformly. Between two steady-state speeds, we encounter the clustering phenomenon, first observed in [Mishuris, Movchan and Slepyan (2009)], where fracture propagates in regular periodic bursts. As an example, in Figure 6.16, we report three cases in which the clustering phenomenon occurs. Figure 6.16(a) shows a magnification of Figure 6.15 taken between the speeds $\bar{v} = 0.6307$ and $\bar{v} = 1.7484$. In this region, the results of the computations corresponding to $\mathcal{P} = 16$, 18, 20, are highlighted in red, blue and orange, respectively, in Figure 6.16(a). The corresponding failure phenomena is presented in Figure 6.16(b) and it can be seen that the transition front propagates in periodic bursts that increase in size as the load amplitude increases.

Additionally, with reference to Section 6.4, we show that the analytical model can be used to efficiently predict the initial load amplitudes when steady-state failure regimes can appear. In Table 6.1, we present data from the *Matlab* simulations when

Matlab results		Analytical results	Regime
$\bar{v}$	$\mathcal{P}_{\min}$	$\mathcal{P}_{\min}$	
0.1773	8.985	8.932	1
0.2162	9.376	9.366	2
0.2768	10.045	10.055	1
0.3848	10.715	10.686	2
0.6307	11.887	11.742	1
1.7484	23.048	23.00	2

Table 6.1: Load amplitude values that initiate steady-state failure regimes for $\omega_0 = 3.1$ and $r = 0.4$. The first two columns show the values for the average speed and the corresponding minimum load amplitude $\mathcal{P}_{\min}$ when the regime was first identified from the numerical scheme of *Matlab*. The third column presents the analytical predictions for the load amplitude based on the results of Section 6.3 and the theory of [Nieves, Mishuris and Slepyan (2016), Nieves, Mishuris and Slepyan (2017)]. In the last column, we specify the regime encountered, where "1" represents the alternating generalised strain regime and "2" indicates the pure steady-state regime.

the steady-state regimes are initiated and we supply the classification of each regime. The analytical predictions for these load amplitudes, based on the right-hand side of (6.72) and the results of [Nieves, Mishuris and Slepyan (2016), Nieves, Mishuris and Slepyan (2017)], are also given. We note that there is an excellent match between the analytical results and those obtained from the numerical scheme implemented in *Matlab*.

Note that here we have shown only a finite collection of the predicted speeds is obtained in the simulations. The intervals of the load amplitude for when these steady-state speeds can occur have the form $[\mathcal{P}_{\min}, \mathcal{P}_{\max}]$. For the alternating generalised strain regime, $\mathcal{P}_{\min}$ is determined using (6.72) and (6.73), whereas for the pure steady-state regime it is determined using the results of [Nieves, Mishuris and Slepyan (2016), Nieves, Mishuris and Slepyan (2017)]. On the other hand, the maximum value $\mathcal{P}_{\max}$ of the load amplitude for which a steady-state regime can exist may be obtained by analysing the profile of the structure based on the analytical solution, as shown in [Nieves, Mishuris and Slepyan (2017)]. Here, for particular failure modes, as the failure speed decreases the distance between $\mathcal{P}_{\min}$ and $\mathcal{P}_{\max}$ becomes smaller (for instance, see Figure 6.15). In the case when the analytical model predicts $\mathcal{P}_{\min} > \mathcal{P}_{\max}$, which is a physically unacceptable scenario, the corresponding failure regimes cannot be realised.

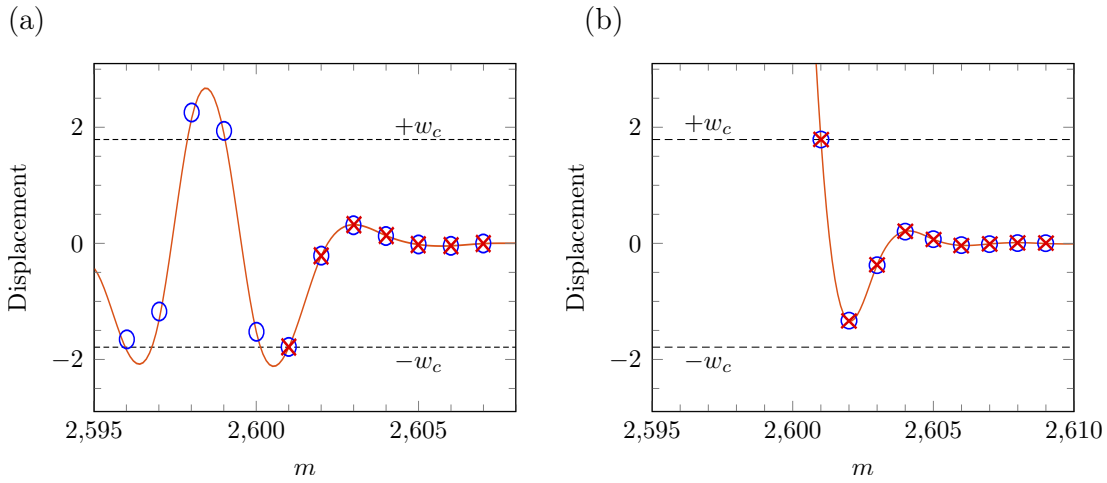

Figure 6.17: Snapshots of the transition front steadily propagating, with two different regimes, through the structure excited by a harmonic load of frequency $\omega_0 = 3.1$. In (a) the snapshot is taken at $t = 1012.4$ for $\mathcal{P} = 13.115$ and there the alternating generalised strain regime propagates with the average speed $\bar{v} = 0.6307$. In (b) $t = 403$ with $\mathcal{P} = 33.484$ and this corresponds to a pure steady-state failure regime with the average speed $\bar{v} = 1.7484$. The blue circles in each panel are based on the analytical results presented in Section 6.3 and represent the mass displacements. The crosses indicate those masses situated in the supported region. The critical displacement for the links in the supported region is $w_c = 1.7919$ and the limits corresponding to this value are shown by horizontal dashed lines. The profiles shown are obtained from the *Matlab* simulations by identifying the nodal displacements and rotations and using the results of Appendix 6.1.2 to reconstruct the deformation for the massless beams. In both computations the heterogeneity parameter $r = 0.4$.

Behaviour of the system during the dynamic failure processes

For $\mathcal{P} = 13.115$, Figure 6.17(a) shows the system undergoing failure at a particular time $t = 1012.4$ after the fracture of 600 pairs of transverse links. The failure here propagates steadily under the alternating generalised strain regime. The average speed of this process observed from the *Matlab* simulations is $\bar{v} = 0.6307$. In this case, one can observe the combination of the feeding and reflected waves behind the transition front. Ahead of this point, there exists an evanescent wave. We note that at approximately $t = 1034.0$, when the next failure occurs, the profile of the structure can be obtained from that shown in Figure 6.17(a) mirrored about a horizontal line that corresponds to zero displacement. In Figure 6.17(b), we consider a pure steady-state regime resulting from when external load amplitude $\mathcal{P} = 33.484$. The time when the snapshot is taken is $t = 403$. The average steady-state speed achieved is $\bar{v} = 1.7490$ and as the failure propagates steadily, the profile of the structure local to the transition front is preserved. Figure 6.17(b) is an example of the pure steady-state regimes studied in [Nieves, Mishuris and Slepyan (2016), Nieves,

Mishuris and Slepyan (2017)] that also occur in the simulations presented here.

In Figures 6.17(a) and 6.17(b), we compare the *Matlab* simulation data for the arrangement of the masses along the profiles with the analytical results of Section 6.3 and [Nieves, Mishuris and Slepyan (2016), Nieves, Mishuris and Slepyan (2017)]. In Figure 6.17(a), for the computations based on the analytical results, the inverse Fourier transform of (6.40) and (6.41) is computed using (6.71), ensuring that (6.46) holds for the feeding wave phase determined from (6.44). For the computations in Figure 6.17(b), the same procedure is followed based on the results of [Nieves, Mishuris and Slepyan (2016), Nieves, Mishuris and Slepyan (2017)]. We emphasise there is again an excellent agreement between the *Matlab* results and the analytical predictions.

Failure induced by a high frequency.

Here, we give an example of when the alternating generalised strain regime is never realised. In this illustration, $\omega_0 = 5.9$ and $r = 0.4$. As mentioned earlier in Section 6.5.2, the analytical model predicts a semi-infinite list of possible speeds for both the alternating generalised strain regimes and the pure steady-state regimes (also see the dispersion curves of Figure 6.9 with the intersection points for $\omega = 5.9\,(= \omega_0)$). However, we observe only one of the predicted steady-state speeds in the *Matlab* simulations.

Figure 6.18(a), shows the average speed $\bar{v}$ as a function of the point load amplitude $\mathcal{P}$. This particular regime identified is a pure steady-state regime and the average failure speed is $\bar{v} = 2.3020$. The load amplitude interval for where this regime is realised is $46.2172 \leq \mathcal{P} \leq 52.612$. There is once again a good agreement with the predictions of analytical model in [Nieves, Mishuris and Slepyan (2016), Nieves, Mishuris and Slepyan (2017)].

In Figure 6.18(b), we show the position of failure within the supported region as a function of the time when $\mathcal{P} = 46.534$, $\mathcal{P} = 49.7$ and $\mathcal{P} = 51.282$. These values are located within interval defining the plateau for the pure steady-state failure process. For $\mathcal{P} = 46.534$, we see that the transition front speed is constant and equal to the

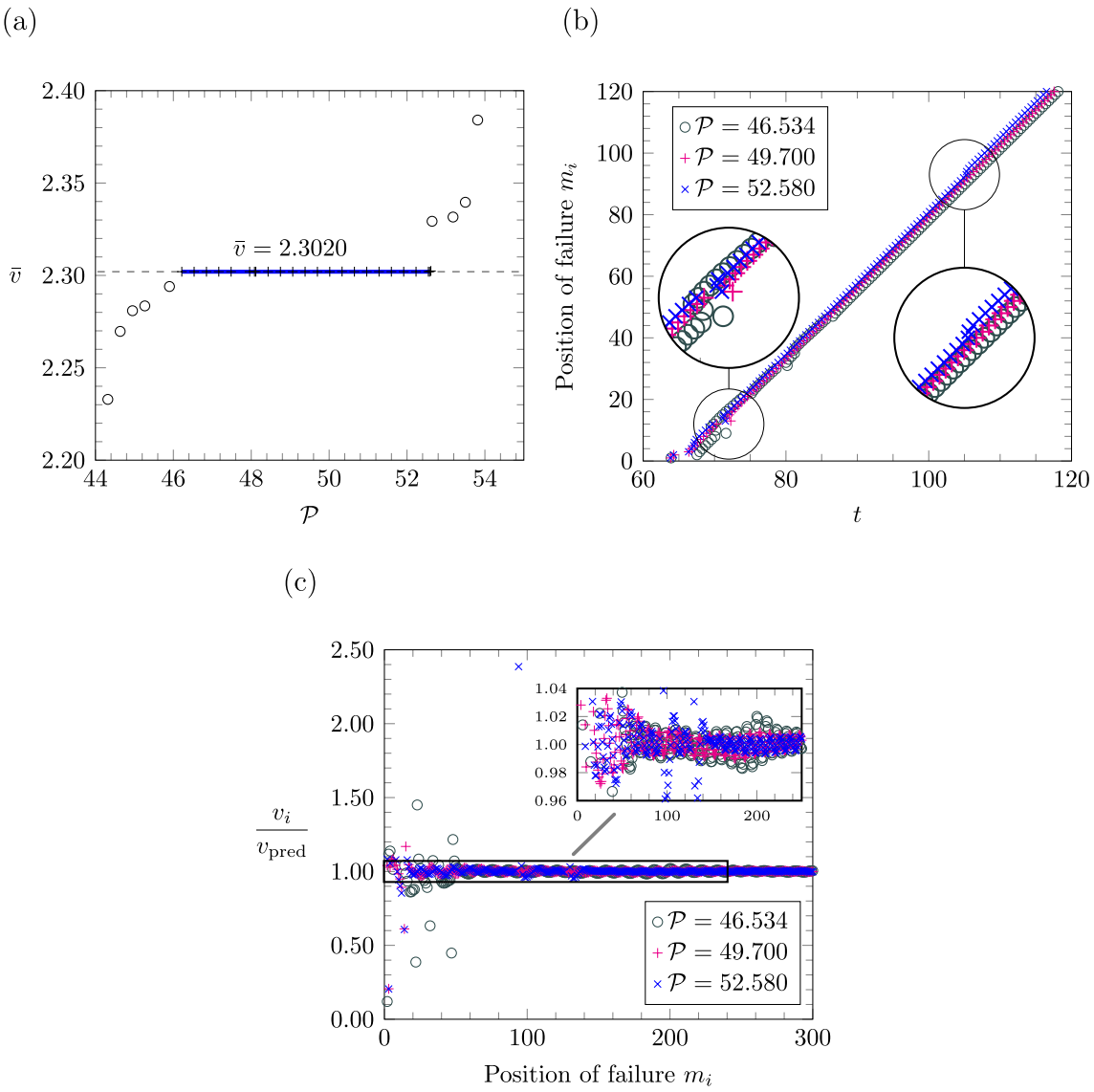

Figure 6.18: Failure regimes identified for $\omega_0 = 5.9$ and $r = 0.4$. (a) The average failure speed is shown as a function of $\mathcal{P}$. The crosses represent results of the *Matlab* simulations where steady-state failure propagation is achieved, whereas as circles correspond to the non-steady failure regimes. The horizontal dashed lines are the predictions for the steady failure speeds based on the analytical model. In (b), we show the position of failure inside the supported part of the structure as a function of time. On the inset in (b), we present magnifications of the profiles where various non-steady propagation phenomena can be observed that are associated with the transient failure process. (c) The normalised instantaneous speed v_i/v_{pred} computed using (6.79) as a function of the failure position.

predicted steady-state speed $v = 2.3020$, after approximately 44 breakages. Prior to this, the front propagates non-steadily in the transient regime. For $\mathcal{P} = 49.7$, the pure steady-state regime is reached earlier at approximately the 13^{th} breakage. For $\mathcal{P} = 51.282$, we see the failure inside the system settles to the steady-state regime after 100 breakages.

For the same amplitudes, in Figure 6.18(c), we present the instantaneous speed v_i, defined by (6.79), as a function of the position of fracture. The instantaneous speeds again oscillate about the speed predicted by the analytical model. It is apparent from Figure 6.18(c) that for those load amplitudes, situated at the extremes of the steady-state plateau in Figure 6.18(a), the failure process will behave irregularly during a large initial period of the failure process. For $\mathcal{P} = 49.700$, which is situated inside the plateau of Figure 6.18(a), the process is seen to converge to a more regular oscillatory behaviour earlier in the failure process.

6.5.3 Case 2 - stiff supports

Here we analyse the failure process in a structure possessing transverse links that are "stiffer" than the links along the central axis of the structure.

Stiffer supports and intermediate load frequency.

Here the supports in the system are characterised by the parameter $r = 3.4$. We first study the case when this structure is subjected to an oscillating force with a frequency $\omega_0 = 3.1$. Although the flexural stiffness of the transverse links inside the supported region is now larger compared to that of the beams along the central axis, the list of admissible steady-state speeds for failure, outlined in Section 6.5.2, remains the same. The *Matlab* simulations described below indicate which of these regimes are realised.

In Figure 6.19(a), we show the average speed $\bar{v}$ as a function of $\mathcal{P}$. We recall the results of Section 6.5.2, where the same load frequency was considered and the structure was supported by transverse links with a lower flexural stiffness. There, it

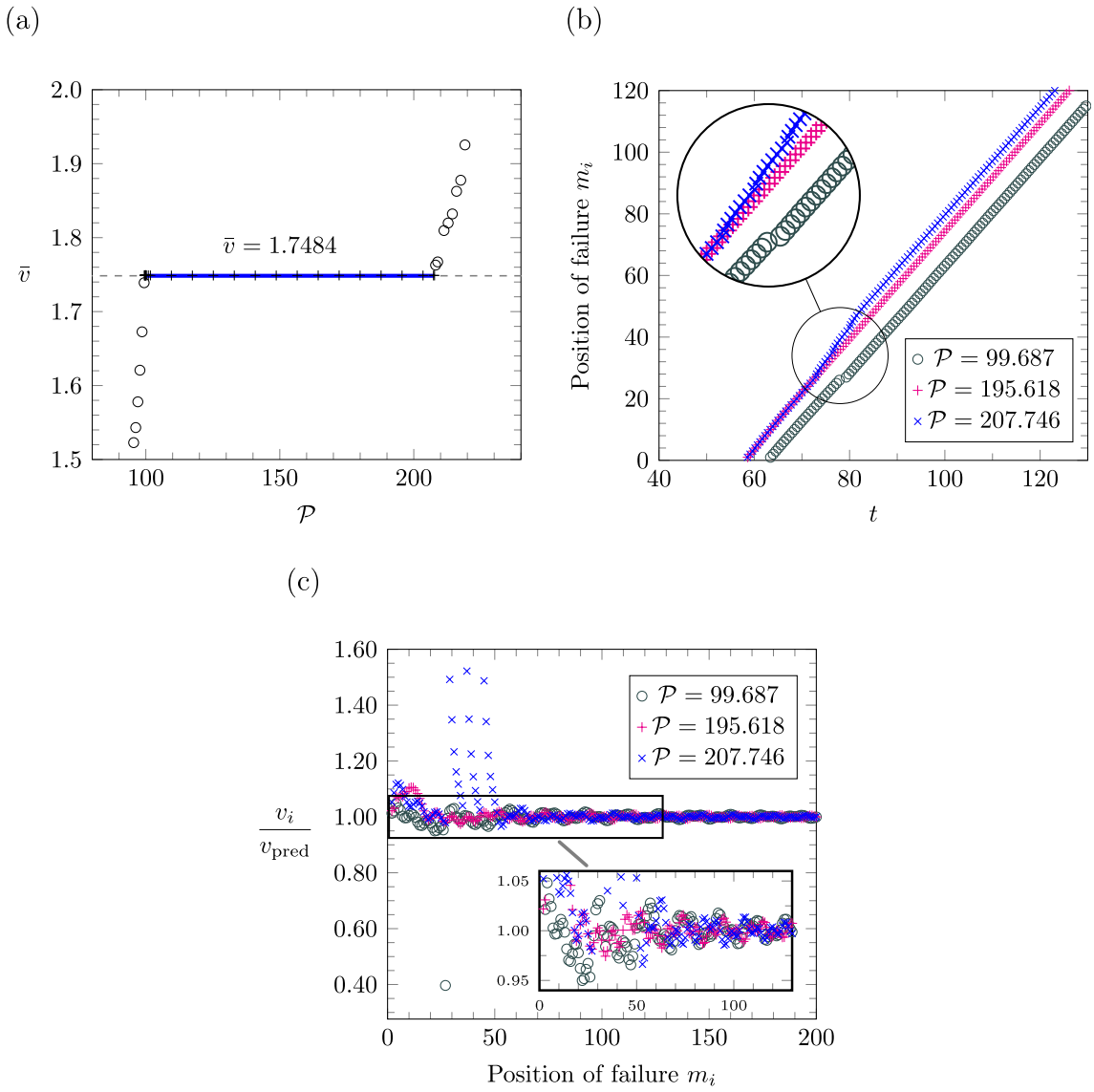

Figure 6.19: Computations for the failure process in the structure with supports characterised by $r = 3.4$ subjected to a load with frequency $\omega_0 = 3.1$. (a) The average failure speed shown as a function of $\mathcal{P}$. Crosses represent the results of the *Matlab* simulations where steady-state failure propagation is achieved. The circles correspond to the non-steady failure regimes. The horizontal dashed lines are the predictions of the failure speeds from the analytical model. In (b), we show the position of failure inside the supported part of the structure as a function of time. (c) The normalised instantaneous speeds based on (6.79) as a function of the position of failure.

was possible to find six failure regimes (both alternating generalised strain regimes and pure steady-state regimes) with different speeds.

When $r = 3.4$, we only observe one of the predicted steady-state speeds, $v = 1.7484$, which corresponds to a pure steady-state regime with the highest possible speed. The regimes analysed in Sections 6.1-6.3 are not observed. In comparing with the computations of Figure 6.15 for the case of a structure with softer supports, we note that the stiffer supports require larger load amplitudes to initiate and maintain the failure propagation, as expected. Moreover, the stiffer supports allow for a larger range of load amplitudes where the highest steady-state speed can be observed (compare Figure 6.19(a) with Figure 6.15). The plateau in Figure 6.19(a) is defined by the interval $99.452 \leq \mathcal{P} \leq 211.972$. This agrees with the predictions based on the results in [Nieves, Mishuris and Slepyan (2016), Nieves, Mishuris and Slepyan (2017)].

Figure 6.19(b), shows the position of failure against time for $\mathcal{P} = 99.687, 195.62$ and 211.815, located in the interval defining the plateau for the steady-state regime. For the load amplitude $\mathcal{P} = 195.62$ the time interval for the initial transient failure process appears to be small and the steady-state regime is realised with the average speed $\bar{v} = 1.7484$. For $\mathcal{P} = 99.687$, the transition front converges to the steady-state regime after approximately 27 breakages. For the largest amplitude $\mathcal{P} = 211.815$, the steady-state failure process is achieved after approximately 48 breakages. It is interesting to note that for this larger load amplitude, the non-steady failure process attributed to the transient regime is visible and the profile propagates in steps that overlap (see inset of Figure 6.19(b)). This failure process is known as a forerunning fracture and was first identified in the study concerning the separation of a beam from an elastic foundation [Slepyan, Ayzenberg-Stepanenko and Mishuris (2015)].

In addition, the normalised instantaneous speeds v_i, calculated using (6.79), are shown in Figure 6.19(c) as a function of the failure position. These computations reveal large fluctuations in the transition front speed about the analytically predicted speed 1.7484, (represented by unity on the vertical axis in this figure). It is evident that the failure process corresponding to the load amplitudes $\mathcal{P} = 99.687$ and 211.815

(located at the extremes of the plateau in Figure 6.19(a)) give large fluctuations in the instantaneous speed of the transition front at the beginning of the failure process. After some time, for all cases shown, the instantaneous speeds oscillate about the predicted speed value in a regular manner and the amplitude of the oscillations decrease as the fracture process develops (see inset of Figure 6.19(c)).

The example presented here shows that the number of failure regimes observed for different structures subjected to a remote sinusoidal load with a fixed frequency can vary. In this case, the stiffer supports have reduced the number of possible failure regimes that are realisable.

High frequency loading of structure with stiff supports.

Finally, we consider a structure with stiff supports and this structure is subjected to a sinusoidal load with a high-frequency loading configurations, which is located near the upper boundary of the passband for unsupported part of the structure.

This particular example shows that the alternating generalised strain regime can be realised in high frequency regimes. In fact, the results of the *Matlab* simulations show there are two regimes encountered, as shown in Figure 6.20(a). In this figure, it can be seen that plateaus exist for $90.386 \leq \mathcal{P} \leq 105.341$ and $218.57 \leq \mathcal{P} \leq 376.664$. These intervals again agree well with the analytical predictions. The plateau corresponding to the alternating generalised strain regime (with predicted speed 1.0344) is very narrow in comparison to plateau belonging to the pure steady-state regime (having the predicted speed 2.3020). If we compare with the computations of Figure 6.13 for the same loading frequency, but for the structure with softer supports, we see the present configuration admits additional failure regimes at lower speeds.

Figure 6.20(b) shows how the position of failure varies as a function of time for load amplitudes chosen inside the plateaus of Figure 6.20(a). The non-steady behaviour of the transition front in the transient regime is noticeable and there exists a visible variation in the failure speed. After this initial period, the system begins to settle to the steady-state failure process. The instantaneous speed distribution obtained using (6.79) for the cases analysed in Figure 6.20(b) is presented in Figure 6.20(c). It

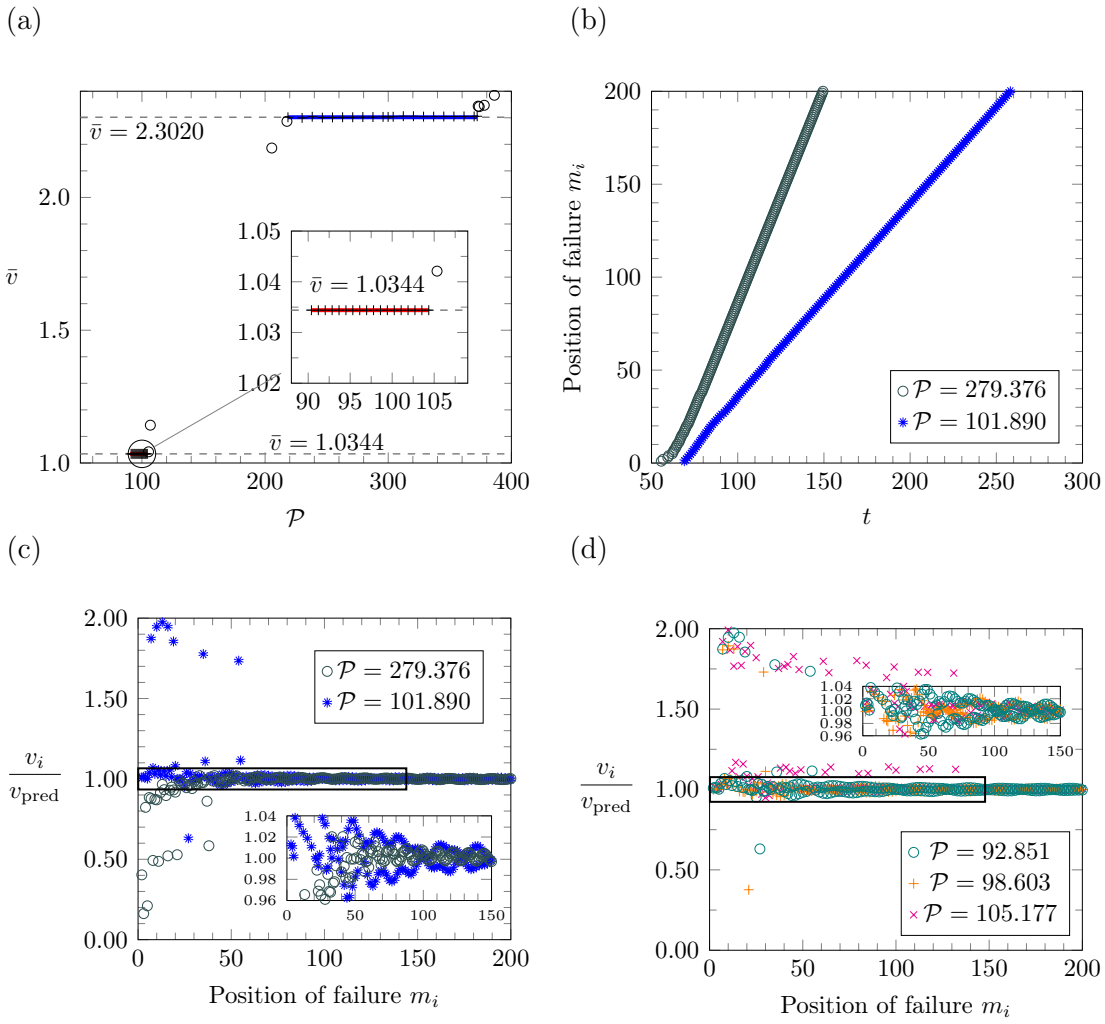

Figure 6.20: Results showing the behaviour of the transition front in the *Matlab* simulations for $r = 3.4$ and $\omega_0 = 5.9$. In (a), the average failure speed shown as a function of $\mathcal{P}$. The crosses are the results of the *Matlab* simulations where steady-state failure is achieved and the circles represent the non-steady failure regimes. The plateau indicated in red is for the alternating generalised strain regime, whereas the blue plateau is for the pure steady-state regime analysed in [Nieves, Mishuris and Slepyan (2016), Nieves, Mishuris and Slepyan (2017)]. Horizontal dashed lines correspond to the predictions for possible failure speeds based on the analytical model. In (b), we show the position of failure as a function of time for load amplitudes situated inside each plateau shown in (a). In (c), the normalised instantaneous speed distributions v/v_{pred} are presented for the data in (b). In (d), for three load amplitudes in the plateau representing the alternating generalised strain regime we present the normalised instantaneous speeds of the failure.

is again evident that there are large oscillations in failure speed about the analytically predicted values in the initial period of the failure process. When the failure process settles, the instantaneous speeds follow a regular oscillatory pattern about the predicted speed. In this example, the computations for the pure steady-state regime ($\mathcal{P} = 279.376$) appear to converge the fastest to the predicted speed (see inset of Figure 6.20(c)) than those for the alternating generalised strain regime. Finally, we comment on the instantaneous speed distributions, shown in Figure 6.20(d), for some load amplitudes within the lowest plateau corresponding to the alternating generalised strain regime. The instantaneous speeds associated with $\mathcal{P} = 92.851$ and $\mathcal{P} = 105.177$, at the extremes of the load amplitude interval defining this plateau, clearly require a large duration of time to settle to the steady-state failure speed. In fact in the case of $\mathcal{P} = 105.177$, several higher speeds are observed up to the 140^{th} instant of failure. Following this, the instantaneous speed eventually settles into steady oscillations about the predicted speed from the analytical model for all cases shown in Figure 6.20(d).

6.6 Conclusions

Here, we have developed the analytical model that characterises a particular failure propagation regime in a flexural system, composed of beams connecting periodically placed masses. The regime identified corresponds to the scenario where the generalised strains, represented by bending moments and shear forces in the beam connections, alternate in sign as the failure advances through the system.

This also marks the first occasion that the failure of 1D infinite flexural structure has been modelled to occur as a result of achieving a critical positive and negative displacement at the failure front. This has previously only been considered in [Mishuris, Movchan and Slepyan (2009)] for systems embedding periodically placed masses connected by elastic rods. Thus the considered failure regime is more realistic due to the fact physical systems, such as those considered in [Mishuris, Movchan and Slepyan (2009)] for Mode III failure, can break if the loading is allowed to change

sign. The system modelled here may also represent a simplified model of the failure of a bridge, whose supporting columns may break due to extension or compression, further supporting the need to consider such failure regimes.

In the considered problem, as in [Brun, Movchan and Slepyan (2013)], we also found that the discrete medium could fail at a steady-state, analogous to the domino effect. Unlike [Nieves, Mishuris and Slepyan (2016), Nieves, Mishuris and Slepyan (2017)], we have identified two regimes that this can occur with: an alternating generalised strain regime and pure steady state regime, where the latter appears in [Nieves, Mishuris and Slepyan (2016), Nieves, Mishuris and Slepyan (2017)].

The analytical results characterising the dynamics of the system during its failure and when possible failure regimes occur have been determined. In particular, the results have been shown to provide excellent predictions for the behaviour of sufficiently long finite systems subjected to sinusoidal loads modelled with independent numerical schemes. There, we confirm the appearance of the two special failure regimes identified for the considered failure condition.

In particular, the numerical simulations revealed that the existence of regimes modelled here is dependent on the parameters governing structure and sinusoidal loading. Perhaps, counter-intuitively, the results here show that the newly identified alternating steady failure regimes can occur for intervals of the sinusoidal load amplitude, agreeing with observations seen in [Mishuris, Movchan and Slepyan (2009)] mass-spring systems.

The analysis presented can be generalised to consider different types of loading and more complicated failure criteria, where other types of special failure phenomena may exist. Applications of the tools developed here are envisaged in civil engineering, where the dynamics and failure of large multi-structures are considered.

Chapter 7

Conclusions

Here, we carried out the dynamic analysis of structured media formed from connecting hexagonal or triangular elastic lattices to gyroscopic spinners. In the time-harmonic regime, we have developed a method for realising interfacial waves in a hexagonal lattice attached to non-uniform arrays of spinners, where this array partitions the hexagonal lattice into subdomains. The subdomains can be unbounded or bounded. The generation of interfacial waves relies on the knowledge of high-frequency dispersion degeneracies possessed by the uniform gyro-elastic medium, known as Dirac points. The spinners can be used to open up small high-frequency stop bands at such points.

An interesting phenomena, highlighted for the first time here arises for frequencies in the vicinity of these small high-frequency stop bands. Namely, for pass band frequencies situated in the immediate neighbourhood of these stop bands, one can generate uni-directional interfacial waves, whose direction is dependent on the loading frequency. Within the stop band, associated frequencies can lead to highly localised waveforms that can propagate along the boundaries of a lattice and the propagation direction is frequency dependent. In the case of interfacial waves, the internal boundary, determined by the spinner array, is also an important feature in the control of the path taken by these waves. We have shown that path traversed by the interfacial waves is easily determined and relies on the choice of the spinner array attached to the lattice.

These effects have also been achieved in hexagonal gyro-elastic systems, whose hexagonal cells have been re-enforced by soft elastic connections, making an inhomogeneous triangular lattice. By increasing the link stiffness in the system, we have shown that there exists a threshold value of this stiffness for which the interfacial waves having preferential directionality can be achieved. These effects are lost as we approach the case of an uniform triangular lattice attached to gyroscopic spinners, resulting from the loss of the high-frequency stop band and the emergence of partial or full pass bands.

We have also undertaken a transient analysis of gyro-elastic systems, motivated by questions concerning if special dynamic phenomena in gyro-elastic media, such as uni-directional highly localised waveforms and interfacial waves, can be realised in these systems. This has led to the development of a novel asymptotic transient model that characterises how a gyroscope interacts with a truss system. In addition to the existing results formulated in the time-harmonic regime [Carta et al. (2018), Nieves et al. (2018)], which show the gyroscope couples the in-plane displacements of the mass in the truss system, the physical parameter known as the gyricity has been identified to be significant in determining the response of the system. The gyricity, which is a quantity associated with the initial dynamic configuration of the gyroscope, acts as an additional input parameter and can be easily tuned to retrieve existing results identified in the time-harmonic regime [Brun, Jones and Movchan (2012)]. Additionally, the ability to freely choose the gyricity potentially offers for a high degree of flexibility in designing new structured materials for a variety of technological applications.

The transient model presented here has been show to give an excellent agreement with independent finite element computations produced in *Comsol*, despite the fact the dimensionality of the model developed and the numerical model differ. For a single gyroscope attached to a mass embedded in a truss system, the mass can describe both typical and atypical trajectories. These trajectories depend on the initial configuration of the system. Illustrative examples linked to this system have also shown that the gyroscopic forcing term coincides with that derived in [Brun,

Jones and Movchan (2012)], for the steady-state regime, when the system's motion describes circular trajectories linked to special choices of initial conditions associated with the system's eigenmodes. However, much more complicated trajectories are possible for more general initial configuration, and the system's motion can be described using linear combinations of eigenmodes.

We have used the transient model to demonstrate that special waveforms identified in the literature [Garau et al. (2018)] and Chapter 3 can be realised in the transient regime with a transient force different from that used in [Wang, Lu and Bertoldi (2015)]. These transient models have also provided insight as to how these special dynamic phenomena evolve in time. In particular cases, we have also shown that these effects can be achieved without the constraint that the gyricity should be equal to the radian frequency of lattice vibration as in [Brun, Jones and Movchan (2012), Garau et al. (2018)].

Applications of the transient model developed here have also been created. We have demonstrated that the gyro-elastic hexagonal structured materials can be used to design novel topological insulators that have potential applications in the design of earthquake barriers. This structure, within a given frequency range, admits a highly localised edge wave with a preferential direction and that traverses the exterior boundary of the medium, leaving the interior of the structured system undisturbed.

Another application developed here includes the first discrete gyro-elastic cloaking device that can be used for the cloaking of elastic waves in lattices. The cloak enables one to reroute waves around defects situated in the lattice medium, preventing significant dynamic interactions between the load and the defects, and reconstructing the wave pattern in the wake of the defects as if the lattice were homogeneous.. Moreover, the design developed here demonstrates such devices can be constructed from a variety of gyroscopic spinners with their gyricity selected so that the cloaking effect can be achieved. For a given gyroscopic spinner, we have also demonstrated that the gyricity can also be used to influence the reconstructed field in such a way that the source appears closer or further away from the observer. We believe that the cloaking effect can be achieved for different lattice loading frequencies by simply

tuning the value of the gyricity inside the cloak.

The failure of a structured flexural system as a result of a remote harmonic load has also been studied in Chapter 6. We have demonstrated that the model considered can be used to reveal vital information about potential failure speeds and regimes in the structure, and that these processes are accompanied by wave radiation phenomena. In particular, we have studied the failure response of the system under a more complex failure criterion previously only considered in [Mishuris, Movchan and Slepyan (2009)] for mass-spring systems. This criterion allows the supporting beams of the structure to fail when a critical positive or negative displacement is achieved by the node that is re-enforced by these members. This new model allows us to incorporate the influence of bending moments and shear forces in modelling the failure processes, where as in [Mishuris, Movchan and Slepyan (2009)] only shear forces brought by the springs plays a role. As a result of the imposed criterion, the identified failure regime impacts on the transient behaviour of the generalised stresses (bending moments and shear forces) inside the structure. The magnitude of these stresses may play an important role in the collapse of the system and the failure process can cause them to alternate in sign as the failure front progresses through the medium. In comparison with the failure processes studied in [Nieves, Mishuris and Slepyan (2016), Nieves, Mishuris and Slepyan (2017)], the failure criterion analysed here allows us to consider more realistic failure regimes in flexural systems that may represent simplified models of collapsed bridges and rooftops exposed to mechanically oscillating loads.

In modelling the failure processes, we have shown that one can obtain the waves radiated into the structure as a result of the collapse of the supporting beams. These waves have been traced from a Wiener-Hopf equation identified from the governing equations of the medium via the Fourier transform. This equation has been solved using the Wiener-Hopf technique and used to understand the behaviour of the medium as it undergoes failure. Additionally, we have constructed a *Matlab* routine that models the failure process inside a sufficiently long finite structure subjected to a sinusoidal mechanical load and we have demonstrated that the analytical model

can fully predict the dynamic phenomena occurring in a finite medium as it fails. This includes the appearance of failure regimes of a given speed and the profile of the structure assumed during these processes. The numerical code has also been shown to reveal information about non-steady failure regimes that may occur in the medium. This includes (i) forerunning regimes, [Slepyan, Ayzenberg-Stepanenko and Mishuris (2015)], where voids ahead of the failure front can appear and coalesce with main failure region and (ii) clustering, [Slepyan, Movchan and Mishuris (2010)], where the crack can propagate in periodic bursts.

Weakness and limitations of the study

Concerning the lattice models considered in this thesis, an important aspect of their study is the assumption these periodic materials are of infinite extent. While this allows for the straightforward implementation of standard techniques in their dynamic analysis, the associated results are only applicable to sufficiently large finite lattices or computational domains supplied with layers of PML, as demonstrated here. They can be very limited in their application to much smaller systems, where the interaction of neighbouring boundaries can be significant. The latter essentially can limit the applicability of the models considered in practical applications.

An additional drawback of the considered models for gyro-elastic lattices considered in the thesis is that they are based on linearised governing equations appearing from the model problem of a gyroscope interacting with a mass in a truss system. In that problem, we did not consider if the nonlinear terms in Euler's equations, neglected under the assumption of small gyroscopic nutations, play a significant role in the dynamic response of the system for larger values of time. If present, such effects could also lead to a variety of different interesting dynamic features in the associated lattice systems than those presented here.

In this work, we also only considered one type of method for linking a gyroscope to a truss system, hence once more limiting the applications of the proposed model. However, utilising the tools developed here and in [Garau et al. (2019)], the range

of possible gyro-elastic structured devices can be extended. Possible consequences of this may include systems embedding rods, gyroscopes and beams and the effects linked to altering the angle at which the gyroscope is hinged at its base.

A limitation of the failure problem considered in Chapter 6 concerns the simplicity of the modelling assumptions used, that may limit the models applicability to analysing collapsing civil engineering systems. These assumptions allow the problem to be treated using methods from the theory of partial differential equations and complex analysis and lead to simple representations of dynamical effects in the system. Our model possesses a lower dimensionality to those commonly encountered in large engineering systems. Additionally, the mass in the structure of Chapter 6 is assumed be distributed at the nodes at its junctions whereas this is not the case, for instance, in a bridge or pipeline system. Hence, in studying the latter one can encounter additional dynamic effects not found in our system. However, the model of Chapter 6 may provide useful information about the collapse of such systems in relatively simple situations. For instance, in [Brun et al. (2014b)], such a simple model was shown to provide highly accurate predictions about the behaviour of the San Saba bridge, Texas, that collapsed as a result of exposure to fire.

The oscillatory loading chosen for the system analysed in Chapter 6 enables one to understand how unwanted vibrations in civil engineering systems such a bridges can be induce possible failure modes. However, there exist several loading considerations where such phenomena can also occur that were not considered here. Such examples include moving forces, which can also be combined with the vibrational loads, and the application of a moments acting behind the transition front. Additionally, loading from ahead of the transition front may also be considered, raising interesting questions such as can one attract a crack? In these cases, our model should be adapted to incorporate such loading configurations, leading to new Wiener-Hopf problems to solve that could lead to a new understanding of the dynamic phenomena brought by these loads.

One may also extend the model to understand new possible mechanisms for which the failure of the flexural system can occur. Possible criteria to be considered

include the failure introduced by the critical rotations or bending moments that will influence when failure regimes can appear and how they behave.

In contrast to the theoretical model of Chapter 6, the associated numerical computations show that the speed of failure can fluctuate around predicted steady-state speeds between consequent breakages of the supports within the flexural system. This is not an artefact of the numerical computations, but reveals the failure process contains phenomena that cannot be predicted by the theory as a result of our modelling assumptions. Hence a different modelling approach would be required to capture such effects observed in the numerical simulations. Finally, we mention the numerical computations of Chapter 6 were performed for a sufficiently long structure, without the use of PML, in an attempt to simulate the infinite medium studied there. We note that such an approach can create significant problems in identifying slow moving failure regimes due to the fact that in such cases, waves generated by the load can be reflected from the computational boundaries and are capable of interacting with the transition front. Thus results agreeing with the theoretical predictions can be extremely difficult to trace.

Future directions

The models presented here will be very useful in the design of civil engineering and seismic protection systems, where understanding failure processes and methods for mitigating the effects of adverse environmental conditions is of high importance. For such applications, it is important to generalise the results presented here to incorporate different loading and failure mechanisms and alternate gyro-elastic connections, leading to the identification of novel dynamic phenomena in the considered lattice systems. This would consequently allow for new concepts of structured materials. In addition, the above limitations and weaknesses of the proposed models should also be addressed in such studies. An immediate next step of the transient lattice model studied in Chapter 4, is to investigate the effect of the gyricity of the gyroscopes and geometry of the lattice microstructure on the system's dynamics. Another important

analysis related to Chapters 4 and 5, but not treated here, involves the analysis of the effective behaviour of the structured gyro-elastic materials considered in this thesis. Additionally, one can use the non-linear transient model of Chapter 4 to study possible dynamic effects induced by this non-linearity. This may provide a valuable alternative tool in the design of metamaterials, which are usually constructed or modelled assuming these materials undergo infinitesimal deformations.

An entirely new and natural research direction arising from the combination of the considered topics includes the analysis of failure in gyro-elastic systems. This is particularly important as the lattice systems proposed here have potential applications in seismic protection and civil engineering. Such an analysis would enable stronger gyro-elastic materials capable of inhibiting and controlling failure processes. The above mentioned studies would provide valuable information about the macroscopic behaviour of these systems and lead to innovative structured devices with novel dynamic phenomena having use in a variety of applications.

Bibliography

[Aboudi and Ryvkin (2014)] J. Aboudi and M. Ryvkin (2014): *Dynamic overshooting in 2D periodic materials with square voids caused by sudden flaw appearance*, Int. J. Solids Struct. 51, 2345–2359.

[Adamou, Craster and Smith (2007)] A. Adamou, R.V. Craster and S.G.L. Smith (2007): *Trapped edge waves in stratified rotating fluids: numerical and asymptotic results*, J. Fluid Mech, 592, 195–220.

[Armanini et al. (2017)] C. Armanini, F. Dal Corso, D. Misseroni and D. Bigoni (2017): *From the elastica compass to the elastica catapult: an essay on the mechanics of soft robot arm*. Proc. Roy. Soc. A. 473: 20160870.

[Atrash and Sherman (2012)] F. Atrash and D. Sherman (2012): *Dynamic fracture instabilities in brittle crystals generated by thermal phonon emission: Experiments and atomistic calculations*, J. Mech. Phys. Solids 60, no. 5, 844-856.

[Bacigalupo and Gambarotta (2016)] A. Bacigalupo and L. Gambarotta (2016): *Simplified modelling of chiral lattice materials with local resonators*, Int. J. Solids Struct., 83, 126-141.

[Berinskii and Slepyan (2017)] I.E. Berinskii and L.I. Slepyan (2017): *How a dissimilar-chain is splitting: Quasi-static, subsonic and supersonic regimes*, J. Mech. Phys. Solid 107, 509–524.

[Bigoni et al. (2014)] D. Bigoni, F. Dal Corso, D. Misseroni and F. Bosi (2014): *Torsional locomotion*, Proc. Roy. Soc. A. 470, 20140599.

[Bordiga et al. (2018)] G. Bordiga, L. Cabras, D. Bigoni and A. Piccolroaz (2018): *Free and forced wave propagation in a Rayleigh-beam grid: Flat bands, Dirac cones, and vibration localization vs isotropization*, Int. J. Solids Struct., 161, 64–81.

[Bosi et al. (2015)] F. Bosi, D. Misseroni, F. Dal Corso and D. Bigoni (2015): *Self-encapsulation, or the 'dripping' of an elastic rod*, Proc. Roy. Soc. A. 471: 20150195.

[Brillouin (1946)] L. Brillouin (1946): *Wave Propagation in Periodic Structures*, McGraw-Hill Book Company, Inc.

[Brun, Guenneau and Movchan (2009)] M. Brun, S. Guenneau and A.B. Movchan (2009): *Achieving control of in-plane elastic waves*, Appl. Phys. Lett. 94, 061903.

[Brun, Jones and Movchan (2012)] M. Brun, I.S. Jones and A.B. Movchan (2012): *Vortex-type elastic structured media and dynamic shielding*, Proc. R. Soc. A, 468, 3027–3046.

[Brun, Movchan and Slepyan (2013)] M. Brun, A.B. Movchan and L.I. Slepyan, (2013): *Transition wave in a supported heavy beam*, J. Mech. Phys. Solids 61, 10, 2067–2085.

[Brun et al. (2014a)] M. Brun, D.J. Colquitt, I.S. Jones, A.B. Movchan and N.V. Movchan (2014): *Transformation cloaking and radial approximations for flexural waves in elastic plates*, New J. Phys. 16, 093020.

[Brun et al. (2014b)] M. Brun, G.F. Giaccu, A.B. Movchan and L.I. Slepyan, (2014): *Transition wave in the collapse of the San Saba Bridge*, Front. Mater., 1–12.

[Cabras, Movchan and Piccolroaz (2017)] L. Cabras, A.B. Movchan and A. Piccolroaz (2017): *Floquet-Bloch waves in periodic networks of the Rayleigh beams: honeycomb systems, dispersion degeneracies and structured interfaces*, Mechanics of Solids, A Journal of Russian Academy of Sciences 5, 93–108.

[Carta et al. (2013)] G. Carta, I.S. Jones, M. Brun, N.V. Movchan and A.B. Movchan (2013): *Crack propagation induced by thermal shocks in structured media*, Int. J. Solids Struct. 50, 2725-2736.

[Carta et al. (2014)] G. Carta, M. Brun, A.B. Movchan, N.V. Movchan and I.S. Jones (2014): *Dispersion properties of vortex-type monatomic lattices*, Int. J. Solids Struct., 51, 2213–2225.

[Carta, Brun and Movchan (2014)] G. Carta, M. Brun and A.B. Movchan (2014): *Dynamic response and localisation in strongly damaged waveguides.* Proc. Roy. Soc. A 470, 2167, 20140136

[Carta and Brun (2015)] G. Carta and M. Brun (2015): *Bloch–Floquet waves in flexural systems with continuous and discrete elements*, Mech. Mater., 87, 11-26.

[Carta et al. (2017a)] G. Carta, I.S. Jones, N.V. Movchan, A.B. Movchan and M.J. Nieves (2017): *"Deflecting elastic prism" and unidirectional localisation for waves in chiral elastic systems*, Sci. Rep., 7, 26.

[Carta et al. (2017b)] G. Carta, I.S. Jones, N.V. Movchan, A.B. Movchan and M.J. Nieves (2017): *Gyro-elastic beams for the vibration reduction of long flexural systems*, Proc. Math. Phys. Eng. Sci., 473, 20170136.

[Carta et al. (2018)] G. Carta, M.J. Nieves, I.S. Jones, N.V. Movchan and A.B. Movchan (2018): *Elastic chiral waveguides with gyro-hinges*, Quart. J. Mech. Appl. Math. 71, 157–185.

[Cazzolli and Dal Corso (2019)] A. Cazzolli and F. Dal Corso (2019): *Snapping of elastic strips with controlled ends*, Int. J. Solids Struct., 162, 285–303.

[Chen and Wu (2016)] Z.G. Chen and Y. Wu (2016): *Tunable topological phononic crystals*, Phys. Rev. Appl., 5, 054021.

[Cherckaev and Ryvkin (2018)] A. Cherkaev and M. Ryvkin (2018): *Damage propagation in 2d beam lattices: 1. Uncertainty and assumptions*, Arch. Appl. Mech. 89, 485–501.

[Cherckaev and Ryvkin (2019)] A. Cherkaev and M. Ryvkin (2019): *Damage propagation in 2d beam lattices: 2. Design of an isotropic fault-tolerant lattice*, Arch. Appl. Mech. 89, 503–519.

[Colquitt et al. (2014)] D.J. Colquitt, M. Brun, M. Gei, A.B. Movchan, N.V. Movchan and I.S. Jones (2014): *Transformation elastodynamics and cloaking for flexural waves*, J. Mech. Phys. Solids 72, 131–143.

[Cserti and Tichy (2004)] J. Cserti and G. Tichy (2004): *A simple model for the vibrational modes in honeycomb lattices*, Eur. J. Phys., 25, 723-736.

[Dal Corso et al. (2017)] F. Dal Corso, D. Misseroni, N.M. Pugno, A.B. Movchan, N.V. Movchan and D. Bigoni (2017): *Serpentine locomotion through elastic energy release*, J. R. Soc. Interface 14: 20170055.

[Del Vescovo and Giorgio (2014)] D. Del Vescovo and I. Giorgio (2014): *Dynamic problems for metamaterials: Review of existing models and ideas for further research*, Int. J. Engng. Sci. 80, 153–172.

[D'Eleuterio and Hughes (1984)] G.M.T. D'Eleuterio and P.C. Hughes (1984): *Dynamics of gyroelastic continua*, J. Appl. Mech., 51, 415-422.

[D'Eleuterio and Hughes (1987)] G.M.T. D'Eleuterio and P.C. Hughes (1987): *Dynamics of gyroelastic spacecraft*, J. Guidance 10, 401–405.

[D'Eleuterio (1988)] G.M.T. D'Eleuterio (1988): *On the theory of gyroelasticity*, J. Appl. Mech., 55, 488-489.

[Evans and Linton (1993)] D.V. Evans and C.M. Linton (1993): *Edge waves along periodic coastlines*, Q. Jl Mech. Appl. Math., 46, no 4, 643–656.

[Farhat et al. (2009)] M. Farhat, S. Guenneau, S. Enoch and A.B. Movchan (2009): *Cloaking bending waves propagating in thin elastic plates*, Phys. Rev. B 79, 033102.

[Farokhi et al. (2017)] H. Farokhi, M. H. Ghayesh, A. Gholipour and S. Hussain (2017): *Motion characteristics of bilayered extensible Timoshenko microbeams*, Int. J. Engng. Sci. 112, 1–17.

[Gao et al. (2015)] W. Gao, M. Lawrence, B. Yang, F. Liu, F. Fang, B. Béri, J. Li and S. Zhang (2015): *Topological photonic phase in chiral hyperbolic metamaterials*, Phys. Rev. Lett., 114, 037–402.

[Garau et al. (2018)] M. Garau, G. Carta, M.J. Nieves, I.S. Jones, N.V. Movchan and A.B. Movchan (2018): *Interfacial waveforms in chiral lattices with gyroscopic spinners*, Proc. Roy. Soc. A. 474, 20180132.

[Garau et al. (2019)] M. Garau, M.J. Nieves, G. Carta and M. Brun (2019): *Transient analysis of a gyro-elastic structured medium: unidirectional waveforms and cloaking*, Int. J. Eng. Sci. (accepted)

[Gei, Movchan and Bigoni (2009)] M. Gei, A.B. Movchan and D. Bigoni (2009): *Band-gap shift and defect-induced annihilation in prestressed elastic structures.* J. Appl. Phys. 105, 063507.

[Ghayesh, Farokhi and Gholipour (2017)] M. H. Ghayesh, H. Farokhi and A. Gholipour (2017): *Oscillations of functionally graded microbeams*, Int. J. Engng. Sci. 110, 35–53.

[Ghayesh (2018)] M. H. Ghayesh (2018): *Dynamics of functionally graded viscoelastic microbeams*, Int. J. Engng. Sci. 124, 115–131.

[Ghayesh (2019)] M. H. Ghayesh (2019): *Viscoelastic dynamics of axially FG microbeams*, Int. J. Engng. Sci. 135, 75–85.

[Gibson and Ashby (1997)] L.J. Gibson and M.F. Ashby (1997): *Cellular solids: structure and properties*, 2nd edn. Cambridge, UK, Cambridge University Press.

[Goldman et al. (2014)] N. Goldman, G. Juzeliūnas, P. Öhberg and I.B. Spielman (2014): *Light-induced gauge fields for ultracold atoms*, Rep. Prog. Phys., 77, 126401, 1–60.

[Goldstein, Poole and Safko (2001)] H. Goldstein, C. Poole and J. Safko (2001): *Classical Mechanics*, 3rd Edition, Pearson.

[Gorbushin and Mishuris (2016)] N. Gorbushin and G.S. Mishuris (2016): *Analysis of dynamic failure of the discrete chain structure with non-local interactions*, Math. Method Appl. Sci. 40, no. 9, 3355–3365.

[Gorbushin et al. (2017)] N. Gorbushin and G. Mishuris (2017): *Dynamic fracture of a discrete dissimilar chain: transient, subsonic and supersonic regimes*, ArXiv, arXiv:1709.02725.

[Gorbushin and Mishuris (2017)] N. Gorbushin and G.S. Mishuris (2017): *On admissible steady-state regimes of crack propagation in a square-cell lattice*, Mech. Sol. 5, 541–548.

[Gorbushin et al. (2018)] N. Gorbushin, G. Vitucci, G.S. Mishuris and G. Volkov (2018): *Influence of fracture criteria on dynamic fracture in discrete chain*, Int. J. Fract. 209, 131–142.

[Gorbushin and Mishuris (2018)] N. Gorbushin and G.S.Mishuris (2018): *Dynamic fracture of a discrete media under moving load*, Int. J. Solid Struct. 130–131, 280–295.

[Graff (1975)] K.F. Graff (1975): *Wave motion in elastic solids*, Oxford, Clarendon Press.

[Hassanpour and Hepper (2016a)] S. Hassanpour and G.R. Heppler (2016): *Theory of micropolar gyroelastic continua*, Acta Mech., 227, 1469-1491.

[Hassanpour and Hepper (2016b)] S. Hassanpour and G.R. Heppler (2016): *Dynamics of 3D Timoshenko gyroelastic beams with large attitude changes for the gyros*, Acta Astron., 118, 33-48.

[He et al. (2010)] C. He, X.L. Chen, M.H. Lu, X.F. Li, W.W. Wan, X.S. Qian , R.C. Yin and Y.F. Chen (2010): *Left-handed and right-handed one-way edge modes in a gyromagnetic photonic crystal*, J. Appl. Phys., 107, 123–117.

[He an Chan (2015)] W.Y. He and C.T. Chan (2015): *The emergence of Dirac points in photonic crystals with mirror symmetry*, Sci. Rep. 5, 8186.

[He et al. (2016)] C. He, X. Ni, H. Ge, X.C. Sun, Y.B. Chen, M.H. Lu, X.P. Liu and Y.F. Chen (2016): *Acoustic topological insulator and robust one-way sound transport*, Nature Phys., 12, 1124-1129.

[Hochstadt (2011)] H. Hochstadt (2011): *Integral Equations*, John Wiley & Sons, New York.

[Hou and Chen (2015)] J.M. Hou and W. Chen (2015): *Hidden symmetry and protection of Dirac points on the honeycomb*, Sci. Rep. 5, 17571.

[Huber (2016)] S.D. Huber (2016): *Topological mechanics*, Nature Phys., 12, 621–623.

[Huges and D'Eleuterio (1986)] P.C. Hughes and G.M.T. D'Eleuterio (1986): *Modal parameter analysis of gyroelastic continua*, J. Appl. Mech., 53, 918-924.

[Hughes (1986)] P.C. Hughes (1986): *Spacecraft Attitude Dynamics*, Wiley, New York.

[Jin et al. (2017)] D. Jin, T. Christensen, M. Sojačić, N.X. Fang, L. Lu and X. Zhang (2017): *Infrared topological plasmons in graphene*, Phys. Rev. Lett., 118, 245301, 1–6.

[Joannopoulos et al. (2008)] J.D. Joannopoulos, S.G. Johnson, J.N- Winn, R.D. Meade (2008): *Photonic Crystals, Molding the flow of light*. Princeton: University Press.

[Kariyado and Hatsugai (2015)] T. Kariyado and Y. Hatsugai (2015): *Manipulation of Dirac cones in mechanical graphene*, Sci. Rep., 5, 18107.

[Khanikaev et al. (2013)] A.B. Khanikaev, S.H. Mousavi, W.K. Tse, M. Kargarian, A.H. MacDonald and G. Shvets (2013): *Photonic topological insulators*, Nature Mater., 12, 233–239.

[Khanikaev et al. (2015)] A.B. Khanikaev, R. Fluery, S.H. Mousavi and A. Alú (2015): *Topologically robust sound propagation in an angular-momentum-biased graphene like resonator lattice*, Nat. Commun., 6, 8260.

[Kirillov (2009)] O.N. Kirillov (2009): *Campbell diagrams of weakly anisotropic flexible rotors*. Proc. R. Soc. A 465(2109): 2703–2723.

[Kirillov (2013)] O.N. Kirillov (2013): *Nonconservative stability problems of modern physics*, De Gruyter, Berlin, Boston.

[Klitzing et al. (1980)] K.V. Klitzing, G. Dorda and M. Pepper (1980): *New method for high-accuracy determination of the fine-structure constant based on quantized Hall resistance*, Phys. Rev. Lett., 45, 494-497.

[Kochmann and Bertoldi (2017)] D. Kochmann and K. Bertoldi (2017): *Exploiting Microstructural Instabilities in Solids and Structures: From Metamaterials to Structural Transitions*, Appl. Mech. Rev. 69: 050801.

[Kucherov and Ryvkin (2014)] L. Kucherov and M. Ryvkin (2014): *Fracture toughness of open-cell Kelvin foam*, Int. J. Solids Struct. 51, 440–448.

[Lu et al. (2014)] L. Lu, J.D. Joannopoulos and M. Soljačić (2014): *Topological photonics*, Nature Photon., 8, 821-829.

[Luo et al. (2012)] Y. Luo, D.Y. Lei, S.A. Maier and J.B. Pendry (2012): *Broadband light harvesting nanostructures robust to edge bluntness*, Phys. Rev. Lett., 108, 023901.

[Maddalena et al. (2009)] F. Maddalena, D. Percivale, G. Puglisi and L. Truskinovsky (2009): *Mechanics of reversible unzipping*, Continuum Mech. Thermodyn. 21, 251–268.

[Makwana and Craster (2018a)] M.P. Makwana and R.V. Craster (2018): *Geometrically navigating topological platonic modes around gentle and sharp bends*, Phys. Rev. B 98, 184105.

[Makwana and Craster (2018b)] M.P. Makwana and R.V. Craster (2018): *Designing multi-directional energy-splitters and topological valley supernetworks*, Phys. Rev. B 98, 235125.

[Maling and Craster (2017)] B. Maling and R.V. Craster (2017): *Whispering Bloch modes*, Proc. R. Soc. A, 472, 20160103.

[Marder (1993)] M. Marder (1993): *Simple models of rapid fracture*, Physica D: Nonlinear Phenomena 66, no. 1: 125-134.

[Marder and Gross (1995)] M. Marder and S. Gross (1995): *Origin of crack tip instabilities*, Journal of the Mechanics and Physics of Solids 43, no. 1, 1–48.

[Marder (2006)] M. Marder (2006): *Supersonic rupture of rubber*, Journal of the Mechanics and Physics of Solids 54, 491–532.

[Marder, Deegan and Sharon (2007)] M. Marder, R.D. Deegan and E. Sharon (2007): *Crumpling, buckling, and cracking: Elasticity of thin sheets*, Physics Today 60, no. 2, 33-38.

[Milton, Briane and Willis (2006)] G.W. Milton, M. Briane and J.R. Willis (2006): *On cloaking for elasticity and physical equations with a transformation invariant form*, New J. Phys. 8, 248.

[Mishuris, Movchan and Slepyan (2007)] G.S. Mishuris, A.B. Movchan and L.I. Slepyan (2007): *Waves and fracture in an inhomogeneous lattice structure*, Waves in Random and Complex Media 17, no. 4, 409–428.

[Mishuris, Movchan and Slepyan (2008a)] G.S. Mishuris, A.B. Movchan and L.I. Slepyan (2008): *Dynamical extraction of a single chain from a discrete lattice*, Journal of the Mechanics and Physics of Solids 56, 487–495.

[Mishuris, Movchan and Slepyan (2008b)] G.S. Mishuris, A.B. Movchan and L.I. Slepyan (2008): *Dynamics of a bridged crack in a discrete lattice*, Quarterly Journal of Mechanics and Applied Mathematics 61, no.2, 151–159.

[Mishuris, Movchan and Slepyan (2009)] G.S. Mishuris, A.B. Movchan and L.I. Slepyan (2009): *Localised knife waves in a structured interface*, Journal of the Mechanics and Physics of Solids 57, 1958–1979.

[Misseroni et al. (2016)] D. Misseroni, D.J. Colquitt, A.B. Movchan, N.V. Movchan and I.S. Jones (2016): *Cymatics for the cloaking of flexural vibrations in a structured plate*, Sci. Rep. 6, 23929.

[Morini and Gei (2018)] L. Morini and M. Gei, (2018): *Waves in one-dimensional quasicrystalline structures: dynamical trace mapping, scaling and self-similarity of the spectrum*, J. Mech. Phys. Solid 119, 83–103.

[Morini, Eyzat and Gei (2019)] L. Morini, Y. Eyzat and M. Gei (2019): *Negative refraction in quasicrystalline multilayered metamaterials.* J. Mech. Phys. Solids 124, 282–298.

[Mousavi, Khanikaev and Wang (2015)] S.H. Mousavi, A.B. Khanikaev and Z. Wang (2015): *Topologically protected elastic waves in phononic metamaterials*, Nat. Commun., 6, 8682.

[Nalitov, Solnyshkov and Malpuech (2015)] A.V. Nalitov, D.D. Solnyshkov and G. Malpuech (2015): *Polariton $\mathbb{Z}$ Topological Insulator*, Phys. Rev. Lett., 114, 116401, 1–5.

[Nash et al. (2015)] L.M. Nash, D. Kleckner, A. Read, V. Vitelli, A.M. Turner and W.T.M. Irvine (2015): *Topological mechanics of gyroscopic metamaterials*, Proc. Natl. Acad. Sci., 112, 14495-14500.

[Ni et al. (2015)] X. Ni, C. He, X.C. Sun, X.P. Liu, M.H. Lu, L. Feng and Y.F. Chen (2015): *Topologically protected one-way edge mode in networks of acoustic resonators with circulating air flow*, New J. Phys., 17, 053016.

[Nieves et al. (2013)] M.J. Nieves, A.B. Movchan, I.S. Jones and G.S. Mishuris (2013): *Propagation of Slepyan's crack in a non-uniform elastic lattice*, Journal of the Mechanics and Physics of Solids 61, no 6, 1464–1488.

[Nieves, Mishuris and Slepyan (2016)] M.J. Nieves, G.S. Mishuris and L.I. Slepyan, (2016): *Analysis of dynamic damage propagation in discrete beam structures*, Int. J. Solids Struct. 97–98, 699–713.

[Nieves, Mishuris and Slepyan (2017)] M.J. Nieves, G.S. Mishuris and L.I. Slepyan, (2017): *Transient wave in a transformable periodic flexural structure*, Int. J. Solids Struct. 112, 185–208.

[Nieves et al. (2018)] M.J. Nieves, G. Carta, I.S. Jones, A.B. Movchan and N.V. Movchan (2018): *Vibrations and elastic waves in chiral multi-structures*, J. Mech. Phys. Solids 121, 387–408.

[Noble (1958)] B. Noble (1958): *Methods based on the Wiener-Hopf technique for the solution of partial differential equations*, Vol. 162, Pergamon press, London.

[Norris (2008)] A.N. Norris (2008): *Acoustic cloaking theory*, Proc. R. Soc. A 464, 2411–2434.

[Norris and Shuvalov (2011)] A.N. Norris and A.L. Shuvalov (2011): *Elastic cloaking theory*, Wave Motion 48, 525–538.

[Padovan (1978)] J. Padovan (1978): *On gyroscopic problems in elasticity*, Int. J. Engng. Sci. 16, 1061–1073.

[Padovan (1979)] J. Padovan (1979): *Gyroscopic effects in micropolar elasticity*, Int. J. Engng. Sci. 17, 433–439.

[Padovan and Adams (1980)] J. Padovan and M. Adams (1980): *On nonconservative gyroscopic eigenvalue problems in elasticity*, Int. J. Engng. Sci. 18, 1333-1348.

[Pal and Ruzzene (2017)] R.K. Pal and M. Ruzzene (2017): *Edge waves in plates with resonators: an elastic analogue of the quantum valley Hall effect*, New J. Phys., 19, 025001.

[Parnell (2012)] W.J. Parnell (2012): *Nonlinear pre-stress for cloaking from antiplane elastic waves*, Proc. R. Soc. A 468, 563–580.

[Pendry, Martin-Moreno and Garcia-Vidal (2004)] J.B. Pendry, L. Martin-Moreno and F.J. Garcia-Vidal (2004): *Mimicking surface plasmons with structured surfaces*, Science, 305, 5685, 847–848.

[Piccolroaz, Movchan and Cabras (2017a)] A. Piccolroaz, A.B. Movchan and L. Cabras (2017): *Rotational inertia interface in a dynamic lattice of flexural beams*, Int. J. Solids Struct. 112, 43–53.

[Piccolroaz, Movchan and Cabras (2017b)] A. Piccolroaz, A.B. Movchan and L. Cabras (2017): *Dispersion degeneracies and standing modes in flexural waves supported by Rayleigh beam structures*, Int. J. Solids Struct.109, 152–165.

[Prall and Lakes (1997)] D. Prall and R.S. Lakes (1997): *Properties of a chiral honeycomb with a Poisson's ratio of -1*, Int. J. Mech. Sci., 39, 305-314.

[Rafsanjani et al. (2018)] A. Rafsanjani, Y. Zhang, B. Liu, S.M. Rubinstein and K. Bertoldi (2018): *Kirigami skins make a simple soft actuator crawl*, Science Robotics 3, 15, eaar7555.

[Raghu and Haldane (2008)] S. Raghu and F.D.M. Haldane. (2008): *Analogs of quantum-Hall-effect edge states in photonic crystals*, Phys. Rev. A, 78, 033–834.

[Ryvkin and Slepyan (2010)] M. Ryvkin and L. Slepyan (2010): *Crack in a 2D beam lattice: Analytical solutions for two bending modes*, Journal of the Mechanics and Physics of Solids 58, 902–917.

[Ryvkin (2012)] M. Ryvkin (2012): *Analytical solution for a Mode III crack in a 3D beam lattice*, Int. J. Solid Struct. 49, 2839–2847.

[Sharma (2015)] B.L. Sharma (2015): *Diffraction of waves on square lattice by semi-infinite crack*, SIAM J. Appl. Math., 75(3), 1171–1192.

[(2016a)] B.L. Sharma (2016): *Edge diffraction on triangular and hexagonal lattice: Existence, uniqueness, and finite section*, Wave Motion 65, 55–76.

[(2016b)] B.L. Sharma (2016): *Wave propagation in bifurcated waveguides of square lattice strips*, SIAM J. Appl. Math 76, no. 4, 1355-1381.

[(2016c)] B.L. Sharma (2016): *Diffraction of waves on triangular lattice by a semi-infinite rigid constraint and crack*, Int. J. Solids Struct., 465–485.

[(2017)] B.L. Sharma (2017): *On scattering of waves on square lattice half-plane with mixed boundary conditions*, Z. Angew. Math. Phys. 68: 120.

[Sherman and Be'ery (2004)] D. Sherman and I. Be'ery (2004): *From crack deflection to lattice vibrations–macro to atomistic examination of dynamic cleavage fracture*, J. Mech. Phys. Solids 52, 1743–1761.

[Sherman (2011)] D. Sherman (2011): *Phonon Emission Induced Dynamic Fracture Phenomena*, Phys. Rev. Lett. 106, 085502.

[Siroki, Huidobro and Giannini (2017)] G. Siroki, P.A. Huidobro and V. Giannini (2017): *Topological photonics: From crystals to particles*, Phys. Rev. B, 96, 041408(R).

[Skirlo et al. (2015)] S.A. Skirlo, L. Lu, Y. Igarashi, Q. Yan, J.D. Joannopoulos and M. Soljačić (2015): *Experimental observation of large Chern numbers in photonic crystals*, Phys. Rev. Lett., 115, 253901.

[Slepyan (2001a)] L.I. Slepyan (2001): *Feeding and dissipative waves in fracture and phase transition I. Some 1D structures and a square-cell lattice*, Journal of the Mechanics and Physics of Solids 49, 469–511.

[Slepyan (2001b)] L.I. Slepyan (2001): *Feeding and dissipative waves in fracture and phase transition II. Phase-transition waves*, Journal of the Mechanics and Physics of Solids 49, 513–550.

[Slepyan (2001c)] L.I. Slepyan (2001): *Feeding and dissipative waves in fracture and phase transition. III. Triangular-cell lattice*, Journal of the Mechanics and Physics of Solids 49, 2839–2875.

[Slepyan and Ayzenberg-Stepanenko (2002a)] L.I. Slepyan and M.V. Ayzenberg-Stepanenko (2002): *Some surprising phenomena in weak-bond fracture of a triangular lattice*, Journal of the Mechanics and Physics of Solids 50, 1591–1625.

[Slepyan (2002b)] L.I. Slepyan (2002): *Models and Phenomena in Fracture Mechanics*, Foundations of Engineering Mechanics, Springer-Verlag Berlin Heidelberg.

[Slepyan (2005)] L.I. Slepyan (2005): *Crack in a material-bond lattice*, Journal of the Mechanics and Physics of Solids 53, 1295–1313.

[Slepyan, Movchan and Mishuris (2010)] L.I. Slepyan, A.B. Movchan and G.S. Mishuris (2010): *Crack in a lattice waveguide*, International Journal of Fracture 162, 91–106.

[Slepyan, Ayzenberg-Stepanenko and Mishuris (2015)] L.I. Slepyan, M.V. Ayzenberg-Stepanenko and G.S. Mishuris (2015): *Forerunning mode transition in a continuous waveguide*, Journal of the Mechanics and Physics of Solids 78, 32-45.

[Souslov et al. (2017)] A. Souslov, B.C. van Zuiden, D. Bartolo and V. Vitelli (2017): *Topological sound in active-liquid metamaterials*, Nature Phys., published online on 2017-07-17.

[Spadoni et al. (2009)] A. Spadoni, M. Ruzzene, S. Gonella and F. Scarpa (2009): *Phononic properties of hexagonal chiral lattices*, Wave Motion, 46, 435-450.

[Spadoni and Ruzzene (2012)] A. Spadoni and M. Ruzzene (2012): *Elasto-static micropolar behavior of a chiral auxetic lattice*, J. Mech. Phys. Solids, 60, 156-171.

[Süsstrunk and Huber (2015)] R. Süsstrunk and S.D. Huber (2015): *Observation of phononic helical edge states in a mechanical topological insulator*, Science, 349, 6243, 47–50.

[Tallarico et al. (2016)] D. Tallarico, N.V. Movchan, A.B. Movchan and D.J. Colquitt (2016): *Tilted resonators in a triangular elastic lattice: Chirality, Bloch waves and negative refraction*, J. Mech. Phys. Solids, 103, 236–256.

[Tallarico et al. (2017)] D. Tallarico, A. Trevisan, N.V. Movchan and A.B. Movchan (2017): *Edge Waves and Localization in Lattices Containing Tilted Resonators*, Front. Mater. 30, 1–16.

[Thomson (1894)] W. Thomson (1894): *The molecular tactics of a crystal*. Oxford: Clarendon Press.

[Trevisan et al. (2016)] A. Trevisan, G.P. Borzi, N.V. Movchan and M. Brun (2016): *Thermal shock driven fracture in a structured solid: dynamic crack growth and nucleation*, Int. J. Fract. 201, no. 2, 167–177.

[Truskinovsky and Vainchtein (2005)] L. Truskinovsky and A. Vainchtein (2005): *Kinetics of Martensitic Phase Transitions: Lattice model*, SIAM J. Appl. Math. 66, no. 2, 533–553.

[Vila et al. (2017)] J. Vila, R.K. Pal and M. Ruzzene (2017): *Observation of topological valley modes in an elastic hexagonal lattice*, Phys. Rev. B, 96, 134307.

[Wang et al. (2008)] Z. Wang, Y.D. Chong, J.D. Joannopoulos and M. Soljačić (2008): *Reflection-free one-way edge modes in a gyromagnetic photonic crystal*, Phys. Rev. Lett., 100, 013–905.

[Wang et al. (2009)] Z. Wang, Y.D. Chong, J.D. Joannopoulos and M. Soljačić (2009): *Observation of unidirectional backscattering-immune topological electromagnetic states*, Nature, 461, 772–775.

[Wang, Lu and Bertoldi (2015)] P. Wang, L. Lu and Bertoldi K. (2015): *Topological phononic crystals with one-way elastic edge waves*, Phys. Rev. Lett., 115, 104302.

[Yamanaka, Heppler and Huseyin (1996)] K. Yamanaka, G.R. Heppler and K. Huseyin (1996): *Stability of gyroelastic beams*, AIAA J., 34, 1270-1278.

[Yang et al. (2015)] Z. Yang, F. Gao, X. Shi, X. Lin, Z. Gao, Y. Chong and B. Zhang (2015): *Topological Acoustics*, Phys. Rev. Lett., 114, 114301.

[Zhang and Qiu (2014)] J. Zhang and X. Qiu (2014): *Non-symmetric deformation of lattices under quasi-static uniaxial compression*, Int. J. Mech. Sci., 78, 72–80.

[Zheng et al. (2018)] L.-Y. Zheng, G. Teocharis, V. Tournat and V. Gusev (2018): *Quasitopological rotational waves in mechanical granular graphene*, Phys. Rev. B 97, 060101(R).

[Zhu et al. (2014)] R. Zhu, X.N. Liu, G.K. Hu, C.T. Sun and G.L. Huang (2014): *Negative refraction of elastic waves at the deep-subwavelength scale in a single-phase metamaterial*, Nat. Commun., 5, 5510.